

Experimental Investigation on Interfacial and Surface Phenomena of Clathrate
and Semi-clathrate Hydrates

by

Yu Wei

A thesis submitted in partial fulfillment of the requirements for the degree of

Doctor of Philosophy

in

Petroleum Engineering

Department of Civil and Environmental Engineering

University of Alberta

© Yu Wei, 2023

Abstract

Clathrate hydrates are compounds where guest molecules are trapped in cages formed between water molecules via hydrogen bonding. They have many promising applications, such as gas storage, energy storage, gas mixture separation and seawater desalination. They may also form inside the oil & gas pipelines at a fast rate and pose a threat to flow assurance. Despite extensive research on physicochemical properties of clathrate hydrates, many knowledge gaps still remain to be filled.

This study presented a systematic investigation on interfacial and surface phenomena of clathrate and semi-clathrate hydrates, including the determination of specific surface free energy and tangential adhesive strength, the quantification of CO₂ hydrate nucleation kinetics, the elucidation of the memory effect and the evaluation of the effect of dispersion on nucleation kinetics and gas uptake capacity of CO₂ hydrate.

The specific surface free energy (γ_{sv}) value of THF hydrate was deduced using an indirect method in the range from 60.4 to 124.2 mJ/m², with an average of 92.3 mJ/m², which was somewhat lower than that of ice. The determination of this fundamental parameter is essential to the understanding of surface phenomena of clathrate hydrates.

Tangential adhesive strength (τ) of THF hydrate and TBAB semi-clathrate hydrate on substrates with different hydrophobicity was measured. Results showed: 1) diminished values of τ as heating

which was speculated to be caused by pre-melting; 2) increased values of τ upon the addition of PVP (a kinetic hydrate inhibitor) on all substrates and 3) higher values of τ on the hydrophobic substrates than on the hydrophilic ones. Our findings may be valuable to hydrate-related flow assurance problems in oil & gas pipelines during hydrodynamic transport.

Nucleation rate of CO₂ hydrate (sI) was determined using a linear cooling ramp method in the presence and absence of a solid wall. It was found: 1) the convergence of nucleation curves with an increasing number of data points; 2) the promoting effect of a stainless-steel wall on hydrate nucleation kinetics; 3) the limitation of Classical Nucleation Theory in explaining hydrate nucleation and 4) the major effect of the guest type on hydrate nucleation kinetics. Our findings offered new insights into the quantification of CO₂ hydrate nucleation kinetics and impact factors of it.

The mechanism of the memory effect was investigated by comparing nucleation curves of CO₂ hydrate formation in fresh and dissociated water. Despite different “amount”, the memory effect was detected when CO₂ hydrate formed in dissociated water both in the presence and absence of a solid wall. A new mechanism was proposed—the memory effect was caused by two components, interfacial gaseous states and bulk guest supersaturation (with or without nanobubbles), with the former one being more effective in size. Our hypothesis supplemented and improved existing hypotheses and might solve this mystery.

The effect of dispersion on CO₂ hydrate formation kinetics was researched in dry water. Results showed that dry water remained stable after being doped with a small amount of nucleation promoters. The presence of SDS and nucleation promoters had no promoting effect on the nucleation kinetics of CO₂ hydrate but significantly promoted crystal growth kinetics of the CO₂ hydrate formation in dry water. We concluded that dispersion and additives promoted CO₂ hydrate nucleation and crystal growth, respectively. Our findings can be utilized to store more CO₂ in a hydrate form at a faster rate.

Overall, we deduced the essential parameter that characterizes the surface properties of hydrates, specific surface free energy. This offered a pathway for the estimation of the work of adhesion and nucleation work. We investigated the influencing factors on hydrate-substrate shear adhesive strengths, which is meaningful for flow assurance. We derived nucleation rates of CO₂ hydrate and elucidated the influencing factors of it, providing a baseline for the industry. We proposed a mechanism explaining the memory effect and it shed light on this long-standing mystery. We investigated the effect of dispersion and additives on CO₂ hydrate formation kinetics. The main findings are significant for the application of gas hydrates in carbon capture and sequestration and relief of the greenhouse effect. This thesis not only advanced the basic understanding and the fundamental knowledge of the surface and interfacial properties of gas hydrates but also provided insightful guidance for the hydrate-related industry.

Preface

This thesis is an original work by Yu Wei. The research was carried out under the supervision of Dr. Nobuo Maeda at the University of Alberta. The data acquisition, data analysis and composition of research papers have all been completed by Yu Wei. My co-authors were responsible for providing funding support, insightful discussion as well as reviewing and revising the manuscript drafts. All contents (except Introduction, Literature Review and Conclusion chapters) have been published in peer-reviewed journals or submitted to journals for review.

Part of Chapter 2 was published in *molecules* journal entitled as “Wei, Yu, and Nobuo Maeda. "Dry Water as a Promoter for Gas Hydrate Formation: A Review." *Molecules* 28.9 (2023): 3731.” The literature review and manuscript writing have all been accomplished by Yu Wei.

Chapter 3 was published in *Energy & Fuels* journal entitled as “Wei, Yu, and Nobuo Maeda. "Critical surface tension and specific surface free energy of clathrate hydrate." *Energy & Fuels* 36.1 (2021): 407-414.” Data acquisition, analysis, and manuscript writing have all been accomplished by Yu Wei.

Chapter 4 was published in *Energy & Fuels* journal entitled as “Wei, Yu, et al. "Critical Shear Stress of Clathrate and Semi-clathrate Hydrates on Solid Substrates." *Energy & Fuels* 36.7 (2022): 3619-3627.” Data acquisition, analysis, and manuscript writing have all been accomplished by Yu Wei.

Chapter 5 was published in *Energy & Fuels* journal entitled as “Wei, Yu, and Maeda Nobuo. "Nucleation Curves of Carbon Dioxide Hydrate in the Absence of a Solid Wall." *Energy & Fuels* 37.5 (2023): 3760-3774.” Setup assembly, data acquisition, analysis, and manuscript writing have all been accomplished by Yu Wei.

Chapter 6 was published in *Chemical Engineering Science* journal entitled as “Wei, Yu, and Nobuo Maeda. "Mechanisms of the memory effect of clathrate hydrates." *Chemical Engineering Science* 270 (2023): 118538.” Data acquisition, analysis, and manuscript writing have all been accomplished by Yu Wei.

Chapter 7 has been submitted to *ACS Sustainable Chemistry and Engineering* journal for possible publication entitled as “Kinetic Promotion of Gas Hydrate Formations Using Dispersions”. Setup assembly, data acquisition, analysis, and manuscript writing have all been accomplished by Yu Wei.

Dedication

This dissertation is dedicated to my beloved parents.

Acknowledgements

Looking back on this four-year journey, I have received a great deal of help and support. First, I would like to express my thankfulness to my supervisor, Dr. Nobuo Maeda, who gave me a valuable opportunity to step into the field of gas hydrate research. During my Ph.D. program, he has been giving me priceless help and continuous supervision. I not only learned knowledge from him but also learned how to think and conduct research in a correct manner. Also, his rigorous attitude towards research and critical and innovative thinking will benefit me my whole life.

I would like to acknowledge my supervisory committee (Dr. Huazhou Li and Dr. Zhehui Jin). My background knowledge in thermodynamics has been greatly strengthened after attending their courses. They also gave me invaluable suggestions and comments to improve this work.

I want to express my gratefulness to my candidacy exam chair and examiners (Dr. Lijun Deng, Dr. Huazhou Li, Dr. Alireza Nouri, Dr. Zhehui Jin and Dr. Bo Zhang). Their advice and comments are indispensable for polishing the deficiencies in my research. I sincerely thank the committee members of my defense (Dr. Carolyn Koh, Dr. Huazhou Li, Dr. Alireza Nouri, Dr. Zhehui Jin and Dr. Bo Zhang).

This study has been conducted as part of the research project supported by Natural Sciences and Engineering Research Council of Canada (NSERC; RGPIN-2019-04241) and Future Energy Systems (T02-Q01). I would like to thank the financial support from China Scholarship Council (No. 201906400035).

I would like to acknowledge the technical help that I received from Mr. John Czuroski, the fruitful discussion and the critical questions raised by Dr. Xuehua Zhang. I would thank Dr. Ergun Kuru and Dr. Samer Adeeb for the permission of conducting experiments in their labs.

I would like to acknowledge my classmates and colleagues (Mr. Qimeng Yang, Mr. Lin Du, Dr. Xinxiang Yang, Dr. Shanshan Yao, Ms. Ying Zhou, Ms. Xin Zhang, Ms. Yawen Gao and Ms. Yanan Li) for their kind help.

Finally, I own a deep sense of gratitude to my parents (Mr. Xiguang Wei and Mrs. Yongmei Mang) for their endless love and unconditional support. Without them, I could not get through difficult times.

Table of Contents

| | |
|--|------|
| Abstract | ii |
| Preface..... | v |
| Dedication..... | vii |
| Acknowledgements..... | viii |
| Table of Contents | x |
| List of Tables..... | xiii |
| List of Figures..... | xiv |
| 1 Introduction..... | 1 |
| 1.1 Overview..... | 1 |
| 1.1.1 What is clathrate hydrate | 1 |
| 1.1.2 Hydrate-related problems..... | 3 |
| 1.1.3 Potential applications of clathrate hydrates | 4 |
| 1.2 Problem Statement..... | 5 |
| 1.3 Objectives of the thesis | 10 |
| 1.4 Hypothesis of the thesis | 11 |
| 1.5 Contributions of the thesis | 12 |
| 1.6 Structure of the thesis..... | 14 |
| 2 Literature Review on Surface and Interfacial Properties of Clathrate Hydrate..... | 16 |
| 2.1 Wetting | 16 |
| 2.2 Adhesion and cohesion..... | 20 |
| 2.3 Nucleation and formation..... | 26 |
| 3 Critical Surface Tension and Specific Surface Free Energy of Clathrate Hydrate | 39 |
| 3.1 Introduction | 39 |
| 3.2 Materials and methods..... | 41 |
| 3.3 Results | 44 |
| 3.4 Discussion | 53 |

| | | |
|-----|---|-----|
| 3.5 | Conclusions | 59 |
| 3.6 | Summary and Relationship to Chapters that Follow | 59 |
| 3.7 | Appendix | 60 |
| 4 | Critical Shear Stress of Clathrate and Semi-Clathrate Hydrates on Solid Substrates..... | 62 |
| 4.1 | Introduction | 62 |
| 4.2 | Materials and methods..... | 66 |
| 4.3 | Results | 73 |
| 4.4 | Discussion | 82 |
| 4.5 | Conclusions | 85 |
| 4.6 | Summary and Relationship to Chapters that Follow..... | 86 |
| 4.7 | Appendix | 86 |
| 5 | Nucleation Curves of Carbon Dioxide Hydrate in the Absence of a Solid Wall | 90 |
| 5.1 | Introduction | 90 |
| 5.2 | Materials and methods..... | 97 |
| 5.3 | Results | 106 |
| 5.4 | Discussion | 115 |
| 5.5 | Conclusions | 132 |
| 5.6 | Summary and Relationship to Chapters that Follow..... | 133 |
| 5.7 | Appendix | 134 |
| 6 | Mechanisms of the Memory Effect of Clathrate Hydrates | 138 |
| 6.1 | Introduction | 138 |
| 6.2 | Materials and methods..... | 145 |
| 6.3 | Results | 152 |
| 6.4 | Discussion | 164 |
| 6.5 | Conclusions | 171 |
| 6.6 | Summary and Relationship to Chapters that Follow..... | 172 |
| 7 | Kinetic Promotion of Gas Hydrate Formations Using Dispersions..... | 173 |

| | |
|---|-----|
| 7.1 Introduction..... | 173 |
| 7.2 Material and methods..... | 177 |
| 7.3 Results..... | 182 |
| 7.4 Discussion..... | 193 |
| 7.5 Conclusions..... | 196 |
| 7.6 Summary and Relationship to Chapters that Follow | 197 |
| 7.7 Appendix..... | 197 |
| 8 Conclusions, Limitations, and Future Works..... | 199 |
| 8.1 Conclusions..... | 199 |
| 8.1.1 Specific Surface Free Energy of Clathrate Hydrate..... | 199 |
| 8.1.2 Critical Shear Stress of Clathrate and Semi-Clathrate Hydrates on Solid Substrates | 199 |
| 8.1.3 Nucleation Curves of Carbon Dioxide Hydrate in the Absence of a Solid Wall 200 | |
| 8.1.4 Mechanisms of the Memory Effect of Clathrate Hydrates | 201 |
| 8.1.5 Kinetic Promotion of Gas Hydrate Formations Using Dispersions..... | 202 |
| 8.2 Industrial contributions | 202 |
| 8.3 Limitations | 204 |
| 8.4 Future works | 206 |
| Reference | 208 |

List of Tables

| | |
|--|-----|
| Table 1-1 Composition of a unit cell of clathrate hydrate | 2 |
| Table 3-1 Surface tension of testing liquids..... | 44 |
| Table 3-2 Contact angle of various liquids on an ice surface | 47 |
| Table 3-3 Critical surface tension of ice | 49 |
| Table 3-4 Contact angles of various liquids on THF hydrate | 50 |
| Table 3-5 Critical surface tension of THF hydrate | 52 |
| Table 3-6 Comparison between studies of γ_{sl} (interfacial tension between hydrate and water) ... | 56 |
| Table 4-1 Summary of chemical used in this work..... | 66 |
| Table 4-2 Advancing and receding contact angles of water on substrates used in this work | 69 |
| Table 5-1 Function of valves in the setup | 105 |
| Table 6-1 Summary of the nucleation rate normalized to the unit interfacial area..... | 164 |
| Table 7-1 The relationship between the morphology of final products and the content of nucleation promoters in 100 g of dry water..... | 179 |

List of Figures

| | |
|---|----|
| Figure 1-1 Illustration of three common clathrate hydrate structures..... | 2 |
| Figure 1-2 Phase diagram of CO ₂ hydrate | 3 |
| Figure 1-3 Schematic illustration of hydrate aggregate formation in an oil-dominant flow | 4 |
| Figure 1-4 Number of publications related to clathrate hydrate during the last 20 years..... | 5 |
| Figure 1-5 Big picture of the primary research objectives | 10 |
| Figure 2-1 Sketch of three-phase contact..... | 17 |
| Figure 2-2 Front view of breaking a bulk solid into two pieces in vacuum. | 21 |
| Figure 2-3 Schematic illustration of the particle (P)–substrate (S) (panel a) and particle (P) – particle (P) (panel b) interaction with the capillary liquid bridge, showing relevant parameters. | 24 |
| Figure 2-4 Schematic diagram of hydrate-substrate sintering (a) and solid-solid adhesion (b). .. | 25 |
| Figure 2-5 Hydrate nucleation in guest supersaturated aqueous solution, from state 1 to state 2. | 26 |
| Figure 2-6 Overall Gibbs free energy change as a function of the radius of nuclei at constant pressure and temperature | 28 |
| Figure 2-7 Dry water prepared with 5 g of hydrophobic nanosilica and 95 g of water and mechanism of hydrophobic nanosilica-stabilized dry water (water-in-air Pickering dispersion). | 31 |
| Figure 2-8 (a) Thermodynamic promoting effect of dry water containing different weight percent of hydrophobic nanosilica on CO ₂ hydrate equilibrium condition; (b) Local gas enrichment at a hydrophobic surface-water interface..... | 33 |
| Figure 2-9 Kinetic promoting effect of dry water on clathrate hydrate formation. | 35 |
| Figure 3-1 Image of the petri dish containing the sample. | 42 |
| Figure 3-2 Schematic illustration of contact measurement setup. | 43 |
| Figure 3-3 Typical droplet of testing liquids on an ice surface..... | 46 |
| Figure 3-4 The relationship between the cosine of the contact angle on ice and the surface tension of the liquid. | 48 |
| Figure 3-5 Typical droplet of testing liquids on a THF hydrate surface..... | 50 |
| Figure 3-6 The relationship between the cosine of the contact angle on THF hydrate and the surface | |

| | |
|--|-----|
| tension of the liquid. | 52 |
| Figure 4-1 Schematic illustration of the shear adhesive strength measurement setup and the sample holders..... | 71 |
| Figure 4-2 Relationship between PVP aqueous solution and PVP monomer molar concentration. | 74 |
| Figure 4-3 Typical images during the process of a shear adhesive strength experiment..... | 75 |
| Figure 4-4 Effect of temperature on the critical shear stress of the hydrate – substrate interface | 77 |
| Figure 4-5 Effect of the addition of 1 wt% kinetic hydrate inhibitor (KHI) PVP10 and PVP360 on TBAB semi-clathrate hydrate – substrate shear adhesive strength..... | 79 |
| Figure 4-6 Effect of the addition of 1 wt% kinetic hydrate inhibitor (KHI) PVP10 and PVP360 on THF hydrate – substrate shear adhesive strength. | 80 |
| Figure 4-7 Effect of the hydrophobicity of the substrate on the critical shear stress of the hydrate – substrate interface. | 81 |
| Figure 5-1 Schematic configuration, top view and side view of the quasi-free water droplet samples. | 99 |
| Figure 5-2 Schematic configuration, top view and side view of the quiescent bulk water samples. | 101 |
| Figure 5-3 Schematic configuration of the high-pressure chamber and the linear cooling system. | 102 |
| Figure 5-4 Schematic illustration of the high-pressure setup. | 105 |
| Figure 5-5 Typical photos of the Teflon sample cell with quasi-free water droplets supported by a thick layer of perfluoromethyldecalin at different states during a linear cooling ramp experiment. | 107 |
| Figure 5-6 Typical photos of the stainless-steel sample model with quiescent bulk water sample at different states during a linear cooling ramp experiment. | 108 |
| Figure 5-7 Survival curves of CO ₂ hydrate formation on a quasi-free water droplet (blue open circle) and on a quiescent water surface in the presence of a stainless-steel wall (red open triangle). | |

| | |
|---|-----|
| | 112 |
| Figure 5-8 Natural logarithm of the survival curves ($\ln F$ vs ΔT) of CO ₂ hydrate formation on a quasi-free water droplet (blue open circle) and on a quiescent water surface in the presence of a stainless-steel wall (red open triangle)..... | 113 |
| Figure 5-9 Experimental nucleation rate of CO ₂ hydrate formation on a quasi-free water droplet (blue open circle) and CO ₂ hydrate formation on a quiescent water surface in the presence of a stainless-steel wall (red open triangle)..... | 114 |
| Figure 5-10 Gas-water interfacial area normalized nucleation curves (nucleation rate per unit area as a function of supercooling) of CO ₂ hydrate formation on a quasi-free water droplet (blue open circle) and on a quiescent water surface in the presence of a stainless-steel wall (red open triangle)..... | 115 |
| Figure 5-11 Survival curves of CO ₂ hydrate formation on a quasi-free water droplet constructed with different datasets. | 116 |
| Figure 5-12 Natural logarithm of the survival curves ($\ln F$ vs ΔT) of CO ₂ hydrate formation on a quasi-free water droplet constructed with different datasets. | 118 |
| Figure 5-13 Gas-water interfacial area normalized nucleation curves of CO ₂ hydrate formation on a quasi-free water droplet constructed with different datasets..... | 119 |
| Figure 5-14 Analysis of nucleation data based on the Classical Nucleation Theory..... | 121 |
| Figure 5-15 Gas-water interfacial area normalized nucleation curves of CO ₂ hydrate formation on quasi-free water droplets (black circle) and methane/propane (C1/C3) mixed gas hydrate formation on quasi-free water droplets (blue triangle), both derived using a linear cooling ramp method. | 125 |
| Figure 5-16 Gas-water interfacial area normalized and TPCL normalized nucleation curves of CO ₂ hydrate formation on a quiescent water surface in the presence of a stainless-steel and a glass wall. | 129 |
| Figure 5-17 Comparison of gas-water interfacial area and TPCL normalized semi-logarithmic nucleation curves of CO ₂ hydrate and that of other gas hydrate in the presence of a SS wall. .. | 132 |
| Figure 6-1 Schematic configuration and the top view of quasi-free ice particles as a seeding. . | 149 |

| | |
|--|-----|
| Figure 6-2 Typical sample image of the ice seeding system (a) and CO ₂ hydrate crystals (b)... | 153 |
| Figure 6-3 Typical images of quasi-free water droplets during different stages of a CO ₂ hydrate reformation experiment..... | 154 |
| Figure 6-4 Typical images of quiescent bulk water during different stages of a CO ₂ hydrate reformation experiment..... | 156 |
| Figure 6-5 Survival curves of CO ₂ hydrate formation or reformation on different samples. | 158 |
| Figure 6-6 Natural logarithm of the survival curves of CO ₂ hydrate formation on different samples. | 159 |
| Figure 6-7 Experimental nucleation curves of CO ₂ hydrate formation on different samples..... | 161 |
| Figure 6-8 Gas-water interfacial area normalized nucleation curves of CO ₂ hydrate formation on different samples. | 163 |
| Figure 6-9 Gas-water interfacial area normalized nucleation curves of CO ₂ hydrate and C1/C3 mixed gas hydrate on quasi-free water droplets | 166 |
| Figure 6-10 Illustration of the dual mechanism of the memory effect. | 171 |
| Figure 7-1 Schematic illustration of the preparation of dry water dispersions and example photographs of powder-like and free-flowing dry water dispersion..... | 178 |
| Figure 7-2 Schematic illustration of the gas line design and experimental setup used for inducing CO ₂ hydrate formation in a linear cooling ramp..... | 182 |
| Figure 7-3 Microscopic images of DW (panel a), DW (SDS) (panel b), DW doped with 0.01 wt % of Snomax (panel c) and DW doped with 0.1 wt % of Snomax (panel d)..... | 183 |
| Figure 7-4 Pressure profiles during a linear cooling ramp experiment under an isochoric condition. | 185 |
| Figure 7-5 Histogram of average supercoolings when CO ₂ hydrate nucleated in a bulk water phase (purple bar), in a bulk SDS solution phase (black bar), in DW in the absence of nucleation promoters (red bar), in DW made from SDS solution (yellow bar) and in DW in the presence of nucleation promoters but different doses (blue bars for 0.1 wt% and green bars for 0.01 wt%). | 187 |

Figure 7-6 a) final average percentage of CO₂-to-hydrate conversion, b) final average gas uptake capacity (mol/mol) normalized to per mole of water. The error bars represent the standard deviations from the average value. 191

1 Introduction

In this chapter, we will briefly introduce clathrate hydrate and the hazards and applications of clathrate hydrate formation. After that, we will present scientific problems to be solved in this thesis. To these problems, objectives and hypotheses that are made in this thesis will then be presented, followed by the contributions of this thesis to academia and industry. The structure of this thesis will be presented at the end of this chapter. This chapter will help non-expert readers access this thesis more easily and have a basic and preliminary understanding of this thesis.

1.1 Overview

1.1.1 What is clathrate hydrate

Gas hydrates, or clathrate hydrates, are ice-like non-stoichiometric compounds where the gas molecules are trapped in the cages formed between water molecules by hydrogen bonding. Many gas molecules, or so-called guest molecules, such as methane, carbon dioxide, propane and hydrogen can form gas hydrates of different crystal structures with water under specific thermodynamic conditions (temperature and pressure). Other than the above-mentioned guest gas, other non-polar liquid molecules like tetrahydrofuran (THF) or cyclopentane (CP) and quaternary ammonium salts like tetrabutylammonium bromide (TBAB) also form clathrate crystals or semi-clathrate crystals with water, respectively. Therefore, gas hydrates are also broadly referred to as clathrate hydrates.

There are three most common crystal structures of clathrate hydrate: sI, sII and sH. The illustration of a unit cell of each structure was shown in Figure 1-1 with each polyhedron representing a cage, reproduced from (Hassanpouryouzband, Joonaki et al. 2020) with permission. Details of the composition of a unit cell of hydrate crystal was shown in Table 1-1. For clarification, a unit cell of sI-forming clathrate hydrate was composed of two 5^{12} small cages (12 pentagons) and six $5^{12}6^2$ large cages (12 pentagons and 2 hexagons), a total of 46 water molecules.

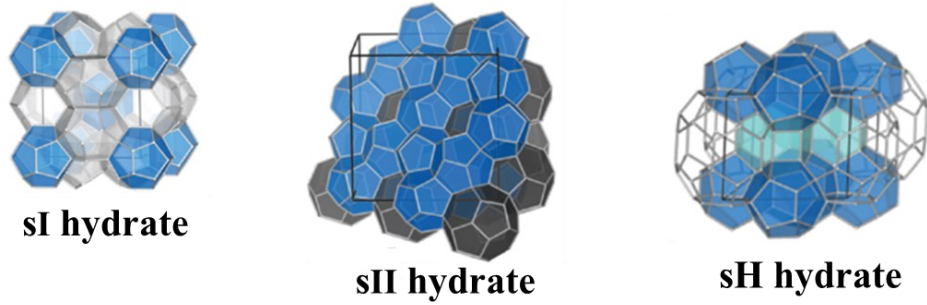


Figure 1-1 Illustration of three common clathrate hydrate structures

Table 1-1 Composition of a unit cell of clathrate hydrate

| Crystal structure | Unit cell |
|-------------------|--|
| sI | $2 (5^{12}) \cdot 6 (5^{12}6^2)$: 46 H ₂ O |
| sII | $16 (5^{12}) \cdot 8 (5^{12}6^4)$: 136 H ₂ O |
| sH | $3 (5^{12}) \cdot 2 (4^35^66^3) \cdot 1 (5^{12}6^8)$: 34 H ₂ O |

Other than clathrate hydrates formed between water and guest molecules, quaternary ammonium salt, TBAB for instance, forms semi-clathrate crystals with water molecules. Since the anion of quaternary ammonium salt is too large to be accommodated in a single cage, several cages break to accommodate it. Therefore, it was also called semi-clathrate hydrate. Both clathrate and semi-clathrate hydrates will be involved in this thesis.

Generally, clathrate hydrates usually form at high-pressure and low-temperature conditions. Figure 1-2 showed the phase diagram of CO₂ hydrate which will be involved in investigation in this work. The solid line is the phase equilibrium curve of CO₂ hydrate where hydrate crystals coexist with CO₂ aqueous solution. On the left side of the phase equilibrium curve, the hydrate

crystal is stable phase because of the lower chemical potential than CO₂-supersaturated solution.

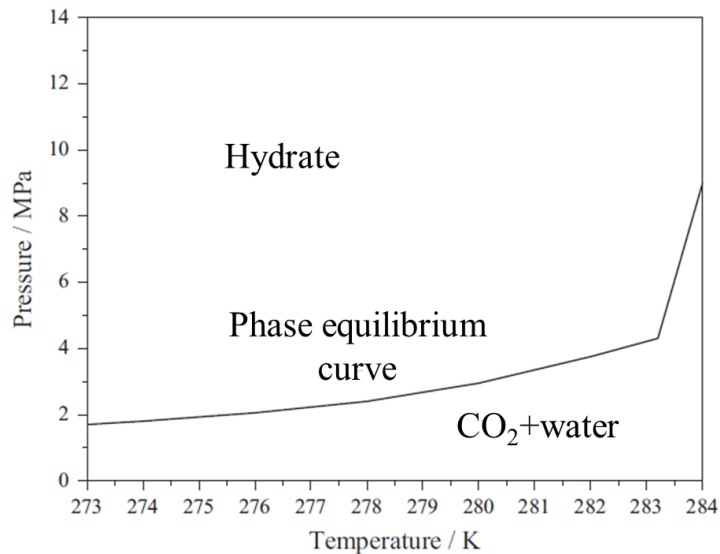


Figure 1-2 Phase diagram of CO₂ hydrate

1.1.2 Hydrate-related problems

Gas hydrates are readily formed in oil & gas pipelines under specific thermodynamic conditions (usually high pressure and low temperature) and then aggregate to a bulk phase from a hydrate slurry with time, finally adhering to the inner wall of pipelines, posing a threat to flow assurance. The formation process of hydrate aggregates in an oil-dominant multiphase flow was illustrated in Figure 1-3, reproduced from (Hu and Koh 2017) with permission. Every year the cost spent on clearing hydrate blockage in pipelines was estimated to exceed \$100 million at a rate near \$1 million per mile of affected pipelines (Tabaaza, Haq et al. 2022). Gas hydrates also pose a threat to drilling engineering. It has been widely acknowledged numerous problems associated with gas hydrates when drilling into a naturally existing gas hydrate formation, including blowouts and well-bore casing failures because of gas hydrate formation in the annulus. Therefore, it is necessary to manage gas hydrate formation in pipelines and drill pipes for safe production and save on costs.

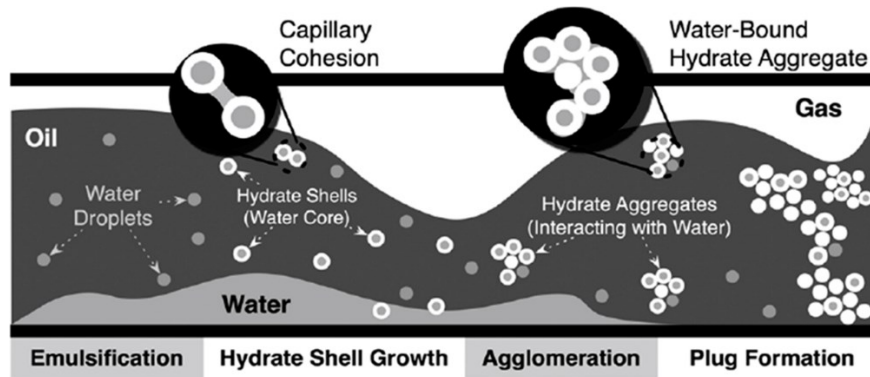


Figure 1-3 Schematic illustration of hydrate aggregate formation in an oil-dominant flow

1.1.3 Potential applications of clathrate hydrates

Despite the aforementioned hydrate-related flow risks, clathrate hydrates have many promising applications. Methane hydrate forms in seafloor (Zatsepina and Buffett 1997, Suess, Torres et al. 2001) and permafrost (Max 2003) because of thermodynamically favorable conditions there. Located on the bottom of the energy pyramid, methane hydrate reservoir was estimated to be around 10^{15} m³ in size. Upon dissociation, 1 m³ of methane hydrate can release about 164 m³ of methane and 0.87 m³ of water (Max and Johnson 2018), which renders methane hydrate a vast reserve of energy. Because clathrate hydrate is capable of enclathrating a huge amount of guest molecules in its structure, it can be employed for gas storage. Hydrogen storage, CO₂ capture and sequestration in the form of clathrate hydrate are recent hot topics. Because of the exclusion of electrolytes from clathrate hydrate crystals during the formation process, clathrate hydrate formation is a novel technology for seawater desalination. By taking advantage of different thermodynamic conditions for the formation of clathrate hydrates of different guest gases, it can also be used for separations of gas mixtures.

As some semi-clathrate hydrates can form at atmospheric pressure and have a relatively high latent heat associated with phase transition, they are promising mediums for cold energy storage

(Yin, Zheng et al. 2021). Semi-clathrate hydrate also serves as a thermodynamic promoter of some clathrate hydrates like hydrogen hydrate and methane hydrate (Veluswamy, Chin et al. 2014, Veluswamy, Kumar et al. 2014) whose thermodynamically stable conditions are demanding on its own because the small cages in semi-clathrate hydrate structure are empty for the accommodation of small guest gas molecules, like H₂ and CH₄.

Given the problems and potential applications associated with clathrate hydrate, it has received extensive attention from researchers around the world. During the last 20 years, the number of publications related to clathrate hydrate showed a rapid increase, as seen in Figure 1-4, reproduced from (Esmaeilzadeh, Hamed et al. 2020) with permission.

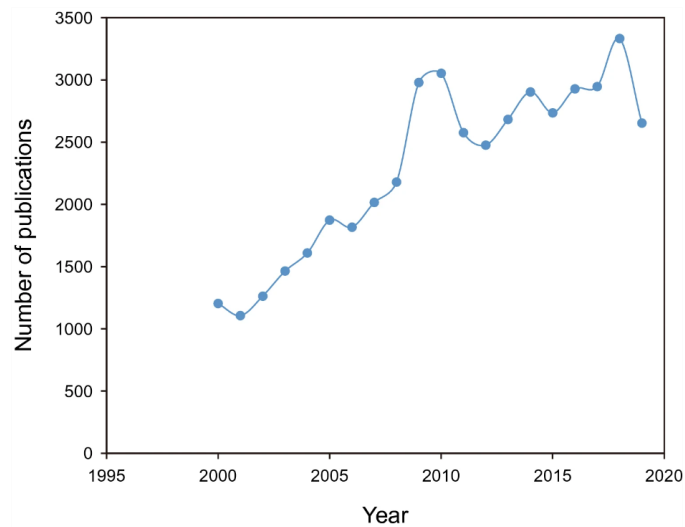


Figure 1-4 Number of publications related to clathrate hydrate during the last 20 years.

1.2 Problem Statement

Despite the wide research on clathrate hydrate, many knowledge gaps remain to be filled and many problems remain to be solved. A majority of these problems originated from the insufficient understanding of the surface and interfacial properties of gas hydrate.

The cohesion between hydrate particles and the adhesion between a hydrate surface and a foreign solid surface plays an important role in hydrate-related flow assurance problems. A majority of previous research has been dedicated to the measurement of normal adhesive/cohesive force. Among these work, it was found that supercooling (Nguyen, Berger et al. 2021), the contact time (Aman, Brown et al. 2011), the surface pre-melting (Nguyen, Berger et al. 2019), roughness (Chenwei, Zhiyuan et al. 2020) and the surface free energy (Aspenes, Dieker et al. 2010) of the foreign solid surface have significant effects on the normal adhesive/cohesive force.

In oil & gas pipelines, formed hydrate particles are subjected to the lateral force (shear force) of the multiphase flow. If the shear adhesive strength between hydrate crystals and the inner wall of pipelines can be well characterized and minimized, then it is possible to transport hydrate particles in the form of hydrate slurry without adhering to the inner wall of pipelines as an aggregate and mitigate hydrate-related flow assurance problems. However, it remains to be addressed if aforementioned influencing factors have the same effect on shear adhesive strength. Besides, additives such as kinetic hydrate inhibitors are commonly used in industry to delay or avoid hydrate formation. The effect of the addition of such additives on the shear adhesive strength is not fully understood up to now. Therefore, it is necessary to quantitatively investigate the shear adhesive strength between hydrate and a solid surface and identify influencing factors and how they take effect.

The adhesion/cohesion of gas hydrate is a function of the specific surface free energy (γ_{sv}) of it. Generally, a solid of high surface free energy is prone to cohere with each other or adhere to other foreign surfaces. Therefore, the value of γ_{sv} of gas hydrate can be used as an indicator of aggregation tendency. This fundamental parameter is closely related to other surface phenomena of gas hydrate, such as pre-melting and nucleation. However, the experimental determination of the specific surface free energy of clathrate hydrate is very difficult, this parameter was only

estimated in the literature. Kashchiev et al. (Kashchiev and Firoozabadi 2002) estimated the value of γ_{sv} of methane hydrate to be around 90 mJ/m² which is comparable to that of ice (100 mJ/m²) reported earlier (Dufour and Defay 1963). Unfortunately, this estimation has not been validated by experiments.

It has been argued that pre-melting exists in gas hydrate as well as in ice based on qualitative reasoning (Maeda 2015). The pre-melting, in return, has a great influence on the adhesion/cohesion of gas hydrate (Aman, Brown et al. 2011, Hu and Koh 2017) and the relative viscosity of a hydrate slurry (Zerpa, Aman et al. 2012). The value of γ_{sv} directly determines the thickness of the pre-melting layer. Because of lack of the accurate values of γ_{sv} , quantitative data on the thickness of the quasi-liquid layer due to pre-melting is very rare with only rough estimation available (Nguyen, Berger et al. 2019). Furthermore, it also determines the activation energy barrier to nucleation, nucleation work. Without knowing the value of γ_{sv} , nucleation work that is essential to nucleation kinetics cannot be accurately theoretically calculated, which hinders us from further understanding nucleation. Therefore, an approach to solve for the value of γ_{sv} of gas hydrate is necessary and will be addressed in this thesis.

As aforementioned, CO₂ hydrate has a potential application on carbon capture and sequestration. However, as the first step of hydrate formation, nucleation usually has a slow kinetics because of gas diffusion barrier (mass transfer limit) and exothermic nature of hydrate nucleation (heat transfer limit) which hinders its large-scale application. To better understand CO₂ hydrate nucleation kinetics, the quantification of the most essential parameter, nucleation rate, is necessary. Recently, several hydrate formation promoters were developed (Nesterov and Reshetnikov 2019, Khandelwal, Qureshi et al. 2020) and the solid wall was regarded to have a crucial effect on hydrate nucleation kinetics (S. B. Cha 1988, Stoporev, Svarovskaya et al. 2018). However, to what extent different solid walls or additives, as a standalone promoting measure, accelerate CO₂ hydrate nucleation in well-defined systems of different sizes cannot be answered

without knowing the nucleation rate of it. The quantification of nucleation rates renders decoupling of the triple effects of increasing interfacial areas, increasing mass transfer rates and lowering activation energy barrier on the promotion of hydrate nucleation kinetics. Only CO₂ hydrate nucleation kinetics in the presence of a glass wall has been thoroughly investigated before (Maeda 2019) but it still needs the understanding of CO₂ hydrate nucleation kinetics in the absence of a solid wall for a comparison, which will be done in this thesis.

Tradition wisdom investigating nucleation kinetics relies on the measurement of induction time but this method has several disadvantages. First of all, given the stochasticity of hydrate nucleation, the determination of a reliable nucleation rate requires a large dataset on induction time statistically. Secondly, at shallow supercooling, the induction time becomes very long, rendering the experiment quite time-consuming. Thirdly, the induction time measurement only enables one to calculate the nucleation rate at a fixed supercooling, not over a continuous supercooling range. Therefore, the determination of nucleation rate as a function of supercooling is crucial for the maximization or minimization of CO₂ hydrate nucleation kinetics. The nucleation rate of CO₂ hydrate in different systems will be determined by an experimental method in this thesis.

The memory effect is one of the longest mysteries in clathrate hydrate nucleation. It is anticipated in terms of hydrate applications but unanticipated if hydrate formation should be avoided. To better take advantage of or suppress the memory effect, an unambiguous picture on it is necessary. Although the properties of the memory effect have been well-documented, the mechanism of it is still a puzzle. Several hypotheses have been put forward to explain the cause of the memory effect, including structural memory (Sloan, Subramanian et al. 1998, Takeya, Hori et al. 2000), guest supersaturation (Rodger 2000), nanobubbles in bulk water (Bagherzadeh, Alavi et al. 2015, Uchida, Yamazaki et al. 2016, Uchida, Yamazaki et al. 2016), impurity imprinting (Zeng, Moudrakovski et al. 2006) and interfacial gaseous states (Maeda 2018). However, none of them succeeds in explaining all known attributes of the memory effect. More interestingly,

manifestation of the memory effect not only depends on thermal history of water but also shows a strong dependence on the solid wall present in the system, which increases the difficulty in explaining the memory effect. Because of the stochastic nature of the memory effect (Bylov and Rasmussen 1997, Fandiño and Ruffine 2014) superimposed on the stochasticity of nucleation itself, it has difficulties in confirming the existence of the memory effect, let alone quantifying its magnitude.

Similar to the study on nucleation kinetics, induction time was normally used as an indicator of the manifestation of the memory effect. It was reported that the induction time of methane hydrate and natural gas hydrate did not become shorter when formed from dissociated water (Bylov and Rasmussen 1997). The credibility of this finding is doubtable owing to the limitation of dual stochasticity and the limited number of data points. Therefore, for a long time, the accurate quantitative investigation on the degree of memory effect is a knowledge gap. Although several influencing factors on the memory effect like nanobubbles and the presence of a solid wall were proposed, how important they play in the “amount” of the memory effect is still unclear. Based on the fact that the memory effect is complex, more than one mechanism might be at play concurrently (Sowa and Maeda 2015). However, what these mechanisms are and how they contribute to the memory effect quantitatively is still a question worth investigating.

Dry water, as a kinetic hydrate promoter, has been shown to behave robustly in promoting gas hydrate formation and gas uptake capacity (Weixing Wang 2008, Carter, Wang et al. 2010), compared to gas hydrate formation in bulk water. Previous research concentrated on the effect of dry water made from either pure water or surfactant aqueous solution on gas hydrate formation kinetics. In this kind of dry water dispersion, the dispersed liquid droplet is single-phase and contains no solid phase. Since the introduction of a water-insoluble but water-dispersible solid particle into the aqueous phase was supposed to be conducive to heterogeneous nucleation (Zhang and Maeda 2022), it is necessary investigating the effect of dry water doping with solid nucleation

promoters on hydrate formation kinetics. If dry water dispersion remains stable after doping a low dose of solid nucleation promoters, this novel dry water in the presence of a solid phase is expected to further promote hydrate formation kinetics and gas consumption, which is beneficial for gas storage in the hydrate form. This topic will be studied in this thesis.

1.3 Objectives of the thesis

The primary objective of this study is to conduct comprehensive experimental studies on the surface and interfacial phenomena of clathrate hydrate including wetting, adhesion and nucleation. From these studies, some essential parameters characterizing surface and interfacial properties were derived or calculated and some influencing factors on surface and interfacial properties were illustrated. The big picture of objectives of the study and correlation between them was shown in Figure 1-5.

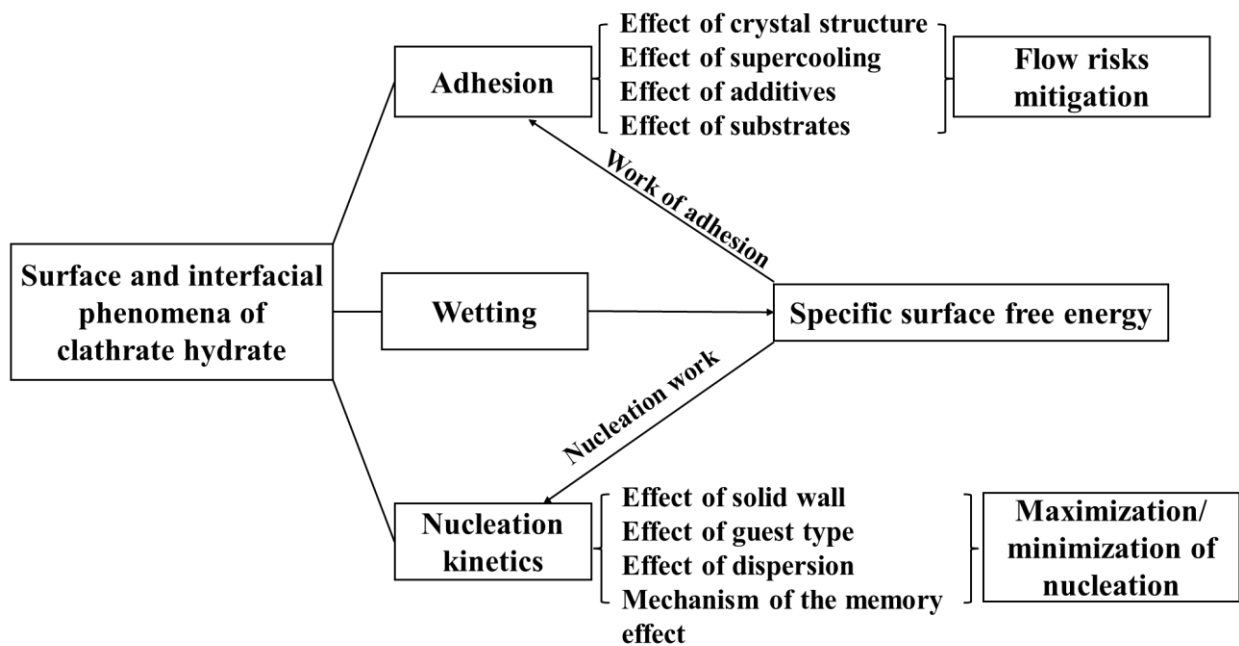


Figure 1-5 Big picture of the primary research objectives

More specifically, this study has the following objectives:

- Establish an indirect method to determine the specific surface free energy of model clathrate hydrate that do not require high pressure to form and use this method to deduce the specific surface free energy of model hydrate.
- Evaluate the effect of supercooling, hydrophobicity of substrates, KHIs on tangential adhesive strength of THF clathrate hydrate-substrate and TBAB semi-clathrate hydrate-substrate.
- Characterize CO₂ hydrate nucleation kinetics in the presence and absence of a solid wall using nucleation curves and evaluate the convergence of nucleation curves.
- Investigate the effect of guest type, solid wall on CO₂ hydrate nucleation kinetics and identify measures to accelerate CO₂ hydrate nucleation kinetics based on this.
- Elucidate the manifestation of the memory effect.
- Propose a reasonable hypothesis explaining the memory effect and quantify the size of it using nucleation curves.
- Investigate CO₂ hydrate formation kinetics in dry water dispersion and analyze the effect of dispersion and nucleation promoters.
- Improve gas uptake capacity and nucleation kinetics of CO₂ hydrate formation in dry water dispersion.

1.4 Hypothesis of the thesis

On one hand, the main hypothesis of this thesis is that the quantification of the relevant surface and interfacial physical parameters of clathrate hydrates such as the specific surface free energy, the tangential adhesive strength and the nucleation rate will give new insights on understanding surface and interfacial properties of clathrate hydrates which cannot be obtained without knowing these parameters. On the other hand, we hypothesize that these parameters will be useful in practical applications because either they are conducive to the mitigation of hydrate-related flow risks or they advance the formation kinetics of clathrate hydrates.

Specific hypotheses were summarized and listed as following:

- The specific surface free energy of ice and clathrate hydrate is comparable.
- The presence of a quasi-liquid layer is assumed to decrease tangential adhesive strength, contrary to its effect on the normal adhesive strength.
- As a surface-active hydrophilic polymer, Polyvinylpyrrolidone (PVP) is hypothesized to affect the tangential adhesive strength between hydrate and substrate.
- The tangential adhesive strength decreases with the increase of hydrophobicity of substrates.
- 400 data points will be sufficient to derive a reliable nucleation curve considering the stochasticity of nucleation.
- Guest is presupposed to have an influence on hydrate nucleation kinetics in a way that the more affinity of it with water, the easier (lower supercooling required) for nucleation and the faster nucleation kinetics (nucleation rate).
- A solid wall is expected to have a crucial effect on promoting hydrate nucleation.
- The memory effect can manifest itself from the comparison between nucleation curves.
- The memory effect might be caused by multi factors given its complexity.
- Dispersion is supposed to have a promoting effect on gas hydrate nucleation kinetics.
- Dispersion and additives function synergistically in enhancing gas hydrate formation kinetics (nucleation and crystal growth).

1.5 Contributions of the thesis

To summarize, the first major contribution of this thesis is the development of the methodology for the determination of the specific surface free energy of clathrate hydrate and the successful determination of it, which is directly related to adhesive strength and the nucleation work. The second contribution is the characterization of tangential adhesive strength between hydrate and substrates, revealing a clearer picture of the adhesion of hydrate on substrates. The third contribution is the determination of hydrate nucleation rate, which enabled systematic and quantitative comparisons between different guest gases and also contributed to the elucidation of

the memory effect. The fourth contribution is the proposal of the mechanism causing the memory effect. The fifth contribution is the improvement of the formation kinetics of gas hydrate in dispersion.

The main contributions of this research can be summarized as follows:

- Established a reliable method for the determination of specific surface free energy of a solid.
- Filled the knowledge gap of the specific surface free energy of clathrate hydrate.
- Investigated and rationalized the influencing factors on the tangential adhesive strength between hydrate and substrates.
- Determined nucleation rates of CO₂ hydrate in the presence and absence of a solid wall.
- Illustrated and quantified some influencing factors on CO₂ hydrate nucleation kinetics.
- Detected the memory effect of CO₂ hydrate in the presence and absence of a solid wall.
- Proposed a dual mechanism hypothesis and quantified the size of the memory effect triggered by each component from derived nucleation curves.
- Evaluated the effect of dispersion and additives on CO₂ hydrate formation kinetics.
- Realized the faster and more storage of CO₂ in the form of hydrate.

These contributions can both advance fundamental knowledge and be used for industrial applications. The successful determination of the specific surface free energy of clathrate hydrate enables the more accurate estimation of work of adhesion and nucleation work. Investigation on the tangential adhesive strength is conducive to the mitigation of hydrate-related flow risks caused by adhesion. Investigation on the CO₂ hydrate formation kinetics not only sheds light on how to maximize and/or minimize the nucleation kinetics of CO₂ hydrate but also improves the gas storage efficiency in a hydrate form which is of great significance to the application of gas hydrate in CO₂ capture and sequestration.

1.6 Structure of the thesis

This PhD thesis is composed of the following 8 chapters which are organized as following:

Chapter 1 provided a general introduction and offered a brief overview of clathrate hydrate and semi-clathrate hydrate, followed by problem statement, objectives of the thesis, hypothesis of the thesis, contributions of the thesis and structural organization of the thesis.

Chapter 2 thoroughly summarized the literature related to the surface and interfacial properties of clathrate hydrate. More specially, wetting, adhesion/cohesion, nucleation and gas uptake kinetics.

Chapter 3 conducted a comprehensive study on determination of the specific surface free energy of THF model hydrate. In this chapter, a new approach deducing the specific surface free energy of THF model hydrate from the measured value of critical surface tension of it was developed and validated. Using this approach, we determined the range of values of the specific surface free energy of THF model hydrate and the most probable value which were compared with that of methane hydrate estimated in the literature and that of ice.

Chapter 4 presented an investigation on the tangential adhesive strength between THF hydrate/TBAB semi-clathrate hydrate and different substrates. The effect of supercooling, crystal structure, addition of kinetic hydrate promoters and the surface chemistry of substrates on the tangential adhesive strength was studied and discussed.

Chapter 5, 6 and 7 focused on the study of CO₂ hydrate nucleation and formation kinetics. Chapter 5 investigated CO₂ hydrate nucleation kinetics in fresh water sample (without hydrate formation history) in the presence and absence of a solid wall. Nucleation curves were derived in these two cases. In comparison with literature data, guest type, mechanical stirring and a solid wall

were found to have a crucial effect on the nucleation kinetics. The limitation of Classical Nucleation Theory in explaining gas hydrate nucleation was realized.

Chapter 6 investigated CO₂ hydrate nucleation kinetics in dissociated water sample (with hydrate formation history) in the presence and absence of a solid wall. Based on the comparison with the results shown in Chapter 5, the memory effect was detected in both cases. After the inspection on existing hypotheses, a dual component hypothesis was proposed to explain the cause of the memory effect. The contribution of each component to the “amount” of the memory effect was quantified based on derived nucleation curves.

Chapter 7 investigated CO₂ hydrate nucleation and formation kinetics in a water-in-air dispersion—dry water. Dry water dispersion and the addition of SDS promoted CO₂ hydrate nucleation and crystal growth, respectively. Doping a tiny amount of nucleation promoters into dry water did not ruin its stability and did not weaken the promoting effect of dry water on CO₂ hydrate nucleation kinetics but improved CO₂ uptake capacity and CO₂-to-hydrate conversion ratio. Promotion of CO₂ hydrate crystal growth did not depend on the concentration of the nucleation promoters present in dry water over the limited range that preserved its stability.

Chapter 8 provided key conclusions and limitations of this study and recommendations for future research.

2 Literature Review on Surface and Interfacial Properties of Clathrate Hydrate

Since the main topic of this thesis is surface and interfacial phenomena of clathrate and semi-clathrate hydrates, this chapter will provide a literature review on three main surface interface phenomena of hydrates: wetting, adhesion and cohesion and nucleation and formation. Research progress and knowledge gaps in these three topics will be presented in this chapter, together with necessary equations that are relevant to these topics. This chapter not only helps the readers understand the research background of the relevant topics but also highlights the necessity of the research conducted in this thesis.

2.1 Wetting

Wetting refers to the spreading ability of a certain liquid on the surface of a solid substrate. Considering three-phase contact, as depicted by Figure 2-1, contact angle (θ) is the angle between the tangential line of liquid-vapor interface and the liquid-solid contact line. γ_{sv} , γ_{sl} and γ_{lv} are specific surface free energy of the solid, specific interfacial free energy between the solid and liquid and surface tension of the liquid, respectively. An equation can be derived according to horizontal force balance, which is Young's equation (eq 2-1):

$$\gamma_{lv}\cos\theta = \gamma_{sv} - \gamma_{sl} \quad \text{eq 2-1}$$

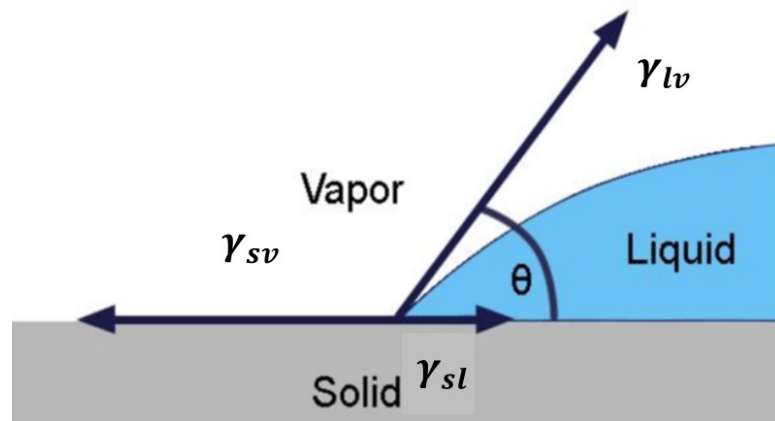


Figure 2-1 Sketch of three-phase contact

The wettability of a solid surface is defined by the contact state of a liquid droplet (usually water) on it. Complete wetting refers to when the liquid spreads on the surface and the contact angle is 0. Partially wetting is defined as when the liquid droplet has a contact angle of less than 90° on the surface. A contact angle of 90° is the boundary between partial wetting and non-wetting. Because the wettability of a solid was usually characterized through the water contact angle on it, the water wettability of solid surfaces is also known as “hydrophilicity/hydrophobicity”. This parameter can also be an interpretation to the surface free energy of a solid, thus being significant. For example, water has a high contact angle of 108° on the surface of polytetrafluoroethylene, according to Zisman et al. (Fox and Zisman 1950, Ellison, Fox et al. 1953). Therefore, the surface of polytetrafluoroethylene was classified as a low energy surface and the spreading of water on it is unfavorable so it is also referred to as hydrophobic. In contrast, water has a low contact angle on the smooth surface of glass or stainless-steel so they were classified as high energy surfaces.

It has been recognized that water wettability of gas hydrate plays a crucial role in optimizing flow assurance in pipelines (Phan, Stoner et al. 2022) as it is related to the cohesive/adhesive forces responsible for hydrate agglomeration and plugging. By using low dosage hydrate inhibitors, the

water wettability of gas hydrate can be altered so that gas hydrate formation and agglomeration behaviors can be inhibited (Zerpa, Salager et al. 2011, Brown, Hu et al. 2018). Anti-agglomerant, for example, is a kind of surface-active component that adsorbs to the surface of hydrate crystals and change the surface wettability of them (Meng, Yang et al. 2018), thus preventing them from agglomerating to a hydrate plug so that dispersed hydrate crystals can be transported in a hydrate slurry. There is also molecular dynamic (MD) simulation research stating the insufficiency to predict anti-agglomerant's performance by the water contact angle on the hydrate surface (Naullage, Bertolazzo et al. 2019).

The assessment of the water wettability of a solid surface can be done by measuring the water contact angle on it. However, this approach is difficult for gas hydrates for several reasons. First of all, gas hydrates usually require high-pressure and low-temperature conditions to form. Different from the contact angle measurements conducted at atmospheric pressure, the contact angle measurement procedure under such conditions is a challenge. Secondly, a flat and smooth surface is required for measurements of contact angle. The preparation of such a hydrate surface is difficult because hydrate surface morphology was reported to vary differently when changing gas compositions and supercooling (Li, Sun et al. 2014). Thirdly, a water droplet has a possibility to form hydrate crystal under the thermodynamic stable conditions of gas hydrates which results in a failure.

Despite the mentioned experimental difficulties, some researchers reported the water contact angle on the surface of gas hydrates. Brown et al. reported the average water contact angle on a CP hydrate of $94.2^\circ \pm 8.5^\circ$ (Brown, Hu et al. 2018). However, recently Thomas et al. reported a fully water wettable CP hydrate surface (Thomas, Dalmazzone et al. 2021). The reason causing such a big discrepancy was speculated that the preparation of hydrate surface greatly impacts the measured contact angle. Stoner et al. reported that the experimental measurement of water contact angle on a CP hydrate surface was influenced by annealing time which influences surface porosity

and by supercooling which influences surface roughness (Stoner, Phan et al. 2021). Although the contact angle of water on CP hydrate which forms at atmospheric pressure has been determined, the contact angle of methane hydrate or natural gas hydrate that requires elevated pressure to form through water has not been determined experimentally so far.

To reconcile the difference in water wettability of gas hydrate reported in the literature and overcome the experimental difficulties, alternatively, MD simulations were implemented to study the water wettability of gas hydrate. Phan et al. (Phan, Stoner et al. 2022) reported the water contact angle on a surface of CP hydrate immersed in CP of 22.3° which correlates well with experimental results under similar temperature and pressure conditions. They also investigated the effect of contact line pinning caused by surface heterogeneities on water contact angle.

Given the hydrate formation in oil/water emulsion in pipelines, it is necessary to study the hydrate wettability under this condition. Høiland et al. developed a method to indirectly quantify the wettability of hydrate particles in a crude oil system using a parameter named Wetting Index and found that the presence of crude oils of different composition strongly affects the wettability of Freon hydrate and that the oil-wet hydrate has a low tendency to agglomeration (Høiland, Askvik et al. 2005). In his another publication in 2009, it was found that the acid extracts extracted from three oils with low hydrate plugging tendency are responsible for the wettability change of Freon hydrate towards a more oil-wet state by the preferential adsorption to a hydrate-oil interface (Erstad, Høiland et al. 2009). The type and structure of these petroleum acids that effectively alter hydrate wettability were found to be more important in functioning than their concentrations in the crude oil (Hoeiland, Barth et al. 2001). Although the average molecular weight of these plug-inhibiting components was determined to be approximately 500 g/mol, the molecular structure of them remains to be uncovered (Borgund, Høiland et al. 2009). As an indicator of hydrate wettability, Fossen et al. (Fossen, Hatscher et al. 2023) determined the Wetting Index for an uninhibited system, a system inhibited by 10 % monoethylene glycol and a system inhibited by

anti-agglomerants. The results indicated that the addition of anti-agglomerant is conducive to the dispersion of hydrate and thus lower hydrate plugging risk. Combining the evaluation of Wetting Index and a flow loop experiment, a conclusion that the dosage of anti-agglomerant for sufficient protection against hydrate plugging depends on the water cut of a multi-phase flow was drawn. From the above review, we can conclude that the wettability change of a hydrate surface from water-wet to oil-wet is conducive to the mitigation of hydrate plugging tendency.

2.2 Adhesion and cohesion

Energy of molecules on the surface is higher than energy of molecules in the bulk because of lacking bonding density of surface molecules. Surface molecules have a tendency to move towards the bulk to minimize the surface area. That's the reason why additional work is required to break a bulk phase and create surfaces. The surface free energy is the excess energy on the surface compared to the bulk. If the surface free energy is divided by the surface area, the specific surface free energy, γ , is obtained. This parameter is used to quantify the work needed to create a unit area of new surfaces. If a bulk of material is subject to external load and break into two pieces in vacuum, as shown in Figure 2-2, the work of cohesion (W) can be expressed as eq 2-2. γ_{sv} is the specific surface free energy of a solid and the A is the area of surface newly created (marked in red in Figure 2-2). Similarly, the work of adhesion was defined as the work required to break the contact between two dissimilar materials.

$$W = 2\gamma_{sv}A \qquad \text{eq 2-2}$$

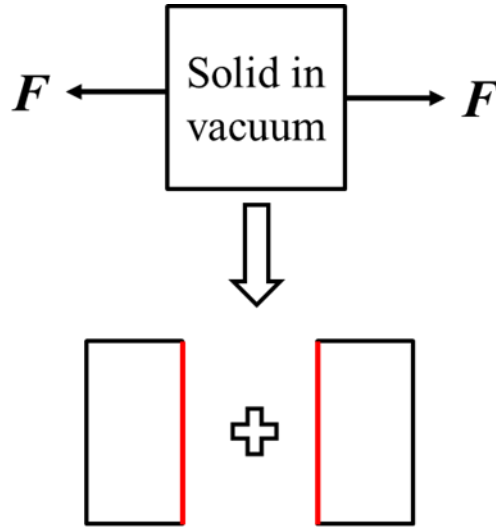


Figure 2-2 Front view of breaking a bulk solid into two pieces in vacuum.

When the temperature and pressure condition inside oil & gas pipelines fall within the stable zone of the hydrate phase diagram, hydrate may form then growing hydrate crystals either cohere with each other or adhere to the inner wall of the oil & gas pipelines, causing flow assurance problems. Therefore, gas hydrate adhesion/cohesion has been widely studied. The normal adhesion between gas hydrate and solid substrates was studied extensively using optical tweezers (Sugimoto, Takahashi et al. 1997), micropipette aspiration (Yeung and Pelton 1996, Simons and Fairbrother 2000), atomic force microscopy (Döppenschmidt, Kappl et al. 1998, Bowen, Lovitt et al. 2000) and micromechanical force measurement (Fan, Ten et al. 2003, Yang, Kleehammer et al. 2004, Taylor, Dieker et al. 2007, Dieker 2009).

The normal hydrate-substrate adhesion force is related to many factors: substrate's hydrophobicity (Aspenes, Dieker et al. 2010), surface roughness of a substrate (Nicholas, Dieker et al. 2009), contact time (Aman, Brown et al. 2011, Hu and Koh 2017), supercooling (Aman, Brown et al. 2011), presence of water on a substrate (capillary bridge effect), solid precipitation and surface corrosion (Liu, Zeng et al. 2020). Nicholas et al. (Nicholas, Dieker et al. 2009) found the adhesion strength between a CP hydrate and a carbon steel was significantly lower than the

cohesion strength between CP hydrate particles. Aspenes et al. (Aspenes, Dieker et al. 2010) found that the normal adhesion force between a CP hydrate and a solid surface depends on the surface free energy of the solid and the presence of water deposited on the solid surface. A similar conclusion has been drawn by Dong et al. (Dong, Li et al. 2020) who fabricated a superhydrophobic coating on an X90 steel substrate with water contact angle of approximately 160° which caused a one order of magnitude reduction in the adhesive force between a CP hydrate and the coated steel, compared with the uncoated steel. Although a hydrophobic coating was stated to effectively decrease the adhesive force when a hydrate is in direct contact with a substrate, the effectiveness of the hydrophobic coating in the reduction of adhesive force decreased when a small water droplet was placed on the surface of a chemically modified surface with a pipette (Aman, Sloan et al. 2014), indicating the insufficiency of the use of surface chemical modification as a standalone measure for eliminating hydrate adhesion to the pipelines containing a free water phase. When petroleum acids were present in the continuous phase, both the adhesion between hydrates and solid surfaces and the cohesion between hydrates were dramatically reduced (Aspenes, Dieker et al. 2010), which is consistent with the finding summarized in the last section that the presence of petroleum acids in pipelines reduces the risk of hydrate plugging.

Nguyen et al. (Nguyen, Berger et al. 2021) investigated the normal adhesive force between a THF hydrate surface and a silica sphere as a function of supercooling, roughness and the hydrophobicity of the silica sphere. This study found that the adhesion force decreases significantly upon the increase of surface roughness of substrates and proved the concept of surface coating for reducing hydrate-substrate adhesion and detected high adhesion force at low supercooling. Hu et al. (Hu and Koh 2017) investigated the cohesive/adhesive force of methane/ethane mixed gas hydrate and found that dependence of hydrate cohesive force on annealing (hydrate shell growth) time, contact time and whether the dominant bulk phase is gas or liquid hydrocarbon. Based on the experimental observation, a capillary liquid bridge model was proposed which was illustrated in Figure 2-3. The surface layer of gas hydrate was argued to have a slightly lower equilibrium

temperature than the bulk gas hydrate. Upon heating to a temperature slightly lower than the bulk hydrate equilibrium temperature (low supercooling), the surface layer of gas hydrate dissociates prior to the bulk gas hydrate and forms a nanometer thick quasi-liquid layer (QLL) (Aman, Brown et al. 2011, Nguyen, Berger et al. 2019), which is the so called pre-melting (Maeda 2015, Maeda 2020). The existence of QLL forms a capillary bridge between hydrate particles or at the hydrate/substrate interface (Figure 2-3) which produces a negative Laplace pressure whose expression was shown in eq 2-3. Because of the curvature of this capillary bridge was estimated to be in *nm* scale, the magnitude of this negative Laplace pressure is large, causing the large adhesion force at low supercooling. The decreased cohesion force with annealing time was attributed that hydrate crystal growth consumes water and reduces the size of capillary bridge and/or QLL between hydrate particles thus resulting a decrease in capillary attractive action. The increase of cohesion force with contact time was supposed to originate from the formation of additional hydrate with contact time (hydrate sintering). The schematic diagram of hydrate sintering was shown in Figure 2-4a), reprinted from (Aman, Sloan et al. 2014) with permission. When contact time is long enough, the cohesive force becomes unmeasurably large because of the permanent cohesion between hydrate particles. Aman et al. (Aman, Brown et al. 2011) developed an equation based on experimental data to predict the CP hydrate cohesive force as a function of contact time.

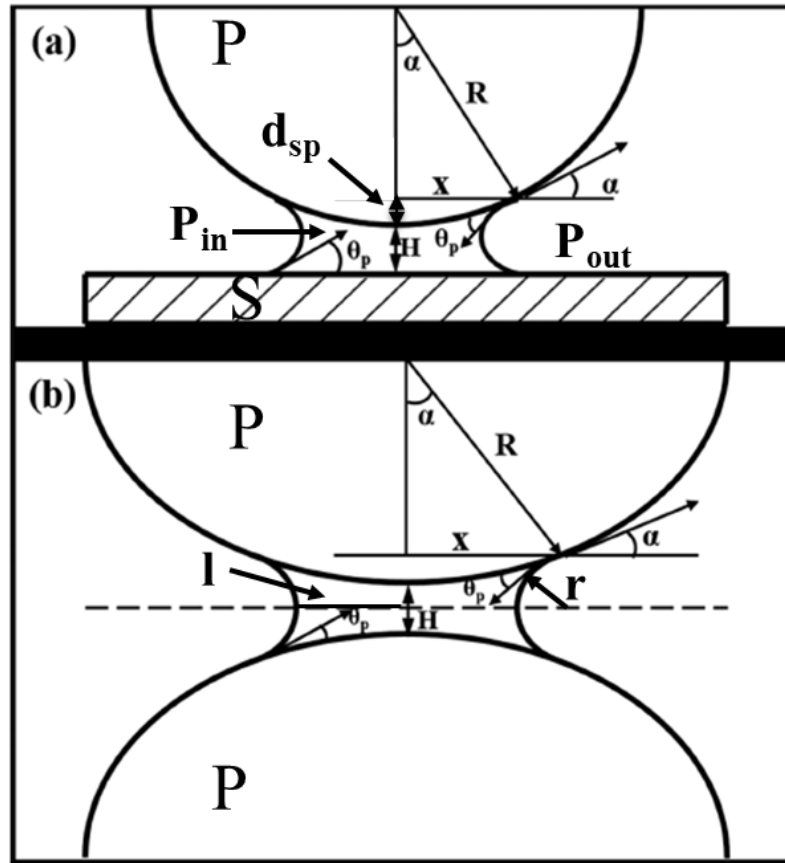


Figure 2-3 Schematic illustration of the particle (P)–substrate (S) (panel a) and particle (P) – particle (P) (panel b) interaction with the capillary liquid bridge, showing relevant parameters. Embracing angle (α), capillary bridge (χ), contact angle (θ_p), immersion depth (d_{sp}), distance between particles (H), bridge radius of curvature (r), particle radius (R). Adapted from (Hu and Koh 2017) with a minor revision.

$$\Delta P = P_{in} - P_{out} = -\gamma\left(\frac{1}{r} - \frac{1}{l}\right) \quad \text{eq 2-3}$$

Where ΔP is the Laplace pressure per unit area; P_{in} and P_{out} are the pressure inside and outside the liquid capillary bridge, respectively; γ is the liquid surface tension; r and l are radii of curvature, as indicated in Figure 2-3.

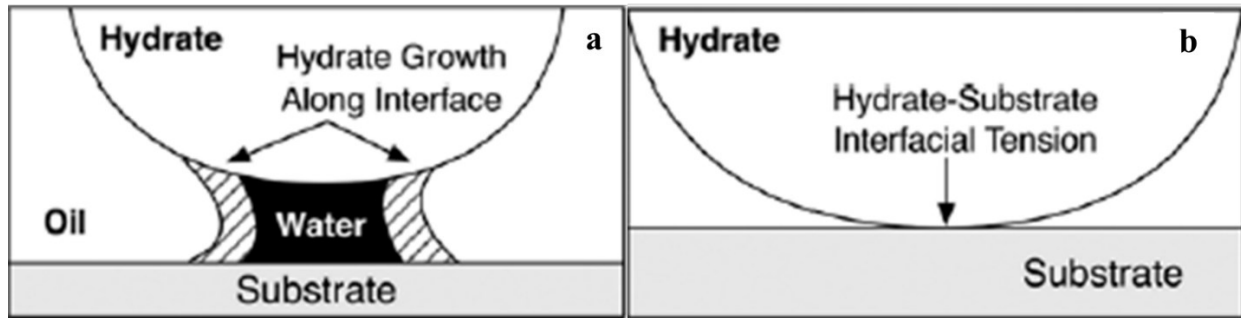


Figure 2-4 Schematic diagram of hydrate-substrate sintering (a) and solid-solid adhesion (b).

Because of different dominant factors, Nguyen et al. divided the adhesion/cohesion of gas hydrate into three temperature-dependent regimes (Nguyen, Berger et al. 2021). At high supercooling region, the adhesion/cohesion force is low and decreases with the increase of supercooling (Aman, Brown et al. 2011) because of the gradually thinning QLL so the dominant factors on hydrate adhesion/cohesion is the Van der Waals forces between hydrate particles or hydrate/substrate. Such a solid-solid adhesion was schematically shown in Figure 2-4b), reprinted from (Aman, Sloan et al. 2014) with permission. At low supercooling, the capillary attraction detailed above governs the adhesion/cohesion force. At even higher temperature than the phase equilibrium temperature of gas hydrate, cohesion/adhesion of gas hydrates no longer exists because of the dissociation of gas hydrates.

Compared to normal adhesive force, another indicator of hydrate adhesion, shear adhesive force was less investigated. With hydrophobic treatment of steel, shear adhesive force between a THF hydrate and a substrate decreased by more than a factor of four as compared with that on a steel surface without any treatment (Smith, Meuler et al. 2012). Liu et al. (Liu, Zeng et al. 2020) measured the shear adhesive force between a sintered CP hydrate (sII) deposit and different solid substrates. The surface corrosion by electrolyte solution, scales, sands and wax precipitation were found to have an influence on the shear adhesive force. Liu et al. (Liu, Wang et al. 2020) also

correlated low shear adhesive force between a CP hydrate and substrates with low supercooling, short hydrate formation time, low roughness and strong hydrophobicity of the surface of a substrate. Matsumoto et al. found that TBAB semi-clathrate hydrate-cooper shear adhesive force was independent of the type of hydrate crystal (type A or type B) but related to supercooling (Matsumoto, Murase et al. 2017).

2.3 Nucleation and formation

Nucleation, generally, refers to the first-order phase transition from a meta-stable phase to a thermodynamically stable phase. For example, the formation of gas bubbles or electrolyte crystals from supersaturated solution and the formation of ice from supercooled liquid water. In this section, we will mainly deal with the gas hydrate nucleation in guest supersaturated aqueous solution which was shown in Figure 2-5 schematically. After nucleation, hydrate crystals start growing spontaneously to a macroscopic size.

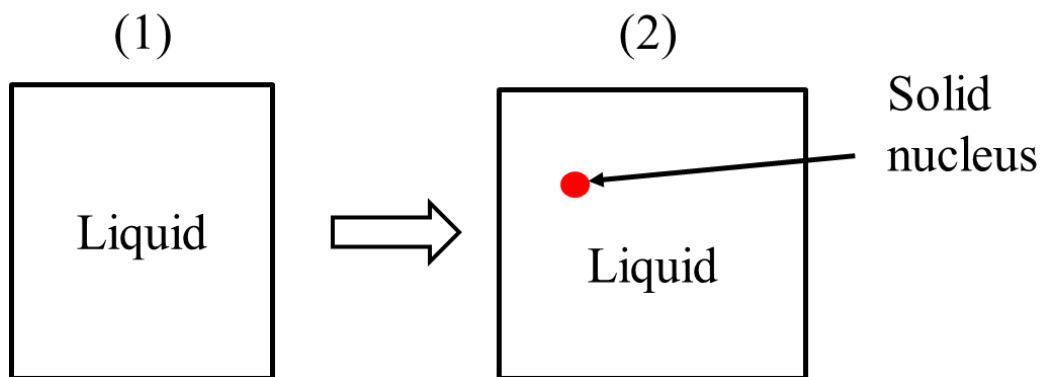


Figure 2-5 Hydrate nucleation in guest supersaturated aqueous solution, from state 1 to state 2.

To start with this section, we have to introduce Classical Nucleation Theory first. From state 1 to state 2 as shown in Figure 2-5, a certain volume of supersaturated solution transitions to hydrate nucleus which causes a decrease in system's free energy because of the lower chemical

potential of the hydrate nucleus than that of the supersaturated solution. On the other hand, a new interface, hydrate nucleus-liquid interface, is created which results in a free energy increase. If the nucleus can be assumed to be a spherical shape, the overall energy change from state 1 to state 2 can be expressed in eq 2-4:

$$\Delta G = 4\pi r^2 \gamma - \frac{4}{3}\pi r^3 \Delta g \quad \text{eq 2-4}$$

Where ΔG is the Gibbs free energy change, r is the radius of a spherical-shaped hydrate nucleus, γ is the specific liquid-solid interfacial free energy and Δg is the energy gain per unit volume. The former term is called solid-liquid interface contribution and the latter term is called the volume contribution.

If ΔG is plotted as a function of radius r , then the overall ΔG shows a trend of first increase then decrease as a function of r because it is a sum of a positive solid-liquid interface contribution in proportional to r^2 and a negative volume contribution in proportional to r^3 (steeper), as shown in Figure 2-6. The radius of nucleus (r^*) at which the overall ΔG gets its maximum (ΔG^*) is defined as the critical size of nucleus because when the size of nucleus is larger than the critical size, the overall ΔG decreases monotonically and the nucleus is stable.

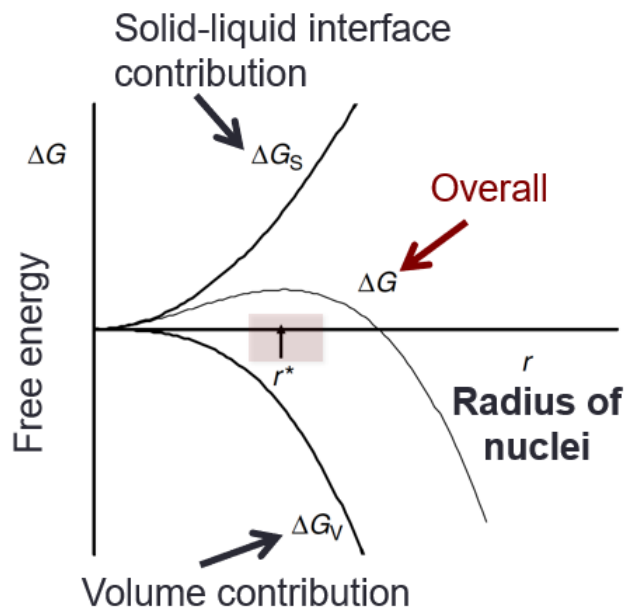


Figure 2-6 Overall Gibbs free energy change as a function of the radius of nuclei at constant pressure and temperature

From Figure 2-6, we can see the nucleation requires a driving force for overcoming the activation energy barrier (ΔG^*). In terms of gas hydrate nucleation, this driving force is the guest supersaturation. Macroscopically, the driving force can be defined as the combination of pressure and supercooling ΔT (the difference between phase equilibrium temperature of hydrate and temperature of supercooled guest supersaturated aqueous solution). The duration of the metastable guest supersaturated solution before the phase transition to a stable hydrate nucleus is the subject of gas hydrate nucleation kinetics. Gas hydrate nucleation kinetics was commonly characterized by the measurement of induction time under a constant driving force, which is the time elapsed from the moment when supersaturation is achieved to the moment of the occurrence of a particular nucleation event. Nucleation rate is defined as the nucleation probability density per unit time per unit system size and can be calculated as the inverse of the most probable induction time (the induction time when half of samples nucleate).

According to Classical Nucleation Theory, nucleation can be further divided into homogeneous nucleation and heterogeneous nucleation. Homogeneous nucleation refers to the nucleation in a homogeneous bulk phase without any container walls or impurities while heterogeneous nucleation refers to the nucleation that occurs at an interface which can either be a container wall or an impurity particle. Homogeneous nucleation and heterogeneous nucleation are correlated by the wettability of the solid surface. Eq 2-5 shows the relationship between the nucleation work of heterogeneous nucleation (ΔG_{heter}^*) and that of homogeneous nucleation (ΔG_{homo}^*) in terms of the contact angle (θ) of a spherical cap-shaped nucleus that forms on the solid surface in the metastable parent phase.

$$\frac{\Delta G_{heter}^*}{\Delta G_{homo}^*} = (1/4)(2 + \cos\theta)(1 - \cos\theta)^2 \quad \text{eq 2-5}$$

In reality, including gas hydrate nucleation, most of nucleation are heterogeneous nucleation because of the lower energy barrier than homogeneous nucleation. Although homogeneous nucleation is unfavorable and unrealistic in most situations, it is still useful as it provides the basis for Classical Nucleation Theory.

Gas hydrate nucleation usually occur at the guest-water interface. This is because guest has a low solubility in water which renders the highest guest supersaturation (thus the highest driving force for nucleation) at the interface. Hydrate films formed at the interface prevent guest molecules from diffusing into bulk water phase because the hydrate phase is mostly impermeable to gases, limiting clathrate hydrate formation to the interface where guest gas contacts water directly. This surface nucleation characteristic renders that the overall heterogeneous nucleation rate of gas hydrate is proportional to the total interfacial areas in the system hence increasing the relevant interfacial areas is conducive to promoting hydrate nucleation kinetics. Because of the guest diffusion barrier, or the mass transfer limitation synonymously, gas hydrate formation kinetics is usually very slow. To address this bottleneck that hinders the application of gas hydrates, several

methods have been employed, such as mechanical stirring (Zhang, Shi et al. 2022), the use of a surfactant as an effective hydrate promoter such as sodium dodecyl sulfate (SDS) (Zhang, Lee et al. 2007, Kang and Lee 2010) which is supposed to increase the solubility of the guest in water and lower the guest aqueous-phase interfacial tension (Kalogerakis, Jamaluddin et al. 1993, Karaaslan and Parlaktuna 2000, Zhong and Rogers 2000, Lin, Chen et al. 2004, Ganji, Manteghian et al. 2007, Okutani, Kuwabara et al. 2008, Kumar, Bhattacharjee et al. 2015), the use of amino acids as an environmentally friendly kinetic hydrate promoter (Liu, Chen et al. 2015, Veluswamy, Hong et al. 2016). Also, Ionic liquids (Lee, Shin et al. 2016) (Gupta, Mondal et al. 2023) (Tariq, Connor et al. 2016) (Zare, Haghtalab et al. 2015) were reported recently to have a promoting effect on gas hydrate formation. However, mechanical stirring consumes a lot of energy which is uneconomical. Many surfactants are toxic and not suitable for some clathrate hydrate applications like water desalination or food processing (Majid, Worley et al. 2021). Another challenge of using a surfactant as a KHP is the severe formation of foams, which have a long lifetime that persists long after hydrate dissociation (Bhattacharjee and Linga 2021). The effectiveness of an amino acid in promoting hydrate formation kinetics was not universal and found to be dependent on the type of the guest gases (Prasad and Sai Kiran 2018).

The following part of this section will introduce an effective method to promote hydrate nucleation and formation kinetics.

In recent years, a novel type of water-in-air Pickering dispersion (aerosol), known as dry water, has emerged as an effective promoter of hydrate formation. Dry water droplets are primarily composed of water and nanoparticles, with water being the primary component. While it was first developed in 1964, it was not until the 1990s that scientists began to extensively study its properties (Saleh, Forny et al. 2011). The application of dry water to hydrate formation promotion was firstly proposed by Wang et al. in 2008 (Weixing Wang 2008). As its name suggests, dry water has the appearance of a free-flowing powder. Although dry water has an appearance of a powder, dry water

is in fact a dispersion (aerosol) in which water is the dispersed phase (droplets) and air is the continuous phase. It is a particle-stabilized dispersion composed of approximately 95% (w/w) water and 5% (w/w) partially hydrophobic nanosilica (Pickering agent). Figure 2-7 depicts the appearance, reproduced from (Weixing Wang 2008) with permission, and stabilizing mechanism of dry water.

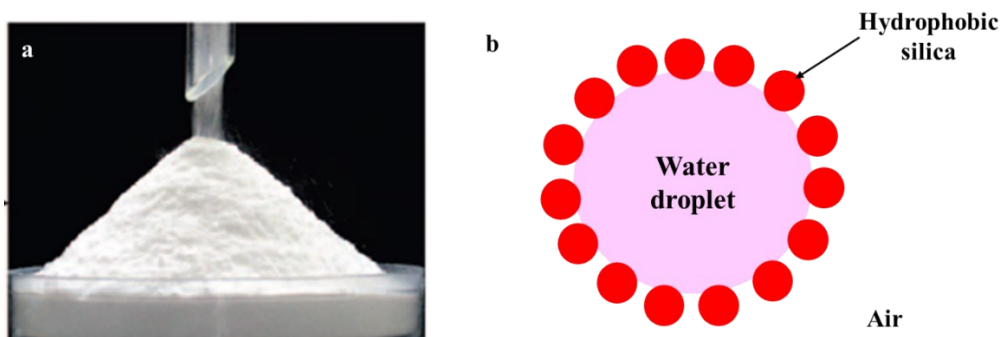


Figure 2-7 Dry water prepared with 5 g of hydrophobic nanosilica and 95 g of water and mechanism of hydrophobic nanosilica-stabilized dry water (water-in-air Pickering dispersion).

As a promoter of hydrate formation, dry water droplets are capable of promoting gas hydrate formation thermodynamically and kinetically. In a thermodynamic point of view, it is the hydrophobic surface of nanosilica that promotes gas hydrate formation via increased guest local density or water ordering. In a kinetic point of view, it is the dispersed water droplet and massively enhanced guest-water contact area that promotes gas hydrate formation.

Park et al. found that the equilibrium conditions for methane hydrate formation in dry water were shifted to higher temperatures and lower pressures compared to bulk water, indicating a thermodynamic effect on promoting hydrate formation (Park, Shin et al. 2015). Zebardast et al. confirmed the thermodynamic promotion of dry water on CO₂ hydrate formation experimentally, utilizing a high-pressure stainless steel reactor by intersecting the heating and cooling curves of

samples, as previously proposed by Tohidi et al. (Tohidi, Burgass et al. 2000), and attributed it to the hydrophobic attraction force (Zebardast and Haghtalab 2022), as shown in Figure 2-8a) (reprinted from (Zebardast and Haghtalab 2022) with permission) which showed that dry water shifted CO₂ hydrate phase boundary to a lower pressure region at a fixed temperature. Circular symbols were equilibrium conditions of CO₂ hydrate determined experimentally, and solid lines represent the phase boundary of CO₂ hydrate predicted by the thermodynamic model suggested by Zebardast et al. at different distances from the hydrophobic surface, δ .

Nguyen et al. proposed that the thermodynamic promoting effect was due to the hydrophobic effect. Water molecules became more ordered and clathrate-favorable near a hydrophobic surface, and the local gas concentration increased, which enhanced the formation of hydrates (Nguyen and Nguyen 2017, Nguyen, Nguyen et al. 2017). Farhang et al. (Farhang, Nguyen et al. 2014) suggested that the formation of a dense gas layer at the hydrophobic nanosilica-water interface provided heterogeneous nucleation sites for hydrate formation, as indicated in Figure 2-8b), reprinted from (Nguyen and Nguyen 2017) with permission, where Δz is the distance measured from the hydrophobic surface-water interface.

Li et al. used Raman spectroscopy to observe that water molecules were more ordered in the vicinity of a hydrophobic surface than in bulk water (Li, Stanwix et al. 2016). They also observed the preferential gas hydrate formation on a hydrophobic surface in a hydrate formation experiment (Li and Wang 2015, Nguyen, Nguyen et al. 2017). Molecular dynamics simulations showed a local gas enrichment at the hydrophobic surface-water interface compared to bulk water. The thermodynamic promoting effect of dry water on CO₂ hydrate equilibrium conditions was also demonstrated.

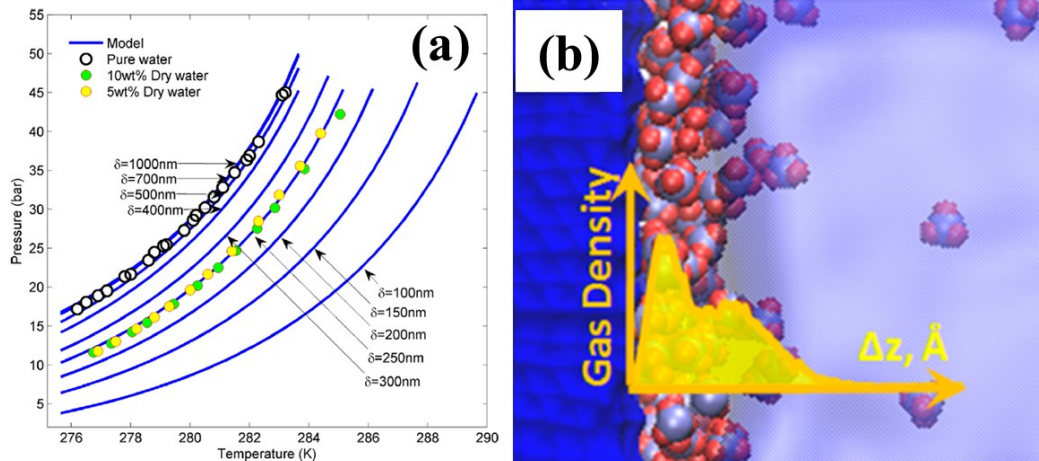


Figure 2-8 (a) Thermodynamic promoting effect of dry water containing different weight percent of hydrophobic nanosilica on CO₂ hydrate equilibrium condition; (b) Local gas enrichment at a hydrophobic surface-water interface.

Zhang et al. investigated the use of dry water hydrate to separate and recover methane from coal mine gas. The researchers discovered that adding dry water not only enhanced the formation rate of methane hydrate, but also improved the purification of methane from raw gas, more so than when hydrate formation was promoted by stirring or other promoters (Zhang, Li et al. 2018). Wang et al. reported that the presence of dry water reduced the induction time of methane hydrate nucleation to 5–10 min under quiescent conditions (Weixing Wang 2008). Additionally, Drachuk et al. observed that an absence of an induction time for propane hydrate formation in frozen dry water compared to the typically long induction time for hydrocarbon gas hydrate (Drachuk, Melnikov et al. 2015). This promoting effect occurred due to the enhanced guest-water contact and therefore more efficient methane diffusion into water, compared to methane hydrate formation at the methane-bulk water interface. This mechanism is consistent with the finding that hydrate formation rate in dry water closely correlated with the water droplet size dispersed by hydrophobic nanosilica (Weixing Wang 2008).

Figure 2-9 showed the kinetic promoting effect of dry water on clathrate hydrate formation. Figure 2-9a) (reprinted from (Zhang, Wang et al. 2022) with permission) showed that the induction time of CO₂ hydrate was shortened to 18.6 min in the presence of dry water as indicated in *P-t* and *T-t* profile. Compared to methane hydrate formation at the methane-bulk water interface, the gas storage capacity of methane hydrate formation in dry water droplets containing different nanosilica content and prepared by different mixing speed consistently exhibited a surge of orders of magnitude, as seen in Figure 2-9b) and Figure 2-9c), reprinted from (Carter, Wang et al. 2010) and (Weixing Wang 2008) with permission, respectively. While large cages of dry water methane hydrate are almost fully occupied, small cages remain approximately 10% vacant (Hu, Ye et al. 2011), indicating that future work could focus on enhancing small cage occupancy to further improve methane storage capacity using dry water clathrate hydrate. Another kinetic parameter, water-to-hydrate conversion, defined as the ratio of the mass of water converted to hydrate crystal to the initial mass of water, also increased with the presence of nanosilica in dry water. In Figure 2-9d), reprinted from (Podenko, Drachuk et al. 2018) with permission, the number aside each curve indicated the nanosilica content present in dry water: (1) 2 wt%, (2) 3 wt%, (3) 5 wt%, (4) 7 wt%, (5) 10 wt%, (6) 12 wt%, and (7) 15 wt%. It can be seen that water-to-hydrate conversion increased with the increase of silica content and approached 100% at highest nanosilica concentration (15 wt%).

The amount of methane stored in dry water methane hydrate depends on temperature (Carter, Wang et al. 2010, Park, Shin et al. 2015) and water droplet size which is influenced by mixing speed and silica-to-water ratio (Weixing Wang 2008), with the highest values observed at a mixing speed of 19,000 rpm (Weixing Wang 2008) and a hydrate formation temperature of 273–277 K (Park, Shin et al. 2015). The mixing speed used for the preparation of dry water has a greater impact on the gas uptake kinetics of dry water methane hydrate than the silica-to-water ratio (Carter, Wang et al. 2010, Park, Shin et al. 2015). Partial hydrophobic nanosilica stabilized water droplets with a size in the tens of micrometers. To further decrease the droplet size, one could increase the

mixing speed, but this requires higher energy input and may not be suitable for the large-scale production of dry water. Alternatively, a superhydrophobic nanomaterial could be synthesized to prepare dry water with a narrower size, thus enhancing the hydrate formation rate. In addition to the mass transfer problem, another obstacle that hinders fast hydrate formation is the heat transfer issue. Fan et al. proposed a solution to this problem by combining frozen dry water with heat-conducting nanoparticles (nanocopper) to improve heat exchange and dissipate the heat released by hydrate formation faster (Lang, Fan et al. 2010).

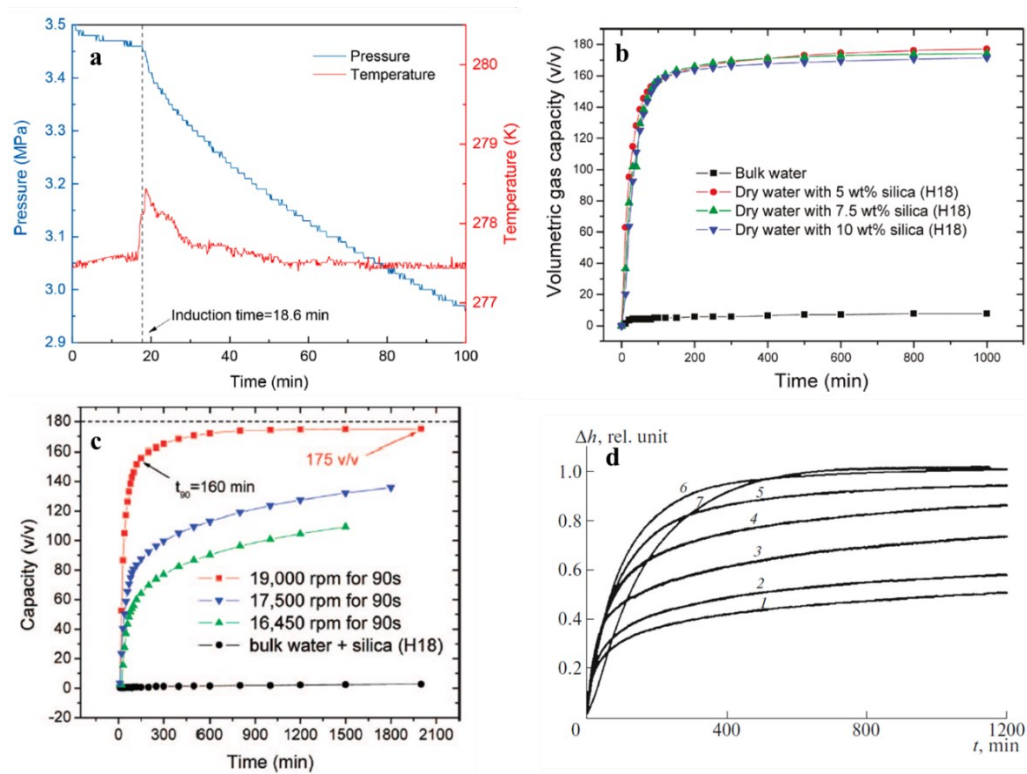


Figure 2-9 Kinetic promoting effect of dry water on clathrate hydrate formation.

Wang et al. conducted a study on CO₂ hydrate formation kinetics in dry water stabilized by Teflon particles of various sizes (Wang, Wang et al. 2014). The presence of dry water was found to significantly decrease the induction time of CO₂ hydrate formation, as a result of the increased

mass transfer across the CO₂-water interface. This reduction depended on both the size of the Teflon particle and its weight percent in dry water. Farhang et al. also reported that CO₂ hydrate formation kinetics was greatly enhanced by dry water, with the degree of enhancement dependent on the mass concentration of nanosilica present (Farhang, Nguyen et al. 2014). Compared to pure water systems, the presence of dry water led to a marked increase in CO₂ consumption, maximum CO₂ uptake, and CO₂-to-hydrate conversion. The induction time was also significantly shortened to 10 min, indicating a prominent promoting effect of dry water on CO₂ hydrate nucleation. Zhang et al. confirmed these findings, observing that the increase in nanosilica content in dry water droplets led to a decrease in induction time, an increase in gas uptake, and an increase in water-to-hydrate conversion of CO₂ hydrate (Zhang, Wang et al. 2022). Based on the shrinking core model, they calculated the effective gas diffusion coefficient through the hydrate shell and found that the impact of the latent heat released by hydrate formation on the formation kinetics was negligible. B.O. Carter et al. investigated the effect of dry water on the formation kinetics of methane hydrate (structure I), carbon dioxide hydrate (structure I), and krypton hydrate (structure II) (Carter, Wang et al. 2010). Their results showed that the gas uptake kinetics of all three types of hydrates were improved, indicating that the promoting effect of dry water is not limited to the crystal structure of clathrate hydrates.

Studies have compared the promoting effects of dry water and surfactants, such as sodium dodecyl sulfate (SDS) and other promoters, on gas hydrate formation and gas storage kinetics. The results indicate that SDS is more effective on enhancing hydrate formation kinetics than dry water (Carter, Wang et al. 2010), while dry water hydrate exhibits a higher gas storage capacity than hydrate formed in the presence of SDS (Carter, Wang et al. 2010, Hu, Ye et al. 2011). The performance of dry water has also been found to be comparable to thermodynamic hydrate promoter (THP) such as THF (Farhang, Nguyen et al. 2014). These findings highlight the potential of combining dry water with other promoters to achieve even greater improvements in gas storage capacity and kinetics.

The synergistic effect of dry water and other hydrate promoters is a topic that is worth exploring, with surfactants being known as effective kinetic promoters for hydrates of different guest types (Zhang, Lee et al. 2007, Kang and Lee 2010, Naeiji and Varaminian 2017, Majid, Worley et al. 2021). Typically, kinetic parameters such as gas uptake capacity, gas uptake rate, water (or guest) conversion to hydrate, nucleation rate, and growth rate of hydrate crystals can be utilized to measure the synergistic effect between dry water and other additives. In one study, Fan et al. performed hydrate formation experiments in a dry solution of a surfactant (sodium dodecyl sulfate) and compared the gas storage kinetics of methane hydrate in dry surfactant solution with that of dry water methane hydrate (Fan, Yang et al. 2014). Both hydrate formation in dry surfactant solution and dry water greatly enhanced methane hydrate formation rates compared to bulk water systems, and the former was found to be more effective. It was also found that methane hydrate in dry surfactant solution exhibited the same final methane storage capacity (around $170 \text{ m}^3/\text{m}^3$) as dry water methane hydrate but with faster storage rates, as confirmed by 60 min of t_{90} (the time taken to achieve 90% of final gas uptake) for dry surfactant solution and 200 min of t_{90} for dry water. The authors attributed the superior gas uptake kinetics of methane hydrate formation in dry surfactant solution to the better dispersion of water by dry water and the lower activity of water due to the presence of sodium dodecyl sulfate molecules.

On the other hand, Farhang et al. reported no synergistic effect (CO_2 to hydrate conversion kept in between 40 and 50% for both dry water and THF + dry water systems) between dry water and the thermodynamic hydrate promoter (THP) tetrahydrofuran (THF) for any of the mixture ratios on CO_2 hydrate formation kinetics (Farhang, Nguyen et al. 2014).

To date, there have been no reports on the synergistic effect of dry water and other water-insoluble additives on the nucleation and formation kinetics of gas hydrates. This has been one of the research topics in our group. Our current research involves investigating the impact of seven

ice nucleation promoters (Zhang and Maeda 2022) on the kinetics of CO₂ hydrate formation which will be elaborated in detail in Chapter 7.

3 Critical Surface Tension and Specific Surface Free Energy of Clathrate Hydrate

In this chapter, we will use an indirect method to estimate the essential physicochemical parameter of a hydrate surface—specific surface free energy. This is the first time this parameter is deduced using an experimental measure. The estimation of this parameter will offer new insights into the understanding of work of adhesion and work of nucleation. Also, the agglomeration tendency of hydrate particles can be quantified by this parameter.

3.1 Introduction

Specific surface free energy (γ_{sv}) is a basic physical property of a solid that governs the contact mechanics such as cohesion and adhesion (Israelachvili 2011). Specific surface free energy of a solid is also related to the nucleation work of the solid phase (Kashchiev 2000) and pre-melting of a solid (Dash, Fu et al. 1995), and is thus of fundamental importance of any solid. Specific surface free energy is defined as the amount of work required to create a unit area of a solid surface in a vacuum (Israelachvili 2011). However, measuring such a work is difficult for many solids in practice and impossible for other solids like clathrate hydrates (gas hydrates) that decompose in a vacuum, which in turn had hindered our understanding of interfacial phenomena of gas hydrates (Maeda 2015, Maeda 2020). Because of the practical difficulties involved in direct measurements of the specific surface free energy of solids, approximations became necessary. A commonly used approximation is to substitute a vacuum with air. Even with this approximation, it has been experimentally challenging to determine the specific surface free energy of a solid. Consequently, an alternative approach has been proposed over time.

One such alternative approach is the use of the so-called critical surface tension (Zisman 1964). The critical surface tension provides an indirect method to deduce the specific surface free energy of a solid by measuring the contact angle, θ , of a broad range of liquids on the surface of the solid of interest. Here, the contact angle of a range of liquids that belong to the same

homologous series are typically measured on the solid surface of interest (Zisman 1964). With the surface tension of each of the liquids known, one can construct a plot of the contact angle vs the surface tension, γ_{lv} , of each liquid, which is often referred to as the “Zisman plot” (Zisman 1964). An extrapolation of a typically linear contact angle vs γ_{lv} relationship to the limit of zero contact angle (where the straight line intersects the γ_{lv} axis) yields the critical surface tension, γ_c , that is unique to the solid.

For ice, several estimates of its specific surface free energy have been reported. Ketcham and Hobbs (Ketcham and Hobbs 1969) estimated γ_{sv} of ice to be 109 ± 3 mJ/m². Reuck (de Reuck 1957) obtained the γ_{sv} of ice at 235 K to be 116 mJ/m². Mason (Mason 1952) used a cleavage-work method to determine the specific surface free energy of ice to be 102 mJ/m² at 233 K. McDonald (McDonald 1953) found three errors in Mason’s calculation (Mason 1952) and corrected Mason’s value to 96 mJ/m². Qiu et al. (Qiu and Molinero 2018) used a Mw water model to estimate the specific surface free energy of ice to be 105 mJ/m² at 273K from the enthalpy of breaking water – water bond while neglecting the entropic contribution. Makkonen (Makkonen 1997) obtained the specific surface free energy of ice to be 77 mJ/m² at 248 K. Boinovich et al. (Boinovich and Emelyanenko 2014) reported the specific surface free energy of polycrystalline ice to be 103.7 ± 0.6 mJ/m² at 255.85 K. He also noticed that due to the relaxation of the surface layer, γ_{sv} slightly decreased with time and plateaued at 98.8 ± 0.4 mJ/m². Kloubek (Kloubek 1974) estimated the γ_{sv} of ice to be 106 mJ/m².

For the critical surface tension of ice, Adamson et al. (Adamson, Shirley et al. 1970) measured the critical surface tension of ice using benzene substitutes and hydrocarbon liquids. They deduced the critical surface tension value of ice to be 29 mN/m and concluded that the ice surface was nonpolar. For clathrate hydrate, neither the specific free energy (γ_{sv}) nor the critical surface tension (γ_c) has been reported to date.

In this study, we investigated the critical surface tension of tetrahydrofuran (THF) hydrate that forms the so-called Structure II (sII) hydrate under the atmospheric pressure. We then provide an estimate of the specific surface free energy of THF hydrate.

3.2 Materials and methods

Chemicals

THF ($\geq 99.9\%$), Fluorobenzene (99%), Chlorobenzene (99.9%), Bromobenzene ($\geq 99.5\%$), Iodobenzene (98%), N-Methylaniline ($\geq 99\%$), Propiophenone (99%), CS₂ ($\geq 99.9\%$), decane ($\geq 95\%$), dodecane ($> 95\%$), squalane ($\geq 95\%$), perfluoromethyldecalin (80%) were procured from Sigma-Aldrich and used without further purification. Milli-Q water from a Millipore unit was used for the production of ice and THF hydrate.

Preparation of Ice surfaces

Ice surfaces were prepared by freezing Milli-Q water in a glass petri dish inside a freezer in which the temperature was maintained at 253 K for overnight. In rare occasions when the ice surface was not smooth over an area that was necessary for the contact angle measurements, small amounts of additional Milli-Q water was placed evenly on the existing ice surface and the sample was placed back inside the freezer.

Preparation of THF hydrate surfaces

A solution of Milli-Q water and THF of the mass ratio of THF: deionized water = 4:17 (or the molar ratio of THF : deionized water = 1:17) was prepared inside a glass petri dish. After the THF aqueous solution was placed inside the petri dish, the petri dish was then covered with a glass lid with vacuum grease (Dow Corning Corporation) at the rim to prevent THF from evaporating, and the sealed petri dish was placed into a freezer (253 K) for overnight. The sealed petri dish was taken out of the freezer the following day. The lid was opened and a small amount of extra THF liquid was placed on the solid surface to compensate for any potential evaporative loss of THF

overnight and the petri dish was covered and sealed again. The petri dish was placed on an ice bath in a metal container and the metal container was placed inside a refrigerator (277 K). We note that in a control experiment the THF hydrate inside the petri dish remained stable even after the ice in the metal container had melted. The THF sample system is shown in Figure 3-1.

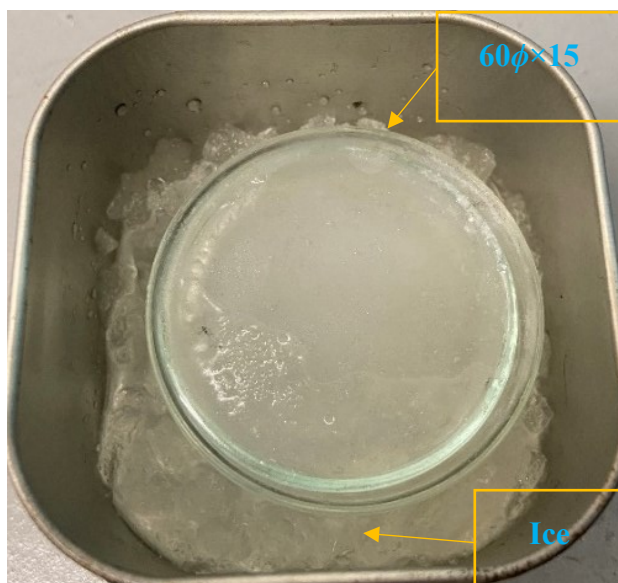


Figure 3-1 Image of the petri dish containing the sample.

Surface tension measurements

The surface tension of testing liquids was measured by the Wilhelmy plate method (Langmuir-Blodgett Deposition Troughs, Biolin Scientific). A testing liquid was placed in a 50 mL beaker that had been pre-cleaned by Piranha solution (70% H_2SO_4 : 30% H_2O_2) and pre-cooled inside a refrigerator (277 K). During a measurement, a roughened platinum Wilhelmy plate (wetting length of 39.24 mm) was connected to a force balance with a hook and the force was recorded in a computer. At the beginning of a measurement, the sample was taken out of the refrigerator and the measurement commenced as soon as possible (typically less than 5 minutes). The force sensor was pre-calibrated using ethanol at 293 K.

Contact angle measurements

A digital camera was supported by a lab stand and connected to a computer. The height of the camera was adjusted beforehand to focus on the sample surface and the distance to the sample was also adjusted appropriately. The pre-cleaned vials containing the testing liquids and the clean pipettes, each of which was designated for each testing liquid, were pre-cooled in the refrigerator. Once a smooth surface was ready for a measurement, the surface was taken out of the freezer and placed in the refrigerator to slow down the dissociation of the THF hydrate or melting of the ice. A small amount (about 0.05 ml) of pre-cooled testing liquid was placed on the surface using a designated pre-cooled pipette. All the testing liquids had also been pre-cooled in the refrigerator. A digital camera was used to record photographs of the droplets. Five independent measurements were carried out to obtain the average value of the contact angle. After the measurements, the numerical value of the contact angle was analyzed using *ImageJ*. The schematic illustration of the experimental setup is shown in Figure 3-2.

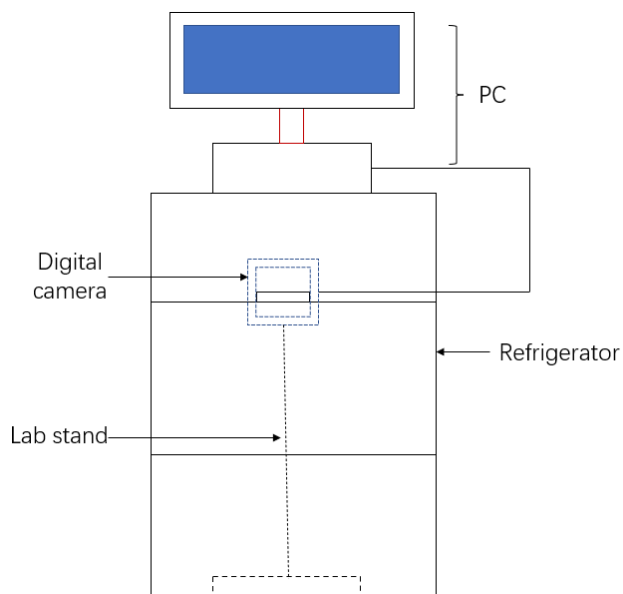


Figure 3-2 Schematic illustration of contact measurement setup.

3.3 Results

Surface tension of the testing liquids

Table 3-1 shows the surface tension of the testing liquids at 277 K from the Wilhelmy plate method. Adamson et al. (Adamson, Shirley et al. 1970) used many of the same testing liquids previously. Meanwhile, the literature value of the surface tension of testing liquids are also reported in Table 3-1.

Table 3-1 Surface tension of testing liquids

| Testing liquids | Measured Surface tension at 277 K (mN/m) | Surface tension from the literature (mN/m) |
|------------------------|---|---|
| Fluorobenzene | 28.3 | 27.3(Korosi and Kovats 1981) |
| Chlorobenzene | 33.6 | 33.0(Korosi and Kovats 1981) |
| Bromobenzene | 36.4 | 35.8(Korosi and Kovats 1981) |
| Iodobenzene | 39.0 | 39.6(Korosi and Kovats 1981) |
| Propiophenone | 37.7 | 37.4(Jasper 1972) |
| N-Methylaniline | 39.1 | 36.9(Egemen, Nirmalakhandan et al. 2000) |
| CS ₂ | 34.0 | 32.8(Shipp 1970) |
| Decane | 24.2 | 23.9(Zdziennicka, Krawczyk et al. 2017) |
| Dodecane | 25.8 | 25.1(Zdziennicka, Krawczyk et al. 2017) |
| Squalane | 28.4 | 28.4(Medina, Pineda et al. 2003) |
| Perfluoromethyldecalin | 19.8 | 19.2(Morita, Matsumoto et al. 1992) |

We note that the surface tension values reported in the literature are obtained at or near room

temperature. Therefore, the surface tension values measured in this work at 277 K are expected to be somewhat higher than the literature values, which is indeed the case as Table 3-1 shows.

For the benzene substitutes, the surface tension progressively increased with the molecular weight of the substituted atom; fluorobenzene, chlorobenzene, bromobenzene and iodobenzene. This is due to the larger Van der Waals interaction with the size of the molecules. Among the saturated hydrocarbons studied, squalane ($C_{30}H_{62}$) had the highest surface tension, which had the highest molecular weight.

Critical surface tension of ice

We first show the contact angle results on ice. Adamson et al. (Adamson, Shirley et al. 1970) reported that alkanes with less than 10 carbon atoms and nitroalkane almost had the same contact angle that was close to 0, so we only measured fluorobenzene, chlorobenzene, bromobenzene, N-Methylaniline, propiophenone, iodobenzene and CS_2 from their work, in addition to our own selections of 3 hydrocarbons and a fluorocarbon. Some typical photographs of the contact angle are shown in Figure 3-3. For each testing liquid, the contact angle was measured at least 5 times and the average value was calculated.

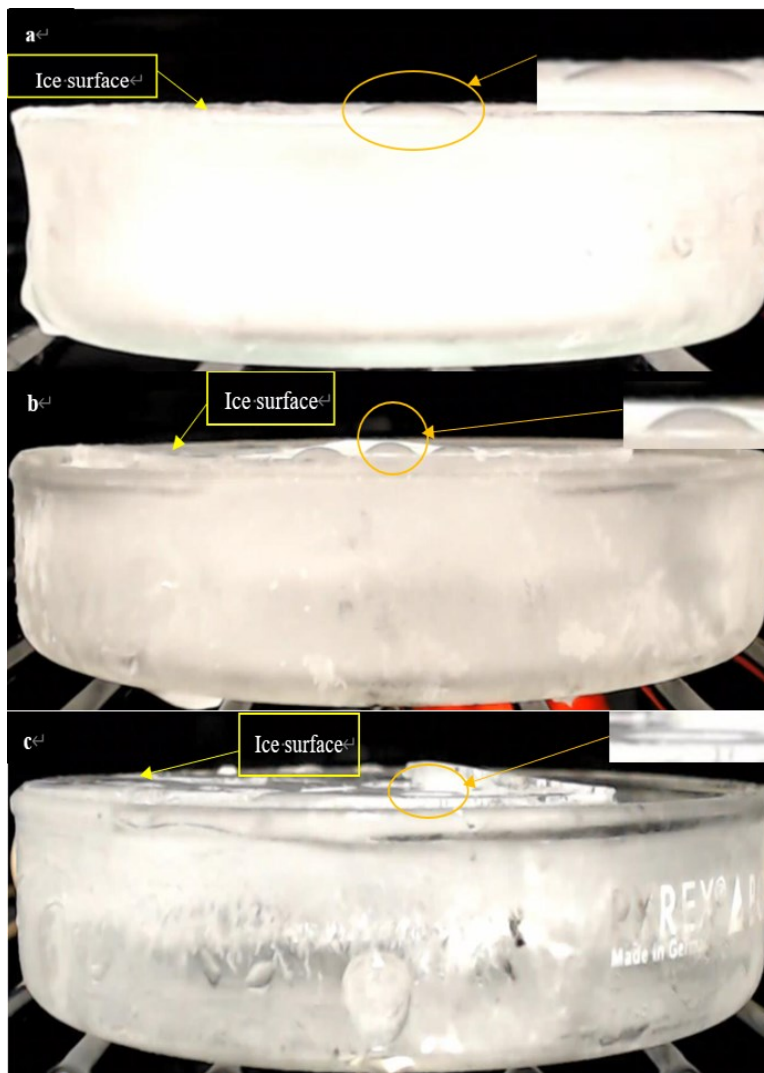


Figure 3-3 Typical droplet of testing liquids on an ice surface.

A droplet was placed on an ice surface using a pre-cooled pipette. Photographs were recorded after the droplet totally stopped moving on the ice surface. The droplet was highlighted with an orange circle. Inset figure: enlargement of the droplet. a) iodobenzene b) squalane c) perfluoromethyldecalin.

Figure 3-3 shows the typical pictures of the droplets of testing liquids on the ice surface. These pictures were recorded with a digital camera. The numerical values of the contact angle

were determined using *imageJ* and are summarized in Table 3-2.

Table 3-2 Contact angle of various liquids on an ice surface

| Testing liquids | Contact angle (°) | Cosine θ | Standard deviation of cosine θ |
|------------------------|-------------------|-----------------|---------------------------------------|
| Fluorobenzene | 0 | 1 | 0 |
| Chlorobenzene | 12 | 0.98 | 0 |
| Bromobenzene | 17 | 0.96 | ±0.01 |
| Iodobenzene | 30 | 0.87 | ±0.02 |
| Propiophenone | 0 | 1 | 0 |
| N-Methylaniline | 29 | 0.88 | ±0.03 |
| CS ₂ | 27 | 0.89 | ±0.02 |
| Decane | 27 | 0.89 | ±0.01 |
| Dodecane | 30 | 0.87 | ±0.03 |
| Squalane | 31 | 0.86 | ±0.04 |
| Perfluoromethyldecalin | 13 | 0.98 | ±0.01 |

Some testing liquids tended to spread on the ice surface and did not form a spherically capped shape. When this situation occurred, the contact angle was regarded as 0 and the corresponding cosine value as 1.

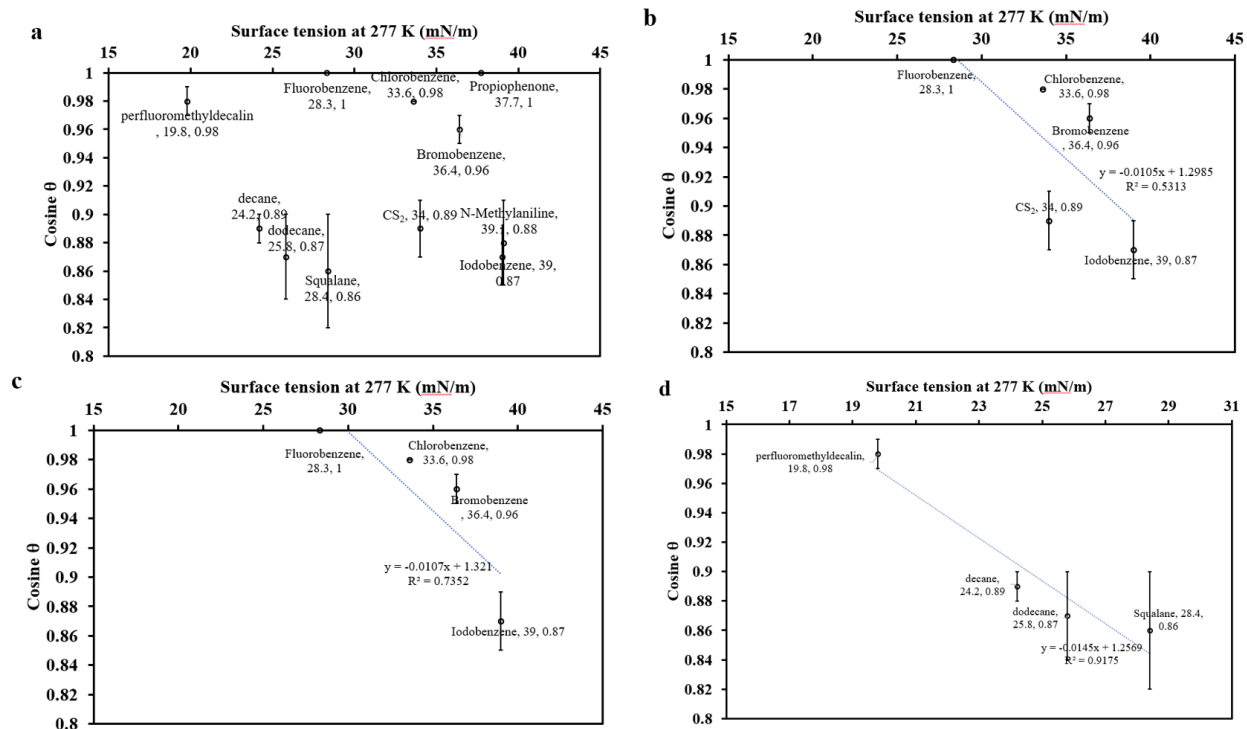


Figure 3-4 The relationship between the cosine of the contact angle on ice and the surface tension of the liquid.

The name of the testing liquid, the surface tension and the $\cos\theta$ value are shown near the data point.

Figure 3-4a shows the raw data for ice. Since these liquids include multiple homologous series, we will not fit a straight line at this stage. Figure 3-4b only includes the benzene substitutes and CS₂ together with the linear fit. It can be seen that our data points are similar to what Adamson et al. (Adamson, Shirley et al. 1970) reported. Figure 3-4c only includes the benzene substitute, together with the linear fit. The correlation between cosine θ (y) and surface tension (x) of testing liquids is $y = -0.0107x + 1.321$. Figure 3-4d only includes the saturated hydrocarbons and fluorocarbons, together with the linear fit.

From the linear fits, three critical surface tension values of ice were obtained from the intercept that the linear fit intersects with the $\cos \theta = 1$ axis. Table 3-3 summarizes the results.

Table 3-3 Critical surface tension of ice

| Testing liquids | Ice critical surface tension (mN/m) |
|--------------------------------------|-------------------------------------|
| CS ₂ +benzene substitute | 28.4 |
| Benzene substitute only | 30 |
| Saturated Fluorocarbon + Hydrocarbon | 17.7 |

Depending on the series of the testing liquids used, the critical surface tension of ice could range from 17.72 to 30 mN/m. For the benzene substitutes and CS₂, which Adamson et al. (Adamson, Shirley et al. 1970) used in their study, the critical surface tension of ice was 28.4 to 30 mN/m. These values are essentially identical to the 29 mN/m reported by Adamson et al. (Adamson, Shirley et al. 1970)

Critical surface tension of THF hydrate

We first show typical photographs of the contact angle the various testing liquids on THF hydrate in Figure 3-5.



Figure 3-5 Typical droplet of testing liquids on a THF hydrate surface.

A droplet was placed on a THF hydrate surface using a pre-cooled pipette. Photographs were recorded after the droplet totally stopped moving on the THF hydrate surface. The droplet is highlighted with an orange circle. Inset figure: enlargement of the droplet. a) bromobenzene b) fluorobenzene c) decane. These pictures were recorded with a digital camera. The numerical values of the contact angle were determined using *imageJ* and are summarized in Table 3-4.

Table 3-4 Contact angles of various liquids on THF hydrate

| Testing liquids | Contact angle (°) | Cosine θ | Standard deviation of cosine θ |
|------------------------|-------------------|-----------------|--|
| Fluorobenzene | 28 | 0.95 | ±0.02 |
| Chlorobenzene | 0 | 1 | ±0 |
| Bromobenzene | 18 | 0.95 | ±0.02 |
| Iodobenzene | 30 | 0.86 | ±0.04 |
| Propiophenone | 0 | 1 | ±0 |
| N-Methylaniline | 0 | 1 | ±0 |
| CS ₂ | 26 | 0.9 | ±0.02 |
| Decane | 25 | 0.91 | ±0.04 |
| Dodecane | 24 | 0.91 | ±0.02 |
| Squalane | 29 | 0.88 | ±0.01 |
| Perfluoromethyldecalin | 18 | 0.95 | ±0.02 |

As was the case with ice, some testing liquids tended to spread on the ice surface and did not form a spherically capped shape. When this situation occurred, the contact angle was regarded as 0 and the corresponding cosine value as 1. The raw data for THF hydrate are shown in Figure 3-6a and three “Zisman plots” are shown in Figure 3-6b, Figure 3-6c and Figure 3-6d.

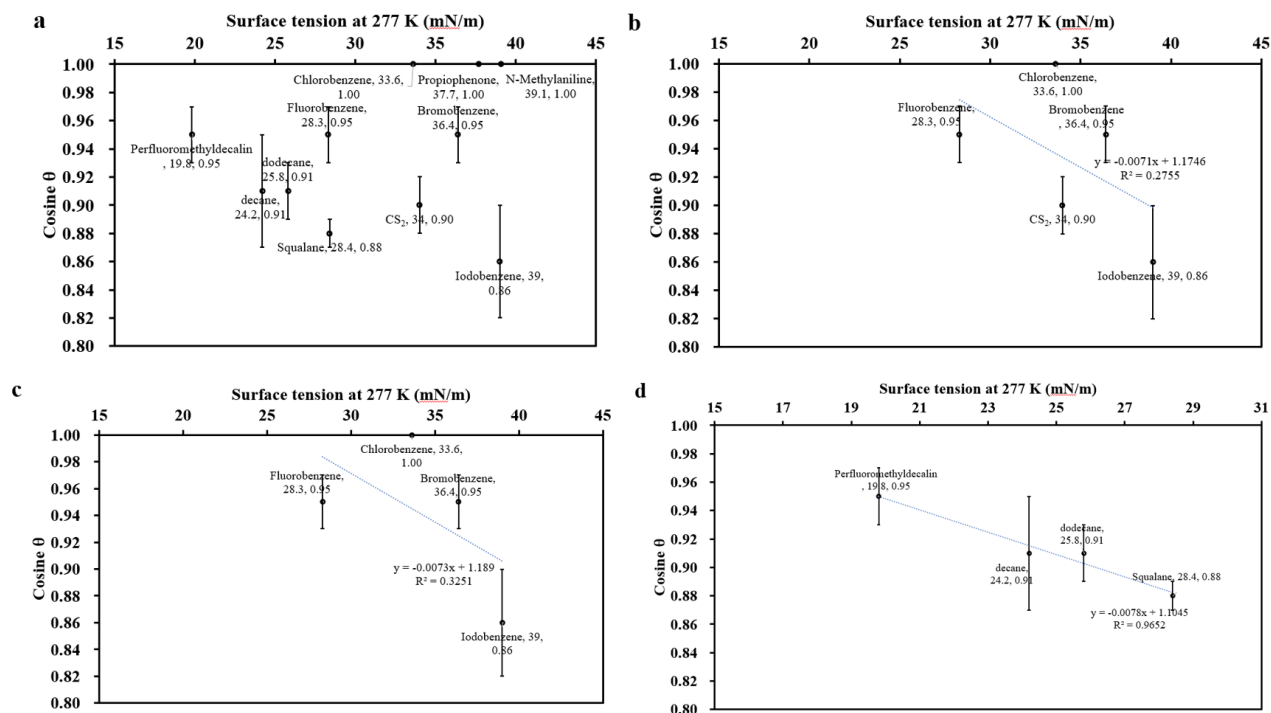


Figure 3-6 The relationship between the cosine of the contact angle on THF hydrate and the surface tension of the liquid.

The name of the testing liquid, the surface tension and the $\cos\theta$ value are shown near the data point. Figure 3-6a) all data points; Figure 3-6b) benzene substitutes+CS₂ with a linear fit; Figure 3-6c) benzene substitutes with a linear fit and Figure 3-6d) saturated hydrocarbons and fluorocarbons with a linear fit.

From the linear fits, three critical surface tension values of THF hydrate were obtained from the intercept that the linear fit intersects with the $\cos\theta = 1$ axis. Table 3-5 summarizes the results.

Table 3-5 Critical surface tension of THF hydrate

| Testing liquid | THF hydrate critical surface tension (mN/m) |
|--------------------------------------|---|
| CS ₂ +benzene substitute | 24.6 |
| Benzene substitute only | 25.9 |
| Saturated Fluorocarbon + Hydrocarbon | 13.4 |

Compared to the critical surface tension of ice summarized in Table 3-3, the critical surface tension of THF hydrate was consistently somewhat lower for each of the homologous series of the testing liquids used for the study; 24.6 vs 28.4 mN/m for CS₂ + benzene substitute, 25.9 vs 30 mN/m for the benzene substitute only and 13.4 vs 17.7 mN/m for the saturated fluorocarbon + hydrocarbon series.

3.4 Discussion

The basic idea behind the concept of the critical surface tension is that a liquid will spread on the solid of interest as long as the free energy cost of wetting by the liquid, ΔG_{spread} , is less than the free energy gains due to the loss of the dry solid surface. Perhaps as expected, a liquid with a low surface tension, γ_{lv} , will spread on a given solid surface (that has a given γ_{sv}) whereas a liquid with a high γ_{lv} will not spread on the same solid surface (that has the same γ_{sv}). It follows that, for a given solid, there will be a critical surface tension of a liquid, γ_{c} , below which the liquid will spread on the solid and above which it does not. A liquid that has the surface tension of exactly γ_{c} will neither spread nor de-wet the solid; $\Delta G_{\text{spread}} = \gamma_{\text{lv}} + \gamma_{\text{sl}} - \gamma_{\text{sv}} = \gamma_{\text{c}} + \gamma_{\text{sl}} - \gamma_{\text{sv}} = 0$. It follows that $0 = \gamma_{\text{c}} + \gamma_{\text{sl}} - \gamma_{\text{sv}}$, OR $\gamma_{\text{c}} = \gamma_{\text{sv}} - \gamma_{\text{sl}}$ OR $\gamma_{\text{sv}} = \gamma_{\text{c}} + \gamma_{\text{sl}}$.

It can be seen that the higher the γ_{c} of a *solid*, more liquids will spread on the solid, and for a very high γ_{c} of the *solid*, virtually all liquids will spread on the solid. Therefore, a high γ_{c} of a *solid* equates to a high γ_{sv} . Conversely, the lower the γ_{c} of the *solid*, more liquids will de-wet the solid, and for a very low γ_{c} of a *solid*, virtually no liquids will spread on the solid. Therefore, a low γ_{c} of a *solid* equates to a low γ_{sv} .

Then, if one can find a liquid that has the “right” surface tension that neither wets nor de-wets the solid, then the surface tension of this particular liquid yields the critical surface tension of the solid, γ_c . Once γ_c of a solid is known, the specific surface free energy of this solid surface, γ_{sv} , is equal to the sum of γ_c of this solid and the interfacial tension between the solid and this particular liquid that has the surface tension of γ_c , which we may refer to as γ_{slc} . In other words, $\gamma_{sv} = \gamma_c + \gamma_{slc}$.

In reality, though, a liquid that happens to have exactly the same surface tension γ_c as the critical surface tension of the solid of interest may not exist, as may be expected from the fact that γ_c of a given *solid* is obtained from an extrapolation of a linear trend of γ_{lv} of a range of liquids that do not completely wet the solid. Then, it becomes impossible to measure the interfacial tension between this solid and the liquid, γ_{slc} , or deduce γ_{sv} of the solid of interest from γ_c of the solid.

For ice, for which both γ_c and γ_{sv} have been estimated, it may be possible to back-calculate the value of γ_{slc} . γ_{sv} of ice reported in the literature ranges from 77 mJ/m² to 116 mJ/m² (Mason 1952, McDonald 1953, de Reuck 1957, Ketcham and Hobbs 1969, Kloubek 1974, Makkonen 1997, Boinovich and Emelyanenko 2014, Qiu and Molinero 2018), with an average of 96.5 mJ/m². On the other hand, γ_c of ice reported in the literature is 29 mN/m (Adamson, Shirley et al. 1970). Our own data presented in Table 3-3 show the range of γ_c of ice from 17.7 mN/m for the saturated hydrocarbons and fluorocarbon to 30.0 mN/m for the benzene substitutes. From $\gamma_{slc} = \gamma_{sv} - \gamma_c$, we may estimate that the range of γ_{slc} for ice to be between 47 mJ/m² and 98.3 mJ/m² because γ_{slc} must fall in the range between (the maximum γ_{sv} minus the minimum γ_c) and (the minimum γ_{sv} minus the maximum γ_c).

These values are higher than the estimates for the specific interfacial free energy between ice and water, γ_{sl} , of 28 to 33 mJ/m² (Turnbull 1950, Schaefer, Glicksman et al. 1975, Hardy 1977,

Hillig 1998). The higher value of γ_{slc} than γ_{sl} may be expected, given that a hypothetical liquid that neither wets nor de-wets ($\Delta G_{spread} = 0$) is expected to have a lower affinity to ice than liquid water does.

For THF hydrate, no γ_{sv} values have been reported to date. Our data presented in Table 3-5 show the range of γ_c of THF hydrate from 13.4 mJ/m² for the saturated hydrocarbons and fluorocarbon to 25.9 mJ/m² for the benzene substitutes. If we assume that γ_{slc} of THF hydrate to be equal to γ_{slc} of ice (i.e., the range of γ_{slc} to be between 47 mJ/m² and 98.3 mJ/m²), we would obtain γ_{sv} of THF hydrate to be in the range between 60.4 mJ/m² and 124.2 mJ/m², with the most probable value of 92.3 mJ/m². This result is comparable with the specific surface free energy value of methane hydrate (≈ 90 mJ/m²) Kashchiev et al. deduced (Kashchiev and Firoozabadi 2002).

To examine the validity of the above assumption, we estimate the potential size of errors that could arise from this assumption. The ice – water interfacial tension was reported to be in the range of 28 to 33 mN/m (Turnbull 1950, Schaefer, Glicksman et al. 1975, Hardy 1977, Hillig 1998). Meanwhile, Lee et al. (Lee, Yun et al. 2007). found that THF hydrate – water interfacial tension was in the range of 16 to 31 mN/m. This range is comparable to the interfacial tension between gas hydrates and water listed in Table 3-6 below. Therefore, at least for water, the water – ice interfacial tension and water – clathrate hydrate interfacial tension is comparable and the maximum discrepancy between them is at most by a factor of 2. If γ_{slc} for the THF hydrate and γ_{slc} for ice (of the hypothetical liquid that happens to have the surface tension of γ_c) also at most differed by a factor of 2 (i.e., $\gamma_{slc_ice} = 2\gamma_{slc_THF\ hydrate}$), then we would obtain γ_{sv} of THF hydrate to be in the range between 36.9 mJ/m² and 75.1 mJ/m², with the most probable value of 56 mJ/m² (instead of between 60.4 mJ/m² and 124.2 mJ/m², with the most probable value of 92.3 mJ/m², as shown above). Given the large variations in the reported values of γ_{sl} of clathrate hydrate – water interface themselves, shown in Table 3-6, our assumption appears reasonable.

Unlike γ_{sv} , there have been numerous reports in the literature on the specific interfacial free energy between clathrate hydrate and liquid water, γ_{sl} , which typically used porous media and applied the Gibbs-Thomson equation. Table 3-6 summarizes the literature data.

Table 3-6 Comparison between studies of γ_{sl} (interfacial tension between hydrate and water)

| Study | Method | Guest molecule | γ_{sl} (mJ/m ²) |
|--|----------------------------|-------------------------------|------------------------------------|
| Uchida et al.(Uchida, Ebinuma et al. 1999) | Gibbs-Thomson equation | CH ₄ | 39 |
| Uchida et al. (Uchida, Ebinuma et al. 2002) | Gibbs-Thomson equation | CH ₄ | 17 |
| | | CO ₂ | 14 |
| | | C ₃ H ₈ | 25 |
| Zhang et al. (Zhang, Di Lorenzo et al. 2012) | Heterogeneous nucleation | CO ₂ | 9.3 |
| Sakamaki et al. (Sakamaki 2011) | Molecular simulation | CO ₂ | 7.5 ± 1.4 |
| Anderson et al. (Anderson, Llamedo et al. 2003) | Gibbs-Thomson equation | CH ₄ | 32 ± 3 |
| | | CO ₂ | 30 ± 3 |
| Zachary et al. (Aman, Olcott et al. 2013) | Cohesive force measurement | Cyclopentane | 0.32 ± 0.05 |
| Seo et al. (Seo, Lee et al. 2009) | Gibbs-Thomson equation | C ₂ H ₆ | 39 ± 2 |
| | | C ₃ H ₈ | 45 ± 1 |
| Bahman et al. (ZareNezhad, Mottahedin et al. 2014) | Heterogeneous nucleation | C ₂ H ₆ | 17.3 |
| Song et al. (Song, Couzis et al. 2010) | Contact force measurement | Cyclopentane | 47.3 |
| Zarifi et al. (Zarifi, Javanmardi et al. 2016) | Gibbs-Thomson equation | CH ₄ | 31 ± 3 |

| | | | |
|--|---|---|-------------------------------|
| Liu et al. (Liu, Zhan et al. 2018) | Gibbs-Thomson equation | CH ₄ | 32 ± 2 |
| Naeiji et al. (Naeiji, Varaminian et al. 2017) | MD simulation (water model: SPC/E) | CH ₄ | 31-39.5 depending on pressure |
| Mirzaeifard et al. (Mirzaeifard, Servio et al. 2019) | MD simulation (water model: TIP4P-Ew) | CH ₄ | 32-36.5 depending on pressure |
| Jacobson et al. (Jacobson and Molinero 2011) | MD simulation (water model: mW) | Hypothetical guest intermediate between CH ₄ and CO ₂ | 36 ± 2 |
| Mohr et al. (Mohr, Pétuya et al. 2021) | Microsecond-long molecular dynamics simulations | CH ₄ -C ₃ H ₈ (67-33%) | 64.28 |
| Tsimpanogiannis et al. (Tsimpanogiannis 2021) | Combination of MD simulation and experiment | CH ₄ | around 30 |
| Uchida et al. (Uchida, Ebinuma et al. 1999) ^a | Gibbs-Thomson equation | CH ₄ | 32.72 |
| Uchida et al. (Uchida, Ebinuma et al. 2002) ^b | Gibbs-Thomson equation | CH ₄ | 34 |

^a Corrected by Tsimpanogiannis et al. (Tsimpanogiannis 2021) accounting for the curvature of dissociation and using a different fitting slope.

^b Corrected by Anderson et al. (Anderson, Llamedo et al. 2003) accounting for the curvature of dissociation.

From the above summary, it can be seen that γ_{sl} between clathrate hydrate and liquid water ranges from 0.32 mJ/m² to 64.3 mJ/m² (Uchida, Ebinuma et al. 1999, Uchida, Ebinuma et al. 2002, Anderson, Llamedo et al. 2003, Seo, Lee et al. 2009, Song, Couzis et al. 2010, Jacobson and Molinero 2011, Sakamaki 2011, Zhang, Di Lorenzo et al. 2012, Aman, Olcott et al. 2013, ZareNezhad, Mottahedin et al. 2014, Zarifi, Javanmardi et al. 2016, Naeiji, Varaminian et al. 2017, Liu, Zhan et al. 2018, Mirzaeifard, Servio et al. 2019, Mohr, Pétuya et al. 2021, Tsimpanogiannis 2021), in contrast to the range of γ_{slc} of between 47 mJ/m² and 98.3 mJ/m². As was the case with ice, the higher value of γ_{slc} than γ_{sl} may be expected, given that a hypothetical liquid that neither wets nor de-wets ($\Delta G_{spread} = 0$) clathrate hydrate is expected to have a lower affinity than liquid water to clathrate hydrate.

A potential complication may be the miscibility of the testing liquids with the guests (THF). THF is an excellent solvent and many liquids are soluble in THF. Among the testing liquids we used, only perfluorodecalin and perfluoromethyldecalin are immiscible with THF. We assume that THF as guests were enclathrated in the clathrate structure and did not dissolve into the testing liquids for the short periods required for the contact angle measurements. That (1) the γ_c values for THF hydrate were broadly similar to (albeit somewhat lower than) the γ_c values of ice and (2) the correlation between the γ_c values of THF hydrate and ice that belong to the different homologous series were uniformly consistent, suggests that our assumption may be warranted.

Another question, assuming that our estimate of γ_{sv} of THF hydrate is reasonably correct, is how our estimated value for THF hydrate may be relevant to the γ_{sv} values of other Structure II clathrate hydrates. Given that for γ_{sl} with liquid water, the reported values of THF hydrate by Lee et al (Lee, Yun et al. 2007) and those of the other clathrate hydrates (shown in Table 3-6) are similar to each other, we may speculate that the γ_{sv} values of other Structure II clathrate hydrates may also be broadly similar to γ_{sv} of THF hydrate we deduced.

3.5 Conclusions

In this research, we applied the “Zisman plot” to the determination of critical surface tension, γ_c , of ice and THF hydrate. The value ranges found are 17.7 mN/m -30 mN/m for ice and 13.4 mN/m -25.9 mN/m for THF hydrate. This γ_c value for ice was very similar to the value reported by Adamson et al. for the same homologous series of benzene substitutes. For the other series that included squalane and perfluoromethyldecalin testing liquids, neither Adamson et al. nor anybody else reported any γ_c values. No γ_c values for clathrate hydrate have been reported that can be compared to our results.

We then used the specific surface free energy values, γ_{sv} , for ice reported in the literature and the γ_c we measured to calculate the interfacial tension between ice and a hypothetical liquid that has the surface tension of γ_c , γ_{slc} . Since each of the literature value of γ_{sv} for ice and the γ_c values of ice had a range, we obtained the range of γ_{slc} for ice of 47 mJ/m² to 98.3 mJ/m². We then assumed that γ_{slc} for THF hydrate is the same as γ_{slc} for ice. With this assumption, we calculated the γ_{sv} values for THF hydrate from the measured γ_c values of THF hydrate and the γ_{slc} for THF hydrate. Since each of the deduced value of γ_{slc} for THF hydrate and the γ_c values of THF hydrate had a range, we obtained the range of γ_{sv} for THF hydrate of 60.4 mJ/m² to 124.2 mJ/m², with an average of 92.3 mJ/m². The deduced γ_{sv} value of THF hydrate was found to be slightly lower than that of ice and was comparable with the value estimated in literature for methane hydrate. This is the first time that the specific surface free energy of a clathrate hydrate was determined using an experimental method.

3.6 Summary and Relationship to Chapters that Follow

In this chapter, the specific surface free energy of THF model hydrate was deduced using an indirect method that combined experimental measurements and mathematics. We obtained the range of γ_{sv} for THF hydrate of 60.4 mJ/m² to 124.2 mJ/m², with an average of 92.3 mJ/m². This value is essential for the theoretical determination of work of adhesion, as shown in Chapter 2. Adhesion and cohesion play a crucial role in the formation of hydrate plugs which is the origin of

hydrate-related flow assurance risks. Therefore, not only theoretical determination but also experimental characterization of adhesion and cohesion are required. In the next chapter, shear adhesive strength between THF clathrate hydrate/TBAB semi-clathrate hydrate and different substrates will be investigated under a wide range of experimental conditions, which is supposed to reveal influencing factors and provide implications for industrial flow assurance problems.

3.7 Appendix

SOP of surface tension measurements using the Wilhelmy Plate Method

1. Before the measurement, place testing liquids to be measured inside the fridge where the inside temperature is kept at 4°C or 277 K. This is because the measurement of the contact angle of these testing liquids on a THF hydrate surface will also be carried out at a temperature condition of 277 K.
2. Turn on the Langmuir and Langmuir-Blodgett (LB) systems, calibrate the force balance of the LB device using the calibration ring.
3. Transfer some pre-cooled testing liquid to a pre-cleaned glass beaker and place it on the Teflon trough of the LB device.
4. Put a pre-cleaned Wilhelmy plate hanging on the force balance and wet the plate completely by dipping it into the testing liquid.
5. Raise it then above the testing liquid surface level.
6. Zero the force balance using the software and then slowly lower the Wilhelmy plate.
7. Read the surface tension in the force balance at the exact moment it touches the testing liquid surface.
8. Clean the Wilhelmy plate by ethanol rinsing, followed by flaming using a butane torch.

SOP for measurement of contact angle of testing liquids on a THF hydrate surface

1. Get a bucket of ice from CME building and put them into a freezer for further use. Adjust the temperature of the freezer to about -15 degree.
2. Mix Milli-Q water and pure THF in the mass ratio of 4:17 in a petri dish.

3. Seal the bottom and the cover of the petri dish by vacuum grease.
4. Put the petri dish into a metal tin.
5. Immediately put the metal tin into the freezer and keep it overnight to form THF hydrate.
6. Take the metal tin out from the freezer. At this point, THF hydrate should have formed. Check if the surface of THF hydrate is smooth. If not, place some pure THF onto the solid surface.
7. Add some ice into the metal tin around the petri dish for ice bath. The height of ice should cover the bottom of petri dish.
8. Put the metal tin into the fridge. After a certain period, ice should melt and the remaining solid should be THF hydrate.
9. After ascertaining the smoothness of the surface, place a droplet of a testing liquid above the THF hydrate surface.
10. Fix a web camera by a lab stand. Put the camera direct towards the front of hydrate surface. If necessary, light can be used.
11. Take the side view picture of THF hydrate surface. From the picture, contact angle can be measured with Image J.
12. Use other testing liquids to repeat measurements. Recording the contact angles of different testing liquids on THF hydrate surface.

4 Critical Shear Stress of Clathrate and Semi-Clathrate Hydrates on Solid Substrates

Given that there are scarce reports in the literature on the friction between hydrate and substrates, in this chapter, we will investigate the shear adhesive strength between THF clathrate hydrate/TBAB semi-clathrate hydrate and different substrates. The effect of temperature, the addition of a common kinetic hydrate inhibitor, PVP, and the hydrophobicity of substrates will be researched. This is the first time the impact of PVP and pre-melting layer on the friction is reported. The results in this chapter will provide a quantitative reference for the industry to alleviate hydrate-related flow assurance problems.

4.1 Introduction

Gas hydrates, or clathrate hydrates, are inclusion compounds that typically form at low temperatures and high pressures in which small “guest” molecules are trapped in an ice-like hydrogen-bonded “cage” structure of “host” water (Sloan and Koh 2008). This clathrate structure of individual guest molecules being distributed throughout the water cages can be viewed as a “solid solution” of the guests in the hosts (Vanderwaals and Platteeuw 1959). The much greater guest content in the clathrate form than the solubility of the same guest in liquid water, and the consequently increased entropy of mixing, renders gas hydrates stable at much higher temperatures than ice. Three structures of clathrate hydrate are common: Structure I (sI), Structure II (sII) and Structure H (sH), depending on the size and the compositions of the guest molecules (Ripmeester, Tse et al. 1987, Englezos 1993, Sloan and Koh 2008).

In oil and gas production pipelines and flow lines, clathrate hydrates may form at a water / hydrocarbon interface when the pressure / temperature condition falls within the hydrate stability zone of the phase diagram. Clathrate hydrate particles can then aggregate and deposit on the inner walls of the pipelines and flow lines, and cause a flow assurance problem (Sloan, Koh et al. 2011). Unless such hydrate deposition can be mitigated in a timely manner, the resulting blockage will

cause pressure buildup or even a structural damage to the pipeline.

The tangential adhesive force of gas hydrates to a solid surface, like a pipeline wall, is an important factor that influences the likelihood of dislodgement of gas hydrates off the pipeline walls due to the flow pressure (Turner, Miller et al. 2009, Aman and Koh 2016). Gas hydrates are also at the bottom of the hydrocarbon resource pyramid, which is to say that the amount of gas hydrate deposits around the globe is tremendously large but their recovery is less economical than the other hydrocarbon resources that are higher up in the resource pyramid. Here, natural gas hydrates stick to the sedimentary rocks or hold sand particles together in sand-bearing formations and their adhesive forces in turn influences its stability (Hyodo, Yoneda et al. 2013, Song, Zhu et al. 2014, Li, Xu et al. 2016, Manakov and Stoporev 2021).

Experimental investigations of adhesive forces under high pressures are expensive and unwieldy. Fortunately, a few guests form clathrate structures under the atmospheric pressure that render experimental investigations more tractable. An example guest that forms a clathrate structure under atmospheric pressure is tetrahydrofuran (THF) that forms the so-called Structure II (sII) hydrate of the composition of $(\text{THF} \cdot 17\text{H}_2\text{O})$ below 277.55 K (Yun, Santamarina et al. 2007, Zhao, Yao et al. 2011, Sowa, Zhang et al. 2014). Unlike a clathrate hydrate in which a guest molecule can fit into an individual cage of the clathrate structure, a larger molecule that cannot fit into one of the cages may occupy multiple “cages” under the right circumstances and form semi-clathrates under atmospheric pressure. An example of a guest that can form such a semi-clathrate structure under atmospheric pressure is Tetrabutylammonium bromide (TBAB) (Wang and Dennis 2015).

The adhesive force between a hydrate particle and another hydrate particle, and between a hydrate particle and a solid substrate surface was investigated experimentally by several methods in the past, including optical tweezers, atomic force microscopy and micromechanical force

measurements (Aspenes, Dieker et al. 2010). In micromechanical force measurements (abbreviated as MMF hereafter) a clathrate hydrate particle is mounted on a cantilever of a known spring constant and is pressed against another hydrate particle or against a solid surface and the pull-off force required to separate the clathrate hydrate particle from the surface is measured (Dieker, Aman et al. 2009, Aman, Leith et al. 2013, Aman, Sloan et al. 2014). Here, a normal stress is typically measured. Another parameter that characterizes the clathrate hydrate – surface adhesive strength is the critical shear stress. Here, the clathrate hydrate is directly grown on a solid surface (sometimes expressed as being “sintered”) and the force required to break the contact (the critical shear stress) is measured (Smith, Meuler et al. 2012).

Aspenes et al. (Aspenes, Dieker et al. 2010) measured the adhesive force of cyclopentane (CyC5) hydrate on several substrates and concluded that the higher the specific surface free energy of the substrate, the higher the hydrate – solid adhesive force. For glass and 309 stainless-steel, the adhesive force was around 0.9 and 0.85 mN/m, respectively. Aman et al. (Aman, Sloan et al. 2014) used the MMF method to measure the adhesive force of cyclopentane hydrate on untreated and chemically modified stainless-steel surfaces. They showed that the surface chemistry of the substrate had an important effect on the hydrate – steel adhesive force. Nicholas et al. (Nicholas, Dieker et al. 2009) measured the adhesive forces between CyC5 hydrates and carbon steel. The measured CyC5 hydrate – carbon steel adhesive force was less than either that between ice – carbon steel or that between two CyC5 hydrates. The adhesive force decreased with increasing supercooling and with increasing carbon steel surface roughness. Smith et al. (Smith, Meuler et al. 2012) measured the shear strength of THF hydrate – steel surface which is coated with different chemicals. They found that the adhesive strength was 422 ± 69 kPa for bare steel at 258.15 K and they obtained similar correlations between the adhesive strength and the specific surface free energy as Aspenes et al. did (Aspenes, Dieker et al. 2010). Wang et al. (Wang, Fan et al. 2019) used the MMF method to investigate the effect of corrosion of a carbon steel surface on the adhesive strength of CH₄ and C₂H₆ hydrate onto the steel. They concluded that the adhesive force

was around 3 mN/m for the steel before corrosion which increased with the extent of the corrosion. Das et al. (Das, Farnham et al. 2017) reported that CyC5 hydrate almost had no adhesive strength on a hydrophobic OTS coated silicon substrate. Dong et al. (Dong, Li et al. 2020) made a superhydrophobic coating on X90 steel. Compared with CyC5 hydrate – bare steel adhesion force, the CyC5 hydrate – the coated steel adhesion force was smaller by an order of magnitude.

An important factor that likely plays a major role in the adhesive strength of gas hydrates is the presence of a so-called Quasi Liquid Layer (QLL) (Jimenez-Angeles and Firoozabadi 2014, Maeda 2015, Aman and Koh 2016, Nguyen, Berger et al. 2021). Akin to the pre-melting of ice (Dash, Fu et al. 1995, Dash, Rempel et al. 2006), a QLL on a surface of gas hydrates is expected to grow in thickness with increasing temperature and diverges at the thermodynamic equilibrium dissociation temperature of the gas hydrates. The presence of a QLL gives rise to a capillary force between solid contacts, which in turn increases the normal force between gas hydrate particles (Nguyen, Berger et al. 2021). It remains to be seen if the tangential force (critical shear stress) will also rise in the presence of a QLL.

In this work, we investigated the critical shear stress (shear adhesive strength or tangential adhesive strength) of Structure II (sII) – forming tetrahydrofuran (THF) hydrate on five different solid substrates of stainless-steel, bare glass, piranha solution cleaned glass, (3-Aminopropyl) triethoxysilane (APTES) – coated glass and Octadecyltrichlorosilane (OTS) – coated glass over a range of temperatures and compared the critical shear stress to that of tetrabutylammonium bromide (TBAB) semi-clathrate hydrate on these five substrates. These two guests can form hydrates under atmospheric pressures and can be investigated using our setup that is not equipped to operate under elevated pressures. In addition, THF hydrate has been used as a model of natural gas hydrate (Vlasic, Servio et al. 2019), and TBAB semi-clathrate features a high latent heat of around 200 kJ/kg, which makes it a promising candidate to store and transport cold energies that can save energy by about 23.7% and 13.2% compared to ice and chilled water (Yin, Zheng et al.

2021), respectively. TBAB semi-clathrate hydrate is thus applicable to residential cooling, district cooling, data center cooling, cold chain application (Yin, Zheng et al. 2021), cold storage and transport (Kim, Zheng et al. 2022).


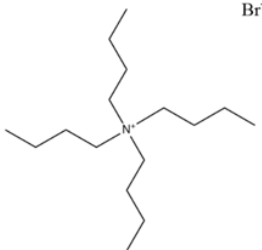
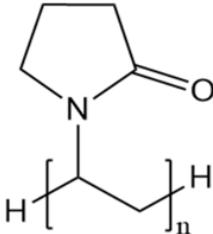
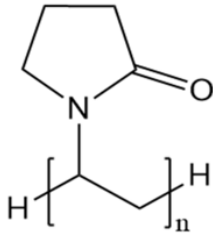
We also investigated the impact of a common Kinetic Hydrate Inhibitor (KHI), Polyvinylpyrrolidone (PVP) on the critical shear stress of these two hydrates. Kinetic Hydrate Inhibitor is a class of hydrophilic polymers that are effective in delaying the nucleation and/or crystal growth of gas hydrates with a low dosage (typically 1 wt%) (Kelland 2006, Tohidi, Anderson et al. 2015). However, it is unclear how their presence might influence the shear adhesive strengths of clathrate hydrates to a solid wall or their critical shear stress. Our findings may shed new light to the nature of the QLL on hydrate surfaces and suggest that the presence of KHIs may be detrimental in reducing the adhesive strength of hydrates to pipeline walls.

4.2 Materials and methods

Materials

Octadecyltrichlorosilane (OTS, purity 95%) was supplied by Acros Organics and used without further purification. Tetrabutylammonium bromide (TBAB, purity $\geq 99.0\%$), (3-Aminopropyl)triethoxysilane (APTES, purity $>98.0\%$), tetrahydrofuran (THF, purity $\geq 99.9\%$), Polyvinylpyrrolidone of average molecular weight of 10,000 Da (PVP 10), Polyvinylpyrrolidone of average molecular weight of 360,000 Da (PVP 360) were supplied by Sigma-Aldrich and used without further purification. Table 4-1 summarizes the chemicals we used in this study. Glass slides substrate (24 mm length \times 60 mm width \times (0.16 to 0.19) mm thickness) were supplied by Fisher Scientific.

Table 4-1 Summary of chemical used in this work

| | | | Hydrate | |
|--------|---|--------------------------|--|--------------------------|
| | Molecular structure | Molecular weight (g/mol) | stoichiometric ratio (Zhao, Yao et al. 2011, Wang and Dennis 2015) | Mass Concentration (wt%) |
| THF |  | 72.11 | THF·17H ₂ O | 19% |
| TBAB |  | 322.37 | TBAB·26H ₂ O | 25% |
| PVP10 |  | ≈10000 | N/A | 1% |
| PVP360 |  | ≈360000 | N/A | 1% |

Cylindrical glass sample holder (inner diameter of 6 mm, equivalent to cross sectional area of 28 mm²) was cut from Pasteur pipets supplied by Fisherbrand and 304 stainless steel substrates were cut to 40 mm × 40 mm. All the water used in this study was ultrapure quality from a Millipore

unit (18.2 M Ω).

Substrate preparations

304 stainless steel substrates were cleaned by ethanol. Piranha solution cleaned glass substrates were prepared by cleaning the glass slides with freshly prepared piranha solution ($\text{H}_2\text{SO}_4 : \text{H}_2\text{O}_2 = 7:3$ by volume) and then rinsing with water. OTS – coated glass substrates were prepared by following the procedure in *Appendix*. APTES – coated glass substrates were prepared by following the procedure in *Appendix*. We also investigated ethanol – cleaned glass substrates for comparison.

Clathrate and semi-clathrate hydrate sample preparations

A THF aqueous solution was prepared in a pre-cleaned flask by dissolving THF into water at the molar ratio of 1:17 or the mass ratio of 4:17 (THF : water = 4:17) because THF hydrate has a formula of $\text{THF} \cdot 17\text{H}_2\text{O}$. When the molar ratio is different from 1:17, there would be either an excess of water or an excess of THF. Then, different sample solutions were prepared in pre-cleaned flasks by dissolving a KHI (PVP10 or PVP 360) into THF aqueous solutions at a mass concentration of 1 wt%, which is a common concentration for a low-dosage KHI. The prepared solutions were left overnight with the flask sealed for complete dissolution. TBAB aqueous solutions were prepared in pre-cleaned flasks by dissolving TBAB into water at the mass concentration of 25 wt% (25 g of TBAB added in 75 g of milli-Q water) (Alhejaili, Babu et al. 2020). After the sample solution was prepared, THF clathrate hydrate or TBAB semi-clathrate hydrate was prepared *in-situ* before the measurements, as described below.

Surface tension measurements

The surface tension of PVP aqueous solutions was measured by the Wilhelmy plate method (Langmuir-Blodgett Deposition Troughs, Biolin Scientific) at 294 K. Before the measurement, the force balance was calibrated with calibration weight coming along with the device and the device

was calibrated with pure ethanol at 294 K. A small amount of a PVP aqueous solution of a controlled concentration was placed in a 50 mL beaker that had been pre-cleaned with Piranha solution (70% H₂SO₄ : 30% H₂O₂). During a measurement, a roughened platinum Wilhelmy plate (with the wetting length of 39.24 mm) was connected to a force balance with a hook and the force was recorded in a computer.

Contact angle measurements

The contact angle of milli-Q water on different substrates were measured by a contact angle meter (DSA 100, Kruss, Germany) at room temperature. A small amount ($\approx 10 \mu\text{L}$) of milli-Q water was placed on the substrate. Then, milli-Q water was added to the droplet at a constant rate of $1 \mu\text{L/s}$ for 5 seconds to measure the advancing contact angle. After this, milli-Q water was withdrawn into the syringe at a constant rate of $1 \mu\text{L/s}$ for 10 seconds to measure the receding contact angle from a recorded video. The steady-state contact angle during the additional injection or the subsequent withdrawal process was regarded as the advancing or the receding contact angle, respectively. The contact angle was measured at three separate locations on each substrate to ascertain the uniform surface wetting property.

The average values of the contact angle are summarized in Table 4-2. The advancing contact angle of a milli-Q water droplet on the stainless steel surface was in the range from 86° to 94° , with the average value and standard deviation of 90° and $\pm 4^\circ$, whereas the contact line continuously shortened when the water was being withdrawn. Therefore, the receding contact angle could not be detected on the stainless steel.

Table 4-2 Advancing and receding contact angles of water on substrates used in this work

| | Advancing contact angle (°) | Receding contact angle (°) |
|----------------------|--------------------------------|-------------------------------|
| Stainless steel | 90 ± 4 | – |
| Glass ⁽¹⁾ | 0 | 0 |
| Glass ⁽²⁾ | 64 ± 2 | 26 ± 3 |
| APTES-coated glass | 53 ± 1 | 35 ± 3 |
| OTS-coated glass | 117 ± 3 | 92 ± 2 |

⁽¹⁾ Cleaned by Piranha solution (volume of H₂SO₄ : volume of H₂O₂ = 7:3)

⁽²⁾ Cleaned by ethanol

It can be seen that the APTES coated glass slide, the stainless steel and the ethanol – cleaned glass slides were partially wet by water, the piranha solution cleaned glass slide was completely wet by water and the OTS coated glass slide was hydrophobic.

Critical Shear stress (tangential or shear adhesive strength) measurements

In this research, we used a setup (Yang, You et al.) that was similar to Smith et al.'s setup (Smith, Meuler et al. 2012) to study the shear adhesive strength between a hydrate and a solid substrate (Figure 4-1a). A heat sink, made of stainless steel with good thermal conductivity, was connected to a coolant circulating system through plastic tubing. The temperature in the coolant circulating system was adjusted within the range between 303.15 and 258.15 K by a temperature controller. Ethylene glycol was used as the coolant.

A piece of Peltier plate was placed on top of the heat sink with a thin layer of thermally conducting compound (MX-4, ARCTIC) in between. A pre-cleaned substrate was fixed to the top surface of the Peltier plate by a double-sided tape. A force transducer (HF-50, Beslands) with a maximum capacity of 50 N exerted a force of desired strength to a sample. The applied force was increased until the contact between the sample and the underlying substrate was broken and the

value of the maximum force was recorded. Finally, the critical shear stress was calculated using the known cross-sectional area of the hydrate – substrate interface. As shown in Figure 4-1b, four cylindrical glass sample holders were placed on a substrate, each of them can be pushed individually, so that four independent experiments could be carried out on a given substrate.

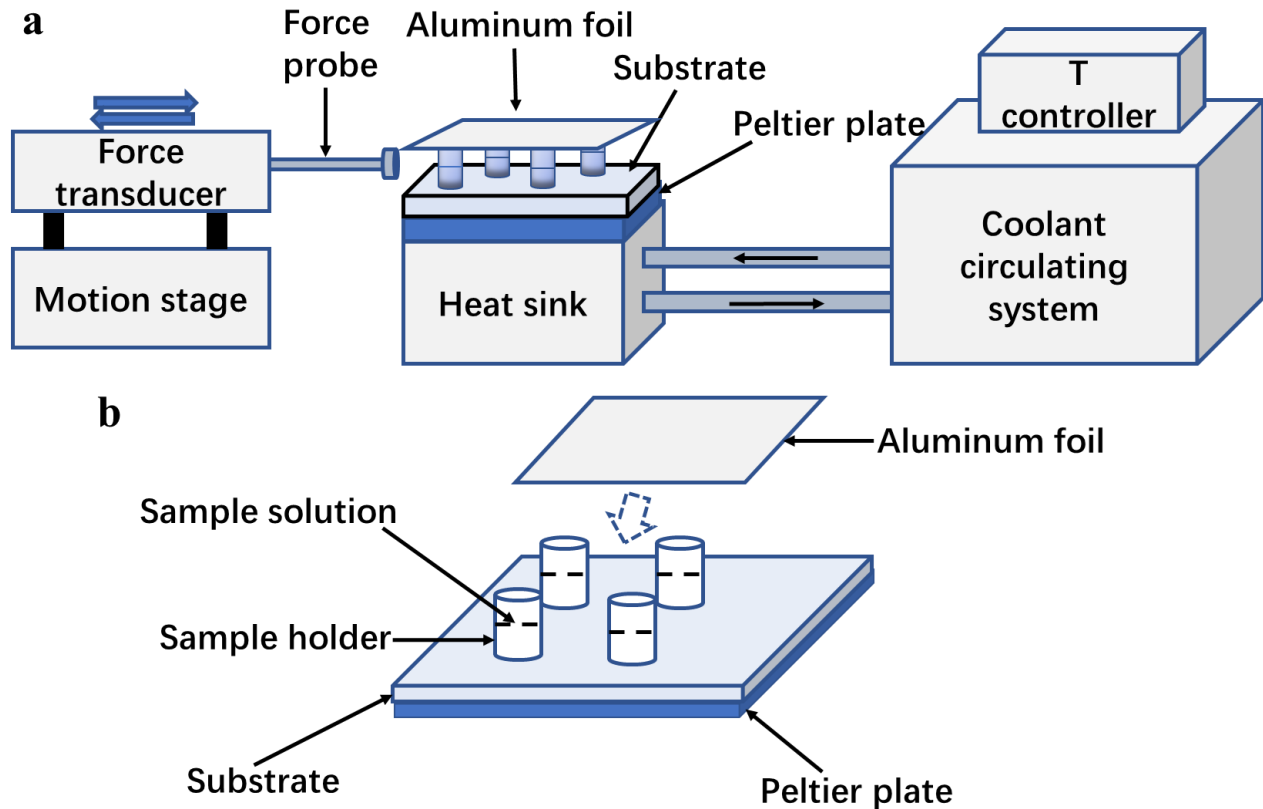


Figure 4-1 Schematic illustration of the shear adhesive strength measurement setup and the sample holders.

As shown in Figure 4-1a), the temperature of the top surface of the substrate was controlled by the combination of a Peltier plate and a coolant circulating system. Above the substrate, a 2×2 array of sample holders was placed. A sample solution was filled to half-full in each sample holder. Aluminum foil was used to cover the top of sample holder. A force transducer with a force probe

was moved by a motion stage to push the sample holder horizontally in a controlled manner until the hydrate broke off the substrate. The maximum shear force was recorded and converted to the critical shear stress using the known cross-sectional area of the hydrate-substrate interface. As shown in Figure 4-1b), the Peltier plate was attached to the top of the heat sink by a thin layer of thermal compound. The substrate was attached to the top surface of the Peltier plate by a double-sided tape. On the pre-cooled substrate, 4 sample holders, each with the cross-sectional area of 28 mm², were placed. Approximately 0.2 mL of sample solution was poured into each sample holder by a pre-cleaned pipette and a layer of aluminum foil covered the top of the sample holder.

A digital thermometer was used to measure the temperature of several locations of the top surface of the substrate to examine the uniformness of the temperature. The temperature uniformity of the top surface of the substrate was within ± 3 K over a stainless-steel surface and within ± 1.5 K over a glass slide surface.

Since many of the experimental temperatures were below the ice point, condensation of ambient moisture onto the pre-cooled substrate surface could form ice, which was undesirable. To prevent this, the substrate was temporarily warmed after the temperature uniformity check and the substrate was dried, before placing the four glass sample holders. The substrate was then pre-cooled before a small amount (≈ 0.2 mL) of sample solution was poured into the four glass sample holders. The pre-cooling of the substrate was important to achieve fast nucleation of the hydrate from the solution and preventing the solution from leaking out from the small gap between the bottom of the sample holders and the substrate. Avoiding such leakage ensured that the hydrate – substrate contact area was equal to the cross-sectional area of the sample holder. The top of the sample holders was then covered with aluminum foil.

Formation of either THF clathrate hydrate or TBAB semi-clathrate hydrate was visually confirmed through the glass walls of the sample holders. All measurements were commenced 10

minutes after all the liquid phases had converted to a solid phase. The force transducer was moved toward the sample holder and pushed a sample holder at the center. The commencement of the movement of the sample holder signaled the breakage of the hydrate – substrate interface. An interfacial failure was confirmed afterward by visual inspection. In rare cases when some hydrate was found to be left on the substrate, it indicated that the breakage occurred at a hydrate – hydrate interface, and such data point was discarded from further analysis. The maximum shear force recorded in the force transducer was divided by the hydrate – substrate interfacial area (which was assumed to be equal to the cross-sectional area of a sample holder), to obtain the critical shear stress in the unit of kPa. At least five independent repeated experiments were carried out for a given sample.

4.3 Results

Figure 4-2 shows the surface tension of the PVP aqueous solutions as functions of the *monomer* concentration (mole fractions). The surface tension of milli-Q water was also measured to be 72.1 mN/m at 294.15 K, as indicated in Figure 4-2 with an arrow. Figure 4-2 shows that the surface tension sharply decreased with the increase of the PVP *monomer* molar concentration, which indicated that both PVP 10 and PVP 360 had large positive surface excesses in accordance with the Gibbs adsorption isotherm (Maeda 2020). We note at this stage that, for a polymer solution, the chemical potential in the Gibbs adsorption isotherm is no longer proportional to $\ln C$ (where C is the mole fraction of the solute with respect to the solvent), as in the ideal solution approximation, but becomes proportional to the volume fraction of the polymer as the concentration increases. For our purpose here, it suffices to state that both PVPs are highly surface active, as expected of a KHI for which the nucleation and growth of gas hydrate typically take place at the aqueous – guest gas interface.

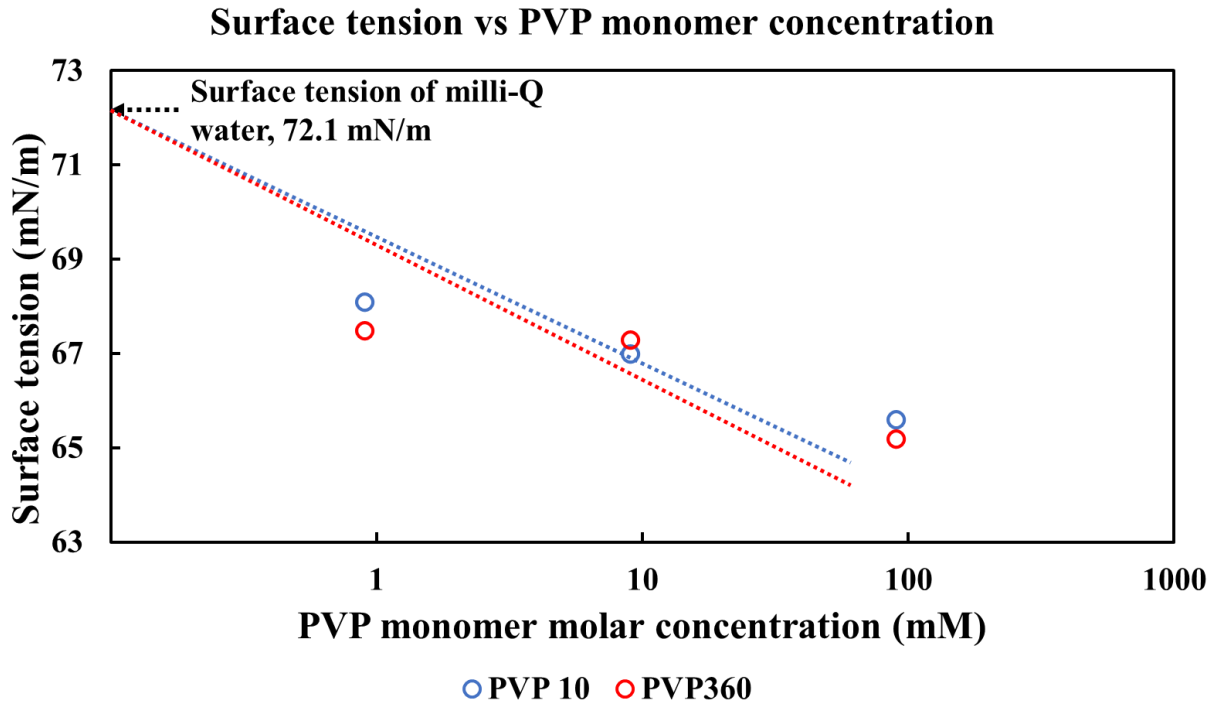


Figure 4-2 Relationship between PVP aqueous solution and PVP monomer molar concentration. The open circle symbols were experimental data points. The dashed lines are guides for eye.

Figure 4-3a is the top view of glass slides and sample holder before a shear adhesive strength measurement. The glass slides were transparent and the underlying black double – sided tape is visible here. Hydrate sample nucleated inside the sample holder before subjecting to the critical shear stress measurement. It can be seen that there was no sample solution outside of the sample holder, and as such the cross-sectional area of the sample holder can be regarded as the hydrate – substrate interfacial area. Figure 4-3b (glass) and Figure 4-3c (stainless steel) show example surfaces after the shear adhesive strength measurements. The blue circles indicate where breaking occurred. No hydrate was left on the surface, which indicated that the breakage had taken place at the hydrate – substrate interface. No hydrate was left in an interfacial failure mode (when the hydrate cleanly broke off the substrate). We encountered more frequent occurrence of a hydrate – hydrate interfacial breaking at a lower temperature. In this case, the force reading was discarded.

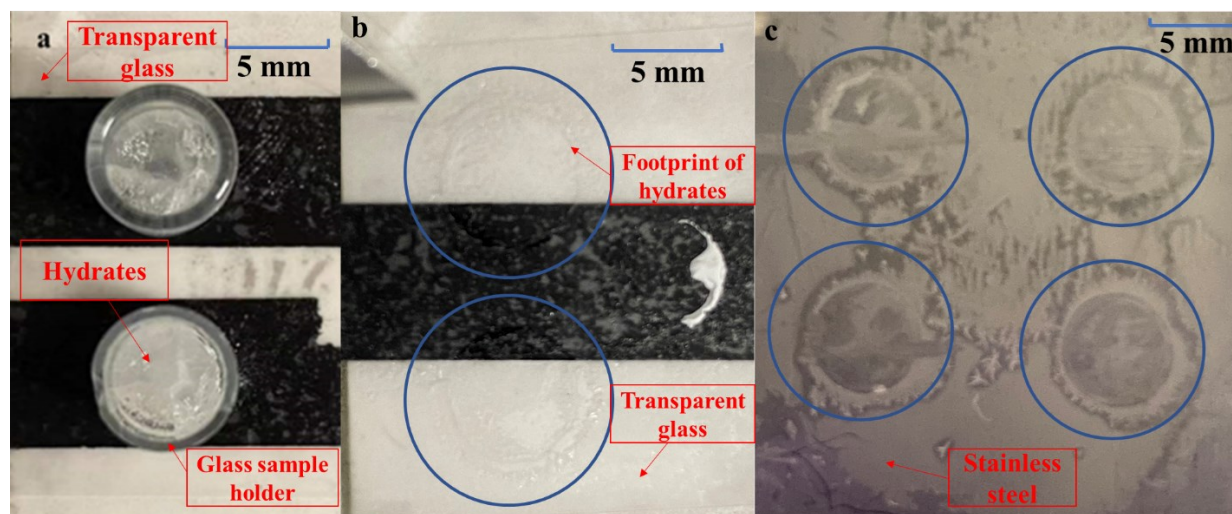
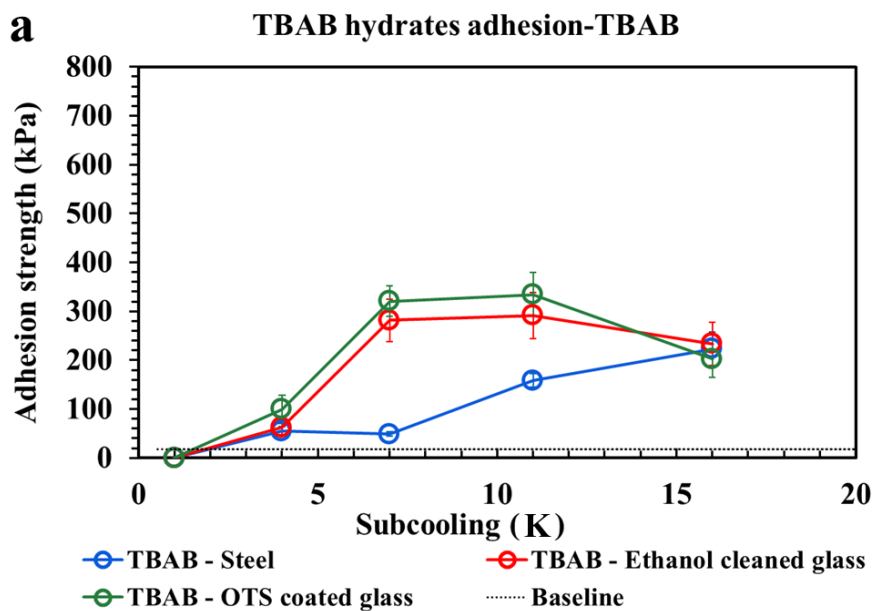


Figure 4-3 Typical images during the process of a shear adhesive strength experiment.

Figure 4-4a) and Figure 4-4b) showed the effect of supercooling (or subcooling, synonymously) on the TBAB semi-clathrate hydrate – substrate critical shear stress and THF clathrate hydrate – substrate critical shear stress, respectively. The horizontal black dotted line near the x-axis (the baseline) indicates the resolution limit of our force sensor. The subcooling (in the unit of K), ΔT , is defined as the temperature difference between the hydrate equilibrium temperature and the sample real temperature. The hydrate – substrate shear adhesive strength generally diminished with heating and became undetectably small (below the resolution of our force transducer) at the highest temperature studied (277.15 K of THF hydrate and 278.15 K of TBAB hydrate) for all substrates studied. For comparison, the dissociation temperature of THF hydrates is 277.55 K (Xue, Zhao et al. 2012) and that of TBAB semi-clathrate hydrate is 279.15 K (Wang and Dennis 2015). We note at this stage that the phase boundaries of TBAB semi-clathrate reported in the literature differ from each other. In this work, the equilibrium temperature of TBAB semi-clathrate hydrate at the mass concentration of 25% was referenced from Figure 4 of the ref.(Wang and Dennis 2015). In this work, the concentrations of the THF and TBAB aqueous

solutions were 19 wt% (molar ratio of THF: water = 1:17) and 25 wt%, respectively. We note that, for TBAB semi-clathrate hydrate, free water exists within a sample at a concentration below 40 wt%. However, if we used 40 wt% TBAB aqueous solutions, the so-called type *A* (TBAB·26 H₂O) and type *B* (TBAB·38H₂O) TBAB semi-clathrate hydrate would form simultaneously, which would complicate our analysis. Excess water is present at 25 wt% we used, nevertheless, it is extremely unlikely that ice can form in the current study for four reasons; (1) The chemical potential of water in TBAB semi-clathrate is always lower than that in ice at a given temperature. This is evidenced by the higher dissociation temperature of the TBAB semi-clathrate than the ice point; (2) Pure water usually requires supercooling of about 10 K before it forms ice (Sowa, Zhang et al. 2014), which is the lowest target temperature in our study; (3) The presence of the counterions of TBAB would depress the freezing point of ice; (4) When we tried to measure the critical shear stress of pure ice on the four substrates we used as a control experiment, the critical shear stress of ice turned out to be too strong for our instrument (the force sensor went out of range).



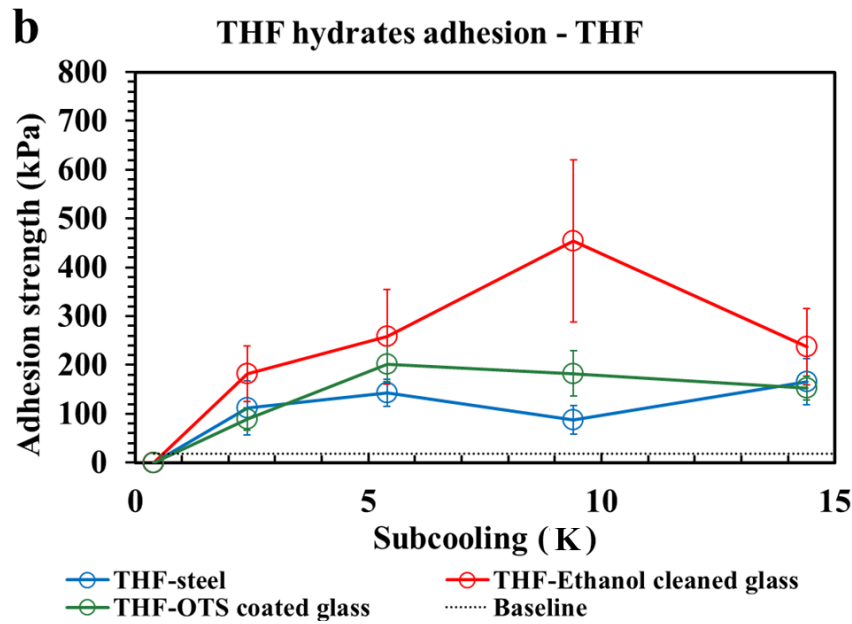
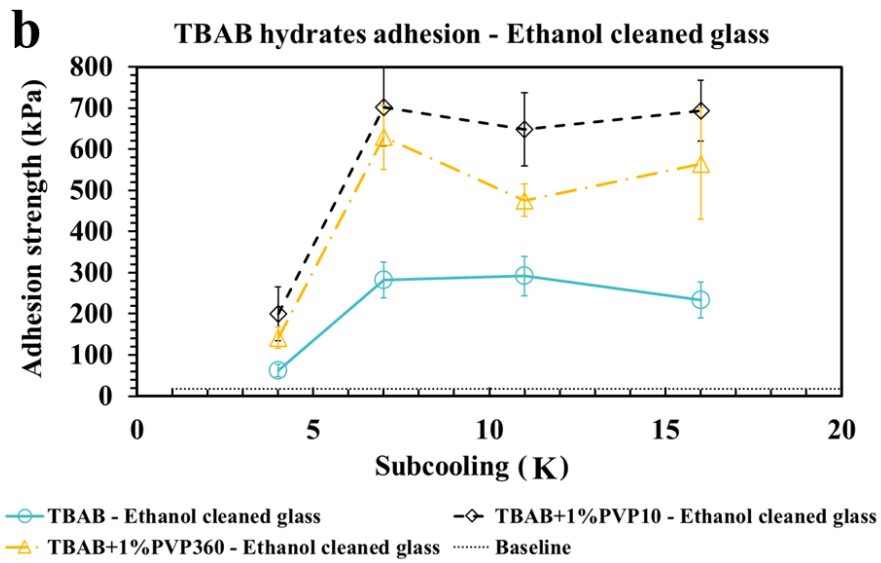
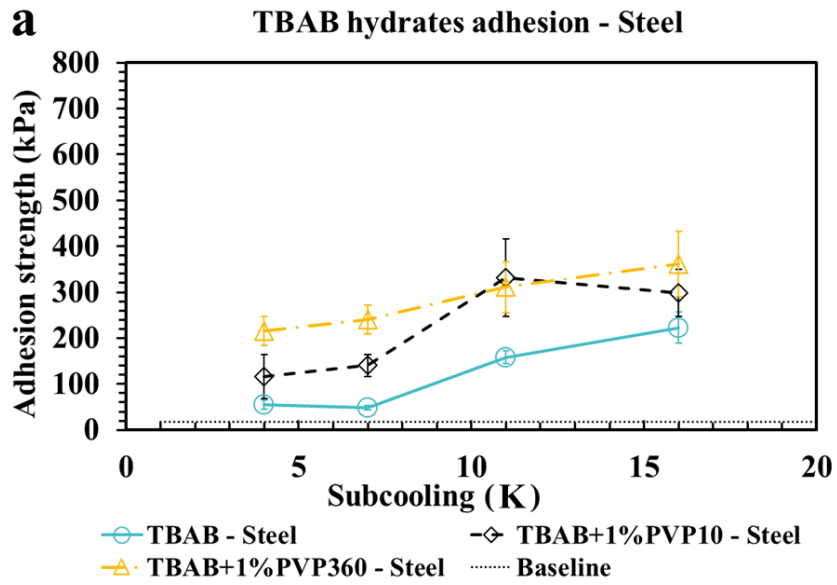


Figure 4-4 Effect of temperature on the critical shear stress of the hydrate – substrate interface

Figure 4-5 showed the effect of the KHIs on a) TBAB semi-clathrate hydrate – stainless steel surface b) TBAB semi-clathrate hydrate – ethanol cleaned glass slide surface. c) TBAB semi-clathrate hydrate – OTS coated glass slide surface. The horizontal black dotted line near the x-axis indicates the resolution limit of out force sensor. Figure 4-6 showed the effect of the KHIs on a) THF clathrate hydrate – stainless steel surface, b) THF clathrate hydrate – ethanol cleaned glass slide surface, c) THF clathrate hydrate – OTS coated glass slide surface. Again, the horizontal black dotted line near the x-axis indicates the resolution limit of out force sensor. It can be seen that the addition of the KHIs did not lead to any decrease in the hydrate – substrate interfacial shear adhesive strength on any of the substrates investigated. To the contrary, KHIs even slightly increased the hydrate – substrate interfacial shear adhesive strength on some substrates.



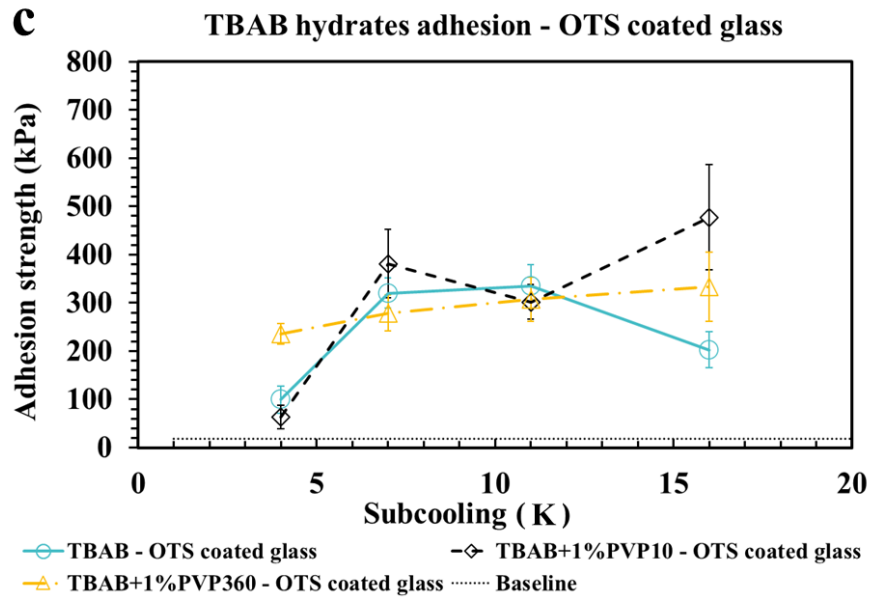
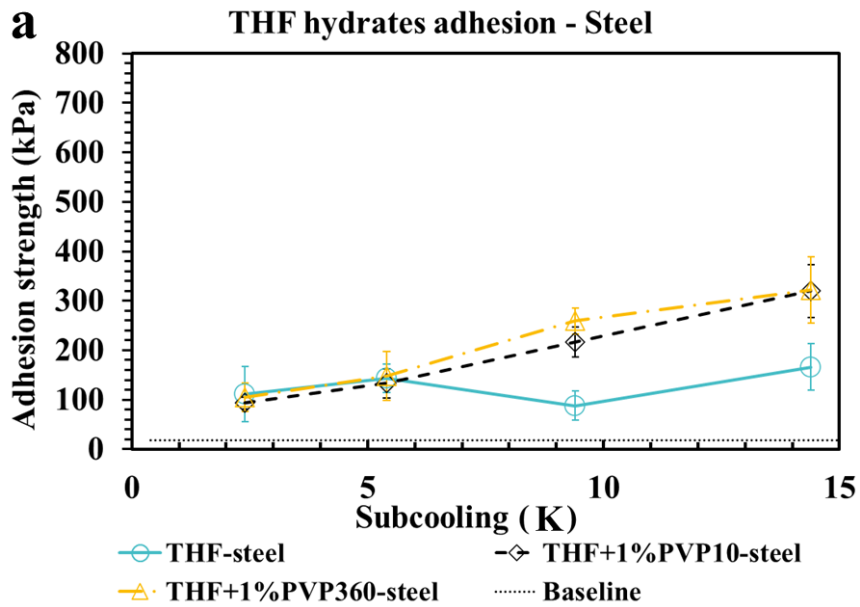


Figure 4-5 Effect of the addition of 1 wt% kinetic hydrate inhibitor (KHI) PVP10 and PVP360 on TBAB semi-clathrate hydrate – substrate shear adhesive strength.



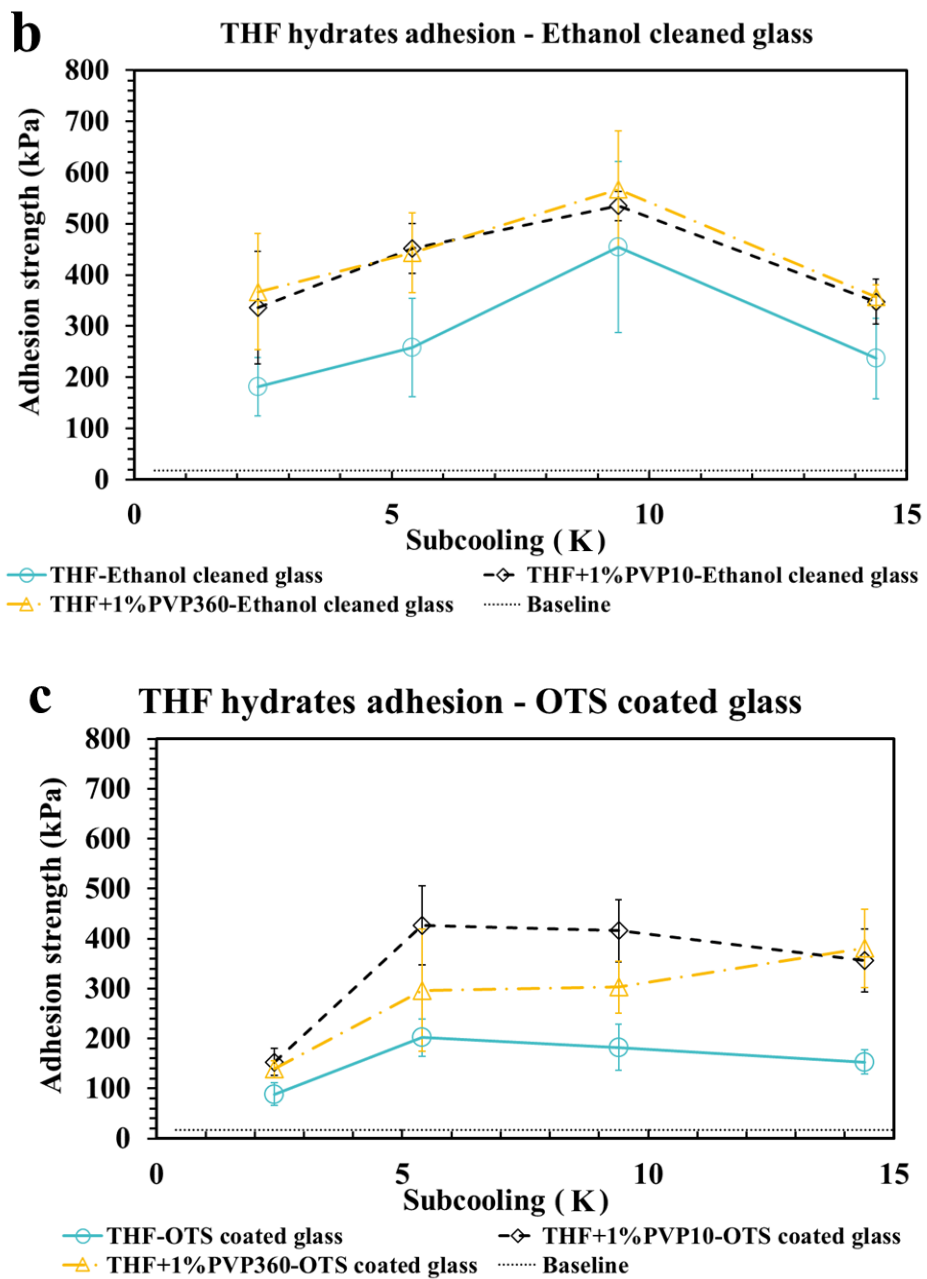


Figure 4-6 Effect of the addition of 1 wt% kinetic hydrate inhibitor (KHI) PVP10 and PVP360 on THF hydrate – substrate shear adhesive strength.

Figure 4-7 showed the effect of hydrophobicity of the substrate (using the contact angle of water as a measure) on the critical shear stress of the hydrate – substrate interface at a selected

temperature. Since the critical shear stress was unmeasurably low at high temperatures for all substrates, we selected 263.15 K (the lowest temperature we used) for the purpose of this comparison. The horizontal black dotted line near the x-axis indicates the resolution limit of our force sensor. Contrary to our expectations, the hydrophobicity of the substrate increased the critical shear stress from that on a hydrophilic surface. Figure 4-7 also showed that the addition of PVP increased the critical shear stress of the substrates over the entire range of hydrophobicity studied.

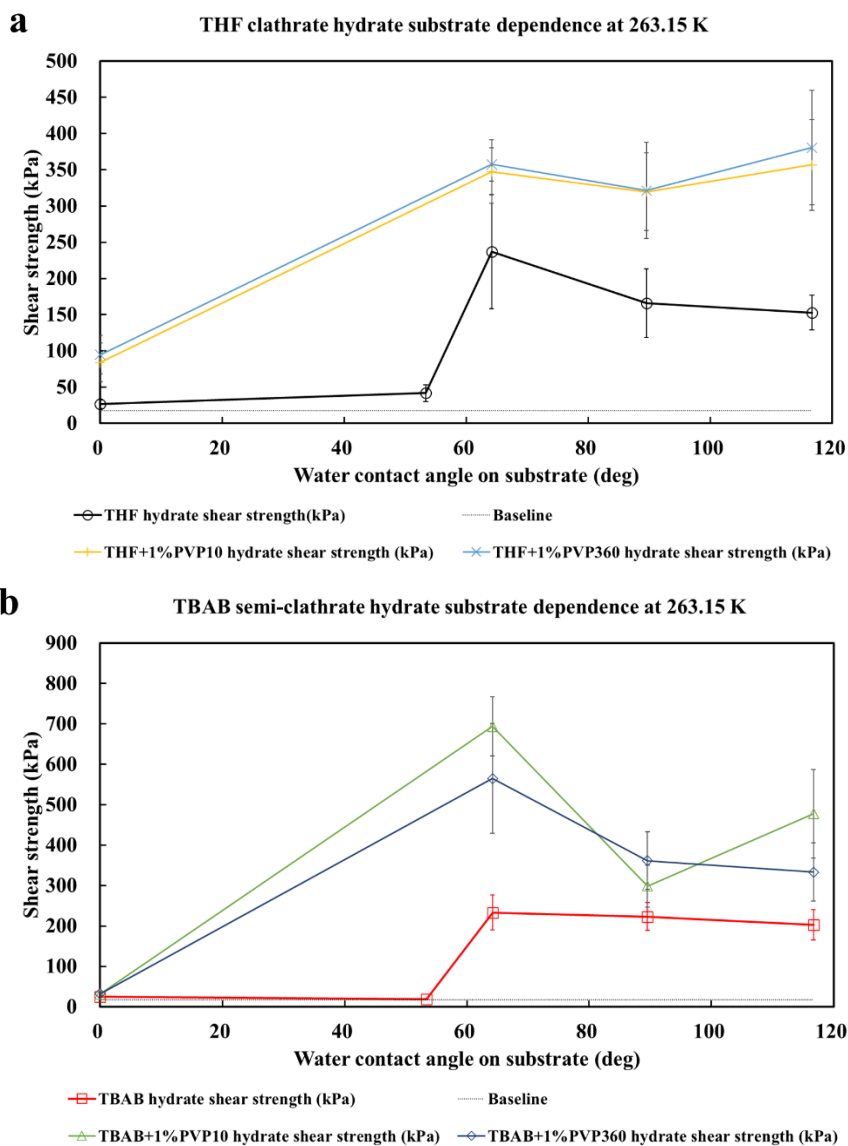


Figure 4-7 Effect of the hydrophobicity of the substrate on the critical shear stress of the hydrate

– substrate interface.

4.4 Discussion

Our results show that (1) the critical shear stress diminished with heating and became unmeasurably small just below the dissociation temperature, (2) the wettability of water on the substrate unexpectedly had no significant effect on the critical shear stress, (3) the addition of PVP increased the critical shear stress of THF hydrate, (4) critical shear stress of THF clathrate hydrate and that of TBAB semi-clathrate hydrate were similar on the same substrate at a comparable temperature.

Among these four findings, the most important one is that the critical shear stress diminished with heating and became negligibly small just below the dissociation temperature. This finding may at first appear contrary to expectations because the normal adhesive force that has been known to be enhanced by the quasi-liquid layer due to the capillary action (Aman, Brown et al. 2011, Nguyen, Berger et al. 2021). However, our finding actually makes sense. To explain why, we start from the fundamental difference between adhesion *forces* and adhesion *hysteresis* (Yoshizawa, Chen et al. 1993).

Cohesion hysteresis between two cyclopentane hydrate particles has been known to be very small (Maeda, Aman et al. 2013), and we expect the same will hold for other clathrate hydrates in general. An important point here is that cohesion hysteresis correlates with friction forces, not with cohesive forces (Yoshizawa, Chen et al. 1993), and it was hypothesized that quasi-liquid layers (pre-melting) on the cyclopentane hydrate surfaces were responsible for the very small frictional forces (Maeda, Aman et al. 2013). Then, our current findings that the critical shear stress diminished with heating and became small just below the dissociation temperature is consistent with the idea that quasi-liquid layers on clathrate hydrate surfaces (which are expected to grow thicker with heating) act as an excellent lubricant layer that reduced the static friction force.

Our second finding that the critical shear stress *increased* with the hydrophobicity of the substrate is unexpected and difficult to explain. We here used the advancing contact angle of water as the measure of the hydrophobicity of the substrate. The observed change was not monotonic and instead the critical shear stress jumped around the contact angle of 60°. No significant change in the critical shear stress was observed with the hydrophobicity of the substrate other than this single jump around the contact angle of 60°. Our prior expectation that was in line with the literature (Smith, Meuler et al. 2012, Aman, Sloan et al. 2014, Dong, Li et al. 2020, Liu, Wang et al. 2020, Liu, Zeng et al. 2020, Nguyen, Berger et al. 2021) has been that the critical shear stress would decrease with the hydrophobicity of the substrate because a clathrate hydrate would have a higher affinity to a hydrophilic substrate than to a hydrophobic one.

Our third finding that the addition of KHI increased the shear adhesive strength of THF hydrate may be expected. Figure 4-2 showed that both PVP10 and PVP 360 are surface-active, as both PVP molecules adsorb positively to the interface in accordance with the Gibbs adsorption isotherm (Maeda 2020). The abscissa of Figure 4-2 is the *monomer* concentration or the mole fraction of the *monomers* that are contained in each PVP. Had we plotted the surface tension of the PVP solutions as functions of the mole fractions of the *polymers* instead, the negative slope and the corresponding positive surface excess would have been much greater. This much greater concentrations of the PVPs at the interface than in the bulk aqueous phase are expected of KHIs because (1) gas hydrates are known to preferentially nucleate and grow at an aqueous – guest gas interface and (2) the KHIs must be present at the interface to function at all.

Once we ascertain their presence at the interface, then the remaining mechanism behind the increased critical shear stress due to the presence of the PVPs may be trivial. Main active ingredients of commercial adhesives are polymers (the strong Van der Waals forces between the polymers and the contacting surfaces after the dissolving solvent has been evaporated are

responsible for the performance of commercial adhesives). Then, it should not come as a surprise if the polymeric KHIs effectively acted as adhesives at the interface and increased the critical shear stress. Basically, a conclusion here is that although PVPs can inhibit nucleation and/or crystal growth of gas hydrates, our results show that additions of PVPs (and also likely other KHIs) are detrimental to flow assurance as far as clathrate hydrate adhesion is concerned.

Our fourth finding is that the critical shear stress of THF clathrate hydrate and that of TBAB semi-clathrate hydrate were similar on the same substrate at a comparable temperature. The main structural difference between a clathrate and a semi-clathrate hydrate is that no single guest molecule occupies multiple cages in a clathrate hydrate (like THF hydrate) whereas a large single guest molecule can occupy multiple cages in a semi-clathrate hydrate (like TBAB hydrate). For THF clathrate hydrate, the crystal structure is sII where THF molecule is trapped in the big cages ($5^{12}6^4$) and has a stoichiometric formula of $\text{THF} \cdot 17\text{H}_2\text{O}$. However, for TBAB semi-clathrate, because TBA cation is too large to be trapped in small (5^{12}) and big ($5^{12}6^4$) cages, the structure is more complicated. According to the literature, there are two main types of TBAB semi-clathrate hydrates depending on the formation conditions. These two types of TBAB semi-clathrate hydrates are $\text{TBAB} \cdot 26 \text{H}_2\text{O}$ (the so-called type *A*) and $\text{TBAB} \cdot 38\text{H}_2\text{O}$ (type *B*). $\text{TBAB} \cdot 26 \text{H}_2\text{O}$ has the needle/columnar shape (Oyama, Shimada et al. 2005) and the TBA cation is located in the merging cage consisting of three tetrakaidecahedrons and one pentakaidecahedron (Shimada, Ebinuma et al. 2003). $\text{TBAB} \cdot 38 \text{H}_2\text{O}$ has the irregular shape (Kim, Zheng et al. 2022) and the TBA cation is located in the merging cage consisting of two tetrakaidecahedrons and two pentakaidecahedron (Shimada, Shiro et al. 2005). In this study, since we used the mass concentration of 25 wt%, the $\text{TBAB} \cdot 26 \text{H}_2\text{O}$ is preferentially formed. Generally, the density of the hydrogen bonds in a semi-clathrate hydrate is lower than that of a clathrate hydrate due to broken cages in the semi-clathrate hydrate, and consequently, a semi-clathrate hydrate is expected to be somewhat mechanically weaker than a clathrate hydrate. We note that Young's modulus of THF hydrate has been reported to be 7.17 GPa at 256 K (Bathe, Vagle et al. 1984) but Young's modulus of TBAB semi clathrate

hydrate has not been reported in the literature, so we cannot make direct comparisons. A softer material is generally expected to yield at a smaller stress than a harder material, thus if our sample did not cleanly break off at the interface and instead left some remnants of hydrates on the substrate after a breakage, we might have expected the critical shear stress of the TBAB semi-clathrate hydrate to be somewhat lower than that of THF hydrate. Given that the crystallographic facets of TBAB semi clathrate hydrate and THF hydrate are similar (THF hydrate has sixteen 5^{12} cages and eight $5^{12}6^4$ cages in the unit cell while TBAB semi clathrate hydrate has ten 5^{12} cages and sixteen $5^{12}6^4$ cages and four $5^{12}6^3$ cages), we expect that their specific surface free energy values (and their adhesive strengths) to be similar. Then, our finding that the two critical shear stresses turned out to be similar to each other supports our visual observations that our samples cleanly broke off at the interface.

4.5 Conclusions

We investigated the shear (tangential) adhesive strength of Structure II (sII) – forming tetrahydrofuran (THF) hydrate on five different solid substrates of stainless-steel, bare glass, piranha solution cleaned glass, (3-Aminopropyl)triethoxysilane (APTES) – coated glass and octadecyltrichlorosilane (OTS) – coated glass, and compared the critical shear stress to that of tetrabutylammonium bromide (TBAB) semi-clathrate hydrate on the same five substrates. We also investigated the impact of a common Kinetic Hydrate Inhibitor (KHI), Polyvinylpyrrolidone (PVP) of two different molecular weights, on the critical shear stress of these hydrates.

Our results show that (1) the critical shear stress diminished with heating and became negligibly small just below the dissociation temperature of the hydrates and (2) the addition of KHI increased the shear adhesive strength of THF hydrate. PVP increased the critical shear stress of both THF clathrate hydrate and TBAB semi-clathrate hydrate, presumably because PVP acted as an adhesive. Contrary to our expectations, the hydrophobicity of the substrate increased the critical shear stress from that on a hydrophilic surface. That the critical shear stress became

unmeasurably small just below the dissociation temperature of the hydrates suggests that the quasi-liquid layer acted as an effective lubricant layer that reduced the static friction. This is in contrast to the normal adhesive force that has been known to be enhanced by the quasi-liquid layer due to the capillary action. Our results imply that the temperature dependence of the impact of a quasi-liquid layer on the normal forces and the tangential forces do not correlate with each other. Finally, there are still many knowledge gaps about the critical shear stress of a clathrate hydrate – substrate interface. For example, other than THF and TBAB, common guests like methane and CO₂, are worthy of future investigations.

4.6 Summary and Relationship to Chapters that Follow

In this chapter, we investigated the shear adhesive strength between THF clathrate hydrate/TBAB semi-clathrate hydrate and different substrates. We found that the pre-melting layer had the opposite effect on the shear adhesive strength as on the normal adhesive strength. The addition of PVP was detrimental to flow assurance as far as adhesion was concerned. The main findings of this chapter are significant for the mitigation of flow assurance problems from the perspective of adhesion. In addition, nucleation, as the first step of hydrate formation is also of great significance for the prevention and control of hydrate plugs. However, due to the involved stochasticity and experimental difficulties, nucleation kinetics was less characterized compared to adhesion. In the next chapter, we will investigate hydrate nucleation kinetics and derive the most essential kinetic parameter, nucleation rate. The elucidation of influencing factors of hydrate nucleation kinetics helps the industry maximize or minimize hydrate nucleation kinetics, depending on the needs.

4.7 Appendix

OTS coated glass slide preparation procedure

Glass slides were taken from the container and rinsed with milli-Q water and ethanol. Piranha solution (volume of H₂SO₄: volume of H₂O₂ = 7:3) was prepared in petri dish. Then glass slides were placed inside the petri dish and the petri dish was placed inside the oven in which temperature was 75 °C for 20 min. This Piranha solution cleaning process was to remove any organic impurities

on the glass surface and make it super hydrophilic. After that, the glass slides were transported to a new petri dish with milli-Q water and placed inside for 20 minutes. This process was repeated for 3 times to rinse the residual Piranha solution on the glass surface thoroughly. Then, the glass slides were sonicated in milli-Q water and then in ethanol for 15 mins each. The glass slides were placed in an oven for 2 hours at 120 degrees. The glass slides were taken from the oven and cooled to room temperature before coating. A 0.5 vol% OTS in hexane solution was prepared in a pre-cleaned petri dish quickly to prevent the polymerization of OTS while in contact with the moisture in air. Then the glass slides were soaked in the 0.5 vol% OTS solution in a sealed dry container at room temperature for 12 hours for the coating reaction. After the coating, the glass slides were rinsed with hexane and the rinsing was repeated for 3 times to wash the residual OTS away. Then glass slides were sonicated in hexane and then in ethanol for 10 mins each. Finally, the coated slides were dried with an air flow and stored in a clean container for future use.

APTES coated glass slide preparation procedure

Glass slides were taken from the container and sonicated in milli-Q water for 15 mins. Then the glass slides were dried with an air flow in the fume hood. Piranha solution (volume of H_2SO_4 : volume of $\text{H}_2\text{O}_2=7:3$) was prepared in a petri dish. Then the glass slides were placed inside the petri dish and the petri dish was placed inside an oven (temperature 75 °C) for 20 min. The glass slides were then placed into milli-Q water in a new petri dish and were left for 10 min. This process was repeated for 3 times. The glass slides were then rinsed with milli-Q water thoroughly then dried with an air flow in the fume hood. A 1.5 vol% APTES in ethanol solution was prepared in a pre-cleaned petri dish and a droplet of APTES in ethanol solution was placed on the cleaned glass surface. A piece of clean paraffin film was placed on the top of the glass to flatten the droplet into a thin liquid film on the cleaned glass. After 3 to 5 minutes the paraffin film was taken off and the glass slides were thoroughly rinsed with ethanol. Finally, the APTES coated glass slides were dried with an air flow and placed into a clean container for future use.

Piranha solution cleaning SOP

1. Rinse glass slides by milli-Q water.
2. Rinse glass slides by ethanol.
3. Use air flow to dry glass slides.
4. Place an oven in the fume hood, the temperature is set as 75 degrees.
5. Place a clean glass petri dish on the oven. Then place the dry glass slides in step 3 into the petri dish.
6. To prepared 100 mL of piranha solution, place 70 mL of 98% H₂SO₄ in a clean beaker and place 30 mL of 30% H₂O₂ in another clean beaker.
7. Pour H₂SO₄ into the petri dish first, then pour H₂O₂ into the petri dish. Let the glass slides be immersed by the piranha solution. Then cover the petri dish with the lid.
8. Wait for 20 min for complete cleaning of glass slides.
9. Quickly move the glass slides to a new petri dish with Milli Q water and place for 20 minutes, repeat it for 3 times. (Use tweezers to clamp the rim of glass slides to move it, all movements of glass slides should be performed in this way, do not touch the middle part of the glass slides)
10. Used piranha solution is slowly poured into the inorganic waste bottle.
11. Sonicate glass slides in Milli-Q water for 15 min.
12. Sonicate glass slides in ethanol for 15 min.
13. Use air flow to dry glass slides and store in a clean container.

SOP for shear adhesive strength between hydrate and a solid substrate

1. Prepare THF aqueous solution (19 wt%) and TBAB aqueous solution (25 wt%).
2. Transfer the prepared solutions to a flask and seal the top of it using aluminum foil to prevent evaporation.
3. Stick the prepared substrate on the surface of a Peltier plate using double-sided tape.
4. Put four glass sample holders on the surface of the prepared substrate.
5. Switch on the bath and the Peltier plate. The top surface of the Peltier plate will cool while the

bottom surface will warm because of the Peltier effect. The heat generated on the bottom surface is dissipated by the coolant circulating inside the heat sink below the bottom surface of the Peltier plate.

6. Use the thermometer to measure the temperature of the surface of substrates and adjust the temperature of the bath accordingly so that the substrate is pre-cooled to ensure the in-situ formation of hydrate sample.

7. Transfer a little amount of THF/TBAB aqueous into the sample holder using a pipette. The liquid level is maintained to be in the middle of the sample holder. Because of the pre-cooled nature of the substrate, THF/TBAB hydrate sample would in-situ form in the sample holder at a fast rate. Therefore, there is no leak from the gap between the sample holder and the substrate.

8. A piece of aluminum foil is covered on the top of the sample holder to prevent sample evaporation during hydrate formation.

9. Hydrate formation can be visually detected with the phase transition from a supercooled liquid phase to a solid bulk crystal.

10. After hydrate formation, the bath temperature is adjusted so that the surface of the substrate reaches the experimental temperature.

11. The force transducer stuck to a motion stage is turned on and switched to the “peak” mode.

12. Adjust the height of the force transducer so that it pushes the sample holder from the bottom. This is to ensure no moment is exerted on the sample holder and only lateral force will be applied.

13. Switch on the motion stage and let the force transducer approach the sample holder and then break the hydrate-substrate contact.

14. The maximum force applied by the force transducer is shown on the panel and recorded.

15. Observe the breaking pattern of hydrate-substrate contact. If this is a cohesive fracture (hydrate-hydrate fracture), this data is disregarded from further analysis.

16. Divide the maximum force recorded in step 14 by cross-sectional area to obtain the shear adhesive strength.

5 Nucleation Curves of Carbon Dioxide Hydrate in the Absence of a Solid Wall

In this chapter, we will derive nucleation curves of CO₂ hydrate nucleation in the presence and absence of a solid wall. The calculated nucleation rates will be compared to the literature data to shed light on the effect of guest type and the presence of a solid wall. The convergence of nucleation curves and the limitation of applying Classical Nucleation Theory in analyzing hydrate nucleation will also be discussed. The baseline of CO₂ hydrate nucleation kinetics is established for the first time. Compared with it, the effect of additives, solid walls and system size can be illustrated, which is beneficial for the industry to control hydrate nucleation kinetics. Also, the nucleation kinetics of natural gas hydrate (methane hydrate) in a gas-dominant flow can be qualitatively inferred.

5.1 Introduction

Clathrate hydrate is a compound in which guest molecules are trapped in the hollow cages formed by hydrogen bonding of water molecules (host). Many low molecular weight guest molecules can form clathrate hydrate of different lattice structures with water when the pressure and temperature condition is within the hydrate stability zone of the phase diagram. Examples include methane hydrate (sI), ethane hydrate (sII), propane hydrate (sII), CO₂ hydrate (sI) and tetrahydrofuran hydrate (sII).

Clathrate hydrate has potential applications in gas storage, gas separation, desalination, air conditioning and others (Koh, Sloan et al. 2011). CO₂ hydrate forms sI structure with theoretical hydration number between 5.75 to 7.67 (Anderson 2003). Owing to the high gas uptake capacity of clathrate hydrate, hydrate formation technology can be applied to CO₂ storage and sequestration. Because CO₂ hydrate is more thermodynamically stable than methane hydrate over a broad range of temperature and pressure, it is theoretically possible to recover methane gas from the methane hydrate in sediments by exposing methane hydrate to CO₂ (Nguyen, Nguyen et al. 2022). This

exchange process would release methane gas from the methane hydrate sediment and sequester CO₂ to the space vacated by methane. The challenge lies with the kinetics that enables prompt conversions.

In contrast, formation of gas hydrates can be undesirable in some cases. Gas hydrate can form in the multi-phase flows inside oil & gas pipelines from hydrocarbons and residual water, and pose threats to flow assurance. It is thus highly desirable to be able to delay or avoid the formation of clathrate hydrates here. It is widely acknowledged that the gas hydrate plug formation is a multi-step process: dissolution, nucleation, crystal growth and agglomeration (Turner 2005). Nucleation refers to a process involved in a first-order phase transition in which a thermodynamically metastable phase is converted to a thermodynamically stable phase. In a clathrate hydrate forming system, the metastable phase usually refers to an aqueous solution that is supersaturated with the guest gas and the supersaturation becomes the driving force for nucleation. Under an isobaric condition, the driving force is proportional to the system supercooling in the first approximation (Kashchiev and Firoozabadi 2002), which is the temperature differential between the temperature of the clathrate phase boundary at the pressure of interest and the temperature of the supercooled aqueous solution. The duration of this metastable state before transitioning to a thermodynamically stable phase is the subject of nucleation kinetics. Experimentally, an induction time, the time interval between the establishment of a supersaturation and the detection of the nucleation event under a constant driving force, has been commonly used to characterize the nucleation kinetics of clathrate hydrates, and its inverse yields the most probable nucleation rate.

Early studies on clathrate hydrate nucleation kinetics can be traced back to the 1980s. Bishnoi and colleagues pointed out several variables influencing hydrate formation kinetics (Bishnoi, Natarajan et al. 1994) including supersaturation, thermal and other histories of water (Makogon 1981, Vysniauskas and Bishnoi 1983), structure of water (Vysniauskas and Bishnoi 1983, Nerheim, Svartaas et al. 1992), hydrophobic hydration (Frank and Evans 1945, Frank and Quist 1961, Glew

1962), the presence of impurities, surface heterogeneities of the reactor wall (Makogon 1981), the rate of gas dissolution (Bishnoi and Natarajan 1996) and stirring. Englezos et al. found the higher local supersaturation of methane / ethane at the water – guest gas interface and the predominant occurrence of hydrate nucleation at the interface (Englezos, Kalogerakis et al. 1987). Bishnoi and co-workers identified the dependence of the induction time on the supersaturation in that the induction time increased and became more stochastic with the decreasing supersaturation, and vice versa (Bishnoi, Natarajan et al. 1994, Natarajan, Bishnoi et al. 1994). Natarajan et al. defined the driving force for nucleation as the difference in the fugacity of the dissolved guest gas in the liquid water (f_g^v) and the three-phase equilibrium fugacity (f_{eq}), both at the experimental temperature (Natarajan, Bishnoi et al. 1994), which is consistent with the general definition of supersaturation. Based on the ratio of f_g^v to f_{eq} , Natarajan et al. proposed a model for predictions of hydrate nucleation induction times (Natarajan, Bishnoi et al. 1994).

Sloan and co-workers carried out detailed investigations on the nucleation kinetics of methane hydrate. They postulated a molecular mechanism of hydrate nucleation process which envisaged the formation of a stable hydrate nuclei from the gas-water clusters (Vysniauskas and Bishnoi 1985, Muller-Bongartz, Wildeman et al. 1992, Christiansen and Sloan Jr 1994) and from the agitated ice surface (Sloan Jr and Fleyfel 1991). From the molecular dynamics (MDs) simulations of spontaneous nucleation of methane hydrate, they reported the resulting structure after nucleation and growth is the coexistence of kinetically preferred sII structure and subsequent thermodynamically favored sI structure. They investigated methane hydrate nucleation rate from MDs simulations and reported the positive correlation between the nucleation rate and the aqueous methane concentrations (Walsh, Beckham et al. 2011). Using a differential scanning calorimetry (DSC), they found that methane hydrate nucleated mostly over a narrow supercooling range of a few Kelvins around 30 K of supercooling, despite the stochasticity of hydrate nucleation and that onset of methane hydrate nucleation was likely to be affected by the wall of the DSC sample cell but unlikely to be affected by the cooling rate (Davies, Hester et al. 2009).

More recently, Manakov and co-workers carried out a series of studies that focused more specifically on the nucleation aspect of hydrate formation kinetics. They investigated different factors that could influence gas hydrate nucleation kinetics in the presence and in the absence of a solid wall and found: (1) the presence of a Teflon wall did not influence methane hydrate nucleation (Adamova, Stoporev et al. 2018); (2) the hydrate nucleation occurred only at the interface between the aqueous phase and the guest saturated phase (Stoporev, Semenov et al. 2018); (3) in the presence of a glass, a stainless-steel or a sapphire wall, hydrate nucleation preferentially occurred at the three-phase contact lines where the water, the guest saturated phase and the solid wall met (Adamova, Stoporev et al. 2018, Stoporev, Semenov et al. 2018, Stoporev, Semenov et al. 2018); (4) stainless-steel and glass promoted hydrate nucleation more than sapphire did (Stoporev, Semenov et al. 2018); (5) in the presence of an oil phase, methane hydrate nucleation rate was influenced differently (Adamova, Stoporev et al. 2018)(Stoporev, Manakov et al. 2015); (6) nucleation probability depended on the type of the guest gas under the otherwise same experimental condition (Stoporev, Semenov et al. 2018, Stoporev, Semenov et al. 2018); (7) higher nucleation probability was observed at prolonged three-phase contact lines (Stoporev, Semenov et al. 2018, Stoporev, Semenov et al. 2018). These important findings notwithstanding, compared to the crystal growth that follows nucleation, nucleation has by and large been comparatively less studied for gas hydrates because of the experimental difficulties encountered.

The size distribution of clusters of a metastable phase at a given supersaturation generally follows a Boltzmann distribution, therefore nucleation is an intrinsically probabilistic event which can only be studied using a statistical approach (Maeda 2020). This feature makes the reproducibility of nucleation measurements poor and renders the scatter in the nucleation data large. Because of the stochastic nature of the hydrate nucleation, a large amount of induction time data is required to obtain an average induction time with reasonable confidence when clathrate hydrate nucleation is investigated in a traditional wisdom. This is often too time-consuming and

even becomes impractical at a small driving force because the induction time would become very long.

To overcome the above drawback of the induction time measurements, an isobaric linear cooling ramp method is an attractive alternative approach to investigate the nucleation kinetics of clathrate hydrates (Maeda 2020). In this approach, clathrate hydrate nucleation is practically forcibly induced by a linear cooling ramp that linearly increases the driving force. A lag time, which is defined as the time interval from the establishment of metastability to the detection of clathrate hydrate nucleation during a linear cooling ramp, is typically measured. A lag time is similar to an induction time except that an induction time is under a constant driving force whereas a lag time is under a linearly increasing driving force. The linear cooling ramp approach has several advantages over the induction time measurements. First, the method effectively compresses the scatter in nucleation data distributions encountered in measurements under a constant supercooling. Second, the accelerated measurements allow collection of data within shorter time frames. Third, the nucleation rate over the entire experimentally accessible range of supercoolings can be simultaneously determined (Maeda 2015, Maeda 2018). This is significant because the nucleation rate is generally a function of the driving force and as such a nucleation curve that relates the nucleation rate to the driving force is generally required, and the linear cooling ramp method allows systematic determination of a nucleation curve over an entire experimentally accessible range of supercoolings at once. However, it should be noted that for all experiment-based study on clathrate hydrate nucleation kinetics, nucleation can only be detected after the fact (when the stable nucleus grows to a detectable size), the assumption behind the linear cooling ramp method is that the time interval between the nucleation event and the subsequent catastrophic growth of the crystal is much shorter than the time taken to change the system temperature by a substantial amount. For a quiescent sample (as opposed to stirred), system supercoolings prior to nucleation are typically large, and consequently, the subsequent catastrophic growth of the crystal, after nucleation, is

typically fast. Thus, this shortcoming can be overcome with the use of a sufficiently slow experimental cooling rate.

Maeda (Maeda 2019) used a High Pressure Automated Lag Time Apparatus (HP-ALTA) to measure the nucleation rate of CO₂ hydrate in quiescent water samples contained in a glass sample cell using the linear cooling ramp method. Maeda (Maeda 2016) also investigated the effect of different types of solid walls on hydrate nucleation rates. His results suggested that a stainless-steel wall and a glass wall had a similar impact on the nucleation rate of clathrate hydrates. Zhang and Lee found that CO₂ hydrate formation kinetics was enhanced by the presence of a small amount of cyclopentane, manifested in the reduced induction time (Zhang and Lee 2009). Kyung et al. suggested that organo-mineral complexes enhanced CO₂ hydrate nucleation kinetics by increasing the number of effective hydrate nucleation sites and by enriching CO₂ and water molecules at the mineral surface (Kyung, Lim et al. 2015). Lim et al. (Lim, Barwood et al. 2022) deduced the nucleation rates of CO₂ hydrate from the induction time measurements and attributed the higher nucleation rate of CO₂ hydrate than that of methane hydrate to the lower nucleation work of CO₂ hydrate. Trivedi and Dalvi (Trivedi and Dalvi 2020) found that coconut fibers had a promoting effect on the heterogeneous nucleation of CO₂ hydrate because of the increased interfacial area. Kar et al. (Kar, Acharya et al. 2021) found the significant promotion effect of a magnesium plate on CO₂ hydrate nucleation.

In parallel with these experimental studies, molecular dynamics simulation has been employed to investigate CO₂ hydrate nucleation kinetics and a key parameter of it, nucleation rate, has been determined. Kvamme (Kvamme, Graue et al. 2004) et al. developed a model based on phase field theory which describes the Helmholtz free energy change during the phase transition from a disordered liquid to an ordered crystalline phases to address the nucleation rate of CO₂ hydrate. For the heterogeneous nucleation occurring at the CO₂/water interface, the lack of accurate interfacial free energy values rendered the estimated nucleation rate to vary by 1 to 2.5

orders of magnitude. Radhakrishnan (Radhakrishnan and Trout 2002) et al. used the Landau–Ginzburg approach and calculated the Gibbs free energy barrier of CO₂ hydrate nucleation. This energy barrier, in conjunction with the use of the transition state theory (TST) resulted in the nucleation rate of CO₂ hydrate of $6.08 \times 10^{-12} \text{ s}^{-1}$. He et al. (He, Mi et al. 2021) also used MDs simulation to investigate the effect of hydrophilicity / hydrophobicity of solid walls on CO₂ hydrate nucleation. A hydrophobic surface (graphite) could strongly adsorb CO₂ molecules and lower the aqueous CO₂ concentration, which made nucleation unfavorable, but a reverse effect was observed when hydrophilic surface (silica) was present. Bai (Bai, Chen et al. 2012) et al. used MDs simulations to investigate the CO₂ hydrate nucleation in the presence of a solid wall (silica). They indicated that CO₂ hydrate nucleated near the water/CO₂/silica three-phase contact line (TPCL) and formed an amorphous crystal. This agrees with the hypothesis that the appropriate measure of the system size of CO₂ hydrate nucleation should be the total length of the three-phase-lines when a solid wall is present (Maeda and Shen 2019). Unfortunately, neither the total length of the TPCL nor the nucleation rate was reported.

Because of the complexities of potential impacts of a solid wall on nucleation rates, such as surface roughness and surface heterogeneities, nucleation rate of gas hydrate in the absence of a solid wall is required as the baseline from which the nucleation rates in the presence of one can be compared. To prepare such a water droplet without any contact with a solid wall, several methods have been applied. Other than the quasi-free water droplets used by Maeda (Maeda 2016), Jeong (Jeong, Metaxas et al. 2019, Jeong, Metaxas et al. 2022) used acoustically levitated water droplets to investigate the nucleation of natural gas hydrate in the absence of a solid wall. The nucleation rate of sII-forming natural gas hydrate on the acoustically levitated water droplets, normalized to the surface area, was found to be similar (within the same order of magnitude) to that of the quasi-free water droplets supported by an immiscible liquid (Maeda 2015, Jeong, Metaxas et al. 2019, Jeong, Metaxas et al. 2022).

Maeda reported nucleation curves of methane/propane (abbreviated as C1/C3 hereafter) mixed gas hydrate in a quiescent quasi-free water droplet supported by an immiscible liquid (Maeda 2016), but not of carbon dioxide hydrate, which remains to be determined. In the current study, we first determined the nucleation curves of CO₂ hydrate on a quiescent quasi-free water droplet and investigated the convergence of the nucleation curves with the increasing number of the nucleation data. Then we derived CO₂ hydrate on a quiescent water surface in the presence of a stainless-steel wall. From the comparison with the baseline, the effect of a stainless-steel wall on CO₂ hydrate nucleation kinetics was obtained and the appropriate normalization constant of nucleation rate was determined. Derived nucleation curves were analyzed within the framework of Classical Nucleation Theory. The kinetic nucleation parameter and the thermodynamic nucleation parameter were calculated and compared to the literature values. We also compared the nucleation curve of CO₂ hydrate in the presence of a stainless-steel wall with that in the presence of a glass wall. Finally, we compared the nucleation curves of CO₂ hydrate to those of clathrate hydrate formed by hydrocarbon guest, both in the presence and in the absence of a solid wall. This study determined the most essential parameter of nucleation kinetics of CO₂ hydrate, the nucleation rate as a function of the driving force, so that the nucleation kinetics of CO₂ hydrate can be quantitatively characterized. With the nucleation rate known, one can optimize the blending of additives and/or the type of solid walls (e.g., surface coatings) that would maximize or minimize the nucleation rate of CO₂ hydrate, depending on the needs, which is practically beneficial to the applications of CO₂ hydrate, such as CO₂ storage, sequestration and pipeline transportation.

5.2 Materials and methods

Materials

CO₂ (99.5%) was supplied by Linde Welding and Supplies. Milli-Q water was purified from a Millipore unit (18.2 M Ω). Perfluoromethyldecalin (technical grade, 80%, CAS number: 51294-16-7) and octadecane (99%, CAS number: 593-45-3) were supplied by Sigma-Aldrich and used

without further purification. Gastight Syringes (Hamilton 100 μ L) were used for handling the liquids.

An Isco syringe pump (model: 260D) was used to first pressurize and then hold the pressure during a cooling ramp. A 2-stage vacuum pump (model: VP10D) from CPS Products Inc was used to get rid of air inside gas lines, the chamber and the gas piston before an experiment. Light guides (ZEISS, model: CL 4500) were used to enhance the optics during experiments. A programmable coolant circulator (Julabo, model: F34-HE) was used for generating linear cooling ramps. A pressure transducer (Heise, model: PM) with the resolution of 0.1 psi monitored the pressure inside the pressure chamber. A gas piston (model: ZR-3) was used for CO₂ replenishment inside the high-pressure chamber. The high-pressure chamber was the reactor for CO₂ hydrate formation. A Pyrex glass petri dish (60 x 15mm) was used for containing the sample. A stainless-steel block with 55 circular through-holes and a Teflon block with 21 circular through-holes were made by the machine shop at the University of Alberta and used as the sample cells together with the glass petri dish. A webcam (C920x HD Pro) from Logitech was used to record sample images during a cooling ramp experiment. Two digital thermometers (model: #119) with the resolution of 0.1 K from BIOS company were used for temperature calibration.

Preparation of quasi-free water droplet samples

In the current study, our assembly minimizes the instrument complexity and enables 21 water droplets to be simultaneously monitored during a linear cooling ramp experiment. A glass petri dish was cleaned by a NaOH solution. About 15 mL of perfluoromethyldecalin was poured into the glass petri dish and a cylindrical Teflon block with 21 vertical through holes was then placed inside the petri dish. A milli-Q water droplet (0.02 mL) was placed in each hole of the Teflon block using a Hamilton syringe. The configuration of the system is shown in Figure 5-1. With this configuration, each perfluoromethyldecalin-supported quasi-free water droplet was separated from

each other and did not contact the Teflon wall. Then, the petri dish was slowly placed at the center of a pressure chamber, after which the lid of the pressure chamber was closed and sealed.

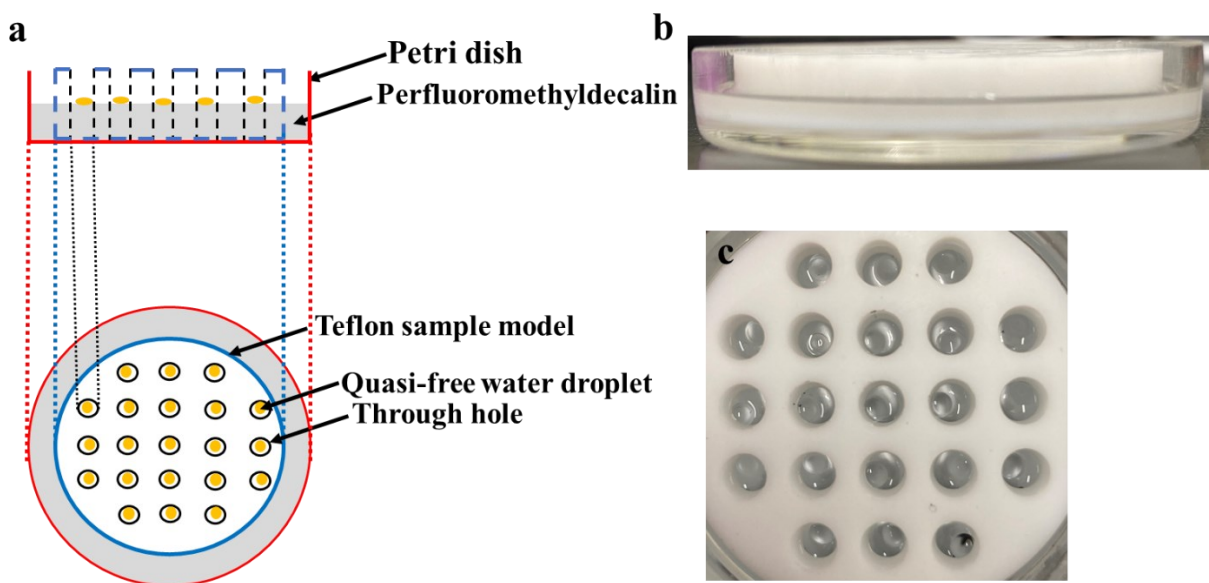


Figure 5-1 Schematic configuration, top view and side view of the quasi-free water droplet samples. a) Schematic configuration of the sample system. The circular Teflon block with 21 through holes was placed inside a glass petri dish and 15 mL of perfluoromethyldecalin was placed inside the petri dish so that each hole in the Teflon block was partially filled with perfluoromethyldecalin. One droplet (0.02 mL) of milli-Q water was placed on the surface of perfluoromethyldecalin in each hole. The petri dish was then fitted into the pressure chamber. b) Side view of the sample system. c) Top view of the sample system. There is one quasi-free water droplet in each hole which can be easily distinguished from the surrounding perfluoromethyldecalin layer.

Determination of the surface area of a quasi-free water droplet

The surface area of a quasi-free water droplet is required for the normalization of the experimental nucleation rate, which would allow comparison of nucleation rates across various systems of different sizes. The first approximation is that we neglected the effect of gravity or the

shape of the lens of each quasi-free water droplet that sits above the perfluoromethyldecalin and assumed a spherical shape. The surface area of a quasi-free water droplet was calculated from the radius, which can be back calculated when the volume of a quasi-free water droplet is known.

To calculate the volume of a quasi-free water droplet and ascertain the uniformity of its sizes, a calibration experiment was carried out. A given nominal volume of water was injected into a beaker on an analytical balance by a gas tight syringe and the change in the mass was recorded. This step was repeated a large number of times to ascertain that the volume of water injected by our gas tight syringe was uniform and repeatable.

Preparation of quiescent water samples in contact with stainless steel walls

Before preparing the quiescent water sample, we first applied a layer of octadecane on one face of the stainless-steel sample model. This is to isolate each hole from the others and to prevent the hydrate crystal propagation from the top of the sample model so that each hole is independent without being affected by the nucleation in neighboring holes. However, it should be noted that the holes would no longer be independent in an unlikely case of a small hydrate crystal detaching from one hole and travelling either through the bottom of the container or through the guest gas phase.

Molten octadecane was applied evenly on one face of a stainless-steel block that had 55 through holes. This octadecane layer soon froze at room temperature. The frozen hydrophobic octadecane layer prevented the water in a through hole from migrating to the water in another hole via a wetting film on the top surface of the otherwise hydrophilic stainless-steel block. Since the solubility of a guest gas in liquid water is low, gas hydrate only nucleates and forms a hydrate film at the surface of a quiescent water. By making the top face of the stainless-steel block hydrophobic and thus preventing formation of continuous wetting films of water between the through holes, water in each hole can be regarded independent for nucleation of gas hydrates.

The glass petri dish was cleaned by a NaOH solution. About 15 mL of Milli-Q water was poured into the glass petri dish and a stainless-steel block with 55 through holes was then placed into the petri dish, with the octadecane-coated side facing up. The configuration of the sample cell is shown in Figure 5-2. Then, the petri dish was slowly placed at the center of the pressure chamber, after which the lid of the pressure chamber was closed and sealed.

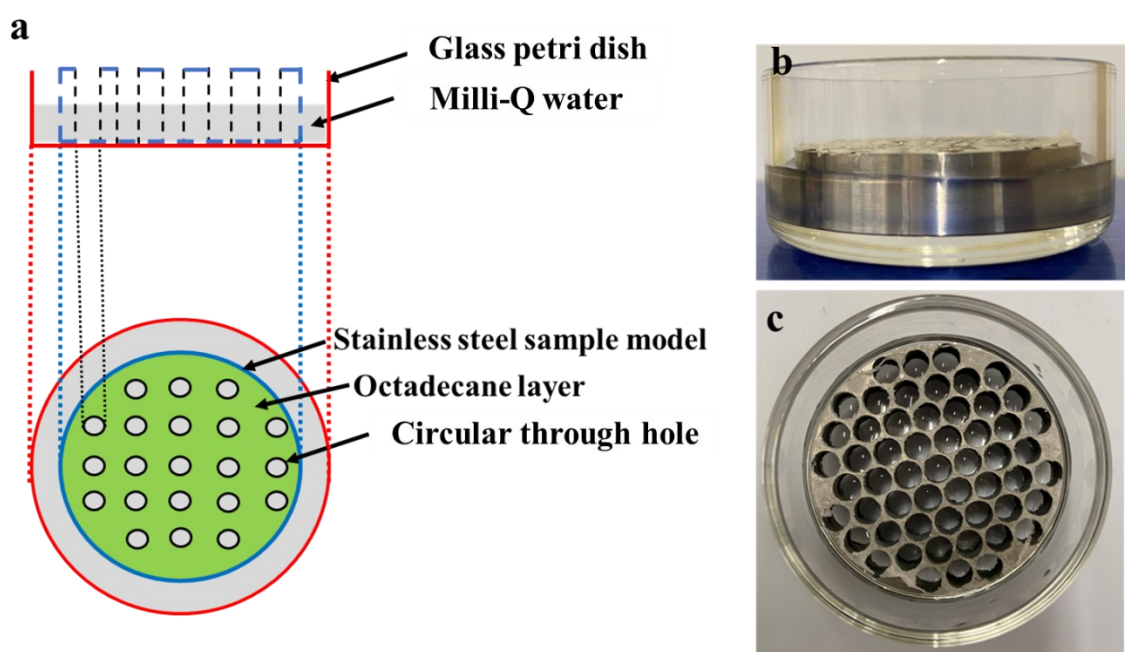


Figure 5-2 Schematic configuration, top view and side view of the quiescent bulk water samples. a) Schematic configuration of the quiescent water samples. The circular stainless-steel block with 55 through holes was placed inside a glass petri dish and 15 mL of Milli-Q water was placed inside the petri dish so that each hole in the stainless-steel block was partially filled with water. A thin layer of octadecane was evenly applied on the top surface of the stainless-steel block (between each hole) to prevent formation of wetting films of water between each hole. The petri dish was then placed into the pressure chamber. b) Side view of the sample system. c) Top view of the sample system.

Assembly of the pressure chamber and the cooling system

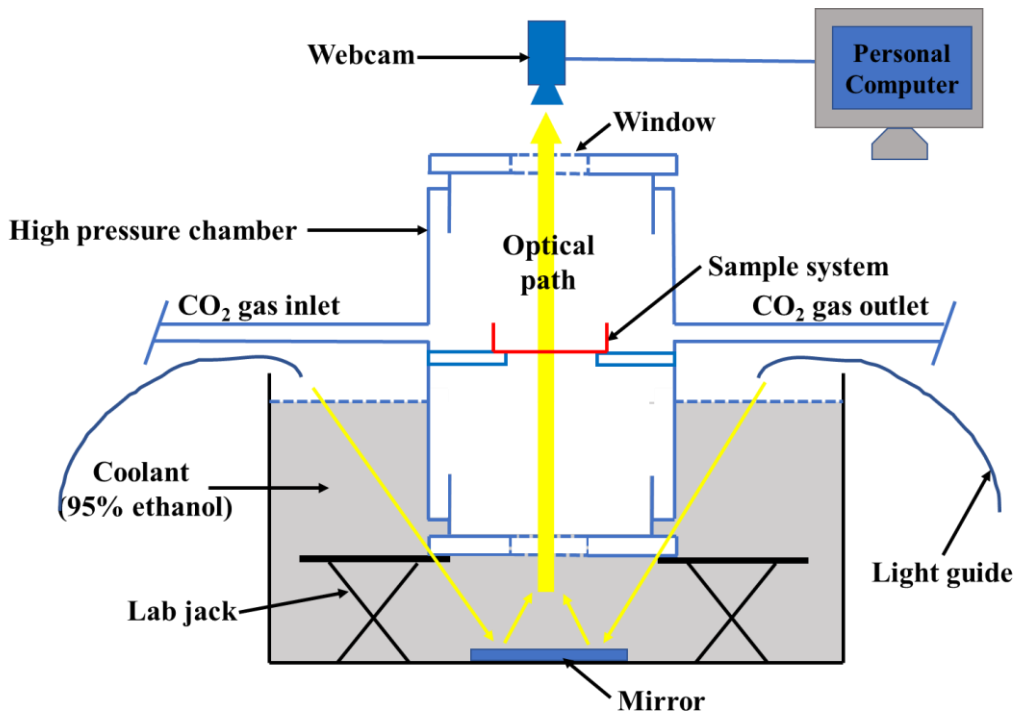


Figure 5-3 Schematic configuration of the high-pressure chamber and the linear cooling system. During a linear cooling ramp, the sample was observed from the top window of pressure chamber. The optics was aided by the light guide and a mirror. The sample image was recorded by a webcam at a fixed time interval and the image was recorded in the PC. During a cooling ramp, the pressure drop caused by cooling or hydrate formation was automatically replenished by a syringe pump from the gas inlet.

Figure 5-3 shows the schematic configuration of the pressure chamber and the cooling system. The pressure chamber was supported by two lab jacks inside a chiller and a mirror was placed at the bottom of the chiller. The chiller was filled with coolant (95% ethanol) and the pressure chamber was half immersed in the coolant. Two light guides were used as the light source. The

light from the light guides was reflected by the mirrors at the bottom of the chiller and passed through the bottom window of the chamber, the sample and the top window of the chamber to the webcam. The webcam was connected to a PC which recorded the sample image at a fixed time interval. The programmable circulator used in this study was set so that the starting temperature was above the phase boundary of CO₂ hydrate at the pressure of interest and cooled at a constant rate of 0.4 K/h to 253.15 K. During each cooling ramp, the pressure drop was automatically replenished by a syringe pump.

Temperature calibrations

The nucleation rate of CO₂ hydrate is most likely affected by the presence of a thermometer when it is directly in contact with the sample. To avoid a direct contact of a sample and a thermometer, we carried out a series of temperature calibrations before the linear cooling ramp experiments. These temperature calibrations were carried out under atmospheric pressure.

For the calibration of the Teflon sample cell, about 15 mL of perfluoromethyldecalin was poured into the glass petri dish and the Teflon block was then placed into the petri dish. A digital thermometer was inserted into a hole near the center of the block and another into a hole near the edge of the block. The lid of the pressure chamber was placed although the pressure inside was kept atmospheric. The temperature of the chiller was set at 282.15 K, which was slightly above the phase boundary of CO₂ hydrate at 3.0 MPa. After the thermal equilibrium has been reached, we started the calibration linear cooling ramp experiment at a constant rate of 0.4 K/h. After the linear cooling ramp, a calibration table was made to relate the temperature of the coolant and the temperature in different sample holes that also accounted for the thermal lag. A similar procedure was used for the calibration of the stainless-steel sample cell.

Experimental procedures

Figure 5-4 shows a schematic illustration of the high-pressure setup and the function and the status of each valve indicated in Figure 5-4 in Roman numerals was tabulated in Table 5-1. After placing the sample inside the pressure chamber, the lid of the pressure chamber was closed and sealed. The brightness of the light guide and the focus of the webcam were adjusted. Then a vacuum pump was used to get rid of air inside the gas lines, the gas piston and the pressure chamber. The vacuum pump was stopped when the reading of the pressure transducer had reached -6 psig to avoid evaporation of the sample water. The vacuum pump was then disconnected from the main gas line. After that, the main valve of the gas cylinder was opened and CO₂ gas was allowed to flush the gas lines, the pressure chamber and the gas piston for 30 seconds. Next a leak check was performed at 120 psi. After confirming the absence of leaks, the CO₂ pressure was gradually increased to the pressure of interest. The system was left to equilibrate for at least several hours before the linear cooling ramp was initiated. Meanwhile, the ISCO pump was switched on and the “constant pressure” mode was selected to hold the pressure and the webcam was set to record the sample image at a fixed time interval. After the linear cooling ramp experiment, recorded images were analyzed to determine the lag time when each nucleation event occurred.

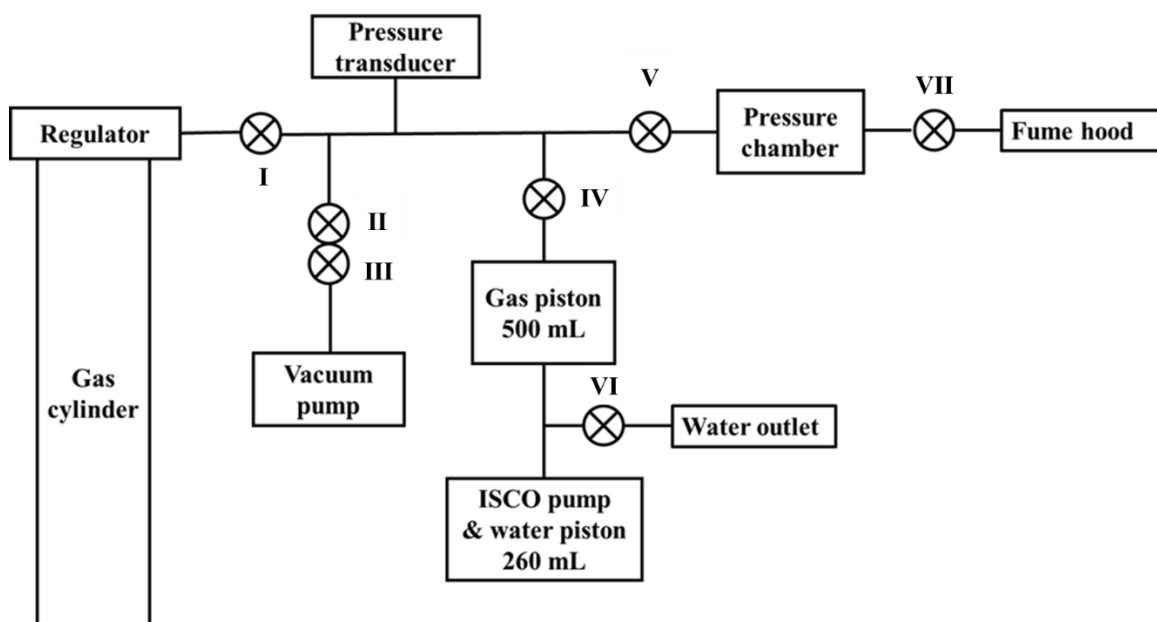


Figure 5-4 Schematic illustration of the high-pressure setup.

Table 5-1 Function of valves in the setup

| Valve number | Function | Status during experiment |
|--------------|---|--------------------------|
| I | Separate the gas lines from the gas source | Close |
| II | Avoid failure of vacuum pump caused by high P | Close |
| III | Protection valve in case of failure of valve II | Close |
| IV | Enable CO ₂ pressure replenishment | Open |
| V | Isolation of pressure chamber during refill | Open |
| VI | Water drainage from water piston | Close |
| VII | CO ₂ venting from pressure chamber | Close |

A nucleation curve relates the driving force for nucleation to the nucleation rate. The driving force can be quantified in terms of supersaturation, superheating, subcooling or supercooling. A convenient measure for a liquid-to-solid phase transition is supercooling. Supercooling is defined as the temperature differential between the temperature at the phase boundary of the CO₂ hydrate at the pressure of interest, T_{eq} , and the temperature of the experimental system, T_{sample} , as shown in eq 5-1:

$$\Delta T = T_{eq} - T_{sample} \quad \text{eq 5-1}$$

The lag time is defined as the duration for which a sample has been in a metastable state. When the cooling rate is constant, the supercooling becomes proportional to the lag time by a factor of cooling rate, α . To account for the thermal lag involved, we constructed a calibration table from a series of calibration measurements that allowed deduction of the real cooling rate of a sample, α_{true} .

With the real sample cooling rate known, the system supercooling, ΔT , and the lag time, t , are related by eq 5-2:

$$\Delta T = \alpha_{\text{true}} t \quad \text{eq 5-2}$$

We set the nominal cooling rate of the programmable bath to 0.4 K/h in order to minimize three sources of systematic errors: 1) the thermal lag within a sample, 2) the detection lag. A nucleation event can only be detected after the crystal has grown to a detectable size. The change in the supercooling during a given detection lag is smaller the slower the cooling rate used, 3) the change in the gas solubility with cooling. A slow cooling rate reduces the undersaturation of CO₂ in the water with cooling.

5.3 Results

Figure 5-5 shows photos of the Teflon sample holder that contains quasi-free water droplets supported by a thick layer of perfluoromethyldecalin. At the beginning of a linear cooling ramp, all the quasi-free water droplets remained liquid and transparent. As the cooling proceeded, CO₂ hydrate formed on more and more quasi-free water droplets. For example, comparison of the panels (a) and (b) of Figure 5-5 reveals that the water droplet marked by a yellow circle became opaque, which indicated that the surface of this particular droplet became covered by a CO₂ hydrate film. By the end of a linear cooling ramp, all the water droplets were covered by CO₂ hydrate films. After each linear cooling ramp, the temperature of the system was raised to 282.15 K, which was above the equilibrium phase boundary of CO₂ hydrate. The dissociation of CO₂ hydrate resulted in formation of many small bubbles, as shown in panel (c) of Figure 5-5. For a clearer observation, the enlarged photos of the circle hole in panel (a) and (b) were shown in panel (d) of Figure 5-5.

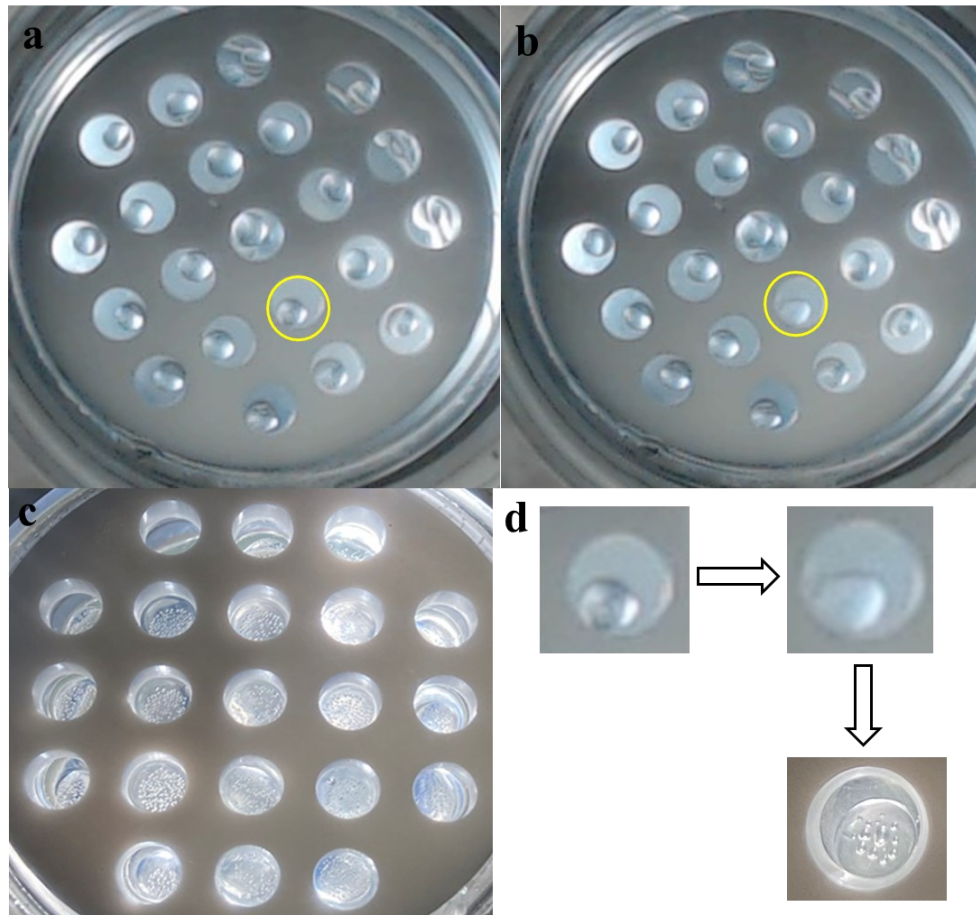


Figure 5-5 Typical photos of the Teflon sample cell with quasi-free water droplets supported by a thick layer of perfluoromethyldecalin at different states during a linear cooling ramp experiment. At the beginning of a linear cooling ramp (a), after the formation of CO₂ hydrate on the circled water droplet (b), after the CO₂ hydrate has been dissociated (c), enlarged photo of the circled water droplet, showing CO₂ hydrate formation-dissociation cycle (d).

Figure 5-6 shows photos of stainless-steel sample model with quiescent bulk water at different stages during a linear cooling ramp. A thin layer of octadecane was applied on the surface of stainless steel to prevent the interconnection of water between holes. All the water did not nucleation at the beginning of the linear cooling ramp experiment and look transparent, as seen from panel (a). As the cooling proceeded, CO₂ hydrate nucleated in some of the holes and the

resulting CO₂ hydrate crystal was visible (marked by the three open yellow circles in panel (b)). By the end of a linear cooling ramp experiment, the water surface in all the holes was covered by CO₂ hydrate. The temperature of the chiller was raised to 282.15 K after each linear cooling ramp, which was above the equilibrium phase boundary of CO₂ hydrate. The dissociation of CO₂ hydrate resulted in formation of a large number of bubbles, as indicated in panel (c). For a clearer observation, the enlarged photos of one of the circle holes in panel (a) and (b) were shown in panel (d). As a whole, Figure 5-6 shows a complete CO₂ hydrate formation-dissociation cycle. All the photos were captured by webcam C920x HD Pro.

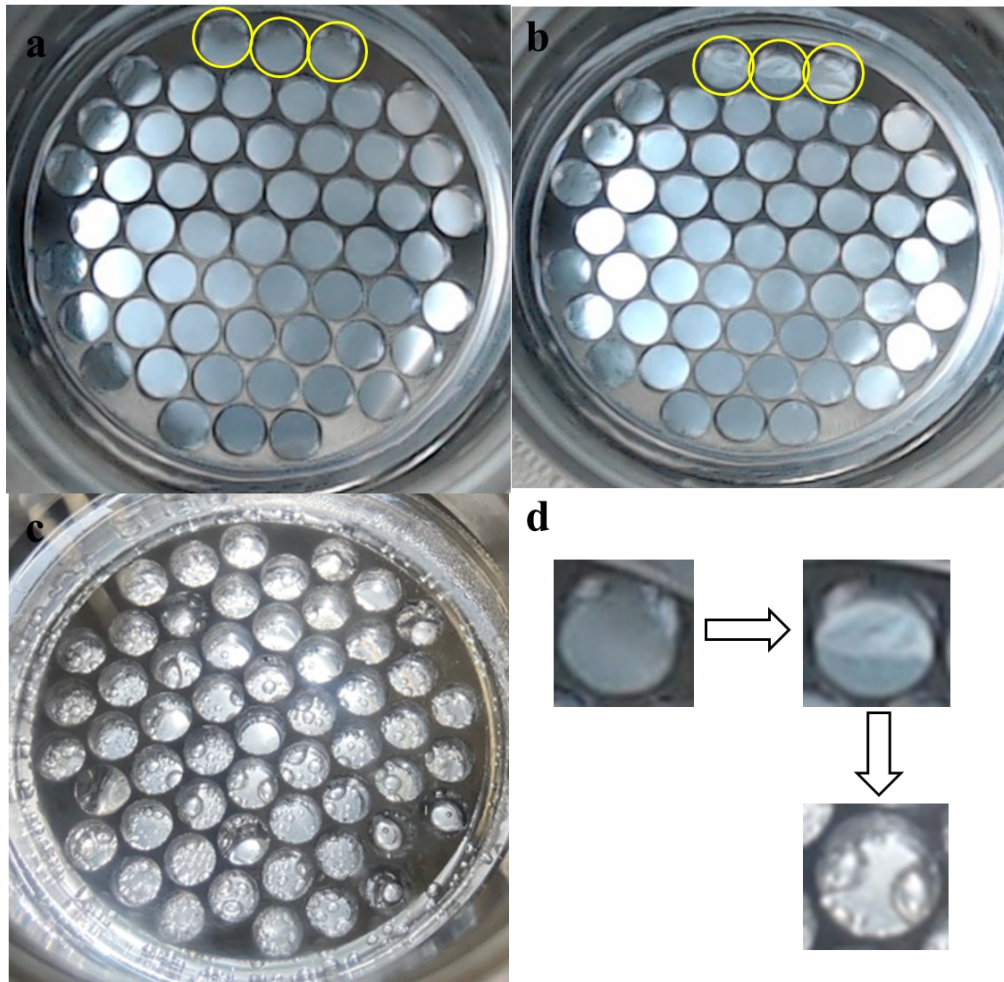


Figure 5-6 Typical photos of the stainless-steel sample model with quiescent bulk water sample

at different states during a linear cooling ramp experiment.

Derivation of CO₂ hydrate nucleation curves on quasi-free water droplet

A nucleation curve shows the relationship between the nucleation rate and the driving force (supercooling) for nucleation. In reality, such as clathrate hydrate formation in oil & gas pipelines, the supercooling for hydrate nucleation is not a single value but keeps changing with locations. Therefore, a nucleation curve that renders the determination of nucleation rates at different supercoolings is required. This point aside, a nucleation curve enables one to compare the nucleation kinetics across systems of various complexities and sizes, evaluate or rank the performance of additive like hydrate inhibitors, or aid to the design and/or blending strategies of functional chemicals.

To derive a nucleation curve, a multi-step mathematical procedure has been proposed (Maeda 2015, Maeda 2018). The first step is the construction of a survival curve. A survival curve is the survival probability, F , as a function of supercooling. The survival probability was calculated from the ratio of the number of samples that have not nucleated to the total number of samples.

From the images recorded by the webcam, it was possible to determine the lag time of a nucleation event. The “true” supercooling at this moment was deduced from application of the calibration table. Then we arranged all the “true” supercoolings corresponding to each nucleation event in an ascending order and calculated the survival probability at each supercooling when a nucleation event was detected. This arrangement resulted in a monotonic decreasing survival probability with the increasing “true” supercooling, as shown in Figure 5-7.

In a linear cooling ramp experiment, the nucleation probability density, p , depends on the sample supercooling which in turn depends on the lag time: $p_{\Delta T}(t)$. Over a small increment of lag time dt , the nucleation probability is the product of nucleation probability density and the time

increment: $p_{\Delta T}(t)dt$. Meanwhile, the survival probability at the time $(t + dt)$ is the probability that the sample has not been nucleated at the time t multiplied by the probability that the same sample does *not* nucleate in the subsequent time increment, dt , as shown in eq 5-3:

$$F_{\Delta T+d(\Delta T)}(t + dt) = F_{\Delta T}(t)[1 - p_{\Delta T}(t)dt] \quad \text{eq 5-3}$$

Rearranging eq 5-3 leads to eq 5-4:

$$d(\ln F_{\Delta T}(t))/dt = -p_{\Delta T}(t) \quad \text{eq 5-4}$$

Therefore, the negative of the nucleation probability density is given by the differentiation of the natural logarithm of the survival probability, $\ln F$, with respect to lag time, t . Since the cooling rate is linear in this research, the shape of $\ln F(t)$ is the same as $\ln F(\Delta T)$, except that the horizontal axis is re-scaled by the cooling rate of the sample. The constructed $\ln F$ vs t curve was shown in Figure 5-8 where each open symbol represents an experimental data point. All data points were measured at the constant nominal system cooling rate of 0.4 K/h.

We now need the local slope of the $\ln F$ vs t curve to obtain the nucleation probability density. The simplest way is to fit a curve of a simple mathematical form to the data in Figure 5-8 and analytically differentiate the fitted curve. Maeda previously chose a power law for such a fitting (Maeda 2020). Here we instead choose an exponential function of the form $\ln F = -A \cdot \exp(Bt) + C$, where A , B and C are constants, for the fitting. The use of an exponential function for the form of the empirical equation is just a matter of convenience. It has been reported that the difference in the functional form of the fitting function does not lead to a substantial difference in nucleation rates within the range where the data exist (Zhang, Li et al. 2021). Nevertheless, an exponential function becomes linear in a semi-log nucleation curve and hence is more convenient when an extrapolation is required.

The numerical values of these fitting parameters for this particular dataset were found to be $A = 0.00052$, $B = 0.0000456$ and $C = 0.16184$. After differentiation with respect to t yields the nucleation probability density as $AB \cdot \exp(Bt)$. The experimental nucleation rate, k , differs the nucleation probability density, p , by a small constant of $\ln 2$ (Maeda 2020). The derived nucleation curve is shown in Figure 5-9. All data points were measured at the constant nominal system cooling rate of 0.4 K/h.

Since the experimental nucleation rate is proportional to the size of the sample used in the experiment, it is not directly transferrable or comparable to other nucleation data in the literature. We thus need to normalize the experimental nucleation rate shown in Figure 5-9 by an appropriate measure of the system size that is most representative of the concentration of potential nucleation sites for the sake of making comparison of nucleation rates across different systems of different sizes. In the absence of a solid wall in a system, the number of potential nucleation sites is expected to scale either proportionally with the volume or with the surface area of a water droplet. The latter mode of surface nucleation is because the system symmetry breaks at the surface even in the absence of any solid wall in the system. For gas hydrates, the supersaturation of the guest gas in water is not uniform but is the highest at the surface. Therefore, surface nucleation is expected and the number of potential nucleation sites is expected to scale with the surface area of a water droplet. The calculated surface area of a quasi-free water droplet in our system is $35.45 \times 10^{-6} \text{ m}^2$ according to the procedure detailed in the previous section. It should be noted that although the assumption of a spherical shape of a quasi-free water droplet might lead to errors, it is expected to be insignificant in the context of nucleation rate for which the order of magnitude accuracy is usually sufficient. The normalized nucleation curve of CO_2 hydrate on quasi-free water droplets is shown in Figure 5-10. The above procedure of the derivation of a nucleation curve is general and hence applicable to gas hydrate of other guest types or compositions.

Nucleation curves of CO₂ hydrate in quiescent water that is in direct contact with a stainless-steel wall

We also determined the nucleation rate of CO₂ hydrate on a quiescent water surface that was in direct contact with a stainless-steel wall. The procedure of the nucleation curve derivation is the same as that described in the previous section. Figure 5-7 shows the survival curve of CO₂ hydrate in the presence of a stainless-steel wall, together with the survival curve of CO₂ hydrate on a quasi-free water droplet.

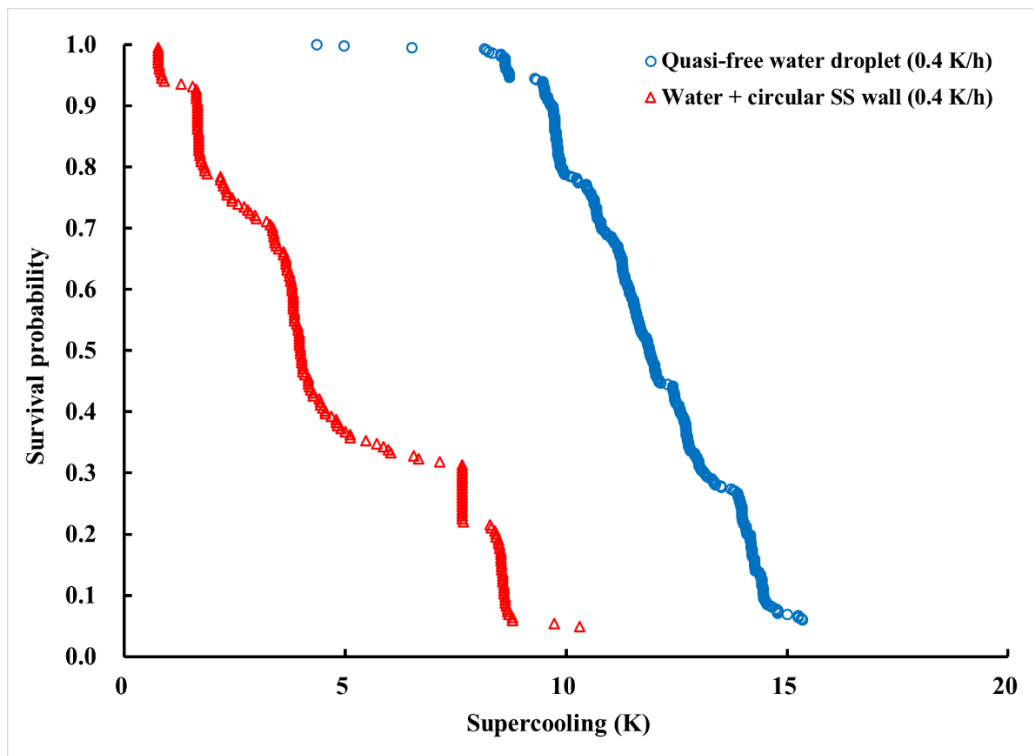


Figure 5-7 Survival curves of CO₂ hydrate formation on a quasi-free water droplet (blue open circle) and on a quiescent water surface in the presence of a stainless-steel wall (red open triangle). The horizontal axis is the supercooling ΔT and the vertical axis is the survival probability. Each open symbol represents a nucleation event. The survival probability starts from 1 and decreases monotonically with the increase of supercooling. All data points were measured at a constant nominal system cooling rate of 0.4 K/h, or true sample cooling rate of 0.288 K/h for quasi-free

water droplet and 0.324 K/s for quiescent water in contact with a stainless-steel wall.

Figure 5-8 shows the $\ln F(t)$ curve of CO₂ hydrate nucleation on a quiescent water surface in the presence of a stainless-steel wall. We again used an exponential function of the form $\ln F = -A \cdot \exp(Bt) + C$ for the curve fitting. The optimal fitting parameters for this particular dataset were found to be $A = 0.0168$, $B = 0.00005$ and $C = 0$.

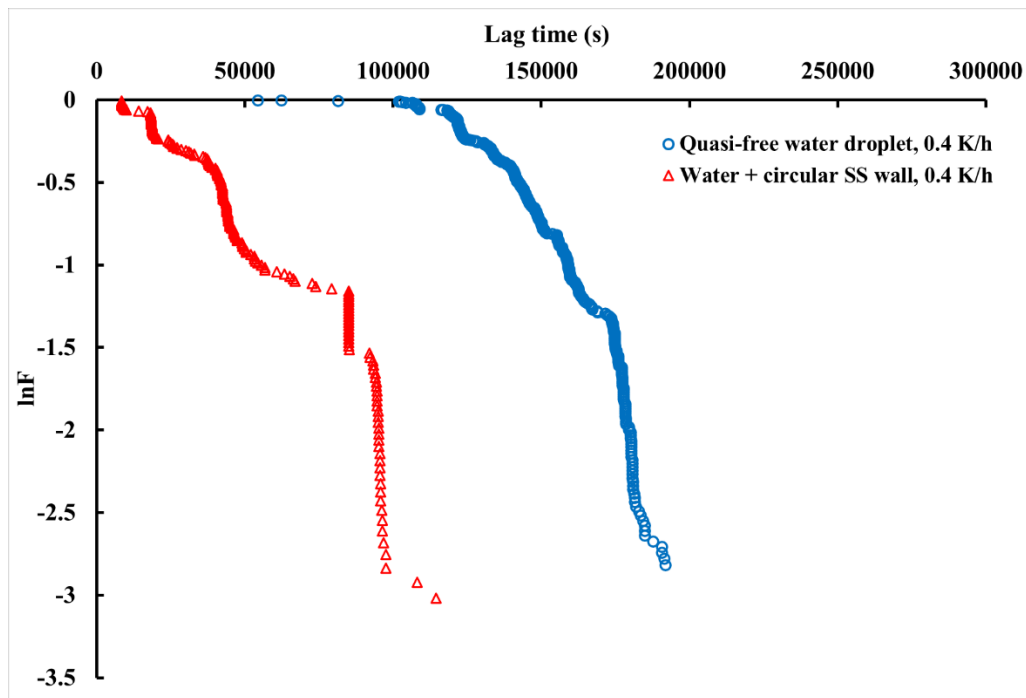


Figure 5-8 Natural logarithm of the survival curves ($\ln F$ vs ΔT) of CO₂ hydrate formation on a quasi-free water droplet (blue open circle) and on a quiescent water surface in the presence of a stainless-steel wall (red open triangle).

We then calculated the first derivative of $\ln F$ with respect to lag time and divided each local slope by a constant of $\ln 2$ to get the experimental nucleation rate, k (s^{-1}). The derived nucleation curve is shown in Figure 5-9.

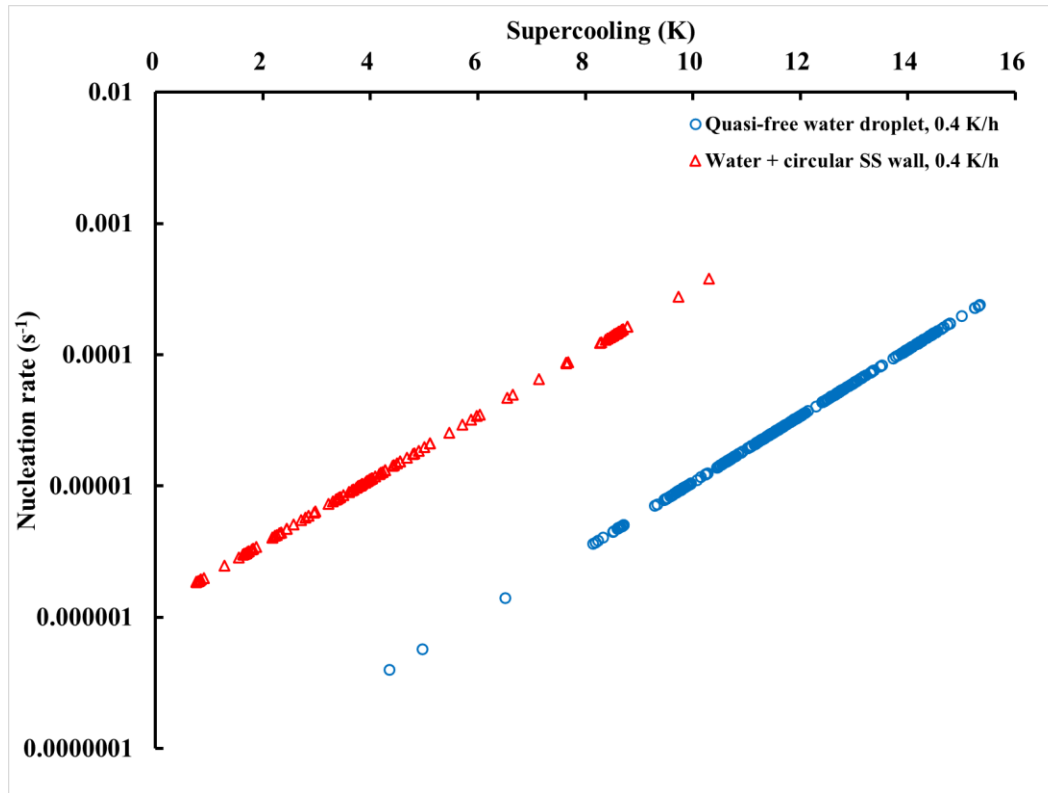


Figure 5-9 Experimental nucleation rate of CO₂ hydrate formation on a quasi-free water droplet (blue open circle) and CO₂ hydrate formation on a quiescent water surface in the presence of a stainless-steel wall (red open triangle).

The nucleation curve after the normalization is shown in Figure 5-10 together with the nucleation curve of CO₂ hydrate formation on a quasi-free water droplet supported by a thick layer of perfluoromethyldecalin (blue open circular symbol) and nucleation data collected by Lim et al. (Lim, Barwood et al. 2022) (signs of different shape and color). It can be seen that the normalized nucleation rate of CO₂ hydrate on a quiescent water surface was higher than that on a quasi-free water droplet.

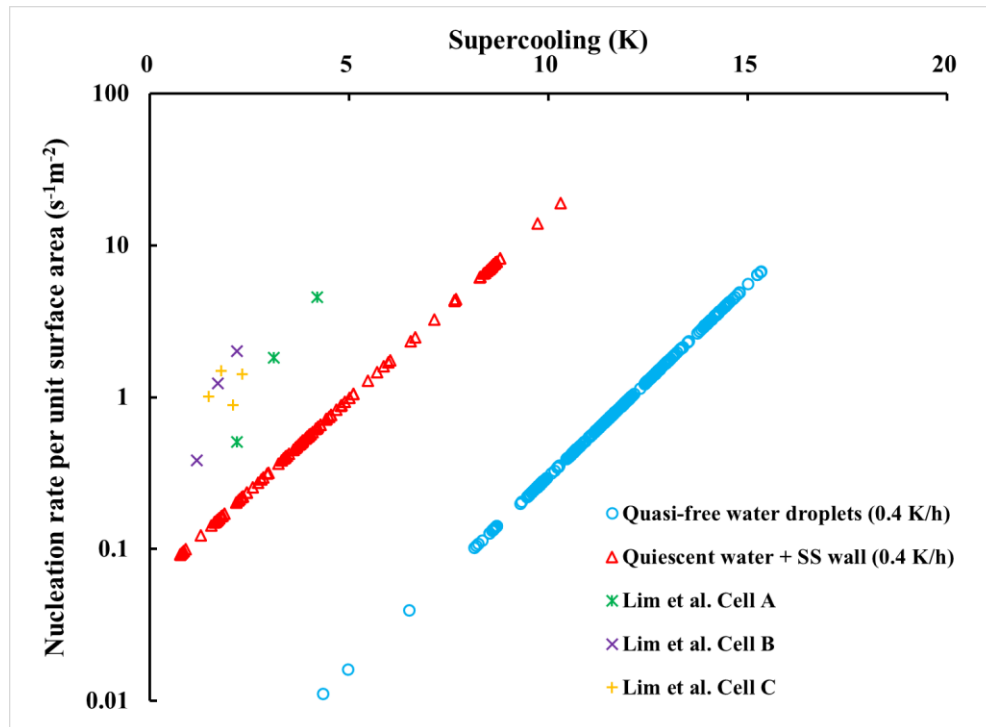


Figure 5-10 Gas-water interfacial area normalized nucleation curves (nucleation rate per unit area as a function of supercooling) of CO₂ hydrate formation on a quasi-free water droplet (blue open circle) and on a quiescent water surface in the presence of a stainless-steel wall (red open triangle). The surface area of a quasi-free water droplet and a quiescent water surface enclosed by a stainless-steel wall are $35.45 \times 10^{-6} \text{ m}^2$ and $2 \times 10^{-5} \text{ m}^2$, respectively. All data points were measured at the constant cooling rate of 0.4 K/h. The nucleation rate of CO₂ hydrate on quasi-free water droplet is slower than that on a quiescent water surface because of the kinetics promotion by the solid wall. For comparison, data points acquired by Lim et al. in different cells were plotted together.

5.4 Discussion

Convergence of the nucleation curve with the number of data points

One of the fundamental questions is as follows: collection of how many nucleation events is sufficient to construct a reliable nucleation curve? To investigate this question, we analyzed the 434 CO₂ hydrate nucleation events on quasi-free water droplet separately, the first 200 data points

and the second 200 data points in Figure 5-11. Different colors of symbols correspond to different individual groups of data points. All data points were measured at the constant cooling rate of 0.4 K/h. It can be seen that most of nucleation events of both groups are concentrated within the supercooling range of 10 to 15 K. The difference between the 200 points datasets and the total dataset that contained 434 data points differed up to 2 K. Since all these 434 water droplets were freshly made and independent of each other, this difference (the gap between three survival curve) was assumed to be purely caused by the stochastic nature of nucleation of CO₂ hydrate.

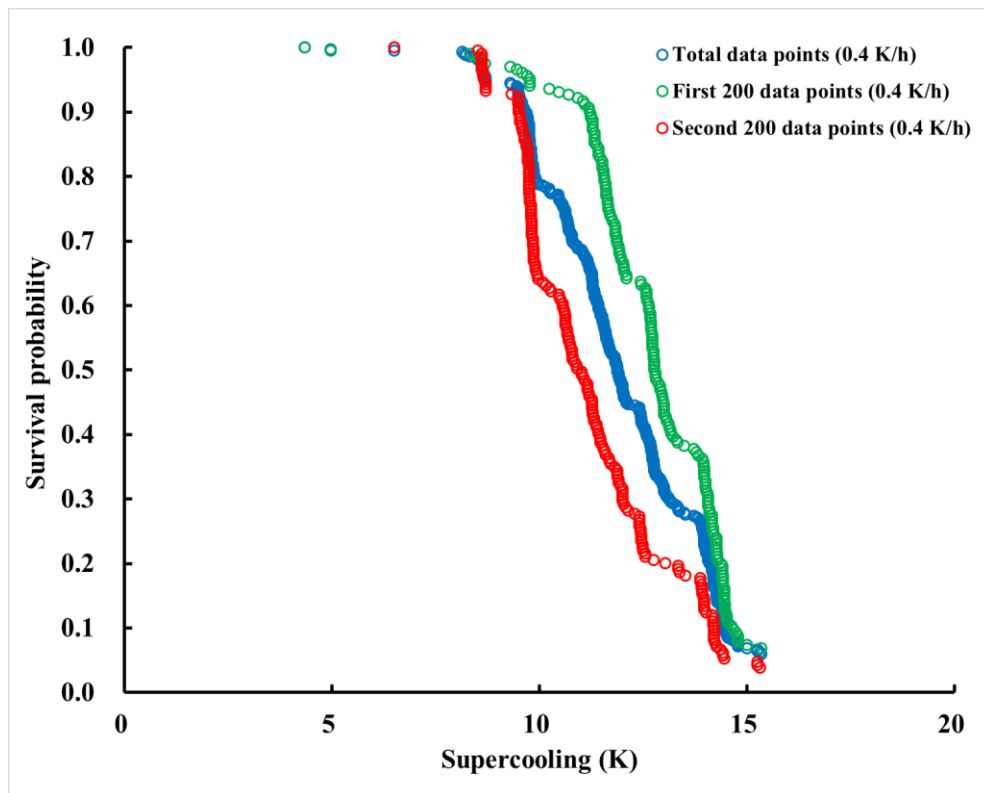


Figure 5-11 Survival curves of CO₂ hydrate formation on a quasi-free water droplet constructed with different datasets.

Other than the issue of convergence, another issue is the smoothness of the survival curves. From Figure 5-7, it can be seen that the CO₂ hydrate survival curve of quiescent water in contact with a stainless-steel wall was not as smooth as that of the quasi-free water droplets. Three possible

factors were postulated to be responsible for it: the hydrophobicity of the solid wall, the thermal conductivity of the solid wall and the number of data points used for the construction of the survival curves.

Maeda (Maeda 2019) previously reported the nucleation curve of CO₂ hydrate in the presence of a glass wall in which the derived nucleation curve was relatively smooth. Given that water wets both clean glass and clean stainless-steel, the hydrophilicity of the solid wall is not a factor that impacts the smoothness of a nucleation curve. As for the thermal conductivity of the solid wall, our temperature calibration showed that the “real” sample cooling rate of the stainless-steel wall was slightly faster than that of our Teflon sample cell. Therefore, this factor can be ruled out because the survival curve in a Teflon sample cell was relatively smooth. The most plausible influencing factor is thus the number of data points used to construct the survival curve. The number of data points used to construct the survival curve in quiescent water system was fewer than that in the quasi-free water droplet system. We expect that the survival curve will become smoother and more continuous as the number of the data points increases. After all, the gaps only appear near both ends of a survival curve where the number density of the data is the lowest, and not near the middle of a survival curve where the number density of the data is high.

This can be confirmed also by the difference between the survival curves that consist of 434 data points and 200 data points. It can be seen from Figure 5-11 that the survival curves constructed from the first 200 data points and from the second 200 points data points each had small gaps near $F = 0.6$ and $F = 0.92$, respectively. In contrast, the survival curve constructed from the total 434 points data set had no such gap in the data points at these locations. Addition of more data points increases the number density of the survival curve (fills the gap) and renders the curve smoother. This densely populated data points in survival curve translated to a more densely populated $\ln F$ vs t curve shown in Figure 5-12 where different colors of symbols correspond to different individual

groups of data points. Such denser data in the $\ln F$ vs t curve rendered the subsequent exponential fitting of the $\ln F$ curve, and the calculation of the local slope of $\ln F$ with respect to t , more reliable.

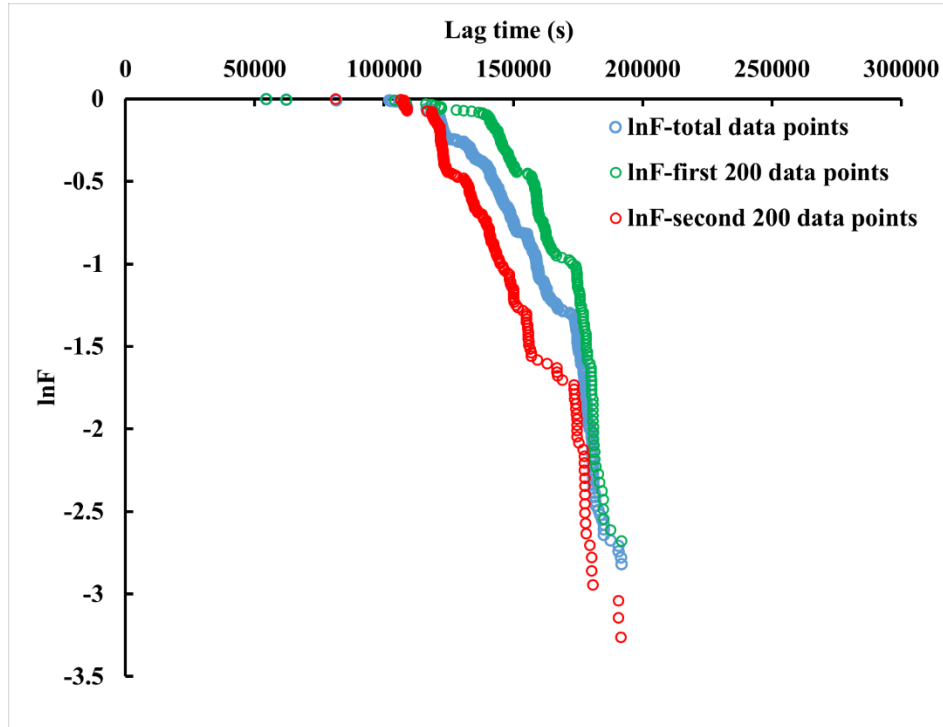


Figure 5-12 Natural logarithm of the survival curves ($\ln F$ vs ΔT) of CO_2 hydrate formation on a quasi-free water droplet constructed with different datasets.

The corresponding normalized nucleation curves of these three datasets are shown in Figure 5-13. The surface area of a quasi-free water droplet is $35.45 \times 10^{-6} \text{ m}^2$. Different colors of symbols correspond to different individual groups of data points. All data points were measured at the constant cooling rate of 0.4 K/h. It can be seen that three nucleation curves overlap each other, which suggests that 400 data points would be sufficient to construct a reliable nucleation curve.

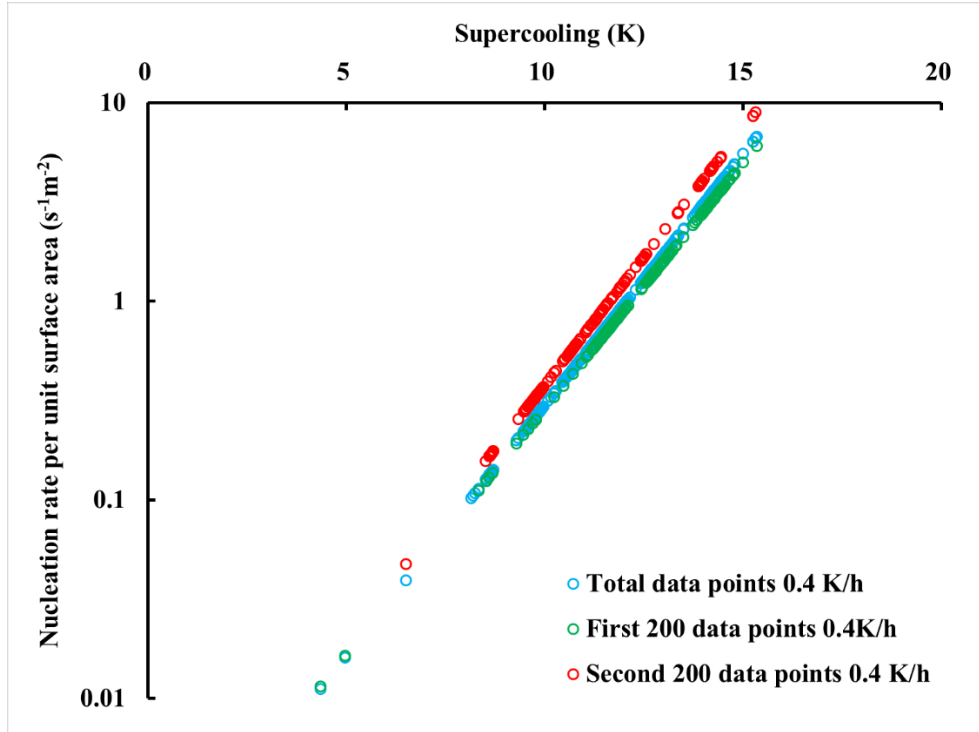


Figure 5-13 Gas-water interfacial area normalized nucleation curves of CO₂ hydrate formation on a quasi-free water droplet constructed with different datasets.

Analysis of CO₂ hydrate nucleation kinetics with the framework of Classical Nucleation Theory (CNT)

According to the Classical Nucleation Theory (CNT), the nucleation rate is an exponential function of supercooling in an isobaric condition. The kinetic parameter, A , and thermodynamic parameter, B' , are incorporated in the expression of the nucleation rate as eq 5-5 (Kashchiev and Firoozabadi 2002):

$$J = A e^{\frac{\Delta s_e \Delta T}{kT}} e^{-\frac{B'}{T \Delta T^2}} \quad \text{eq 5-5}$$

Where J is the nucleation rate ($\text{m}^{-3} \text{s}^{-1}$ or $\text{m}^{-2} \text{s}^{-1}$), Δs_e (J/K) is the dissociation entropy of a hydrate building unit at the equilibrium temperature, k is the Boltzmann constant (J/K), ΔT is the

supercooling (K), T is the sample temperature (K), A is the kinetic parameter ($\text{m}^{-3} \text{s}^{-1}$ or $\text{m}^{-2} \text{s}^{-1}$) and B' is the thermodynamic parameter (K^3). The expressions for A and B' are shown in eq 5-6 and eq 5-7, respectively:

$$A = z f_e C_0 \quad \text{eq 5-6}$$

$$B' = \frac{4c^3 v_h^2 \sigma_{ef}^3}{27k \Delta s_e^2} \quad \text{eq 5-7}$$

Where z is the Zeldovich factor, f_e is the frequency of the hydrate building unit attaching to the nucleus at equilibrium temperature, C_0 is the concentration of the nucleation sites in the system, $c=(36\pi)^{1/3}$ is the shape factor, v_h is the volume of the hydrate building unit and σ_{ef} is the effective specific surface energy of the hydrate-solution interface.

Take logarithm on both sides of eq 5-5 gives eq 5-8:

$$\ln J - \frac{\Delta s_e \Delta T}{kT} = \ln A - B' / T \Delta T^2 \quad \text{eq 5-8}$$

Therefore, if one substitutes values of the nucleation rate, the absolute temperature and the supercooling into eq 5-8 and plots the $\ln J - \frac{\Delta s_e \Delta T}{kT}$ as a function of $1/T \Delta T^2$, it will give a straight line in which the slope is $-B'$ and the y-intercept is $\ln A$. In the current study, we have derived the nucleation curves of CO₂ hydrate nucleation on both quasi-free water droplets and a quiescent water surface in contact with a stainless-steel wall. They enable us to calculate the A and B' given the Δs_e for CO₂ hydrate was reported to be 25k (Lim, Barwood et al. 2022).

In Figure 5-14, we showed the comparison of the plots of $(\ln J - \Delta S_e \Delta T / kT)$ versus $1/T \Delta T^2$ for the nucleation of CO₂ hydrate (black open circular symbol) and C1/C3 mixed gas hydrate (red open square symbol) nucleation in quasi-free water droplets (Maeda 2020) (panel a), and CO₂

hydrate nucleation in a quiescent system in the presence of a stainless-steel wall (black open circular symbol) done in the current study and CO₂ hydrate nucleation in a stirring system in the presence of a stainless-steel wall (red open triangular symbol) done by Lim et al. (Lim, Barwood et al. 2022) (panel b). The x-axes were uniformly scaled by 10⁶ for convenience. The linear fittings to the experimental data are also shown in a dashed straight line of the same color with data points. It should be noted that a downward (convex to the bottom) curvature in Figure 5-14 has been previously observed by Kashchiev and Firoozabadi (Kashchiev and Firoozabadi 2002), and Maeda (Maeda 2020), and thus appears a general feature. This suggests potential limitations of CNT.

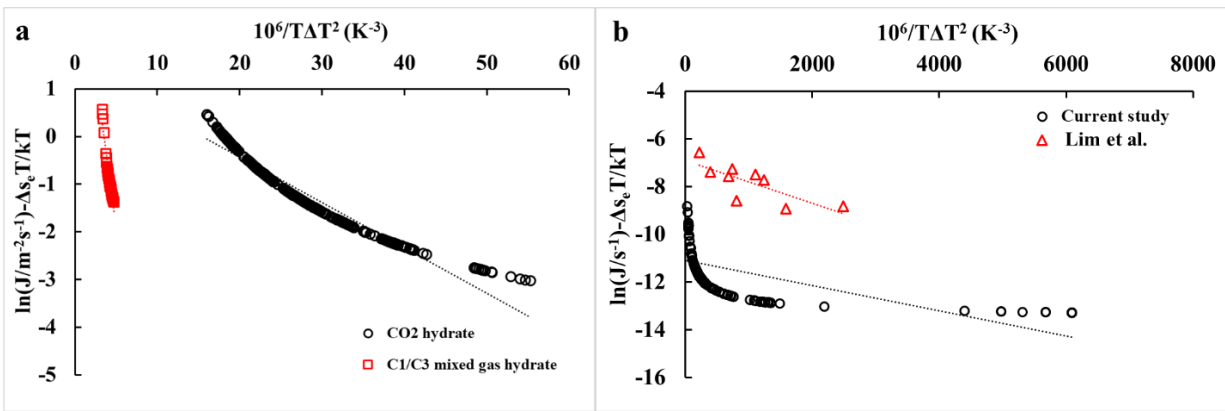


Figure 5-14 Analysis of nucleation data based on the Classical Nucleation Theory

Kashchiev et al. concluded that the theoretical value of $A = 10^{35} \text{ m}^{-2}\text{s}^{-1}$ and $B' = 4.8 \times 10^6 \text{ K}^3$ for methane hydrate homogeneous nucleation. If the linear fitting is warranted, the plot in Figure 5-14a) yielded the A of $59 \text{ m}^{-2}\text{s}^{-1}$ and B' of $1.2 \times 10^6 \text{ K}^3$ for C1/C3 mixed gas hydrate and A of $4.35 \text{ m}^{-2}\text{s}^{-1}$ and B' of $1 \times 10^5 \text{ K}^3$ for CO₂ hydrate. Both values of B' calculated from the experimental data are at most one order of magnitude lower than the theoretically expected value, suggesting that the height of the activation energy barrier to nucleation is within the expectations from the CNT. In contrast, the kinetic parameters derived experimentally were comparable in the C1/C3 system and the CO₂ system, notwithstanding that the numerical values of A and B' are greatly influenced by the exclusion of the outlier data points. Nevertheless, both are more than 30 orders

of magnitude smaller than the theoretically expected value ($10^{35} \text{ m}^{-3}\text{s}^{-1}$) which suggests that A has a lower value due to heterogeneous nucleation as opposed to homogeneous nucleation (Kashchiev and Firoozabadi 2002). However, a reasonable explanation is required to justify such a huge discrepancy. One possibility is the much smaller “real” system size. If the active nucleation sites are concentrated to a small area instead of the total water-guest interfacial area, then the normalization factor becomes much smaller, thus yielding much larger normalized nucleation rates. Another possibility is the existence of a “bottleneck” along the nucleation pathway which is not considered in CNT. Such a “bottleneck” can be the low solubility of guest in water and the viscous slow-downs which prolong the nucleation pathway (Maeda 2020).

Using the experimental nucleation rate, Lim et al. calculated $A = (0.84 \pm 0.04) \times 10^{-3} \text{ s}^{-1}$ and $B' = (725 \pm 270) \text{ K}^3$ for CO_2 hydrate nucleation in a stirred water surface in contact with a stainless-steel wall. For comparison, our quiescent system yielded a numerical value of $A = 0.2 \times 10^{-4} \text{ s}^{-1}$ that is one order of magnitude smaller than their result and $B' = 500 \text{ K}^3$ that is comparable to their result. The discrepancy in the value of A is reasonable and can be attributed to the enhanced mass transfer caused by stirring because A is responsible for the mechanism of attachment of a hydrate building unit to the hydrate nucleus. The consistency in the value of B' confirmed the same thermodynamic energy barrier to nucleation independent on stirring. Compared to the theoretical value of $B' = 4.8 \times 10^6 \text{ K}^3$, the much lower value of B' obtained both in this work and Lim et al. confirmed much lower activation energy barrier to nucleation when a solid wall is present in the system, which will be discussed later.

The impact of cooling rate on derived nucleation curves

We did not investigate the impact of the experimental cooling rate on the experimental nucleation rates in this study because the experimental cooling rate we used was already the slowest one could practically use, and we know that the slower the cooling rate the more accurate the derived nucleation rates. Nevertheless, below we discuss the potential impact of experimental

cooling rate on the experimental nucleation rate in the linear cooling ramp method.

The cooling rate affects the nucleation curves from three main aspects. First, due to the detection delay of nucleation, true supercooling when a nucleation occurred is always smaller (i.e., the temperature is higher) during a cooling ramp than the supercooling when a nucleation is detected. This factor would shift the “true” nucleation curve to a smaller supercooling (to the left) than the experimentally determined one, and this deviation would become worse with increasing cooling rate. Second, due to the thermal lag, the temperature of the sample is always higher than the linearly cooling system temperature. This thermal lag exists over the entire cooling ramp and increases with the cooling rate. We attempted to account for this factor by our systematic seriousness of calibrations. This factor would also shift the “true” nucleation curve to a smaller supercooling (to the left) than the experimentally determined one. Third, due to the increased guest solubility in water with system cooling, the undersaturation of the guest gas with cooling causes the “true” driving force for nucleation to become lower (which is equivalent to the system supercooling becoming smaller). This undersaturation effect also becomes worse with a faster cooling rate. In short, all these three factors of detection delay, thermal lag and guest undersaturation would render the “true” nucleation curve to shift to the left. A shift of a nucleation curve to the left corresponds to the “true” nucleation rate at a given supercooling to be higher than the experimentally detected nucleation rate.

Experimentally, to the contrary, we consistently observed that the nucleation curves shifted to lower nucleation rates as progressively slower cooling rates were used for the linear cooling ramp runs (Maeda 2016, Maeda 2020). Considering the effect of detection delay, thermal lag and undersaturation during a linear cooling ramp on measured experimental nucleation rate, it appears that the experimentally measured nucleation rate represents the upper bound of the “true” nucleation rate. In other words, “true” nucleation rate can only be lower than the measured one but cannot be higher. Furthermore, the gap between them widens with the use of a faster cooling rate.

If we keep this in mind, we can explain the observed trend in this way: the upper bound approaches to the “true” nucleation curve as the cooling rate is reduced (Zhang, Li et al. 2021) and the gap between them becomes narrower. If we assume in a thought experiment that the cooling rate is infinitesimally slow, then an experimentally determined nucleation curve would asymptotically approach and eventually match the “true” nucleation curve.

Comparison to the nucleation curve of methane-propane mixed gas hydrate on quasi-free water droplets

Maeda (Maeda 2016) reported the nucleation rate of sII-forming C1/C3 (90 mol % methane:10 mol % propane) mixed gas hydrate on quasi-free water droplets supported by stable wetting films of squalane. It is pertinent to compare the newly obtained nucleation curve of CO₂ hydrate to that of C1/C3 mixed gas hydrate to investigate the influence of guest gas type on the nucleation rate of gas hydrates. Maeda at the time chose a power law to fit the experimental $\ln F$ vs t curve. However, there is no a priori reason to choose a power law for the fitting purposes and we now consider that an exponential function may be more suitable. To this end, we reanalyzed Maeda’s data using an exponential function of the form $\ln F = -A \cdot \exp(Bt) + C$ here. The change in the choice of functional form does not substantially alter the nucleation rates over the experimentally accessible range (i.e., the two nucleation curves overlap). However, it obviously alters the shape of the nucleation curve and hence it will make a substantial difference when the nucleation curve were to be extrapolated beyond the experimentally accessible range (Maeda 2020).

Figure 5-15 shows the normalized nucleation rate by the surface area of the water droplet. The surface area of a quasi-free water droplet used in this work and Maeda’s work is calculated to be $35.45 \times 10^{-6} \text{ m}^2$ and $74.1 \times 10^{-6} \text{ m}^2$, respectively. Comparison of the normalized nucleation rate of CO₂ hydrate on quasi-free water droplets in this work and that of C1/C3 mixed gas hydrate on quasi-free water droplets reported by Maeda shows that 1) the higher end of C1/C3 mixed gas

hydrate nucleation curves extended to 34 K of supercooling while the corresponding value for CO₂ hydrate is only 15 K of supercooling. CO₂ hydrate clearly required much less supercooling than C1/C3 mixed gas hydrate. 2) although the CO₂ hydrate and the C1/C3 mixed gas hydrate nucleation curves resided over different supercooling ranges, if the upper end of the CO₂ hydrate nucleation curve could be extrapolated to deeper supercoolings, the nucleation rate of CO₂ hydrate would be far higher than that of C1/C3 mixed gas hydrate for the same supercooling. This result may be expected because CO₂ has a higher solubility in water than methane or propane.

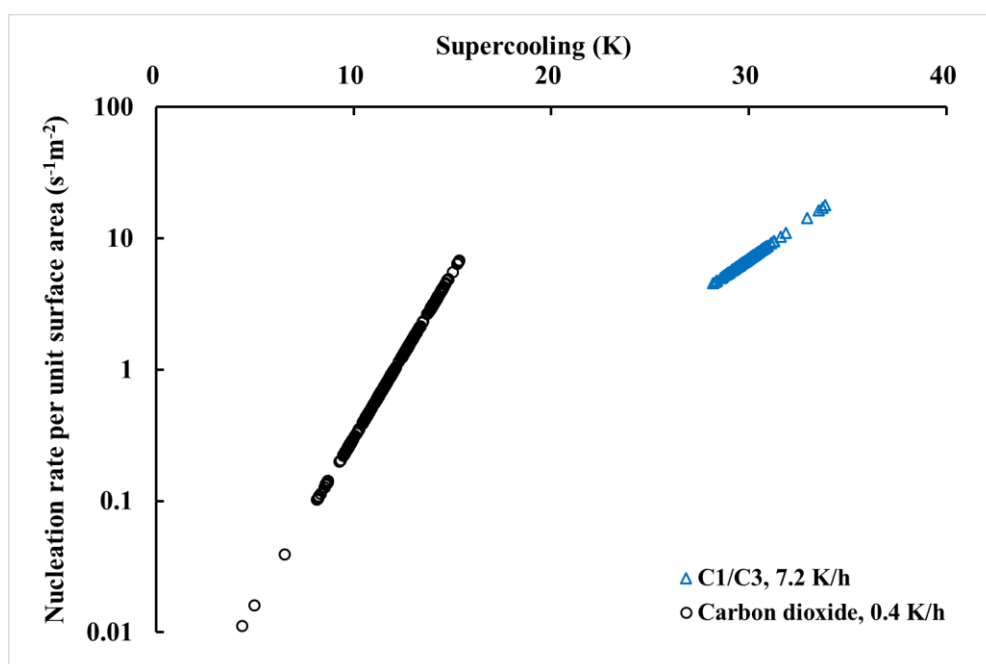


Figure 5-15 Gas-water interfacial area normalized nucleation curves of CO₂ hydrate formation on quasi-free water droplets (black circle) and methane/propane (C1/C3) mixed gas hydrate formation on quasi-free water droplets (blue triangle), both derived using a linear cooling ramp method. A constant system cooling rate of 0.4 K/h was used in CO₂ hydrate formation and a constant cooling rate of 7.2 K/h was used in C1/C3 mixed gas hydrate formation. The surface area of a quasi-free water droplet in CO₂ hydrate nucleation is $35.45 \times 10^{-6} \text{ m}^2$ and the surface area of a quasi-free water droplet in C1/C3 mixed gas hydrate nucleation is $74.1 \times 10^{-6} \text{ m}^2$.

We note that the sample cooling rate used in the current study (0.288 K/h) was much slower than that used by Maeda (0.002 K/s) because of the much larger system size and heat capacity in the current study. From the above analysis of the impact of cooling rate on experimental nucleation rate, it has been known that the cooling rate influences the experimental nucleation rate determined by the linear cooling ramp method in a way that the slower the experimental cooling rate the smaller the experimental nucleation rate (Maeda 2020). It turned out, experimentally, that the derived semi-log nucleation curve shifted downward without any significant change in the slope when the cooling rate was slower (Maeda 2020). Therefore, the nucleation curve of C1/C3 mixed gas hydrate would have been lower than that shown in Figure 5-15 had Maeda also used the cooling rate of 0.288 K/h.

Comparison of the CO₂ hydrate nucleation rate to the literature data

We compared in Figure 5-10 the CO₂ hydrate nucleation rate measured in the current study to the literature data. Lim et al. (Lim, Barwood et al. 2022) reported the induction times of CO₂ hydrate on the surface of 5 mL of degassed and deionized water in contact with a stainless-steel wall at an isothermal and isobaric condition. They reported the experimental nucleation rate that ranged from $1.71 \times 10^{-4} \text{ s}^{-1}$ to $20.6 \times 10^{-4} \text{ s}^{-1}$ at supercoolings between 1.2 and 4.2 K. We normalized their CO₂ hydrate nucleation rate to the aqueous – guest gas contact area using the radius of the cylindrical cell they reported (Metaxas, Lim et al. 2019), and obtained the surface area – normalized nucleation rate of 0.38 to $4.58 \text{ s}^{-1} \text{ m}^{-2}$. These values are very similar to our results shown in Figure 5-10. Given that Lim et al. measured the nucleation rate of CO₂ hydrate in a stirred system (while ours were in quiescent samples) where the mass transfer was enhanced, the agreement is surprisingly good.

Based on Landau–Ginzburg free energy calculations, Radhakrishnan et al. (Radhakrishnan and Trout 2002) calculated homogeneous nucleation rate of CO₂ hydrate at 220 K and 4 MPa (approximate 60 K of supercooling) to be $6.08 \times 10^{-12} \text{ s}^{-1}$, which is 6 - 8 orders of magnitude lower

than the experimental nucleation rate shown in Figure 5-9 at much shallower supercoolings. If our nucleation curve could be extrapolated to the supercooling of 60 K, the discrepancy in the nucleation rates would become 19 orders of magnitude.

Maeda detected the nucleation of CO₂ hydrate in the presence of a glass wall and derived the nucleation rate using a power law fitting (Maeda 2019). To have a better comparison with nucleation data in the current work, we re-analyzed Maeda's nucleation data using an exponential function fitting. The surface area normalized nucleation curves are shown in Figure 5-16a). It can be observed that: 1) CO₂ hydrate nucleated over comparable supercooling range in the presence of a glass wall and in the presence of a stainless-steel wall. 2) At similar supercooling, CO₂ hydrate nucleation rate in the presence of a glass wall was a few orders of magnitude higher than that in the presence of a stainless-steel wall. Although glass and stainless-steel had similar promoting effect on nucleation rate of C1/C3 mixed gas hydrates (Maeda 2016), this discrepancy could be partly attributed to the cooling rate dependence of the nucleation curve noted above. Maeda used the experimental cooling rate of 0.025 K/s, which is about 250 times faster than that used in the current study. The two nucleation curves in Figure 5-16a) are expected to get closer had Maeda also used the cooling rate of 0.288 K/h.

The impact of the presence of a solid wall on the nucleation kinetics of CO₂ hydrate

Figure 5-7 - Figure 5-10 show that the presence of a stainless-steel wall promoted the nucleation kinetics of CO₂ hydrate. The supercoolings required for the nucleation of CO₂ hydrate on a quasi-free water droplet (without a solid wall) was substantially greater than those in the presence of a stainless-steel wall. Likewise, the nucleation rate of CO₂ hydrate at the same supercooling was substantially higher in the presence of a stainless-steel wall than in the absence of a solid wall. The recorded images showed that the nucleation started where the water contacted the surface of the stainless-steel wall and the CO₂ hydrate crystal grew from there, which is consistent with the notion that the stainless-steel wall promoted its nucleation. These results are

consistent with the earlier finding that the supercoolings required for the nucleation of C1/C3 hydrate on a quasi-free water droplet (without a solid wall) was substantially larger than in the presence of a stainless-steel wall (Maeda 2015, Maeda 2016, Maeda 2016).

To account for the influence of a solid wall, we revisited the parameter (Ψ) used by Kashchiev et al. (Kashchiev 2000, Kashchiev and Firoozabadi 2002) that quantitatively relates the nucleation work of heterogeneous nucleation (ΔG_{heter}^*) to that of homogeneous nucleation (ΔG_{homo}^*) in terms of the contact angle (θ) the emerging phase forms on a foreign solid wall in the medium of the parent metastable phase. The parameter Ψ takes a value between 0 and 1 and $\Psi = 1$ corresponds to the case of homogeneous nucleation. For the simplest case of a spherical cap-shaped nucleus on a flat solid substrate, the relationship is given by eq 5-9:

$$\frac{\Delta G_{heter}^*}{\Delta G_{homo}^*} = \Psi^3 = (1/4)(2 + \cos\theta)(1 - \cos\theta)^2 \quad \text{eq 5-9}$$

From eq 5-9, it can be seen that $\Psi < 1$ when $\theta < 180^\circ$, demonstrating that heterogeneous nucleation on the surface of a foreign solid wall is always more energetically favorable (lower nucleation work) than homogeneous nucleation.

Many studies observed that hydrate nucleation initiated from the TPCL (Bai, Chen et al. 2012, Maeda 2016), where the solid wall, the guest gas and the aqueous phase meet. The heterogeneous nucleation sites are concentrated near the TPCL instead of the aqueous-guest gas interface that is far from TPCL. To account for this observation, Maeda proposed a hypothesis that the experimental nucleation rate should be normalized to the unit length of the three-phase contact line in the system ($s^{-1}m^{-1}$ or $Hz \cdot m^{-1}$) in the presence of a solid wall (Maeda and Shen 2019). This hypothesis assumed that potential nucleation sites were concentrated on the water-solid interface just below the surface of the water (a narrow and stripe-like area along the TPCL). Figure 5-16b) shows the nucleation rate of CO₂ hydrate on a quiescent water surface in the presence of different

solid walls normalized to the unit length of TPCL. The red curve is TPCL-normalized CO₂ hydrate in the presence of a stainless-steel wall in this study while the blue curve is TPCL-normalized CO₂ hydrate nucleation curve after reanalysis of Maeda’s nucleation data of CO₂ hydrate in the presence of a glass wall by an exponential fitting. It can be seen that the nucleation rate of CO₂ hydrate in the presence of a glass wall is much higher than that in the presence of a stainless-steel wall. Other than the difference in the cooling rates used, Maeda used custom-made glass sample cells (called “boats” (Maeda, Wells et al. 2011)) whose surface would have been rougher than that of stainless steel. A rough surface would render the “true” length of TPCL much longer than the nominal perimeter (Maeda 2015) and use of a nominal perimeter in the place of a (much longer) real TPCL would overestimate the TPCL-normalized nucleation rates.

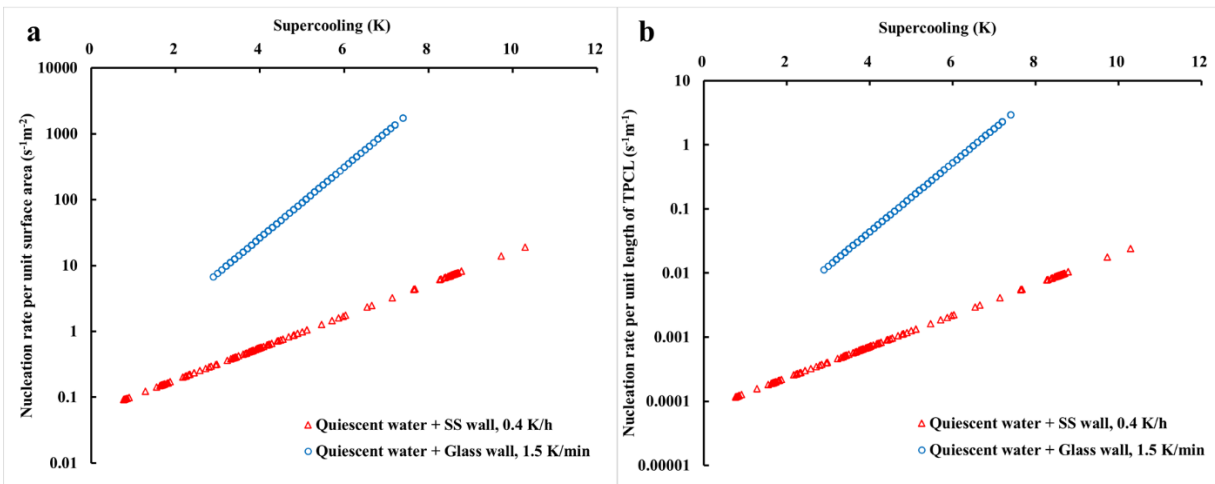


Figure 5-16 Gas-water interfacial area normalized and TPCL normalized nucleation curves of CO₂ hydrate formation on a quiescent water surface in the presence of a stainless-steel and a glass wall. By interfacial area normalization, the influence of a solid wall on nucleation was not taken into account; By TPCL normalization, the influence of a solid wall on nucleation was taken into account.

Comparison of the nucleation rate of CO₂ hydrate and that of other gas hydrate in the presence

of solid walls

Barwood et al. (Barwood, Metaxas et al. 2022) used a 2nd generation High-Pressure Stirred Automated Lag Time Apparatus (HPS-ALTA) to investigate the methane hydrate nucleation in the presence of a stainless-steel wall using linear cooling ramp experiments at two cooling rates (1 and 3 K/min). For comparison, we normalized the experimental nucleation rates derived from their study by the water-methane interfacial area and the length of TPCL reported by Lim et al. (Lim, Metaxas et al. 2020). Maeda derived the nucleation rate of C1/C3 mixed gas hydrate in the presence of a stainless steel wall, without stirring, over a pressure range of 7.0 to 12.5 MPa using linear cooling ramps (Maeda 2016). Since Maeda used a power law for the fitting of the $\ln F$ vs t curves of data at the time, here we re-analyzed Maeda's nucleation data using an exponential function of the form $\ln F = -A \cdot \exp(Bt) + C$ for the fitting of the $\ln F$ vs t curves to enable comparison. It should be noted that all CO₂ hydrate data in the current study used fresh water samples that had no history of hydrate formation. In contrast, Maeda used superheating to 310 K after each linear cooling ramp to erase the possible memory effect (Maeda 2016). We assume that no memory effect was present in either study.

We plotted all these results in the literature together with results obtained in the current study in Figure 5-17a) and Figure 5-17b), where the comparison is made after the respective nucleation rates have been normalized to (a) the unit area of guest gas – water interface or (b) the unit length of the three-phase contact line.

We found that: 1) generally, nucleation data points of clathrate hydrate collected by both Barwood et al. and Maeda at higher cooling rate were above those collected at lower cooling rate, in line with our discussion about the impact of the cooling rate on the nucleation rate above; 2) in the presence of a stainless-steel wall, methane hydrate with stirring nucleated over a comparable supercooling range as CO₂ hydrate without stirring, and both nucleated at much shallower supercooling range than C1/C3 mixed gas hydrate without stirring; The difference between CO₂

hydrate nucleation curves and C1/C3 mixed gas hydrate nucleation curves can be due to the difference of the guest solubility in water. Without stirring, the solubility of a hydrocarbon in water is much lower than that of CO₂ under a given temperature and pressure. The higher solubility of CO₂ means its higher concentration in water, which increases the kinetic factor of the nucleation rate (Kashchiev and Firoozabadi 2002, Kashchiev and Firoozabadi 2003). The higher the concentration of the guest gas molecules, the higher the chance that they come together to form clusters of various sizes which, when time-averaged, are expected to have the size distribution of the Boltzmann type. This explains why CO₂ hydrate nucleated at shallower supercoolings than C1/C3 mixed gas hydrate at the same (non-stirring) condition. Given that methane hydrate had a comparable nucleation curve as C1/C3 mixed gas hydrate at a non-stirring condition (Maeda 2018), we speculate that the difference observed in Figure 5-17 between methane hydrate with stirring and C1/C3 mixed gas hydrate without stirring was caused by the stirring action. With stirring, the mass transfer was facilitated and the guest diffusion was accelerated. 3) methane hydrate nucleation rate under stirring conditions was comparable to the CO₂ hydrate nucleation rate without stirring at shallow supercoolings and higher than CO₂ hydrate nucleation rate by at most two magnitudes with increasing of supercooling. This might be caused by the stirring condition and hundreds of times faster cooling rate Barwood et al. used than ours. Methane hydrate nucleation curve is expected to below our CO₂ hydrate nucleation curve if the effect of cooling rate on nucleation curves is considered.

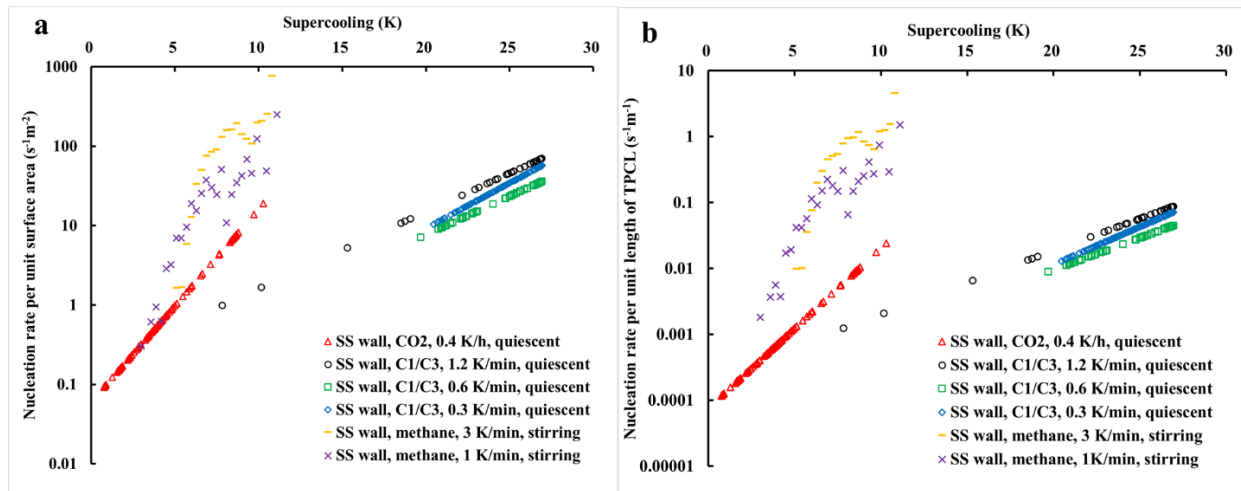


Figure 5-17 Comparison of gas-water interfacial area and TPCL normalized semi-logarithmic nucleation curves of CO₂ hydrate and that of other gas hydrate in the presence of a SS wall. a) gas-water interfacial area normalized CO₂ hydrate nucleation curve in the presence of a stainless-steel wall (red open triangle, the current study), C1/C3 mixed gas hydrate nucleation curves in the presence of a stainless-steel wall (black open circle, blue open rhombus and green open square, Maeda's study) and methane hydrate nucleation curve in the presence of a stainless-steel wall (orange line and purple cross, Barwood's study); and b) TPCL normalized nucleation curves with the same symbol as panel a). Cooling rate and experimental condition (quiescent vs stirring) was indicated in the figure.

5.5 Conclusions

We used a linear cooling ramp experiment to measure the nucleation curves of CO₂ clathrate hydrate on quasi-free water droplets supported by a nonvolatile fluorocarbon liquid, perfluoromethyldecalin. It appeared that 400 data points were sufficient to construct a reliable nucleation curve. Experimental nucleation curves were divided by the CO₂ – aqueous interfacial area to obtain the normalized nucleation curve. Comparison of CO₂ hydrate nucleation curves and C1/C3 mixed gas hydrate nucleation curves previously reported, both in the absence of a solid

wall, showed that the guest type had a major influence on the nucleation curves. CO₂ hydrate nucleated at shallower supercoolings than C1/C3 mixed gas hydrate and was expected to have about 3 orders of magnitude higher nucleation rate than C1/C3 mixed gas hydrate.

We also derived the nucleation curves of CO₂ hydrate on a quiescent water surface in the presence of a stainless-steel wall. Comparison with that in the absence of a solid wall confirmed the kinetic promoting effect of a solid wall on CO₂ hydrate nucleation. To account for the impact of a solid wall, the nucleation rate should be normalized to the unit length of three-phase contact line. We also calculated the kinetic parameter and the thermodynamic parameter based on the derived nucleation curves. It was found that the presence of a solid wall significantly lowered the activation energy barrier to nucleation.

In future, we will extend the study to the synergistic effects of various types of additives and solid walls and/or blending strategies in order to maximize or minimize the nucleation kinetics of CO₂ hydrate.

5.6 Summary and Relationship to Chapters that Follow

In this chapter, we derived nucleation curves of CO₂ hydrate in the presence and in the absence of a solid wall. The quasi-free water droplet can be treated as a model for hydrate formation in the mist of a gas-dominant flow. It was found that the guest type had a prominent effect on the hydrate nucleation kinetics. When a stainless-steel wall was present, hydrate nucleation kinetics was clearly promoted (shallower supercooling range and higher nucleation rate) because of the lower energy barrier. Results also revealed the deficiency of Classical Nucleation Theory in explaining hydrate nucleation, manifested by the large discrepancy in the kinetic nucleation parameter. Results offered a baseline of hydrate nucleation kinetics for comparison across different systems, from which the effect of additives and solid walls can be identified, thereby maximizing or minimizing hydrate nucleation kinetics, depending on the needs. The industry is anticipated to benefit from this. Another important influencing factor on hydrate

nucleation kinetics is the thermal history of water, which is the so-called memory effect. Since it is highly complicated and also shows a stochastic nature like nucleation itself, there is no consensus on the cause of it so far. In the next chapter, we will detect the memory effect from nucleation curves and elucidate the mechanism of it.

5.7 Appendix

SOP of the linear cooling ramp experiment

(The numbers of all valves correspond to the Roman numerals in Figure 5-4)

1. Switch on the pressure transducer and ISCO pump model 260D.
2. Check if all valves are closed. If not, close all the valves.
3. Switch on vacuum pump, vacuum pump starts working. (an alternative method to get rid of air: CO₂ flushing)
4. Slowly open valve 2,3. This is to evacuate the air in the tube between valve 1 and valve 5. Pressure transducer would show an approximate reading of -12.3 psi.
5. Slowly open valve 4 and 5. This is to evacuate the air in the pressure chamber and gas piston. The vacuum should stop when pressure transducer shows a reading of around -6 psi. If the vacuuming takes too long, sample water will boil.
6. Slowly close valve 2,3,4,5.
7. Shut down vacuum pump. Disconnect the vacuum pump from the rest of lines by unplugging the plastic tubing from the vacuum pump.
8. Slowly open the main valve at the top of gas cylinder. There will be a pressure reading on the pressure gauge on the top of gas cylinder. This reading indicates the gas pressure inside the gas cylinder.
9. Slowly open the valve 1,4 and 5. Slowly clockwise rotate the regulator attached to the gas cylinder. The pressure reading in regulator will increase while rotating. This reading is the pressure of the gas inside the pipeline, chamber & gas piston.
10. Increase the pressure to 150 psi. Close main valve and valve 1.
11. Read the pressure on the pressure transducer. Monitor the pressure reading to ensure there is

no leak in the system (pressure should remain constant). Besides monitoring the pressure reading, Swagelok Snoop can be applied to each joint and the thread between chamber and its lid. If there is leakage, continuous bubbles can be seen.

12. If there is no leak, slowly open main valve and valve 1 again.

13. Slowly rotate the knob of pressure regulator until the reading in pressure transducer shows the target pressure.

14. Close valve 1 and main valve on the top of gas cylinder. Slowly count-clockwise rotate the regulator to make it loose.

15. Run the program of the circulator to start the cooling ramp. At the same time, record the sample image at a fixed time interval (5 or 10 mins).

16. Rotate the three-way valve at the top of the ISCO pump to make it point towards the gas piston, press “Constant pressure” button on the control panel of the ISCO pump and then press “A”. Then the screen on the panel should show the text of “input pressure”. Then manually input the target pressure and press “run”.

17. The ISCO pump starts holding the pressure inside the chamber. It can be seen that there is a flow rate showing at the middle top of the pump’s panel and the volume inside the pump which is shown at the top right of the pump’s panel should decrease.

18. After the water piston run out (gas piston is half-full), the control panel would show “cylinder empty”, meaning water piston is at the end of the pump stroke.

19. Insert the other end of the plastic tube connected to the pump into a water reservoir (e.g. a beaker full of water) and adjust the three-way valve at the top of the ISCO pump, letting it point towards the reservoir.

20. Press “refill” button on the control panel. The water in the reservoir is sucked into the pump and the volume inside the pump which is shown at the top right of the pump’s panel should increase.

21. When the water piston is full, the volume will reach to around 266 mL and the control panel would show “cylinder full”.

22. Rotate the three-way valve at the top of the ISCO pump to make it point towards the gas piston,

then pressure “run” so that pump starts holding pressure again.

23. After the water piston run out again (gas piston is full of water), water piston and gas piston should be charged at the same time.

24. Close valve 5 to isolate the pressure chamber. Then drain water in gas piston by opening valve 6, the pressure reading falls very quickly.

25. After all the water has been drained, the water is transferred to the reservoir.

26. Repeat step 19 to 21 to refill the water piston first.

27. Slowly open the main valve and the valve 1 and slowly top up the pressure inside the pipeline (before valve 5) to the target pressure by clockwise rotating the regulator.

28. After the pressure top up, close main valve and valve 1 and count-clockwise rotate the regulator to make it loose.

29. Open valve 5 to make the chamber re-connected to pipeline again.

30. Rotate the three-way valve at the top of the ISCO pump, letting it point towards the gas piston. Then pressure “run” button to hold the pressure again.

31. Because the volume of gas piston is twice as large as the volume of water piston, the gas piston is charged once while the water piston is charged twice. The charging process of water piston alone is step 19-21. The charging process of gas piston + water piston is step 24-30.

32. The technician must go to the lab from time to time to see if there is charging need for both gas piston and water piston. If charging is not in time, the pressure inside the chamber will fall which means the run is not isobaric anymore.

33. After the experiment is done. Double check if the main valve and valve 1 is closed and the regulator is loosened.

34. Drain the water inside the gas piston by open valve 6 so that the gas piston is initialized and the drained water is transferred to the reservoir.

35. Water piston should also be initialized (water piston at the bottom) by refilling the water into the pump.

36. The three-way valve at the top of the pump should be vertical (neither pointing towards

reservoirs nor towards gas piston)

37. There should still be residual pressure inside the chamber. Valve 7 is opened very slowly. The sound of venting should not be heard or the venting is too fast. Too fast venting is detrimental to the O-ring inside the lid of the chamber. The lid cannot be opened until the pressure reading is 0 psi.

38. The circulator is set to be 9 Celsius degree for next run.

39. Close all the valves of the setup.

40. Switch off ISCO pump.

6 Mechanisms of the Memory Effect of Clathrate Hydrates

In this chapter, we will investigate the memory effect of gas hydrate nucleation. From derived nucleation curves, the memory effect can be detected and its relative size can be quantified. Results graphically manifest the elusive memory effect in a straightforward manner, which is innovative. Based on the comparison among the relevant nucleation curves, a new mechanism explaining the memory effect will be proposed which incorporates reasonable principles of existing hypotheses. It might solve the long-standing dispute in academia regarding the cause of the memory effect. Furthermore, it may also help the industry better avoid or utilize the memory effect. For example, it is desirable in terms of the application of gas hydrate technologies but undesirable in terms of the transportation of recovered methane and dissociated water mixtures from hydrate-bearing sediments in pipelines.

6.1 Introduction

Gas hydrates, or clathrate hydrates, are crystals in which guest molecules are trapped in the cages formed by the hydrogen bonding of water molecules (hosts). Gas hydrates received much attention from researchers because they have many potential applications such as gas storage, gas separation and desalination (Englezos 1993). In the context of global warming, CO₂ hydrate has applications for carbon sequestration. These applications require timely formation of gas hydrates, however, nucleation remains one of the least understood aspects of gas hydrates.

Within the framework of Classical Nucleation Theory, nucleation is the process of aggregation of monomers that forms a stable cluster called a “nucleus” (Kashchiev 2000). The stochastic nature of nucleation renders the experimental investigations of nucleation difficult for a few reasons. First, nucleation is not directly detectable because a nucleus is too small and the lifetimes of clusters that are smaller than the critical size are too short for the contemporary technologies to detect. Therefore, a nucleation event can only be detected after the fact, with some delay. Second, the intrinsic stochasticity means that nucleation is not repeatable, let alone reproducible, and can only be investigated statistically. These challenges rendered the

determination of the most essential parameter that quantifies the nucleation kinetics within the framework of Classical Nucleation Theory, the nucleation rate, difficult (Maeda 2020).

A common experimental method for investigations of the nucleation kinetics of gas hydrates has been the measurements of induction times at a constant supercooling (ΔT), which is the differential between the actual sample temperature and the temperature at the thermodynamic phase boundary. Since each induction time can be very long, it has been difficult to collect sufficiently large amounts of statistical data using this approach. An alternative approach is applications of linear cooling ramps under isobaric conditions in which a sample is cooled at a constant rate until nucleation is effectively forcibly induced (Maeda 2019). Advantages of the linear cooling ramp method are: (1) it can compress the large scatter in the nucleation data and (2) it can significantly shorten the experiment time. In the current study, we employ the linear cooling ramp method for the determination of the nucleation rate of CO₂ hydrate.

The longest-standing mystery in the nucleation of gas hydrates is the so-called memory effect which remains unresolved for several decades (Makogon 1981). The memory effect refers to a phenomenon that gas hydrate nucleates faster or easier in a water sample that has a history of gas hydrate formation and dissociation compared to a fresh water sample with no such history. The memory effect has been studied for a long time since it was first discussed in 1884 (Roozeboom 1884, Roozeboom 1884, Ripmeester and Alavi 2016). The earliest hypothesis explaining the memory effect was structural memory (Parent and Bishnoi 1996, Sloan, Subramanian et al. 1998, Takeya, Hori et al. 2000, Wu and Zhang 2010, He, Rudolph et al. 2011, Sefidroodi, Abrahamsen et al. 2013), which hypothesized existence of residual structures in the liquid water after the hydrate had dissociated that triggered the memory effect. Then, since dissociation of gas hydrates always leads to supersaturation of guest gas in water due to the much larger gas content in the hydrate form than the solubility of the same gas in liquid water, guest supersaturation in the dissociated water was thought to be the cause of the memory effect (Rodger 2000). In contrast,

Zeng et al. proposed an impurity imprinting hypothesis (Zeng, Moudrakovski et al. 2006) to account for the observations that the memory effect depended on the solid walls that were present in the system. Bagherzadeh et al. (Bagherzadeh, Alavi et al. 2015) later advanced the guest supersaturation hypothesis and proposed that formation of nanobubbles in liquid water after the dissociation of methane hydrate caused the memory effect. Uchida et al. (Uchida, Yamazaki et al. 2016) confirmed the formation of a substantial number of micro- and nanobubbles (MNBs) in the bulk of liquid water after dissociation of gas hydrates, which was thought to play an important role in the manifestation of the memory effect. Kou et al. reported the dependence of the memory effect on the thermal history of water that suggested the correlation between the long-lived nanobubbles and the memory effect (Kou, Feng et al. 2022).

We can summarize the major attributes of the memory effect known to date as follows. They include: 1) the memory effect is about the nucleation of the gas hydrate as opposed to the subsequent crystal growth (Vysniauskas and Bishnoi 1983); 2) the memory effect also shows the stochastic nature (Bylov and Rasmussen 1997, Fandiño and Ruffine 2014); 3) the extent of the memory effect varies among different samples despite their identical thermal history (Ohmura, Ogawa et al. 2003, Zeng, Moudrakovski et al. 2006, Sowa and Maeda 2015); 4) remnants of hydrate-like structures in the dissociated water have not been observed by neutron diffraction or other methods (Buchanan, Soper et al. 2005); 5) melted ice also induces the memory effect of gas hydrate (Takeya, Hori et al. 2000); 6) the memory effect fades with the increase in the superheating temperature and/or the superheating period (Li, Wu et al. 2021); 7) transferring a small amount of dissociated water to fresh water induces the memory effect that is comparable to that in 100% dissociated water (Sefidroodi, Abrahamsen et al. 2013); 8) the solid wall present in the system has an influence on the memory effect (Ohmura, Ogawa et al. 2003, Zeng, Moudrakovski et al. 2006, Sowa and Maeda 2015).

In contrast, the mechanism causing the memory effect is still unclear. Several leading

hypotheses have been proposed over the years to explain the memory effect; 1) residual structure (Parent and Bishnoi 1996, Sloan, Subramanian et al. 1998, Takeya, Hori et al. 2000, Wu and Zhang 2010, He, Rudolph et al. 2011, Sefidroodi, Abrahamsen et al. 2013), 2) guest supersaturation (Rodger 2000), 3) impurity imprinting (Zeng, Moudrakovski et al. 2006), 4) nanobubbles in bulk water (Bagherzadeh, Alavi et al. 2015, Uchida, Yamazaki et al. 2016, Uchida, Yamazaki et al. 2016) and, 5) interfacial gaseous states (Maeda 2018).

The residual structure hypothesis is the oldest hypothesis and assumes that the water after hydrate dissociation preserves some sort of residual structure or “hydrate postcursor” that has a long lifetime in the dissociated water and increases the number of potential nucleation sites for hydrate nucleation when the system is subjected to the supercooling condition again. Although the fact that transferring of a small amount of dissociated water into fresh water can induce almost the same extent of the memory effect as 100% dissociated water (Sefidroodi, Abrahamsen et al. 2013) may be interpreted to support this hypothesis, it cannot explain why the memory effect depends on the solid wall of foreign materials in the system (Ohmura, Ogawa et al. 2003, Zeng, Moudrakovski et al. 2006, Sowa and Maeda 2015) or how the system temperature can be raised by several Kelvins above the thermodynamic phase boundary while the residual structure is still present in the system.

The guest supersaturation hypothesis assumes that the guest gas released from the hydrate structure after dissociation can accumulate in the aqueous phase because the diffusion of guest gas back to the bulk gas phase needs some time. This hypothesis is compatible with thermodynamics and with the finding that the memory effect was not detected in tetrahydrofuran (THF) hydrate (Wilson and Haymet 2010). THF and water are miscible at all proportions and hence its solubility in water is practically infinite. Supersaturation of THF in dissociated water cannot occur. Thus, supersaturation of guest gas will undoubtedly occur after each dissociation of gas hydrates, its impact on the memory effect is unclear, especially it cannot explain why the memory effect

depends on the solid wall of foreign materials in the system (Ohmura, Ogawa et al. 2003, Zeng, Moudrakovski et al. 2006, Sowa and Maeda 2015).

The nanobubble hypothesis (nanobubbles in bulk water) can be considered a subset of the guest supersaturation hypothesis. Since the amount of the guest gas released after the dissociation of gas hydrates far exceeds the solubility limit of the guest gas in liquid water, it can form nanobubbles in the bulk water phase. Such nanobubbles would remain in the supersaturated aqueous phase for a long time, and if the system is subjected to a supercooling condition again while they are still present, they will provide nucleation sites for gas hydrate nucleation and/or act as local guest gas reservoir that would facilitate gas hydrate nucleation (Takahashi, Kawamura et al. 2003). Bagherzadeh et al. proposed formation of nanobubbles of methane in the bulk of liquid water after dissociation of methane hydrate (Bagherzadeh, Alavi et al. 2015). The formation of such nanobubbles was caused by the nucleation of methane bubbles in dissociated water when the supersaturation reached a critical level. Uchida et al. (Uchida, Yamazaki et al. 2016, Uchida, Yamazaki et al. 2016) experimentally confirmed the existence of C₂H₆ microbubbles and nanobubbles after C₂H₆ hydrate dissociation. The guest supersaturation hypothesis (with or without nanobubbles in the bulk water) is thus most likely correct, however, if guest supersaturation is the *sole* cause of the memory effect, then the presence of a solid wall in the system should not have an impact on the memory effect.

Neither the residual structure hypothesis, the guest supersaturation hypothesis nor the nanobubble hypothesis can reconcile the findings of the solid wall dependence of the memory effect. Zeng et al. (Zeng, Moudrakovski et al. 2006) investigated the memory effect of methane hydrate and THF hydrate in the presence of antifreeze proteins (AFP) and found no evidence of the memory effect. To account for this finding, they proposed the “impurity imprinting” hypothesis, which postulated that the memory effect was only related to heterogenous nucleation and container walls was “conditioned” after hydrate dissociation which provided more potent nucleation sites

for subsequent gas hydrate formation. Similar solid wall dependence of the memory effect was reported by Ohmura et al. and Sowa and Maeda (Ohmura, Ogawa et al. 2003, Sowa and Maeda 2015). Since the memory effect has been known to be erased by high superheating, the remaining puzzle of this hypothesis is how the perceived memory, which is supposed to be in the form of imprinting on the solid walls, can be erased by modest levels of superheating that are far below the Tammann temperature of the solid in question.

Maeda recently proposed the “interfacial gaseous states” or “interfacial nanobubble” hypothesis (Maeda 2019). As noted above, Uchida et al. (Uchida, Yamazaki et al. 2016, Uchida, Yamazaki et al. 2016) experimentally confirmed the existence of C_2H_6 microbubbles and nanobubbles in the bulk of liquid water after C_2H_6 hydrate dissociation. It is virtually impossible to form nanobubbles in the bulk of liquid water without first forming interfacial gaseous states (Zhang, Maeda et al. 2006), including interfacial nanobubbles, on solid walls that are present in the system because heterogeneous nucleation of bubbles on a solid surface is always easier than homogeneous nucleation of bubbles in the bulk of liquid water (Brennen 2014). Indeed, Guo et al. reported direct detection of such interfacial gaseous states on solid walls in dissociated water by Atomic Force Microscopy (Guo, Xiao et al. 2018).

The interfacial gaseous states can be regarded as the entity of the “impurity” of the impurity imprinting hypothesis. The advantage of the interfacial gaseous states hypothesis is that it can largely account for most of the known attributes of the memory effect. For example, the solid wall dependency of the memory effect and the elusive (or hard to quantify) nature of the memory effect could very well be a consequence of the fact that interfacial gaseous states are easier to form on some solids than others (Maeda 2018). Hydrophobicity of the solid is an obvious parameter that influences such ease with which interfacial gaseous states can nucleate, but more than that, it has been known that the nucleation of interfacial gaseous states strongly depends on the surface roughness as well as on the history of the surface treatments (Zhang, Maeda et al. 2006). The

finding that the memory effect was not detected in THF hydrate (Wilson and Haymet 2010) is also compatible with the interfacial gaseous states hypothesis, because dissociation of THF hydrate would not cause any supersaturation of THF and hence would not result in formation of any interfacial gaseous states. That the memory effect could be erased either by superheating of the system of the order of 15 K or by extending the superheating time could also be explained by the interfacial gaseous states hypothesis. The solubility of a gas in water falls with heating in the relevant temperature range. The greater the superheating the greater the reduction in the solubility of the guest gas in water. After a waiting time, the supersaturation of the guest gas in the aqueous phase would have fallen somewhat. When the system was cooled again, the cooling will increase the solubility of the guest gas in water. For a long enough waiting time and/or high enough superheating temperature, the increasing of the solubility due to the cooling could be sufficient to dissolve all the interfacial gaseous states whose amounts would be small to begin with (because the location where the interfacial gaseous states could form in a quiescent system is limited to a small area of the solid wall immediately below the three-phase contact line).

In addition, Maeda recently suggested that the interfacial gaseous states hypothesis could also account for Takeya et al.'s findings that melted water from ice could also induce the memory effect (Maeda 2020). Freeze-thaw processes have been known to degas melted water (i.e., it is impossible to freeze water without phase-separating the dissolved atmospheric gases that typically form tiny bubbles trapped between the grain boundaries of the polycrystalline ice) (Sowa, Zhang et al. 2011). The amount of such dissolved atmospheric gases in pure water is about 1 mM under the atmospheric pressure (Maeda, Rosenberg et al. 2004). Such phase-separated bubbles would not immediately dissolve back into the bulk water after the ice has been melted because the diffusion process is slow (it would take hours) (Maeda, Rosenberg et al. 2004). Furthermore, melting of the ice during heating in Takeya et al.'s study would have taken place from the inner walls of the high pressure chamber which would have been the warmest during heating (and where the solubility of the air in water would have been the lowest). Then, the phase-separated atmospheric gases could

very well have formed interfacial gaseous states on the inner walls of the container. When such a system is subsequently exposed to a pressurized guest gas, the guest gas would quickly diffuse through the interfacial gaseous states and stabilize them. The end result could be similar to the interfacial gaseous states generated by dissociation of gas hydrate.

It has been difficult to come up with a hypothesis that can account for all the known attributes of the memory effect. Sowa and Maeda proposed that multiple mechanisms must be concurrently at play (Sowa and Maeda 2015). Since guest supersaturation (with or without nanobubbles in the bulk water) most certainly occurs in a dissociated water, at least temporarily, it is likely one of the multiple mechanisms. However, the extent of its impact on the memory effect (the relative impact of guest supersaturation on the total “amount” of the memory effect) remains unclear. Likewise, even though the formation of interfacial gaseous states in dissociated water is almost certain in a system that contains a solid wall, the *amount* of interfacial gaseous states would be small because their locations would be limited to just below the three-phase contact line of a quiescent sample (Maeda 2018). Consequently, the extent of its impact on the memory effect also remains unclear.

In the current study, we used the linear cooling ramp method to determine the nucleation curves of CO₂ hydrate in fresh water and in dissociated water, either in the presence of a stainless-steel wall or in a quasi-free water droplet supported by perfluoromethyldecalin. We compared the results to the nucleation curves of methane/propane mixed gas hydrate reported in the literature. We found that the relative impact of interfacial gaseous states and that of the guest supersaturation on the memory effect to be comparable in size, with the former being the greater one.

6.2 Materials and methods

Materials

CO₂ (99.5%) was supplied by Linde. Milli-Q water was purified by a Millipore unit (resistivity = 18.2 M Ω). Perfluoromethyldecalin (technical grade, 80%) and octadecane (99%)

were supplied by Sigma-Aldrich and used without further purification. The purity of perfluoromethyldecalin appears low but most of the impurities are perfluorinated isomers so it does not affect the purpose of our use. Clean gastight Syringes (Hamilton 100 μ L) were used for handling the liquids.

An Isco syringe pump (model: 260D) was used to first pressurize and then hold the pressure inside the pressure chamber constant during a CO₂ hydrate formation experiment either at a constant supercooling mode or under a constant cooling rate mode. A two-stage vacuum pump (model: VP10D) from CPS Products Inc. was used to get rid of air inside the gas lines, the pressure chamber and the gas piston before each experiment. Two light guides (ZEISS, model: CL 4500) were used to enhance the optics. A programmable coolant circulator (Julabo, model: F34-HE) was used for controlling the sample temperature. A pressure transducer (Heise, model: PM) monitored the pressure inside the pressure chamber. A gas piston (model: ZR-3) was used for CO₂ replenishment inside the pressure chamber as the sample cooled so that the pressure inside remained constant. A Pyrex glass petri dish (60 \times 15mm) was used for containing the sample. A stainless-steel block with 55 circular through-holes or a Teflon block with 21 circular through-holes made by the machine shop at the University of Alberta was used together with the glass petri dish. A webcam (C920 \times HD Pro) from Logitech was used to record sample images during a cooling ramp experiment. A digital thermometer (model: #119) from BIOS company was used for temperature calibrations.

The pressure chamber and the cooling system

In last chapter, we showed the schematic configuration of the high-pressure setup in Figure 5-3 and the description of it in Section 5.2. In this study, we used the same setup. Here we only presented a brief revisit on the setup. The pressure chamber was half-immersed into a coolant (95% ethanol). The programmable coolant circulator was used to control the sample temperature in a CO₂ hydrate formation experiment either at a constant supercooling or during cooling at a constant

cooling rate (linear cooling ramp). Two windows on the top lid and on the bottom lid of the pressure chamber made the sample clearly visible with the help of the enhanced optics by the light guide and a mirror placed at the bottom of the chiller. A webcam connected to a PC was used to record the sample image at a fixed time interval and these images were saved on the PC for further analysis. During CO₂ hydrate formation experiment, the pressure drop caused by either cooling or CO₂ hydrate formation was automatically replenished by the combination of a syringe pump and a gas piston from the gas inlet.

Preparation of a quiescent water in the presence of a stainless-steel wall

The preparation procedure of a quiescent water in the presence of a stainless-steel wall was identical with the description in Section 5.2 of last chapter. The configuration of the quiescent bulk water sample system in the presence of a stainless-steel wall was already shown in Figure 5-2.

CO₂ hydrate formation in a fresh quiescent water surface in the presence of a stainless-steel wall

After the preparation of a quiescent water sample in the presence of a stainless-steel wall, the glass petri dish was carefully placed at the center of the pressure chamber, after which the lid of the pressure chamber was closed and sealed. Then the CO₂ hydrate nucleation experiment was initiated using a linear cooling ramp method. The detailed experimental procedure was elaborated in Section 5.2 of last chapter and the schematic illustration of the high-pressure setup is shown in Figure 5-4.

CO₂ hydrate formation in a dissociated quiescent water surface in the presence of a stainless-steel wall (the memory run)

After hydrate formation at the end of the first linear cooling ramp experiment using a fresh sample, the chiller was set to be 278.15 K, which was 2.5 to 3 K below the phase equilibrium temperature of CO₂ hydrate at the experimental pressure. The CO₂ pressure inside the pressure

chamber increased due to the warming. Some excess CO₂ gas was slowly vented from the gas outlet so that the CO₂ pressure inside the pressure chamber went back to the initial pressure. Subsequently, the temperature of the chiller was increased to 285 K (4 to 4.5 K of superheating, which is the temperature differential between the sample temperature and the hydrate phase boundary at the pressure of interest) to induce CO₂ hydrate dissociation. Immediately after the dissociation of CO₂ hydrate (formation of many bubbles), a second linear cooling ramp experiment (1st memory linear cooling ramp) was initiated using the same cooling rate.

Preparation of an ice seeded system

Unfortunately, the quasi-free water droplets were lost during the venting and could not be used for a subsequent cooling ramp. This did not occur in an HP-ALTA because the chamber volume was much smaller than that of the guest gas reservoir connected to it and the pressure remained constant during a cooling ramp, and there was no need to vent the guest gas inside the HP-ALTA after each warming (Maeda, Wells et al. 2011). In the current setup, however, the volume of the chamber was much larger and the pressure increase that resulted from the replenishment of the CO₂ during a cooling ramp was large. In addition, reduction of the built-up pressure was necessary to avoid liquefaction of CO₂ during subsequent linear cooling ramps. Therefore, an alternative method was used to prepare a memory sample.

The ice seeding was prepared by first freezing quasi-free water droplets in a freezer and exposing the frozen quasi-free water droplets to CO₂ gas in the chamber. Ice has been known to promote heterogeneous nucleation of gas hydrate because of good lattice matching between ice and gas hydrate crystal structures (Maeda 2020).

About 15 mL of perfluoromethyldecalin was poured into the pre-cleaned glass petri dish and the Teflon sample model with 21 vertical through-holes was then placed inside the petri dish. A Milli-Q water droplet (0.02 mL) was placed in each hole of the Teflon sample model using a

designated Hamilton syringe. A water droplet in each hole contacted neither the Teflon wall nor each other so it was regarded as a quasi-free water droplet. Then, the petri dish containing 21 quasi-free water droplets separated by the Teflon sample model was covered by the lid of the petri dish to prevent water vaporization and placed inside a freezer where the temperature was 253 K overnight. The sample was inspected the following day and quasi-free water droplets were found to be frozen while perfluoromethyldecalin remained liquid. The ice seeded system is shown in Figure 6-1.

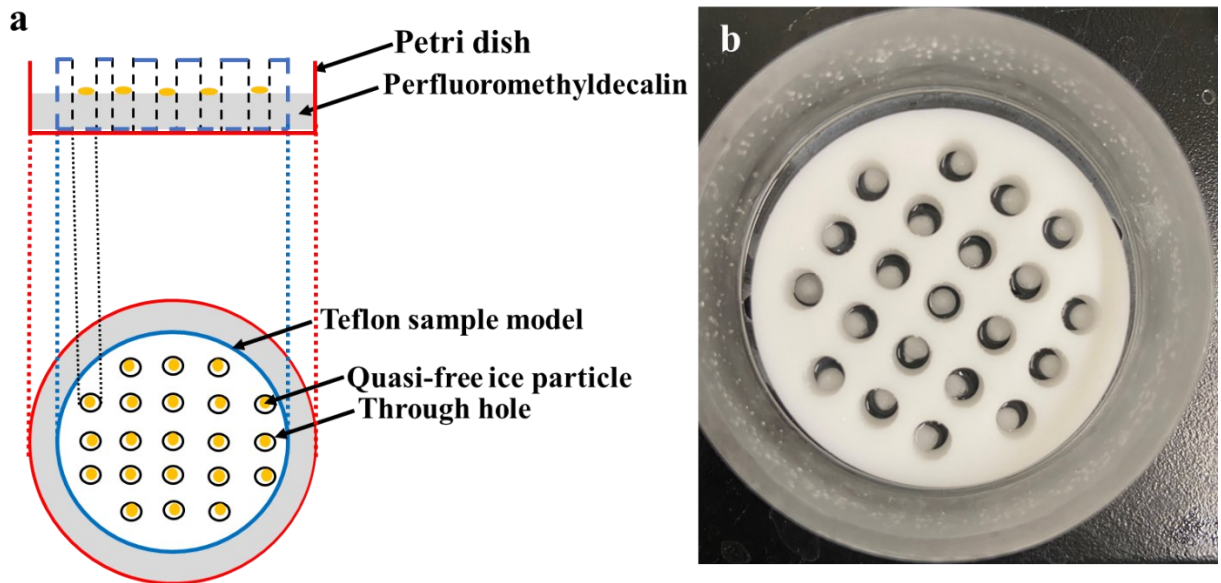


Figure 6-1 Schematic configuration and the top view of quasi-free ice particles as a seeding. The circular Teflon sample model with 21 through holes was placed inside a glass petri dish and 15 mL of perfluoromethyldecalin was placed inside the petri dish so that each hole in the Teflon sample model was partially filled with perfluoromethyldecalin. One droplet (0.02 mL) of milli-Q water was placed on the surface of perfluoromethyldecalin in each hole. The petri dish was then placed inside the freezer overnight to enable the ice particle formation from each quasi-free water droplet. Panel b) showed the top view of the ice seeding system. After taking the petri dish out of the freezer, each frozen quasi-free water droplet was supported by liquid perfluoromethyldecalin.

This ice seeding system was then placed in the pressure chamber.

The pressure chamber half immersed in the coolant (95% ethanol) in the chiller was pre-cooled to 263 K so that the sample temperature was kept at 272 K. This temperature ensured that the ice would not melt after being transported to inside the chamber. The ice seeded system was slowly transferred inside the pressure chamber and the lid of the chamber was placed and tightened to seal the pressure chamber. The brightness of the light guide and the position of the webcam was adjusted to optimize the sample visibility. Then a vacuum pump was used to get rid of the air inside the gas lines, the gas piston and the pressure chamber. After that, the vacuum pump was disconnected from the gas lines and the system was purged with CO₂. After confirming the absence of leaks, the CO₂ pressure was gradually increased to the pressure of interest (2.7 MPa). The chiller was then heated to raise the sample temperature to 275.5 K. Ice slowly melted while the supercooling for CO₂ hydrate nucleation was approximately 3 K. The system was left at an isobaric condition for 24 h. The CO₂ gas consumed by CO₂ hydrate formation was replenished by the combination of a syringe pump and a gas piston.

CO₂ hydrate formation from the dissociated quasi-free water droplets (the memory run)

After CO₂ hydrate formed in the ice seeded system, the chiller was heated to dissociate the CO₂ hydrate. The superheating temperature used in this study was up to 3 K (thermal lag caused the sample temperature to increase slowly during the superheating period), which was supposed to be able to conserve the memory effect. The superheating period was 1.5 h in this study. Unlike 200 s of superheating period in the literature (Sowa and Maeda 2015, Maeda 2018), the large thermal lag caused by the pressure chamber made the sample temperature change at a slow rate, thus hindering us from dissociating CO₂ hydrate in such a short period. Fortunately, it was expected that the memory effect, if existed, would not be erased until the superheating period exceeded 240 min (4 h) (Li, Wu et al. 2021). The dissociation of CO₂ hydrate and was observed through the high pressure window on the top lid of the pressure chamber.

Subsequently, the dissociated quasi-free water droplets were subjected to a linear cooling ramp at 0.4 K/h, the same as what we used for fresh samples. The isobaric pressure during the linear cooling ramp experiment was the pressure after the hydrate dissociation and it was held by the combination of a syringe pump and a gas piston.

Temperature calibrations

In the current study, temperature calibration was necessary owing to a few reasons: 1) the thick pressure chamber caused a large “thermal lag”; 2) The presence of a thermometer, if used in direct contact with the sample, might affect the CO₂ hydrate nucleation kinetics.

For the temperature calibration of the Teflon sample cell, about 15 mL of perfluoromethyldecalin was poured into the glass petri dish and the Teflon sample cell was then placed into the petri dish. The probe of a digital thermometer was inserted into a hole in the Teflon sample cell. Our previous study showed that there was little variation between the temperature in the holes near the center of the Teflon block and those near the edge of the Teflon block. Therefore, the temperature in the 21 through holes was regarded as uniform. Three characteristic temperatures of the chiller when the sample temperature was 272 K (to preserve ice seeding during pressurization), 275.5 K (to melt ice but render CO₂ hydrate nucleation) and 282 K (to dissociate CO₂ hydrate) were determined in advance.

When the hydrate formed on the ice seeded system was heated for dissociation, we directly increased the chiller temperature from 275.5 K to 282 K and waited for 2 h for complete dissociation. During this heating period, a temperature calibration was also required since the sample temperature and the moment when it crosses the phase boundary of CO₂ hydrate need to be determined in order to calculate superheating temperature and superheating period precisely. It was found that due to the thermal lag, sample temperature kept increasing at a very slow rate. The

maximum superheating temperature achieved was 3 K and for 1.5 h.

The temperature calibration of the Teflon sample cell during a linear cooling ramp at a constant rate of 0.4 K/h was also carried out. A calibration table was made that related the temperature of the coolant and the temperature in a sample hole that also accounted for the thermal lag. It was found that the real sample cooling rate was 0.00008 K/s.

A similar procedure was followed for the temperature calibration of the stainless-steel sample cell during a linear cooling ramp at a constant rate of 0.4 K/h, except for the calibration medium was replaced by 95 % ethanol. It was found that the real sample cooling rate was 0.00009 K/s.

6.3 Results

CO₂ hydrate formation in the ice seeded system

Images of the ice seeding system after pressurization and after 24 h of constant supercooling hydrate induction were compared in Figure 6-2.

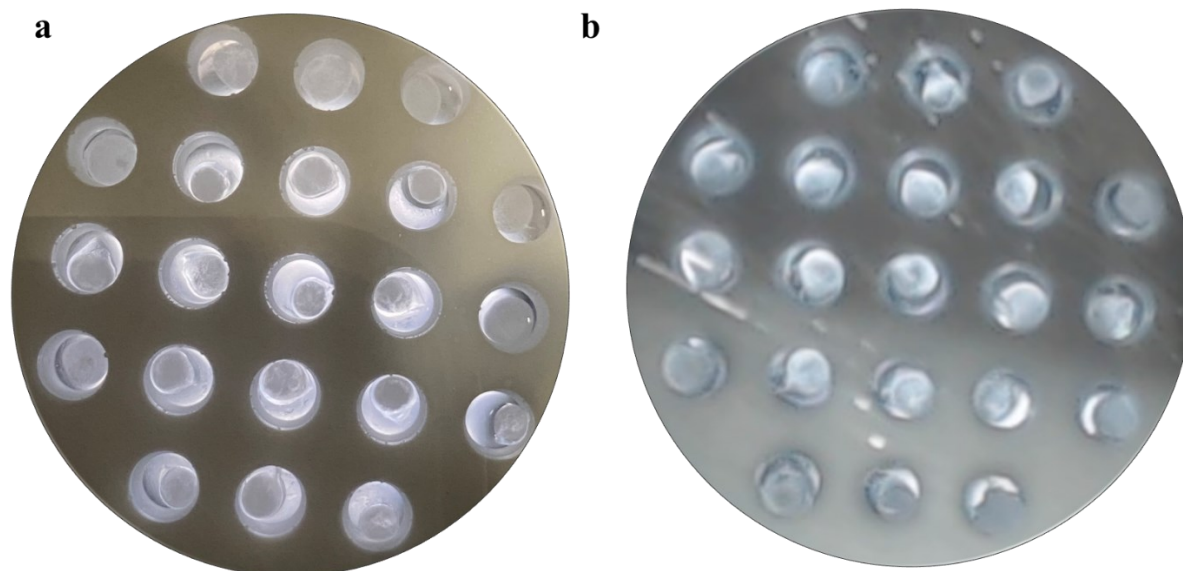


Figure 6-2 Typical sample image of the ice seeding system (a) and CO₂ hydrate crystals (b) After the pressure chamber was pressurized to 2.7 MPa, a total of 21 ice particles in each hole remain intact because the sample temperature was 272 K, lower than the ice melting point. A total of 21 CO₂ hydrate crystals formed after 24 h of constant supercooling induction. The sample temperature was 275.5 K, above the ice melting point but below CO₂ hydrate phase equilibrium temperature. Therefore, the solid formed in each hole shown in panel b was ascertained to be a CO₂ hydrate crystal.

CO₂ hydrate formation from the dissociated quasi-free water droplets

Figure 6-3 showed the image of the dissociation of CO₂ hydrate formed in the ice seeding system and CO₂ hydrate reformation during the subsequent linear cooling ramp experiment. From Figure 6-3a), it can be seen that hydrate crystals turned to transparent quasi-free water droplets saturated with CO₂ after up to 3 K of superheating for 1.5 h. Comparison between panel b and c of Figure 6-3 clearly showed the transformation of the yellow-circled sample from a transparent water droplet to an opaque hydrate crystal. This confirmed that CO₂ hydrate nucleation occurred between these two consecutive frames.

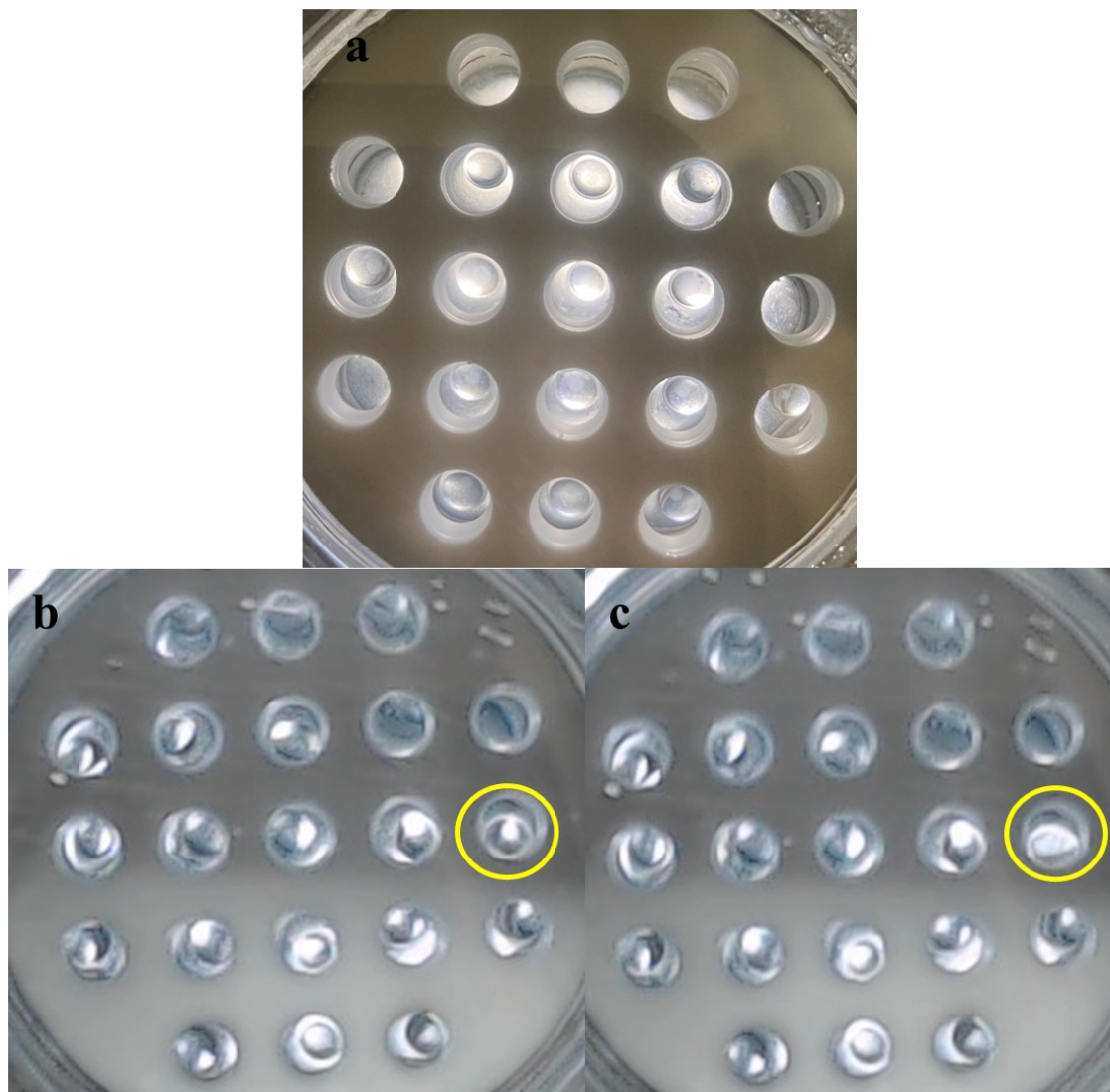


Figure 6-3 Typical images of quasi-free water droplets during different stages of a CO₂ hydrate reformation experiment.

a) CO₂ hydrate dissociation after up to 3 K and 1.5 h of superheating, manifested by the transformation of all samples from hydrate crystal to transparent quasi-free water droplets. Panel b and c are two consecutive frames (5 mins time interval) captured by the webcam. It can be seen that the yellow-circled sample converted from a transparent quasi-free water droplet to an opaque hydrate crystal, which confirmed that CO₂ hydrate nucleation has occurred.

CO₂ hydrate formation in a dissociated quiescent water surface in the presence of a stainless-steel wall

Figure 6-4 showed images of a dissociated quiescent water surface at different stages during a linear cooling ramp experiment (memory linear cooling ramp) which was conducted after 4 K of superheating. Panel a, b and c were captured continuously at 5 mins interval alphabetically. From panel a, a lot of gas bubbles can be seen because CO₂ hydrate formed in the previous fresh linear cooling ramp released a lot of CO₂ upon dissociation. From the comparison of the circled hole on panel a and the next frame, panel b, it can be seen that hydrate crystal formed on the water surface and covered approximately half of the water surface. In panel c, the hydrate crystal grew and covered the whole water surface. The enlargement of the circled hole was shown in panel d.

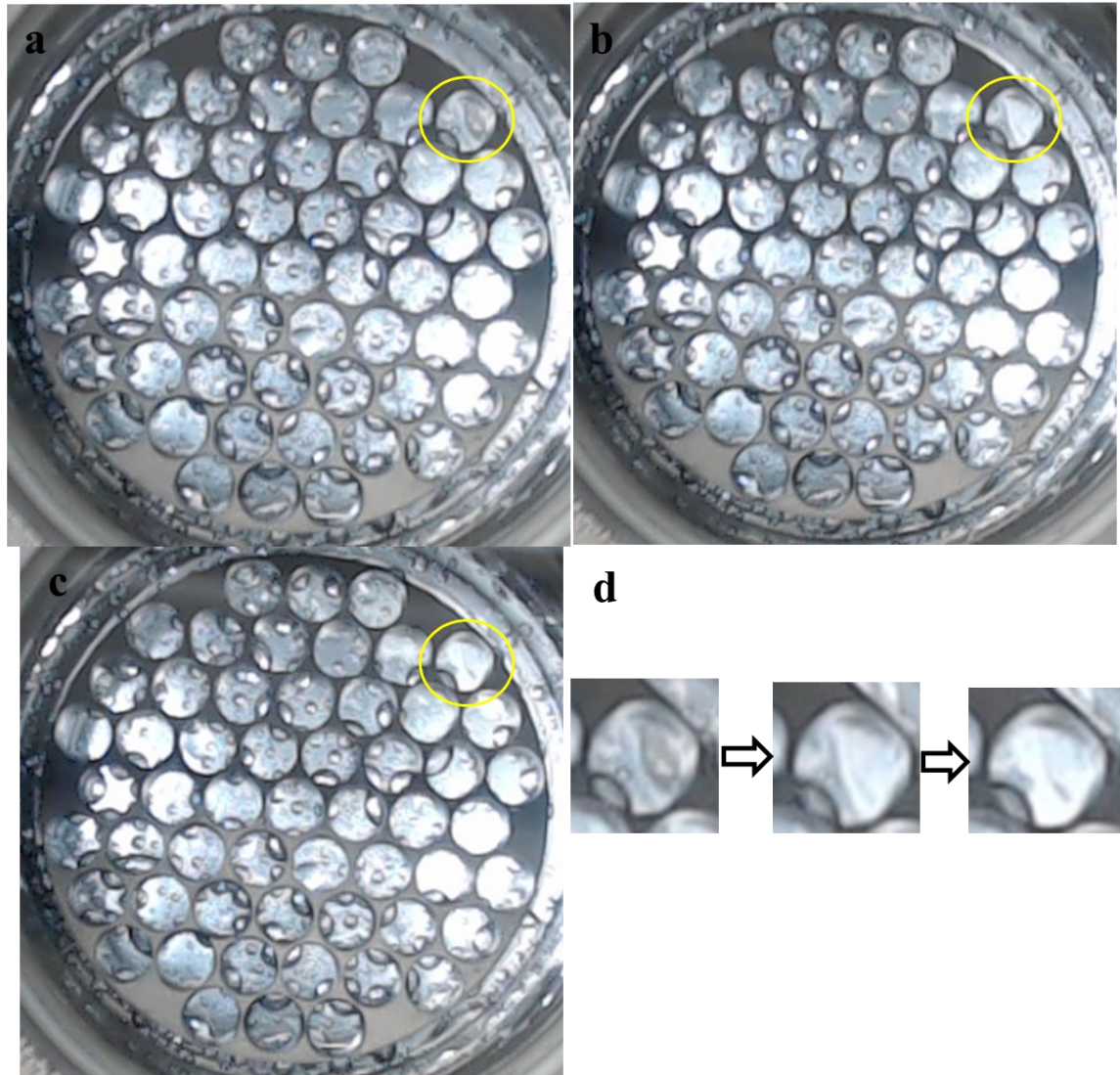


Figure 6-4 Typical images of quiescent bulk water during different stages of a CO₂ hydrate reformation experiment.

a) CO₂ hydrate dissociation after 4 K and 2 h of superheating, manifested by the bubble release. Panel b and c are two consecutive frames (5 mins time interval) captured by the webcam. It can be seen that a CO₂ hydrate crystal formed on the circled water surface (panel b) and then grew and covered the whole water surface enclosed by the stainless-steel solid wall (panel c). d) From left to the right: enlargement of the hole marked by the yellow circles shown in panel a, b and c.

Derivation of CO₂ hydrate nucleation curves on a dissociated quasi-free water droplet and a dissociated quiescent water surface in the presence of a stainless-steel (SS) wall

We have derived the nucleation curve of CO₂ hydrate both on a fresh quasi-free water droplet and a fresh quiescent water surface in the presence of a stainless-steel wall. We will derive the nucleation curve of CO₂ hydrate on dissociated water of the above two systems. A similar derivation procedure was followed here. First, the survival curve which is the survival probability, F , as a function of supercooling was derived. The survival probability is defined as the ratio of the number of samples that have not nucleated to the total number of samples. The mathematical expression of the survival probability is shown in eq 6-1, where n_{tot} is the total number of samples and n is the number of samples that have not nucleated.

$$F = \frac{n}{n_{tot}} \quad \text{eq 6-1}$$

To plot a survival curve, we need to determine the supercooling at which a nucleation event occurred. Fortunately, due to the linear nature of the cooling process, the supercooling was easily determined by multiplying the sample cooling rate, α , by the lag time, t (the time elapsed from the moment of the establishment of the meta-stability to the moment of a nucleation event). Even though the nucleation can only be detected with some delay, the slow cooling rate used in this study was assumed to have rendered the difference between the “true supercooling” when a nucleation event occurred and the system supercooling when the phase transition was experimentally detected negligibly small. The nucleation data from different cooling ramps were combined together when analyzing and the supercooling corresponding to each nucleation event was calculated and arranged in an ascending order. After calculating the survival probability at each supercooling when a nucleation event was detected, a monotonically decreasing survival probability with the increasing supercooling is obtained, as shown in Figure 6-5. For reference, the survival curves of CO₂ hydrate on a fresh quasi-free water droplet and on a fresh quiescent water surface in the presence of a stainless-steel wall are plotted together in Figure 6-5.

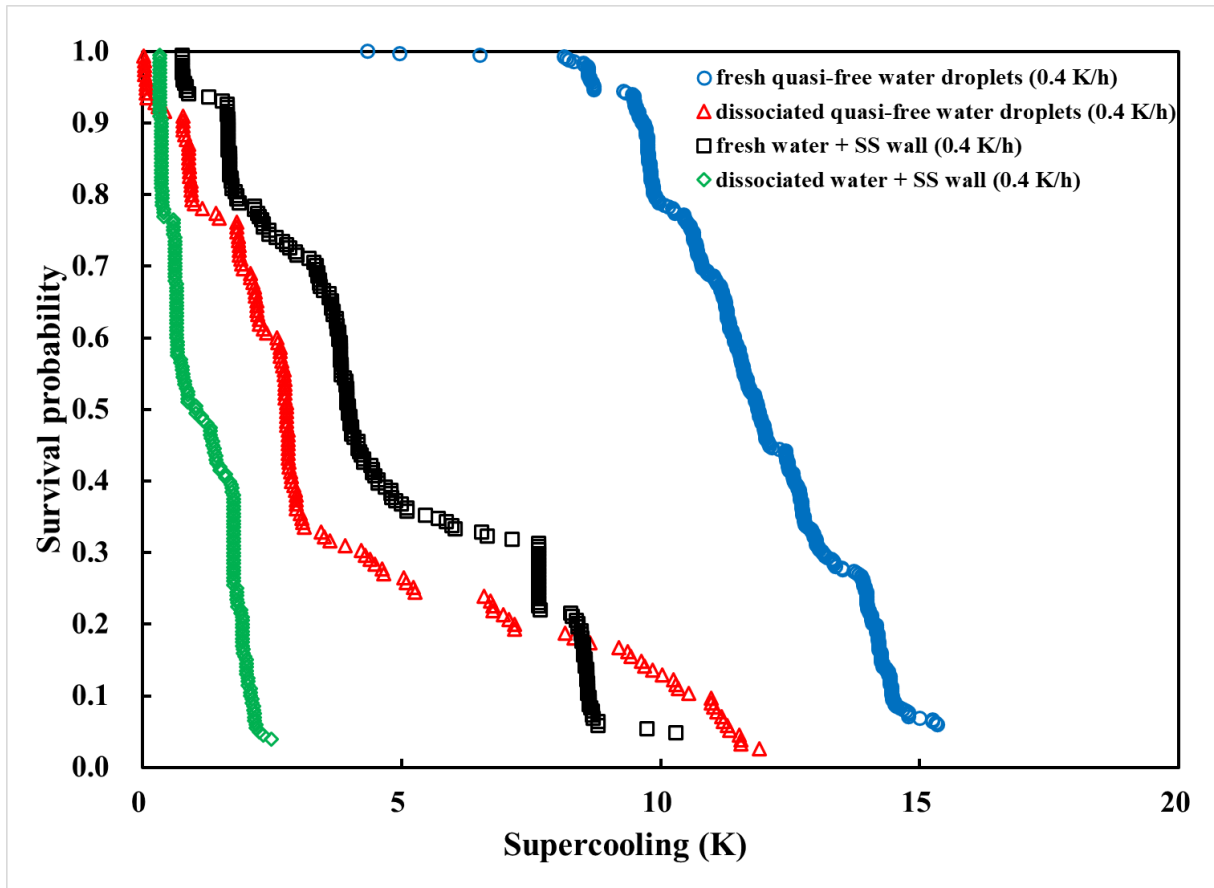


Figure 6-5 Survival curves of CO₂ hydrate formation or reformation on different samples. A fresh quasi-free water droplet (blue circular open symbol), a dissociated quasi-free water droplet (red triangular open symbol), both supported by a thick layer of perfluoromethyldecalin, a fresh water surface (black square open symbol) and a dissociated water surface (green rhombic open symbol) in the presence of a stainless-steel (SS) wall. The horizontal axis is the supercooling, ΔT , and the vertical axis is the survival probability, F . Each open symbol represents a nucleation event. The survival probability starts from 1 and decreases monotonically with the increase of supercooling and falls to a minimum by the lowest temperature has been reached. At least 150 nucleation events were used to construct a nucleation curve considering the stochastic nature of nucleation. All data points were measured at a constant nominal system cooling rate of 0.4 K/h, or true sample cooling rate of 0.00008 K/s for a Teflon sample model and 0.00009 K/s for a stainless-

steel sample model.

Then we calculated the natural logarithm of the survival probability, $\ln F$, and plotted it with the lag time, as shown in Figure 6-6. The purpose of this step is that the derivative of $\ln F$ with respect to t gives us the negative of the nucleation probability density. The detailed reasoning process can be found in ref. (Maeda 2020).

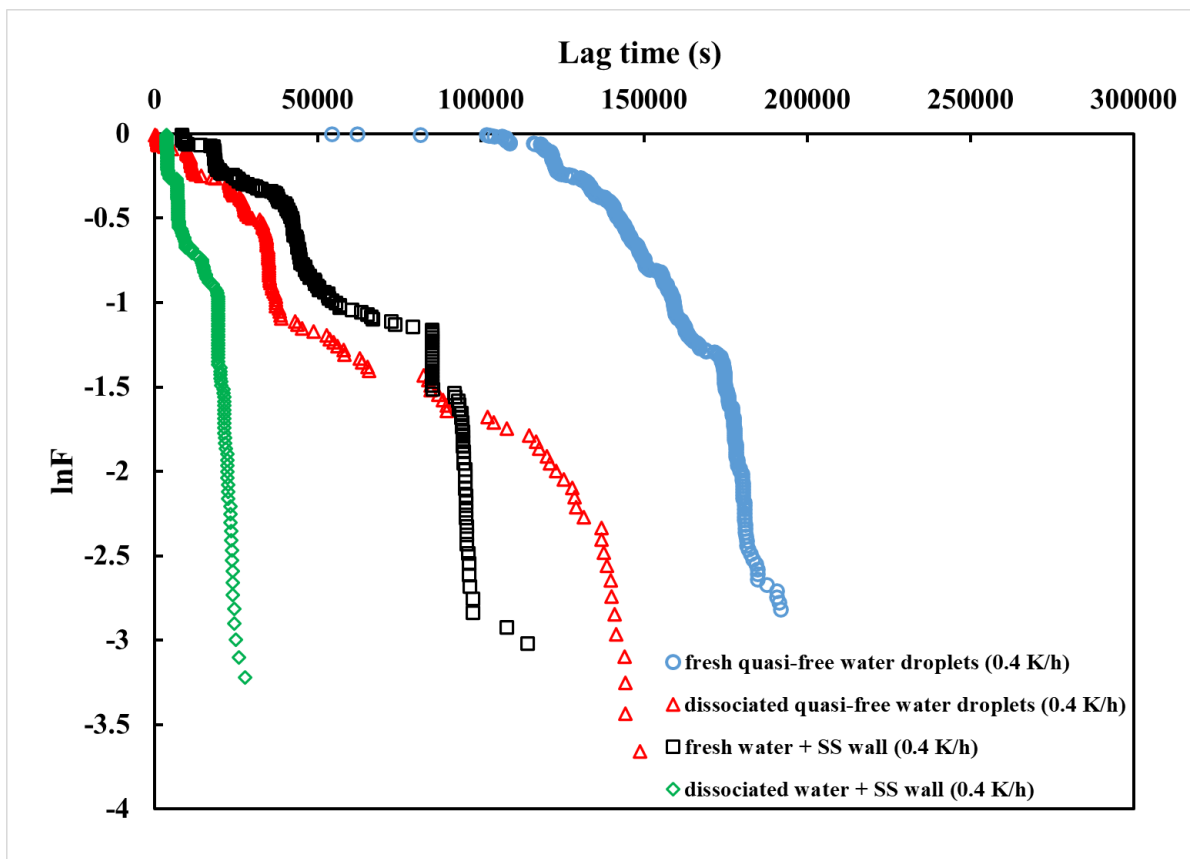


Figure 6-6 Natural logarithm of the survival curves of CO₂ hydrate formation on different samples. A fresh quasi-free water droplet (blue circular open symbol) and a dissociated quasi-free water droplet (red triangular open symbol), both supported by a thick layer of perfluoromethyldecalin; a fresh water surface (black square open symbol) and a dissociated water surface (green rhombic open symbol) in the presence of a stainless-steel (SS) wall. Each open symbol represents an

experimental data point. All data points were measured at the constant nominal system cooling rate of 0.4 K/h.

To allow for a calculation of the derivative or the local slope of $\ln F(t)$, an appropriate function should be selected for fitting. Different types of function forms have been chosen in previous publications, such as a power law (Maeda 2015) and an exponential function (Zhang, Li et al. 2021). Here we employed an exponential function form of $\ln F = -A \cdot \exp(Bt) + C$, where A , B and C are the fitting constants. The numerical values of these constants were found to be 0.000485, 0.000062 and 0 for the dissociated quasi-free water droplet case and 0.017546, 0.000208 and 0 for the dissociated quiescent water surface case, respectively. The nucleation probability density, which was calculated by differentiating the fitting function with respect to lag time, was $AB \cdot \exp(Bt)$. The experimental nucleation rate, k (s^{-l}), was the nucleation probability density divided by a constant, $\ln 2$ (Maeda 2020). The derived nucleation curves were shown in Figure 6-7.

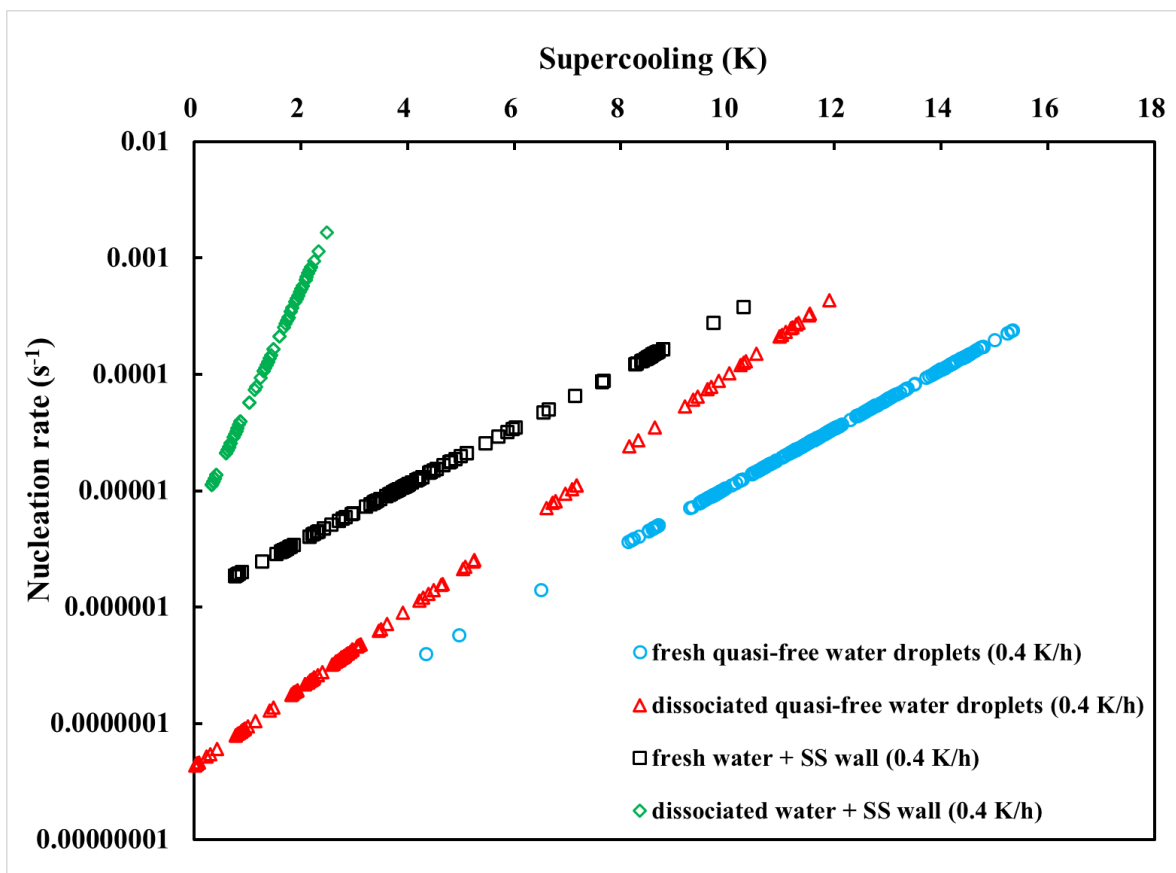


Figure 6-7 Experimental nucleation curves of CO_2 hydrate formation on different samples. A fresh quasi-free water droplet (blue circular open symbol), a dissociated quasi-free water droplet (red triangular open symbol), both supported by a thick layer of perfluoromethyldecalin; a fresh water surface (black square open symbol) and a dissociated water surface (green rhombic open symbol) in the presence of a stainless-steel (SS) wall. Nucleation rates were calculated from taking the first-order derivative of the exponential fitting equation with respect to lag time as a function of supercooling. All data points were measured at the constant nominal system cooling rate of 0.4 K/h.

The final step of the nucleation curve derivation procedure is the normalization of the experimental nucleation rate to a characteristic measure of the system size. This is necessary for any fair comparison of nucleation rate across systems of different sizes. Therefore, we normalized

the nucleation curves shown in Figure 6-7 by an appropriate measure of the system size to which the concentration of potential nucleation sites becomes proportional. For the quasi-free water droplet systems, an appropriate measure of the system size would be the guest – aqueous interfacial area because the guest concentration and the guest supersaturation would be the highest at the interface due to the mass transfer limitations. When gas hydrate nucleates at the interface, gas hydrate crystals would exhaust the guest supersaturation at the interface and also block the gas diffusion through the crystals to the bulk liquid phase. These characteristics would render the clathrate hydrate nucleation a surface phenomenon. The fact that the number of the potential nucleation sites is expected to scale with the interfacial area rationalizes the normalization factor to be the surface area in the absence of a solid wall. When a solid wall is present, in contrast, the situation is different. Previous publications showed that the total lengths of the triple-phase-lines in a quiescent system would be an appropriate measure (Maeda and Shen 2019). Nevertheless, no such triple-phase-lines exist in the quasi-free water droplet systems and as such we cannot use it for comparisons between nucleation rates in a system that contains a solid wall and those in a system that does not. Here, we only showed in Figure 6-8 the nucleation rates that were normalized to the interfacial areas for both systems.

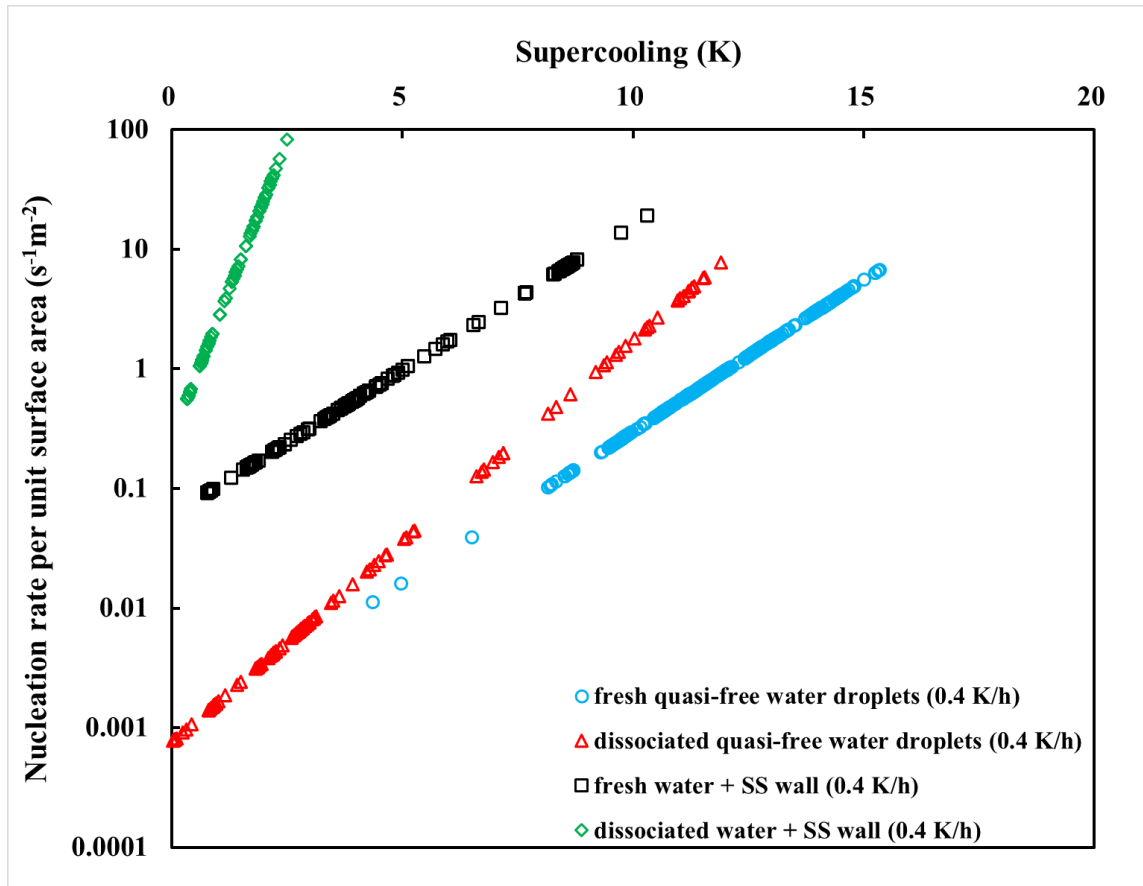


Figure 6-8 Gas-water interfacial area normalized nucleation curves of CO₂ hydrate formation on different samples.

A fresh quasi-free water droplet (blue circular open symbol), a dissociated quasi-free water droplet (red triangular open symbol), both supported by a thick layer of perfluoromethyldecalin; a fresh water surface (black square open symbol) and a dissociated water surface (green rhombic open symbol) in the presence of a stainless-steel (SS) wall. Nucleation rates were calculated from dividing the experimental nucleation rate as shown in Figure 6-7 by the guest-water interfacial area.

We also summarize in Table 6-1 the interfacial area normalized nucleation rate of CO₂ hydrate in the four systems shown in Figure 6-8.

Table 6-1 Summary of the nucleation rate normalized to the unit interfacial area

| System | Supercooling (K) | Area normalized nucleation rate ($s^{-1}m^{-2}$) |
|---------------------------------------|------------------|--|
| Fresh quasi-free water droplets | 4 – 15 | 0.011 – 6.751 |
| Dissociated quasi-free water droplets | 0.02 – 11.9 | 0.00077 – 7.7219 |
| Fresh water + SS wall | 0.77 – 10.3 | 0.09 – 19.06 |
| Dissociated water + SS wall | 0.33 – 2.49 | 0.564 – 83.05 |

6.4 Discussion

Detection of the memory effect in the presence of a solid wall

From Figure 6-5 and Figure 6-7, it can be observed that the memory effect was detected in the quiescent water that was in direct contact with a stainless-steel wall. This result was consistent with the literature data (Takeya, Hori et al. 2000, Sowa and Maeda 2015, Li, Wu et al. 2021), notwithstanding that the guest molecules are CO₂ in the current study as opposed to hydrocarbon gases in the relevant literature. When CO₂ hydrate formed on a fresh quiescent water sample in a stainless-steel container, most samples have nucleated at about 10 K of supercooling. In contrast, when CO₂ hydrate reformed on a dissociated quiescent water sample in a stainless-steel container, only 2.5 K of supercooling was required when the great majority of the samples nucleated. This much shallower supercooling indicated that CO₂ hydrate nucleated easier in the dissociated water than in the fresh water, as expected. The memory effect manifested itself not only in the most probable supercooling but also in the nucleation curves. Figure 6-7 shows that the nucleation rate of CO₂ hydrate in the dissociated water rose much faster than that in the fresh water as supercooling became deeper.

Detection of the memory effect in the absence of a solid wall

In the quasi-free water droplet system, the memory effect was also detected as shown in Figure 6-5 and Figure 6-7. Compared to the survival curve of CO₂ hydrate formation on the fresh quasi-free water droplets, the most probable supercooling was clearly lower when CO₂ hydrate

reformed on the dissociated quasi-free water droplets. Figure 6-7 showed that the nucleation rate of CO₂ hydrate in the dissociated quasi-free water droplets was comparable to that on fresh quasi-free water droplets at shallower supercoolings (less than 10 K) but the gap widened at deeper supercoolings. The nucleation rate of CO₂ hydrate in the dissociated quiescent water sample in a stainless-steel container rose much faster with the supercooling than that of CO₂ hydrate in the dissociated quasi-free water droplets. Also, the gap in the nucleation rates between the fresh water vs the dissociated water was much greater in the quiescent water samples in a stainless-steel container than in the quasi-free water droplets.

Comparison of the memory effect in the absence of a solid wall with the literature data

Maeda investigated the memory effect of methane/propane mixed gas (C1/C3 hereafter) hydrate in quasi-free water droplets using the linear cooling ramp method (Maeda 2018). To enable comparison, we re-analyzed Maeda's data using an exponential function fit instead of a power law fit used in ref. (Maeda 2018) and plotted together with the normalized nucleation curves of CO₂ hydrate derived in the current study in Figure 6-9.

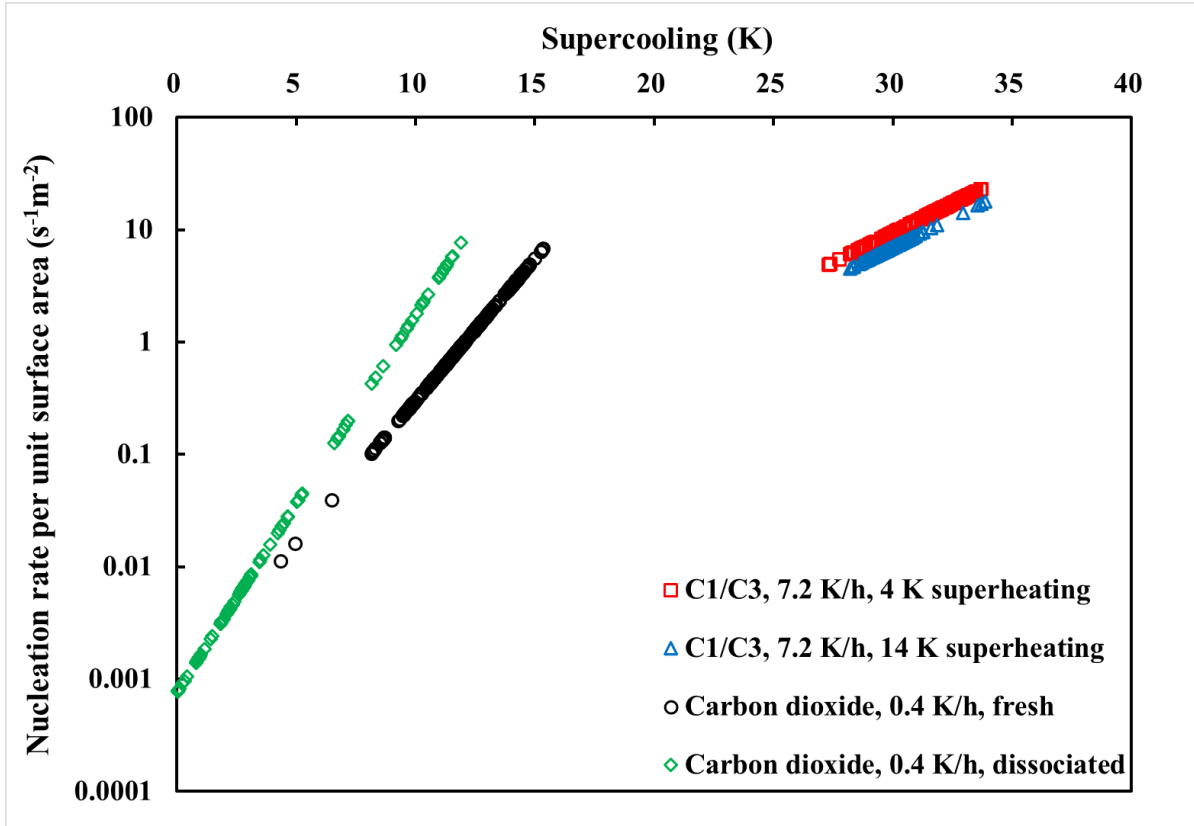


Figure 6-9 Gas-water interfacial area normalized nucleation curves of CO₂ hydrate and C1/C3 mixed gas hydrate on quasi-free water droplets

CO₂ hydrate formation on a fresh quasi-free water droplet (black circular open symbol), CO₂ hydrate reformation on a dissociated quasi-free water droplet (green rhombic open symbol), C1/C3 mixed gas hydrate reformation on a dissociated quasi-free water droplet by 14 K of superheating (blue triangular open symbol) and C1/C3 mixed gas hydrate reformation on a dissociated quasi-free water droplet by 4 K of superheating (red square open symbol). The system cooling rate used in each study was also shown in the legend.

One notable characteristic of Figure 6-9 is that the nucleation rate of C1/C3 mixed gas hydrate was slightly higher than that of CO₂ hydrate and that C1/C3 mixed gas hydrate nucleated at deeper supercooling range than CO₂ hydrate did. Nucleation rate generally depends on the driving force for nucleation which is quantified by the system supercooling in the current study. CO₂, which is

more soluble in water, is easier to establish supersaturation in water than a non-polar guest gas like C1/C3 mixed gas (the kinetics of diffusion is faster). CO₂ hydrate thus nucleated at higher temperatures (shallower supercoolings) while the nucleation rate was lower.

Another difference that can be seen from Figure 6-9 is that the gap in the nucleation rates between the memory samples (i.e., the dissociated samples in the current study and the 4 K superheating one in ref. (Maeda 2018)) and the non-memory samples (i.e., the fresh samples in the current study and the 14 K superheating one in ref. (Maeda 2018)) was much larger in the current study than in ref. (Maeda 2018). There could be several reasons for this result.

First, we used fresh milli-Q water without any history of hydrate formation as the non-memory samples. In Maeda's study, the non-memory samples were not fresh but dissociated at 14 K of superheating after each linear cooling ramp. The implicit assumption was that the 14 K of superheating for 300 s was sufficient to erase the memory effect. Sowa and Maeda reported gradual fading of the memory effect with superheating of the water samples of comparable volumes that were contained in a glass sample cell (Sowa and Maeda 2015). In contrast, Li et al. reported that for the same type of guest, C1/C3, the memory effect was still preserved in a much larger sample of 20 mL at 11 K superheating for 60 mins (Li, Wu et al. 2021). Therefore, it is conceivable that 14 K of superheating for 300 s was insufficient to completely erase the memory effect, which may have resulted in the small gap in the nucleation rates between the 4 K and the 14 K superheating samples shown in Figure 6-9.

Second, the nucleation rate of quasi-free water droplets supported by perfluoromethyldecalin was higher than that of quasi-free water droplets in squalane (Maeda 2016). It was considered that the quasi-free water droplets supported by perfluoromethyldecalin were more prone to contacting a solid wall than the quasi-free water droplets in squalane, due to the repulsive (stable) disjoining pressure of a squalane film and the negative (unstable) disjoining pressure of a

perfluoromethyldecalin film (Maeda 2016). Any contacts of quasi-free water droplets with a solid wall would induce the memory effect in accordance with the interfacial gaseous state hypothesis, which may have resulted in the larger gap in the current study than in ref. (Maeda 2018). However, in light of our results that the gap in the nucleation rates between the fresh vs the dissociated was much greater in the quiescent water samples in a stainless-steel container than in the quasi-free water droplets, we consider a third possibility below, which we think to be more likely.

Dual mechanisms of the memory effect

As noted at the end of Introduction, on the one hand, multiple mechanisms are likely at play in the memory effect and the guest supersaturation hypothesis and the interfacial gaseous states hypothesis are the two most likely candidates. On the other hand, the relative impact of guest supersaturation or interfacial gaseous states on the total “amount” of the memory effect remains unclear. Figure 6-8 shows that the “extent” of the memory effect (the gap between the nucleation curve of the dissociated water and that of the fresh water) was greater in the presence of a stainless-steel wall than in the quasi-free water droplets. Then, we may as well hypothesize that the memory effect consists of two components of the solid wall contribution and the bulk supersaturation contribution.

In the current study, each quasi-free water droplet sat on the top of a bulk of liquid perfluoromethyldecalin in a Teflon sample cell and was in direct contact with the CO₂ guest gas. In contrast, the quasi-free water droplet which sat at the bottom of squalane in an OTS-coated glass sample cell in ref. (Maeda 2018). An important point here is that not only the solubility of C1/C3 mixed gas is much higher in squalane than in water but also the solubility of C1/C3 mixed gas in squalane falls with heating (Jamialahmadi, Emadi et al. 2006). Jamialahmadi et al. (Jamialahmadi, Emadi et al. 2006) investigated the solubility of methane in squalane at elevated pressures and found that the methane solubility in squalane at 10 MPa fell from 30 kg/m³ to 25 kg/m³ with heating from 45 °C to 81 °C. When the system was heated for dissociation after a cooling ramp,

the supersaturated C1/C3 mixed gas in squalane could form interfacial gaseous states on the surface of the OTS-coated glass walls in squalane before the C1/C3 mixed gas hydrate started dissociating. Such formation of interfacial gaseous states would have reduced the supersaturation of the C1/C3 mixed gas in squalane. In contrast, the C1/C3 mixed gas in the quasi-free water droplet would not have formed such interfacial gaseous states because the water was not in contact with any solid wall. When the C1/C3 mixed gas hydrate subsequently dissociated, the released C1/C3 mixed gas at the water – squalane interface (from a C1/C3 mixed gas hydrate rind) could have partitioned into the squalane phase instead of into the aqueous phase because of the already lower chemical potential of the C1/C3 mixed gas in the squalane, which would have lowered the supersaturation of the C1/C3 mixed gas in the dissociated quasi-free water droplet.

In addition to the above potential lowering of the supersaturation of the C1/C3 mixed gas in the quasi-free water droplet during heating after a cooling ramp, another possibility is that the squalane could become undersaturated with C1/C3 mixed gas when the system was re-cooled after the dissociation of C1/C3 mixed gas hydrate at the start of the next cooling ramp because of the increasing solubility of C1/C3 in squalane with cooling. Since the quasi-free water droplet was sitting at the bottom of the squalane and far away from the bulk C1/C3 mixed gas phase above the squalane, it would take time for the C1/C3 mixed gas from the upper bulk gas phase to diffuse all the way down through the squalane to the bottom part of the squalane where the water droplet sat. The undersaturation of the C1/C3 mixed gas in squalane would have rendered the chemical potential of the dissolved C1/C3 mixed gas in squalane lower than that in the bulk gaseous C1/C3 mixed gas above it, which could have lowered the driving force for nucleation of C1/C3 mixed gas hydrate in the quasi-free water droplet in squalane.

The above two factors can occur in the absence of any temperature gradients. In reality, the squalane was directly in contact with the OTS-coated container wall whereas the quasi-free water droplet was not. Since the temperature controls of the HP-ALTA would have induced heat flows

from the outer walls of the container to the interior of the container, the heat transfer during the heating would have rendered the squalane warmer than the water (i.e., the squalane would have been more supersaturated than the water with the C1/C3 mixed gas) while the heat transfer during the cooling would have rendered the squalane colder than the water (i.e., the squalane would have been more undersaturated than the water with the C1/C3 mixed gas). The resulting chemical potential gradients of the dissolved C1/C3 mixed gas would have amplified the above two factors. In short, the squalane in the C1/C3 mixed gas system could have acted as a buffer or a “guest gas sink” that had slowed a buildup of the supersaturation of the C1/C3 mixed gas during a cooling ramp in the quasi-free water droplet (Maeda 2018).

What all these means is as follows: we may hypothesize that the memory effect consists of two components of the solid wall contribution and the bulk supersaturation contribution. This mechanism has been illustrated graphically in Figure 6-10. The contribution from the solid wall component would be eliminated in the quasi-free water droplet on perfluoromethyldecalin but the contribution from the guest supersaturation component (with or without nanobubbles in water) would remain. Both components could have been eliminated in the quasi-free water droplet at the bottom of squalane. Then, Figure 6-9 suggests that the guest supersaturation component of the memory effect is expressed in the *difference in the gaps* between the CO₂ systems and the C1/C3 mixed gas systems, both of which are quasi-free water droplet systems. Likewise, Figure 6-8 suggests that the solid wall component of the memory effect is expressed in the *difference in the gaps* between the memory and the non-memory quiescent water in the stainless-steel cell and between the memory and the non-memory quasi-free water droplet samples. It appears that the solid wall component (with the interfacial gaseous states as the entity of the “impurity” that can be “imprinted” to the solid walls) and the bulk supersaturation component (with or without nanobubbles in the bulk water) are comparable in size, albeit the solid wall component is the larger one.

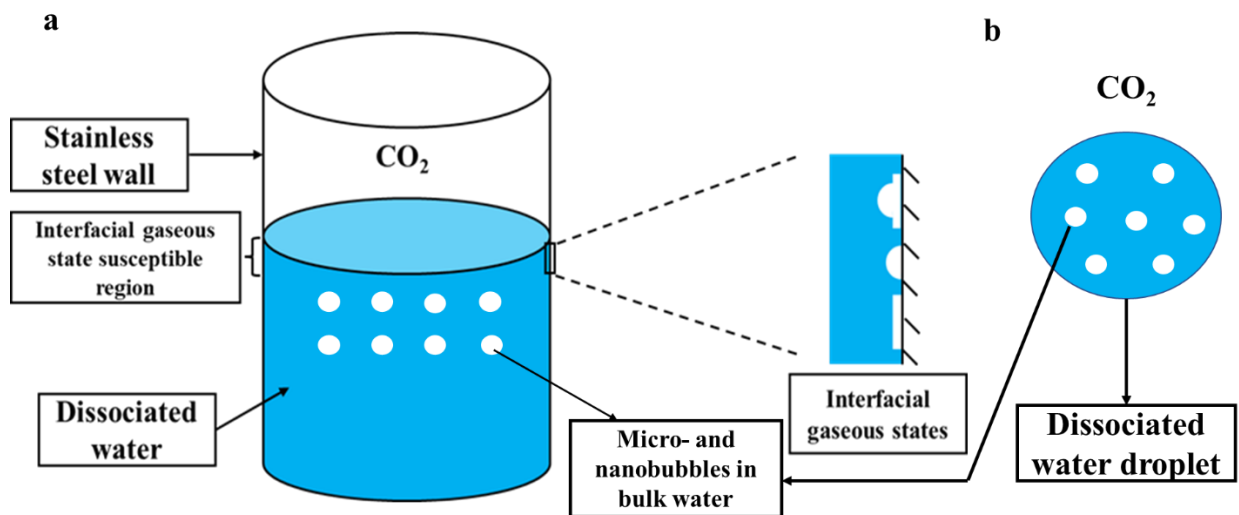


Figure 6-10 Illustration of the dual mechanism of the memory effect.

a) Where a solid wall is present, microbubbles and nanobubbles may form in the bulk water together with the interfacial gaseous states on solid walls. b) When a solid wall is absent, interfacial gaseous states do not form and only microbubbles and nanobubbles may form in the bulk water.

6.5 Conclusions

In this study, we investigated the CO₂ hydrate nucleation kinetics on both dissociated quasi-free water droplets and quiescent water surface in the presence of a stainless-steel wall using the linear cooling ramp method. The nucleation curves of both systems were derived and compared to those derived from the fresh quasi-free water droplets and the fresh quiescent water in the presence of a stainless-steel wall. Several existing hypotheses for the memory effect were examined and we concluded that both the interfacial gaseous states and the bulk supersaturation (with or without nanobubbles in the bulk water) contributed to the memory effect. Finally, the contributions of the solid wall component (with the interfacial gaseous states as the entity of the “impurity” that is “imprinted” to the solid walls) and the bulk supersaturation component (with or without nanobubbles in the bulk water) to the memory effect were estimated from the nucleation curves, and we found that the solid wall component and the bulk supersaturation component were

comparable in size, albeit the former was the larger one.

6.6 Summary and Relationship to Chapters that Follow

In this chapter, we detected the memory effect of gas hydrate nucleation in dissociated quasi-free water droplet and dissociated bulk water surface from derived nucleation curves. After examining the existing hypotheses, a new mechanism explaining the memory effect was proposed—the bulk guest supersaturation (with or without nanobubbles) and the interfacial gaseous states contribute concurrently to the memory effect. This new hypothesis not only sheds light on this long-standing mystery but also has important industrial implications. On the one hand, the memory effect might cause the fast reformation of methane hydrate in pipelines when the released methane from the dissociation of methane hydrate sediments is transported with dissociated water and should be avoided. On the other hand, the memory effect can be utilized for faster gas storage in the hydrate form (acceleration of hydrate nucleation kinetics). Another way to accelerate hydrate nucleation kinetics is to disperse water into droplets and enhance guest-water contact. In the next chapter, we will investigate the effect of a water-in-air dispersion on hydrate nucleation kinetics and the synergistic effect between this dispersion and different additives in enhancing hydrate nucleation and crystal growth kinetics.

7 Kinetic Promotion of Gas Hydrate Formations Using Dispersions

In this chapter, we will investigate the effect of dry water dispersions and additives on CO₂ hydrate formation kinetics. Their effect on hydrate nucleation and crystal growth kinetics will be decoupled and analyzed separately. On the basis of literature report, this chapter innovatively adds additives to dry water dispersion, aiming to further enhance hydrate formation kinetics. The results shown in this chapter will make contributions to the application of gas hydrates in gas storage by realizing faster hydrate nucleation kinetics and higher gas uptake capacities. This chapter also advances carbon capture and sequestration in the hydrate form and contributes positively to the relief of the greenhouse effect, a main environmental concern nowadays.

7.1 Introduction

Gas hydrates, also known as clathrate hydrates, are non-stoichiometric compounds that form when gas molecules are trapped within cages formed by hydrogen bonding between water molecules. Under specific thermodynamic conditions, many gas molecules, including methane, carbon dioxide, propane, and hydrogen, can form gas hydrates of different crystal structures with water. In addition, other non-polar liquid molecules like tetrahydrofuran or cyclopentane and quaternary ammonium salts like tetrabutylammonium bromide can form clathrate crystals or semi-clathrate crystals with water, respectively. As a result, gas hydrates are often referred to as clathrate hydrates.

Gas hydrates have received extensive attention from researchers due to their two-fold characteristics. On the one hand, gas hydrates can form from multi-phase flow in oil & gas flowlines under low temperature and high-pressure conditions. The gradually growing hydrate crystals can aggregate into a hydrate plug that adheres to the inner wall of the flow lines, thereby blocking the flow lines and causing flow assurance problems (Sloan Jr 2003, Sloan 2010, Koh, Sloan et al. 2011, Zerpa, Salager et al. 2011). On the other hand, gas hydrates have many promising

applications. Methane hydrate, which naturally forms in seafloor (Zatsepina and Buffett 1997, Suess, Torres et al. 2001) and permafrost (Max 2003), is located at the bottom of the energy pyramid and is estimated to have a reservoir size of around 10^{15} m³. Upon dissociation, 1 m³ of methane hydrate can release about 164 m³ of methane and 0.87 m³ of liquid water (Max and Johnson 2018). The large methane content in the form of hydrate and the huge scale of methane hydrate reservoir makes methane hydrate a potential energy resource. Clathrate hydrates can also be used for gas storage, like H₂ (Veluswamy, Kumar et al. 2014) and CO₂ (Wang, Teng et al. 2021). The principle can be applied to CO₂ capture and sequestration (CCS) in the form of CO₂ hydrate (Cao, Wang et al. 2022). Moreover, clathrate hydrates can be used for seawater desalination (Kang, Linga et al. 2014, Khan, Peters et al. 2019) due to the exclusion of electrolytes from clathrate hydrate crystals during the clathrate hydrate formation process. Finally, by taking advantage of different thermodynamic conditions for the formation of clathrate hydrates of different guest gases, it can also be used for separations of gas mixtures (Cha, Lee et al. 2010, Eslamimanesh, Mohammadi et al. 2012).

The comprehensive consideration of the hazards and applications of gas hydrates requires maximizing or minimizing gas hydrate formation, depending on the needs. The first step of gas hydrate formation is nucleation, which refers to the transition from a supersaturated guest aqueous solution to a stable clathrate hydrate nucleus. The duration of the guest aqueous solution in the metastable supersaturated state before the phase transitioning to a thermodynamically stable nucleus is the subject of nucleation kinetics, which is often quantitatively characterized by induction time. Due to the mass transfer (Boufares, Provost et al. 2018) and heat transfer limitations (Ke, Svartaas et al. 2019), kinetics of clathrate hydrate nucleation in a bulk phase is usually very slow, which hinders the large-scale applications of gas hydrates. Therefore, promoting hydrate nucleation kinetics has been a long-standing challenge. Several methods have been employed to accelerate clathrate hydrate nucleation kinetics, including mechanical stirring (Zhang, Shi et al. 2022), the addition of chemical additives such as surfactants (Karaaslan and Parlaktuna

2000, Zhong and Rogers 2000, Ganji, Manteghian et al. 2007, Zhang, Lee et al. 2007, Okutani, Kuwabara et al. 2008) and amino acids (Liu, Chen et al. 2015, Prasad and Sai Kiran 2018, Bhattacharjee and Linga 2021, Li, Sun et al. 2021), and ionic liquids (Zare, Haghtalab et al. 2015, Lee, Shin et al. 2016, Tariq, Connor et al. 2016, Gupta, Mondal et al. 2023). Despite the effectiveness of these measures, accompanying problems such as toxicity, foaming, cost, and environmental concerns cannot be neglected.

Gas hydrate nucleation, unlike homogeneous nucleation in the bulk phase, occurs heterogeneously at the guest gas-water interface due to the low solubility of the guest gas in water. This results in the highest guest supersaturation at the interface, creating the highest driving force for nucleation. Therefore, the size of the interfacial area largely determines the probability of heterogeneous nucleation and the nucleation rate of the system as a whole. A larger guest-water interfacial area increases the nucleation probability and promotes earlier hydrate formation. The introduction of a foreign surface, such as a solid wall, also plays a significant role in increasing gas hydrate nucleation kinetics (Maeda 2016, Wei and Nobuo 2023) by providing more potential nucleation sites and lowering the activation energy barrier in the Arrhenius form. Hence, solid surfaces can be purposefully introduced to accelerate hydrate nucleation kinetics.

Colloidal systems with a dispersed phase in a continuous phase massively increase the total interfacial area in the system. For example, a good dispersion of Snomax, a commercial snow inducer, in water has been shown to promote ice nucleation kinetics significantly (Zhang and Maeda 2022). Dry water, a water-in-air dispersion or aerosol with a free-flowing powder appearance, has been used to effectively promote gas hydrate formation since 2008. Dry water is a Pickering dispersion in which partially hydrophobic nanosilica acts as the Pickering agent and disperses bulk water into small water droplets (of the size of μm) under vigorous blending conditions. The dispersed water droplets massively increase the total contact area between water and the guest gas. Dry water dispersions have been used as a kinetic hydrate promoter (KHP) to

shorten the induction time of methane hydrate nucleation under quiescent conditions and to increase gas storage capacity (Weixing Wang 2008, Carter, Wang et al. 2010). They have also been found to reduce the induction time of CO₂ hydrate nucleation (Zhang, Wang et al. 2022). The presence of dry water in CO₂ hydrate formation increases CO₂ gas consumption, maximum CO₂ uptake, and CO₂-to-hydrate conversion (Farhang, Nguyen et al. 2014).

To investigate the effect of dispersion on gas hydrate formation kinetics, we conducted clathrate hydrate formation experiments in dry water using a linear cooling ramp method. We used CO₂ as the guest gas for its relatively mild formation conditions compared to hydrocarbon guests and potential applications in CCS. We prepared dry water dispersions in the presence and absence of different additives (SDS and seven nucleation promoters) and examined their optical images using an optical microscope. In a linear cooling ramp experiment, we used a rapid pressure drop as an indicator of CO₂ hydrate nucleation, calculated the supercooling when CO₂ hydrate nucleation occurred, and compared it among the samples that contained different additives and the blank sample (bulk water and bulk SDS solution baseline). According to the pressure profile, we calculated the CO₂-to-hydrate conversion ratio and normalized the CO₂ uptake capacity based on the compressibility equation of state, from which the CO₂ hydrate crystal growth kinetics can be inferred.

The following are the key findings of this study: (1) Dry water can only maintain its stability at a small doping dose of nucleation promoters. (2) Dry water prepared in this work has a droplet size of hundreds of micrometers. (3) Dry water dispersion was found to decrease the supercooling requirement for CO₂ hydrate nucleation. This effect was not weakened after the addition of nucleation promoters. (4) SDS has no promoting effect on CO₂ hydrate nucleation kinetics, regardless of whether water is dispersed or non-dispersed. (5) SDS and nucleation promoters both promoted CO₂ hydrate crystal growth, manifested as an increased CO₂-to-hydrate conversion ratio and the CO₂ uptake capacity. (6) Promotion of CO₂ hydrate crystal growth did not depend on the

concentration of the nucleation promoters present in dry water over the limited range that preserved its stability. (7) Dispersion and additives can be combined together to realize the faster and more storage of CO₂ in a hydrate form.

7.2 Material and methods.

CO₂ (99.5%) was supplied by Linde Welding and Supplies. Milli-Q water was purified from a Millipore unit (18.2 M Ω). The seven nucleation promoters used in this work are: AgI (purchased from Sigma-Aldrich and used as received), Kaolinite (pure grade, purchased from Fisher Scientific), 2-hydroxyethyl cellulose (molecular weight of 90,000 and 1300000, purchased from Sigma-Aldrich and used as received), cholesterol (99% purity, purchased from Sigma-Aldrich and used as received), Snomax (Snomax International Company) and steroid (progesterone, purchased from Sigma-Aldrich and used as received, purity 99%). The Pickering agent used for preparing water-in-air dispersion (dry water) is HDK H18 nano-silica (partially hydrophobic, supplied by Wacker Chemical Corporation). Sodium dodecyl sulfate (SDS), ≥ 98.5% (GC), was purchased from Sigma-Aldrich and used as received.

A bath (model: FP50, Julabo) was used to generate a linear cooling ramp with 95% ethanol as a coolant. A digital thermometer (model: #119, BIOS company, resolution: 0.1 K) was used for temperature calibrations. A kitchen blender (model: 58240C, 2500 rpm, Hamilton Beach) was used to prepare dry water dispersions. A high-pressure non-stirred reactor (series: 4790, Parr instrument company, volume: 100 mL) was used for CO₂ hydrate formation. An upright microscope (NIKON H6001) coupled with a 4X lens was used to obtain optical images of dry water dispersion. Two webcams (C920x HD Pro) from Logitech were used to record pressure readings and temperature readings during a cooling ramp experiment, respectively.

Preparation of dry water dispersion in the presence and absence of additives

To prepare the dry water in the absence of additives, 47.5 g of milli-Q water and 2.5 g of H18

hydrophobic nano-silica were weighed by an analytical balance. This equals to the mass ratio of nano-silica to water of 5:95, which is used by most of research groups (Weixing Wang 2008, Carter, Adams et al. 2010, Carter, Wang et al. 2010, Hu, Ye et al. 2011, Farhang, Nguyen et al. 2014, Park, Shin et al. 2015). Then the mixture was transferred into a blender and was blended at a speed of 2500 RPM for 90 s. The schematic illustration of the preparation of dry water dispersion is shown in Figure 7-1a). After vigorous blending of the mixture of hydrophobic nano-silica and water, the final product is powder-like dry water, which can flow freely from the narrow channel of a funnel, as indicated in Figure 7-1b) and c), respectively.

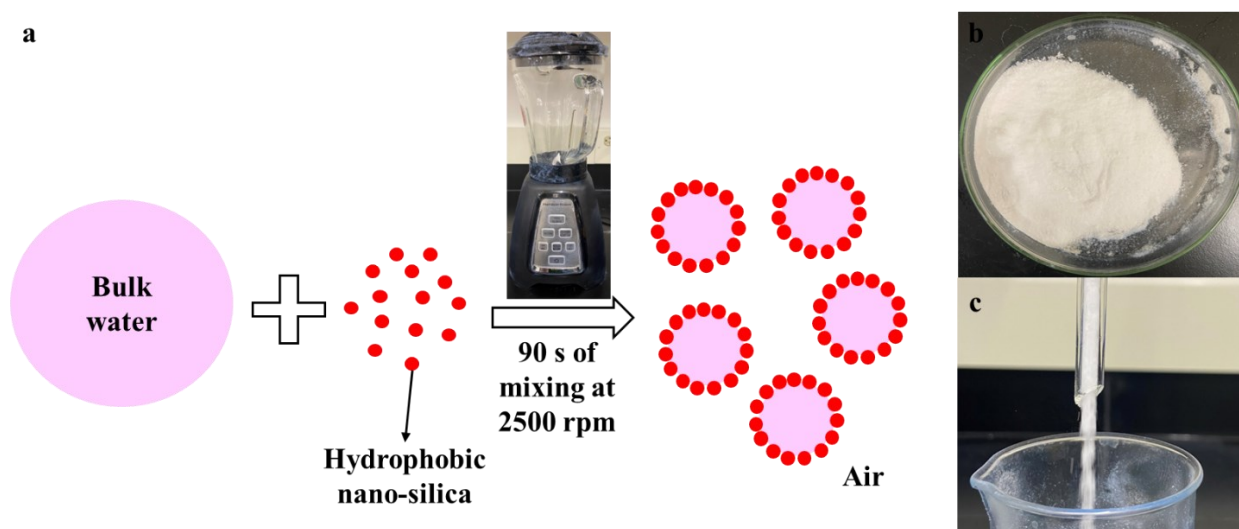


Figure 7-1 Schematic illustration of the preparation of dry water dispersions and example photographs of powder-like and free-flowing dry water dispersion.

To prepare the dry water dispersion in the presence of nucleation promoters, a fixed amount of nucleation promoters and H18 hydrophobic nano-silica were firstly blended for 30 s to make the mixing uniform. After that, the mixture was blended with milli-Q water at 2500 rpm for 90 s also in a mass ratio of 5: 95 (nano-silica to water). The appearance of dry water in the presence of nucleation promoters is identical to that of pure dry water, as seen in Figure 7-1.

Preparation of dry water dispersion made from SDS solution

Here, we referred the dry water dispersion made from SDS solution to as DW (SDS). DW (SDS) is a SDS solution droplet-in-air dispersion formed by mixing SDS solution, H18 hydrophobic nanosilica and air in a blender. Since surfactant has been classified as a kinetic hydrate promoter, we intended to prepare DW (SDS) to see if CO₂ hydrate nucleation kinetics and gas uptake capacity can be improved compared to DW. To prepare DW (SDS), we firstly dissolved SDS into milli-Q water to prepare 0.03 wt% SDS aqueous solution. Then 47.5 g of SDS solution and 2.5 g of H18 hydrophobic nano-silica were weighed and vigorously blended at a speed of 2500 RPM for 90 s, the same as the preparation procedure of dry water. The appearance of final product, DW (SDS), is identical to that of pure dry water.

Critical content of additives without destabilizing dry water (DW) dispersion

We used seven nucleation promoters of ice for the current study (Snomax, Cholesterol, Progesterone, Cellulose of two different molecular weights, Kaolinite and AgI), which we previously investigated for the nucleation of ice (without any dry water) and found to exhibit promoting effects (Zhang and Maeda 2022). Before investigating the kinetics of CO₂ hydrate formation in dry water dispersion in the presence of nucleation promoters, we first investigated the stability of dry water in the presence of these nucleation promoters. We chose four concentrations of additives: 0.01 wt%, 0.1 wt%, 1 wt% and 10 wt%, by mass. The results are summarized in Table 7-1.

Table 7-1 The relationship between the morphology of final products and the content of nucleation promoters in 100 g of dry water

| | 0.01 wt% | 0.1 wt% | 1 wt% | 10 wt% |
|----------------------|-----------|-----------|--------------|------------|
| Snomax | Stable DW | Stable DW | Mousse-like | - |
| Cholesterol | Stable DW | Stable DW | Unstable DW* | - |
| Progesterone | Stable DW | Stable DW | Stable DW | Stable DW |
| Cellulose (MW90000) | Stable DW | Stable DW | Stable DW | Paste-like |
| Cellulose (MW130000) | Stable DW | Stable DW | Stable DW | Paste-like |
| Kaolinite | Stable DW | Stable DW | Unstable DW* | - |
| AgI | Stable DW | Stable DW | Unstable DW* | - |

*: a lot of free water left after the preparation

From Table 7-1, it can be seen that for all nucleation promoters eventually destabilized dry water at high doses. All nucleation promoters destabilized dry water over the doping of 10 wt% - although some dry water could be produced, a lot of visible free water remained at the bottom of the blender after the blending. Based on these observations, therefore, we selected 0.01 wt % and 0.1 wt % doping of nucleation promoters for our investigation of their synergistic effect with dry water on the kinetics of CO₂ hydrate formation.

CO₂ hydrate formation in dry water dispersion using a linear cooling ramp experiment

Potential thermal lag is expected to exist between a dry water dispersion and the coolant during a linear cooling ramp. Therefore, we first carried out a temperature calibration for this system. Here we placed 20 g of dry water into the reactor and put the reactor inside the chiller under the atmospheric pressure. Then the probe of a digital thermometer was inserted into the dry water dispersion and the temperature reading was recorded every 5 mins. The programmable bath was cooled at the same rate as the linear cooling ramp during the experiments with CO₂, 0.001 K/s.

After the temperature calibration, for a CO₂ hydrate formation experiment, 20 g of dry water dispersion was placed inside the Parr high-pressure reactor that was connected to a high-pressure

gas lines, as shown in Figure 7-2a). The top lid of the Parr reactor was closed for sealing and then Valve 1, the ball valve and the inlet valve were opened while Valve 2 was closed. Then we used a regulator to supply CO₂ gas from a gas cylinder to the Parr reactor. When the pressure inside the Parr reactor reached 3 MPa (435 psi), the Swagelok Snoop was applied to each connection to check for any leak. After confirming an absence of leak, the ball valve was closed to isolate the reactor from the high-pressure gas line and Valve 2 was opened to release pressure inside the gas lines to atmospheric pressure. Then, the reactor was detached from gas lines and transferred to the programmable bath. We left the reactor in the bath for 15 mins before the start of a CO₂ hydrate formation experiment. This was to 1) equilibrate the temperature of the sample with the temperature of the coolant (95% ethanol) and 2) make sure CO₂ dissolves in the water droplets. Two webcams connected to a computer were set to record the images of pressure readings of the reactor and temperature readings of the chiller every 5 mins for analysis, after which the linear cooling ramp experiment was started at a constant rate of 0.001 K/s. The starting temperature was 282 K which was above the phase boundary of CO₂ hydrate at 3 MPa and the ending temperature was 246 K, low enough to guarantee CO₂ hydrate formation. The schematic illustration of the setup is shown in Figure 7-2b).

For comparison, a CO₂ hydrate formation experiment was also carried out in a 20 g of bulk milli-Q water and 20 g of bulk SDS solution (the same amount as dry water dispersion) using the same cooling rate, 0.001 K/s.

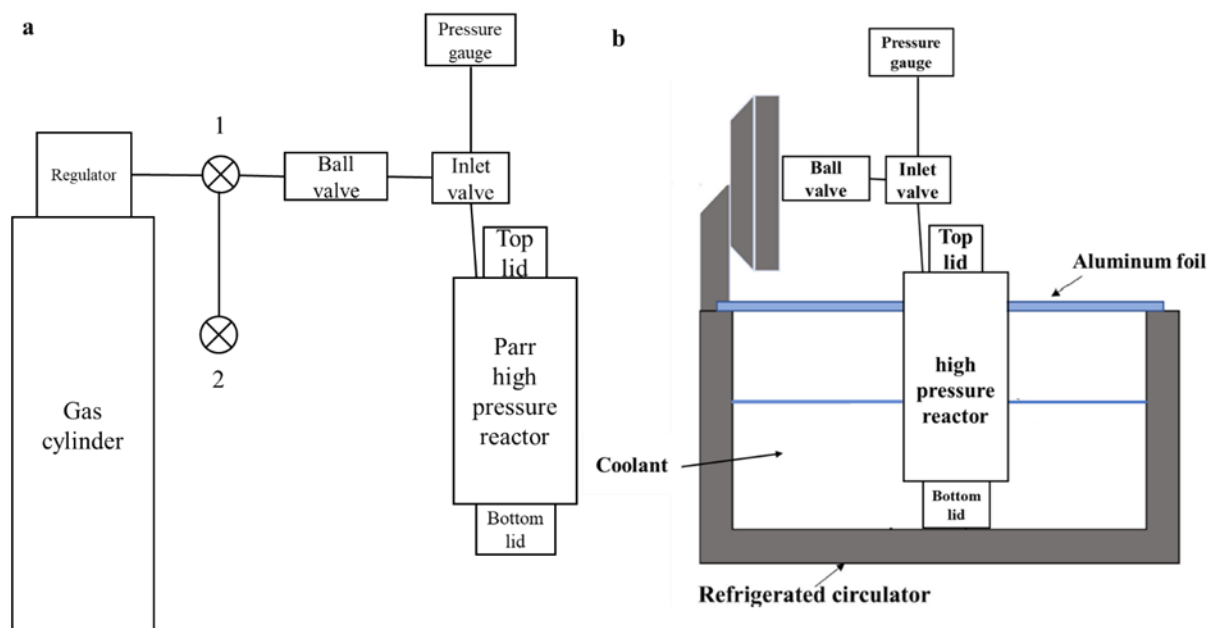


Figure 7-2 Schematic illustration of the gas line design and experimental setup used for inducing CO₂ hydrate formation in a linear cooling ramp.

7.3 Results

Morphology of dry water dispersion

Microscopic images of DW, DW (SDS), DW doped with different doses of nucleation promoters were shown in Figure 7-3. It can be seen that the size of dry water dispersion was larger than 100 μm . This result was different from the result reported in literature that dry water dispersion has a size of tens of μm at the same mass ratio of water to nanosilica (95g of water:5g of nanosilica) (Carter, Adams et al. 2010, Carter, Wang et al. 2010, Park, Shin et al. 2015). The reason causing this difference lies in the mixing speed of the blender which was supposed to have a significant influence on the size distribution of dry water dispersion. Figure 7-3a) showed that pure dry water has a uniform droplet size. With the addition of SDS, size of solution droplet becomes larger. This is because when SDS is present, surface tension of water was lowered and the dispersive property of dry water decreases. When nucleation promoter (Snomax) was doped in

dry water, size of water droplet becomes more irregular, as indicated in panel c. Among all four samples, neither free water nor excess nanosilica was observed, demonstrating the stability of dry water dispersion.

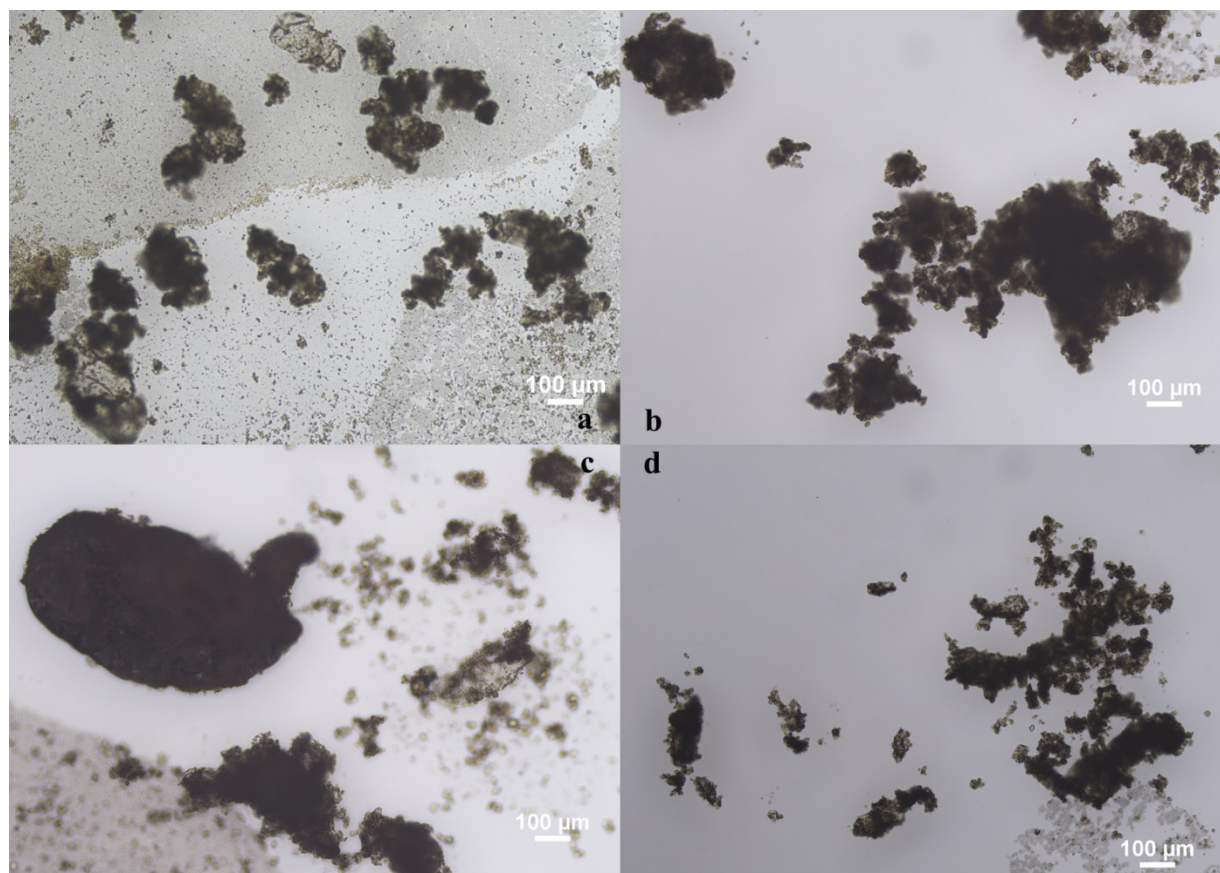


Figure 7-3 Microscopic images of DW (panel a), DW (SDS) (panel b), DW doped with 0.01 wt % of Snomax (panel c) and DW doped with 0.1 wt % of Snomax (panel d).

Kinetics of CO₂ hydrate formation in dry water dispersion

The doping amount of the nucleation promoters in the dry water was kept low to keep the dry water stable. Therefore, we first used a nucleation promoter concentration of 0.1 wt% when prepared dry water with nucleation promoters (47.5 g of water + 2.5 g of nano-silica + 0.05 g of nucleation promoters). As detailed in the last section, 20 g of dry water dispersion or bulk liquid

phase (either water or SDS solution) was placed into the reactor for CO₂ hydrate formation. Since we used an isochoric and linear cooling condition, a sudden pressure drop is used as the indicator of CO₂ hydrate nucleation because it will consume large amounts of CO₂. From Figure 7-4, it can be seen that for all dry water samples with and without nucleation promoters, at the initial stage (induction period), pressure decreased slowly with time, this is because of the compressibility *Equation of State (EoS)*. At a certain moment, pressure showed an abnormal decrease, confirming the nucleation of CO₂ hydrate. After CO₂ hydrate nucleation and crystal growth, fast pressure drop ceased and the slope of pressure drop restored to that during the induction period. In contrast, for bulk water sample and bulk SDS solution sample, a different pattern appeared. At the initial stage, gas pressure gradually decreased. After hydrate nucleation, pressure only decreased at a faster rate without showing a dive. Compared with dry water samples, bulk water sample had the longest induction period and lowest gas consumption. These two points will be analyzed later in more detail.

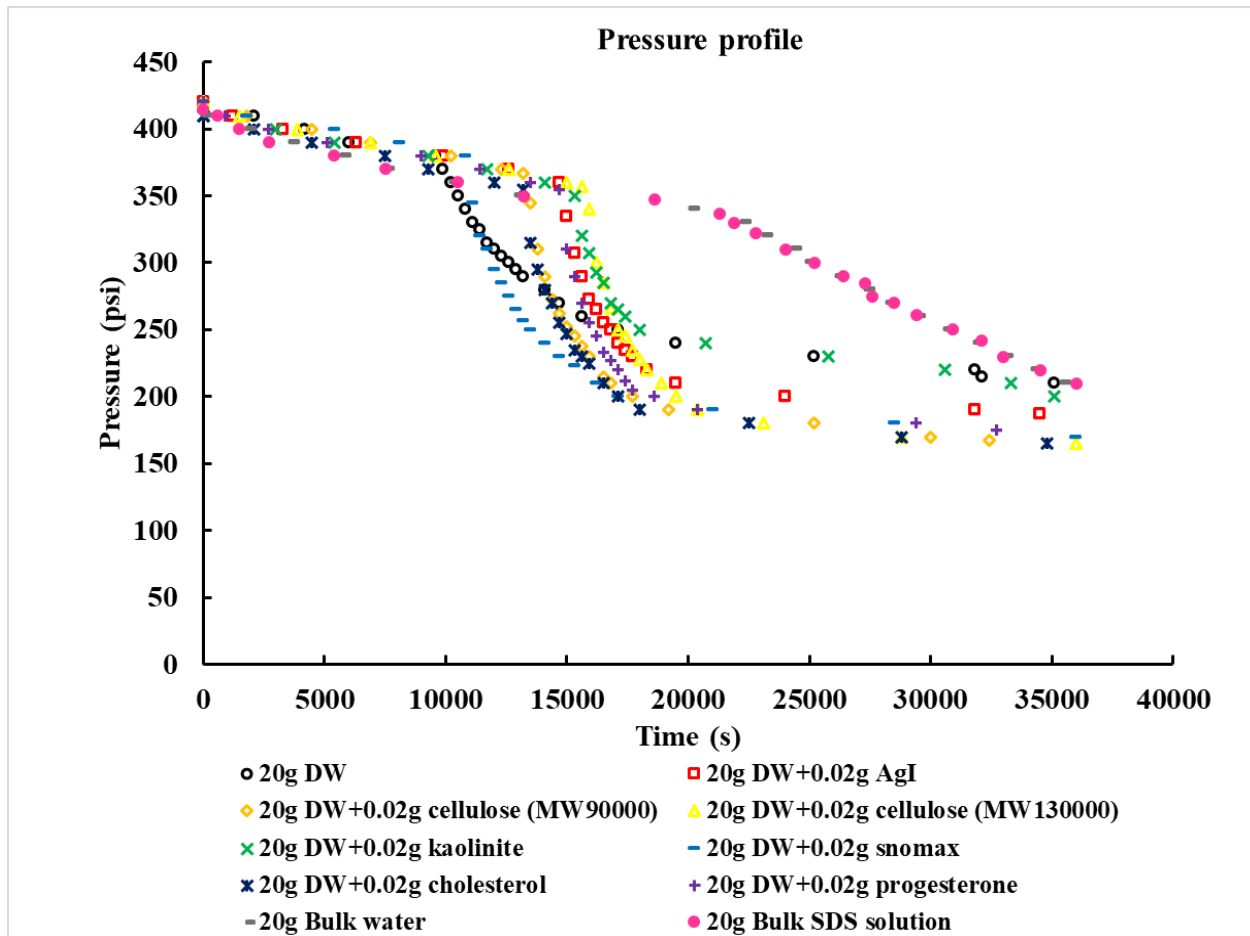


Figure 7-4 Pressure profiles during a linear cooling ramp experiment under an isochoric condition. All linear cooling ramps were from 282 K to 246 K at a constant rate of 0.001 K/s. The starting pressure was around 2.86 MPa (415±5 psi) to ensure CO₂ will remain above its boiling point over the entire cooling ramp.

To illustrate the effect of dry water and the synergy between dry water and additives (SDS or nucleation promoters) on the CO₂ hydrate nucleation kinetics, we calculated the lag time, defined as the time that the sample is in a metastable state, and the supercooling when the nucleation occurred. The supercooling was calculated by multiplying the lag time and the sample true cooling rate so supercooling increases linearly with lag time. After applying the temperature calibration table, it was found that sample has a same cooling rate as the coolant of 0.001 K/s, indicating the

thermal lag between sample true cooling rate and coolant nominal cooling rate is negligible. For bulk water sample and bulk SDS solution sample, phase equilibrium temperature of CO₂ hydrate at 420 psi was determined to be 280.2 K, determined by interpolating “pure water” data points in Fig.11 of the ref (Zebardast and Haghtalab 2022). In this study, SDS was treated as a kinetic hydrate promoter that does not shift the phase equilibrium temperature of CO₂ hydrate. Therefore, we applied the phase diagram of CO₂ hydrate formation in pure water to determine the supercooling in bulk water and bulk SDS solution sample. In contrast, it should be noted that dry water was reported to have a thermodynamic promoting effect on methane hydrate (Park, Shin et al. 2015) and CO₂ hydrate formation (Zebardast and Haghtalab 2022). To rule out the thermodynamic effect of dry water on hydrate phase equilibrium, we used the phase diagram of CO₂ hydrate of dry water reported in ref (Zebardast and Haghtalab 2022) (Fig.9) to calculate the supercooling of CO₂ hydrate nucleation in dry water in the presence and absence of nucleation promoters and dry water made from SDS solution. Each sample was measured for two times to calculate the average supercooling and standard deviation. The results were shown in Figure 7-5.

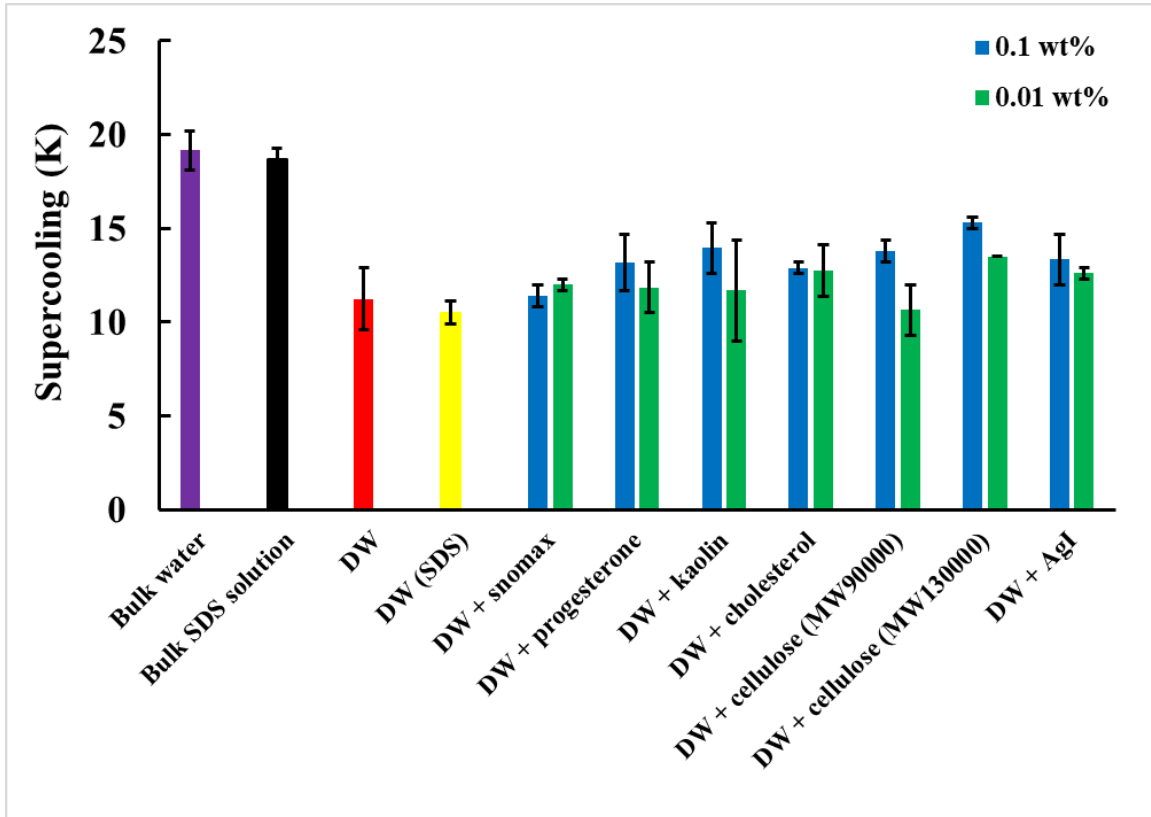


Figure 7-5 Histogram of average supercoolings when CO₂ hydrate nucleated in a bulk water phase (purple bar), in a bulk SDS solution phase (black bar), in DW in the absence of nucleation promoters (red bar), in DW made from SDS solution (yellow bar) and in DW in the presence of nucleation promoters but different doses (blue bars for 0.1 wt% and green bars for 0.01 wt%). Nucleation was detected by an abrupt pressure drop as seen from the pressure profile. The supercoolings were calculated by multiplying the lag time and the true cooling rate of the sample, 0.001 K/s. The error bars represent the standard deviation from the average value.

From Figure 7-5, it can be seen that bulk water sample and bulk SDS solution sample have comparable but the highest supercooling, suggesting that CO₂ hydrate nucleation in these two samples is the most difficult. Although SDS is a surfactant and is capable of decreasing water surface tension thus promoting gas hydrate formation, our results showed that this effect is not significant at all. In contrast, the dispersed water in the form of dry water is much more prone to

CO₂ hydrate nucleation than the bulk one, as indicated by the lower supercooling. The comparison between dry water made from pure water and SDS solution still showed no additional promoting effect caused by SDS on CO₂ hydrate nucleation kinetics, even though the water is dispersed.

It can also be seen from Figure 7-5 that the enhanced water-gas contact area plays a more important role in promoting CO₂ hydrate nucleation than the lowered water surface tension. The mass transfer limitation renders the nucleation of gas hydrate occurs at the guest-water interface. Therefore, the enhanced interfacial area increases the volume of water supersaturated with CO₂ and the number of heterogeneous nucleation sites. Although the nucleation rate cannot be determined by our setup, it is anticipated that CO₂ hydrate has a higher nucleation rate in dry water than in bulk water. On the other hand, it was reported that surfactants effectively lowered the guest-aqueous interfacial tension and increased the effective solubility of the guest in water (the solubility of the guest to the interior of the micelles) (Kalogerakis, Jamaluddin et al. 1993, Karaaslan and Parlaktuna 2000, Zhong and Rogers 2000, Lin, Chen et al. 2004, Ganji, Manteghian et al. 2007, Okutani, Kuwabara et al. 2008, Kumar, Bhattacharjee et al. 2015) and thus promoting gas hydrate formation kinetics. Fan et al. investigated the kinetic promotion of dry water made by SDS solution (the SDS-DS system in their publication) (Fan, Yang et al. 2014) on methane hydrate formation and found the induction time can be shortened to 8.2 min under the condition of 5 MPa, 273.2 K. Based on the results shown in Figure 7-5, we inferred that this promoting effect is caused by dispersion rather than SDS. For dry water dispersions in the presence of nucleation promoters, the induction period fluctuates based on that of dry water samples in the absence of them and they all behaved better than the bulk water sample. From Figure 7-5, we observed that doping a little amount of nucleation promoters in dry water does not have a great influence on supercooling required for CO₂ hydrate nucleation. This indicated that although the addition of nucleation promoters does not ruin the promoting effect of dry water on CO₂ hydrate nucleation kinetics, they do not offer any additional promoting effect.

Based on the pressure profile shown in Figure 7-4, we calculated the CO₂-to-hydrate conversion and CO₂ uptake capacity normalized to per mole of water, as shown in Figure 7-6. CO₂-to-hydrate conversion was defined as the ratio of moles of CO₂ converted to hydrate to moles of CO₂ fed into the high-pressure reactor prior to the hydrate formation experiment, as shown in eq 7-1. CO₂ uptake capacity normalized to per mole of water was defined as the ratio of the moles of CO₂ enclathrated into the hydrate crystal to the moles of water, as shown in eq 7-2:

$$\eta = \frac{\Delta n}{n_{g,0}} \times 100\% = \frac{n_{g,0} - n_{g,t}}{n_{g,0}} \times 100\% \quad \text{eq 7-1}$$

$$NG_t = \frac{\Delta n}{n_w} = \frac{n_{g,0} - n_{g,t}}{n_w} \quad \text{eq 7-2}$$

Where η is the CO₂-to-hydrate conversion, Δn is the moles of CO₂ consumed because of hydrate formation (mol), $n_{g,0}$ is the moles of CO₂ fed initially (mol), $n_{g,t}$ is the moles of CO₂ in the reactor at the time t (mol), NG_t (mol/mol) is the normalized gas uptake at the time t and n_w is the initial moles of water (mol).

In this work the moles of CO₂ as feeding and at time t were calculated based on the compressibility equation of state, as shown in eq 7-3 and eq 7-4, respectively.

$$n_{g,0} = \frac{P_0 V_0}{z_0 R T_0} \quad \text{eq 7-3}$$

$$n_{g,t} = \frac{P_t V_t}{z_t R T_t} \quad \text{eq 7-4}$$

Where P_0 , P_t are pressure as feeding and at time t (psi) read from the pressure gauge, respectively. V_0 and V_t are the volume occupied by CO₂ as feeding and at time t (m³), respectively, which were calculated by subtracting the volume of the dry water dispersion (V_{DW}/m^3) or dry water CO₂ hydrate (V_H/m^3) from the total volume of the reactor (V/m^3). Volume of dry water dispersion before an experiment was measured using a measuring cylinder. It was reported that the conversion

from water to CO₂ hydrate caused an expansion by a factor of 1.234 volumetrically (Zhang, Wang et al. 2022). Therefore, the volume of dry water CO₂ hydrate was 1.234 times the volume of the dry water dispersion. For bulk water sample, we treated the gas volume in the reactor as a constant (80 cm³) because the hydrate film formed at the CO₂-bulk water interface does not cause a notable volume expansion. Z_0 and Z_t are compressibility factor of CO₂ as feeding and at time t, respectively, which were determined by a software named REFPROP developed by NIST. These factors are calculated by using a widely-used Helmholtz energy *EoS* proposed in 1996 (Span and Wagner 1996). R is gas constant 0.001206 m³·psi·K⁻¹·mol⁻¹. T₀ and T_t are absolute temperatures inside the reactor as feeding and at time t (K), respectively. Each sample was measured for two times to calculate the average CO₂-to-hydrate conversion and gas uptake capacity and their standard deviations.

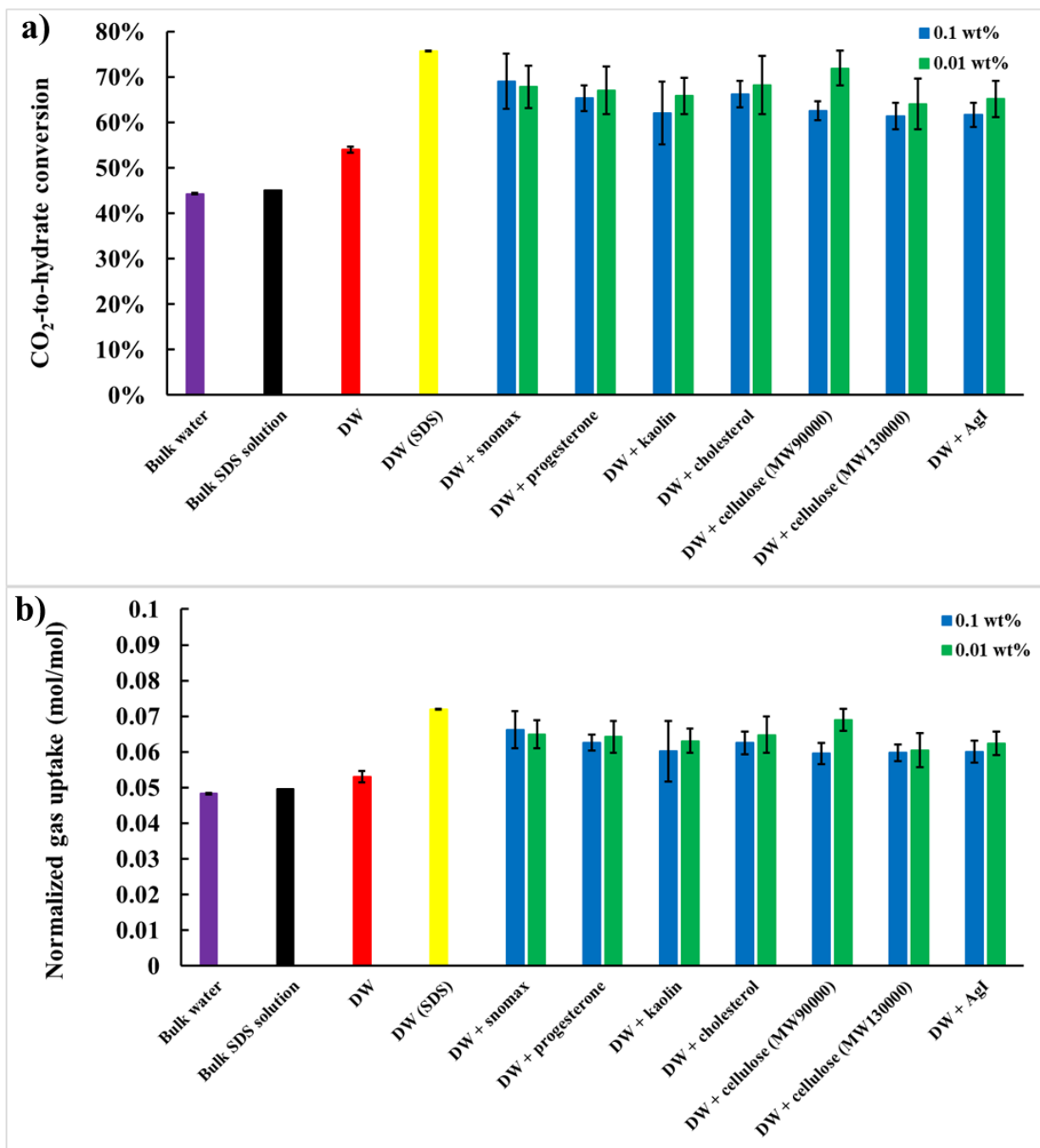


Figure 7-6 a) final average percentage of CO₂-to-hydrate conversion, b) final average gas uptake capacity (mol/mol) normalized to per mole of water. The error bars represent the standard deviations from the average value.

From Figure 7-6, it can be seen that bulk water sample and bulk SDS solution sample had the lowest CO₂-to-hydrate conversion and final gas uptake capacity. Dry water dispersion exhibited slightly better performance on these two kinetic parameters than bulk water/bulk SDS solution. The improvement is not as significant as reported in the literature (Weixing Wang 2008, Carter, Wang et al. 2010) which was speculated by the larger water droplet in the current work because of lower mixing speed of our blender. Surprisingly, DW (SDS) showed an obvious increase in CO₂-to-hydrate conversion and final gas uptake capacity, compared to DW, indicating the effective promotion of SDS on CO₂ hydrate crystal growth, which agrees with the finding of Kumar et al (Kumar, Sakpal et al. 2013). It should be noted that, however, this promotion effect is remarkable only when CO₂ hydrate forms in dry water, not the bulk phase. Unlike dry water, when CO₂ hydrate formation in bulk phase, it is limited to a small guest-water interfacial area. Therefore, the effect of SDS as a crystal growth promoter cannot be manifested. In the presence of nucleation promoters, CO₂ uptake kinetics was further improved compared to that in dry water without them, indicating the positive effect on CO₂ hydrate crystal growth by the introduction of additives. Addition of different types of promoters gave similar promoting effects on CO₂ uptake kinetics.

To illustrate the dependence of CO₂ hydrate formation kinetics on nucleation promoters' concentration, we reduced the concentration of nucleation promoters by a factor of ten and investigated the synergistic effect between the nucleation promoters of the lower concentration and the dry water on CO₂ hydrate formation kinetics. The results of supercooling when CO₂ hydrate nucleation occurred and the results of CO₂ uptake kinetics were also shown in Figure 7-5 and Figure 7-6, respectively. From Figure 7-5, it can be concluded that doping different amounts of nucleation promoters had an insignificant effect on the supercooling given the comparable values in the presence of 0.1 wt% and 0.01 wt% (47.5 g of water + 2.5 g of nano-silica + 0.005 g of nucleation promoters) promoters. Although nucleation has a stochastic nature, the supercooling required for CO₂ hydrate nucleation was reproducible, as indicated by the small error bars shown in Figure 7-5. From Figure 7-6, the reduction in the concentrations of the nucleation promoters

had no adverse effects on CO₂ hydrate formation kinetics, confirmed by the comparable levels of CO₂-to-hydrate conversion (the percentage of CO₂ converted into hydrates) and final normalized gas uptake capacity (the moles of CO₂ consumed per mole of water due to hydrate formation) in the presence of both higher and lower concentration of nucleation promoters. CO₂ hydrate formation in dry water in the presence of lower content of the nucleation promoters exhibited slightly higher CO₂-to-hydrate conversion and final gas uptake capacity than the higher content counterpart. All nucleation promoters, whether at high or low concentrations, had a synergistic effect with the dry water on CO₂ hydrate crystal growth kinetics, manifested by the improved CO₂-to-hydrate conversion and the final gas uptake capacity in comparison to dry water in the absence of nucleation promoters.

7.4 Discussion

We firstly examined the stability of the dry water dispersions in the presence of nucleation promoters. From Table 7-1 we can see that once the doping amount of the nucleation promoters was higher than a critical value, dry water lost its stability. This is because the surface of the partially hydrophobized silica nanoparticles does not have enough hydrophobicity to stabilize the dispersed water droplet. We know that dry water can only be stabilized by nanoparticles that have enough hydrophobicity. Therefore, when the doping amount of nucleation promoters increases, the incomplete coating of hydrophobic nanosilica on the surface of water droplets leads to the failure of preparation of dry water.

Compared to the CO₂ hydrate nucleation in bulk water, as expected, dry water significantly reduced the supercooling required for CO₂ hydrate nucleation, demonstrating the kinetic promotion of dry water. This is because the bulk water was dispersed by nanosilica to small droplets, which increased the CO₂-water contact area and the number of heterogeneous nucleation sites. However, the dissolution of SDS in water has no promotive influence on CO₂ hydrate nucleation kinetics, regardless of whether the water is dispersed or non-dispersed. This indicates

that the supersaturation of CO₂ in water was not significantly increased and the nucleation work was not noticeably lowered. After doping a small amount of nucleation promoters into dry water, supercooling showed little variation, indicating that they did not have a significant influence on the size of the water droplets, namely, the guest-water interfacial area that determines the hydrate heterogeneous nucleation kinetics. During the vigorous blending, as bulk water was dispersed and stabilized by the nanosilica, we speculate that these nucleation promoter particles were also dispersed within the water droplets because they were all insoluble in water. However, these dispersed solid particles do not promote CO₂ hydrate nucleation as a solid wall does. Similar observation has been noted by Cox et al. that methane hydrate nucleation was insensitive to the addition of a wide range of impurity particles (Cox, Taylor et al. 2018). That doping nucleation promoters into dry water does not contribute to the promotion on CO₂ hydrate nucleation is distinct from the finding that Snomax-in-water dispersion greatly promotes ice nucleation (Zhang and Maeda 2022) and the reason might be the different natures between ice and CO₂ hydrate heterogeneous nucleation. As far as freezing of water is concerned, it is a first-order phase transition of a single phase. Therefore, any foreign solid particles that increase water-solid interfacial area are expected to accelerating ice nucleation kinetics. While for CO₂ hydrate nucleation, it is associated with both water with a hydrophilic nature and guest phase with a hydrophobic nature. The surface of a solid particle is unlikely to be amphiphilic that simultaneously display a strong affinity for both species so as to promote hydrate nucleation. Especially for particles like kaolinite with a hydrophilic surface chemistry, local gas density is deficient at a hydrophilic surface (Nguyen, Nguyen et al. 2017), as reported by a previous molecular dynamic simulation study. Therefore, such a surface will not promote hydrate nucleation, even if the solid-water interfacial area is increased by the dispersion of nucleation promoters in water droplets.

The increased CO₂-to-hydrate conversion and the final gas uptake capacity in the dry water without the presence of SDS or nucleation promoters compared to the bulk water system can be

explained from a thermodynamic and a kinetic point of perspective. It has been reported that a hydrophobic surface promoted hydrate crystal growth (Casco, Rey et al. 2016) because of the local gas enrichment in the vicinity of that (Nguyen, Nguyen et al. 2017). In this study, the surface of the nanosilica was partially hydrophobic and the increased local guest density promoted more CO₂ conversion to hydrate, thus increasing the amount of CO₂ stored in the hydrate form. Another influential factor was the increased CO₂-water contact area, which enhanced the CO₂ diffusion into water droplet. We noted in Figure 7-6 that the promotion effect of dry water on CO₂ hydrate crystal growth was not that remarkable as the CO₂-to-hydrate conversion only increased by approximate 10%. With the addition of SDS and solid nucleation promoters in dry water, CO₂-to-hydrate conversion and the final gas uptake capacity showed a further obvious increase. This result implied that SDS has a promoting effect on CO₂ hydrate crystal growth and was consistent with the result reported by Verrett et al. that SDS has an influence on the mole fraction of hydrate former in the bulk liquid during hydrate crystal growth and increases hydrate growth rate (Verrett, Posteraro et al. 2012). Lo et al. proposed that the adsorption of surfactants to hydrate surfaces (Lo, Zhang et al. 2008) decreases hydrate interfacial tension. Aman et al. demonstrated that the surfactant encourages dendritic hydrate growth (Aman, Dieker et al. 2010) which is responsible for rapid hydrate crystal growth rate (Ohmura, Matsuda et al. 2005).

In dry water in the absence of nucleation promoters, CO₂ hydrate nucleates preferentially at the interface of CO₂-water contact and grows inwards the water droplet then forms a hydrate shell covering the surface of water droplet, as depicted by Park et al (Park, Shin et al. 2015). In dry water in the presence of nucleation promoters, although it is widely acknowledged that CO₂ hydrate forms at the CO₂-water interface and a hydrate film grows there, it is reported that when a foreign solid surface presents in the system, hydrate crystal grows towards the surface (Liang, Rozmanov et al. 2011, He, Mi et al. 2021), according to previous molecular dynamic simulations. This was speculated to be caused by the formation of guest bubbles from the guest-supersaturated solution (also a nucleation process) next to the surface which renders the surface being a source

(local reservoir) of guest molecules and facilitating the gas hydrate crystal growth toward the bubble and hence toward the surface. In the dry water dispersions, it is more prone for CO₂ to diffuse and establish supersaturation throughout the entire water droplets of micrometer scales stabilized by nanosilica, and thus forming nano- or microbubbles because 1) the increased CO₂-water contact area promotes CO₂ diffusion into water and 2) CO₂ itself has a higher solubility in water than methane which is the guest molecules used in Liang et al.'s simulation work (Liang, Rozmanov et al. 2011). Therefore, the nucleation promoters evenly dispersed in water droplets additionally promote CO₂ hydrate crystal growth. Finally, from Figure 7-6, we observed a dual increment of the CO₂-to-hydrate conversion and the final gas uptake capacity compared to a bulk water system.

7.5 Conclusions

In the current study, we investigated the stability of a water-in-air dispersion, dry water, in the presence of seven nucleation promoters. Results showed that dry water loses stability if the content of nucleation promoters exceeds a critical value. We examined the morphology of dry water of different compositions. We also investigated CO₂ hydrate formation kinetics in dry water using a linear cooling ramp method. Supercooling, CO₂-to-hydrate conversion and gas uptake capacity was calculated and compared. It was found that CO₂ hydrate nucleation kinetics is promoted by dry water dispersion because of the massively increased interfacial area, as manifested by the reduction of supercooling. The presence of SDS showed no promotive effect on CO₂ hydrate nucleation kinetics. The addition of nucleation promoters does not weaken the promoting effect of dry water on CO₂ hydrate nucleation kinetics because of the comparable size of water droplet. Based on the calculation of CO₂-to-hydrate conversion and gas uptake capacity, we found that SDS and nucleation promoters have a promoting effect on CO₂ hydrate crystal growth, which was attributed to the increase of the mole fraction of guest in SDS solution and additional hydrate crystal growth on the surface of nucleation promoter particles, respectively. The reduction of the concentration of nucleation promoters in dry water by one order of magnitude has

an insignificant effect on CO₂ hydrate gas uptake kinetic parameters, compared to the results obtained at higher concentrations.

After the comprehensive comparison of the effects of dispersion and additives (SDS and nucleation promoters), we concluded that dispersion mainly promotes CO₂ hydrate nucleation kinetics despite the inferior promotion on CO₂ hydrate crystal growth while the addition of additives only promotes CO₂ hydrate crystal growth. We have shown the synergistic effect between dry water and additives on accelerating CO₂ hydrate nucleation and enhancing CO₂ storage in a hydrate form, which is beneficial for the application of gas hydrate in CO₂ storage and sequestration and relief of the greenhouse effect.

7.6 Summary and Relationship to Chapters that Follow

In this chapter, we investigated the effect of dispersions and additives on CO₂ hydrate formation kinetics. It was found that doping a small amount of water-insoluble ice nucleation promoters did not destabilize dry water dispersions, despite the increasing water droplet size with the doping amount. Dispersion had a significant promoting effect on hydrate nucleation kinetics while the addition of additives promoted hydrate crystal growth, as confirmed by the decreased supercooling and increased CO₂-to-hydrate conversion ratio/gas uptake capacity, respectively. Dispersions and additives could work synergistically to realize faster and more gas storage in the hydrate form, which is beneficial for the application of hydrate technology in gas storage and transport and in carbon capture and sequestration.

By the end of this chapter, all completed research work has been reported. In the next chapter, key findings and main conclusions of this thesis will be summarized. Limitations of this thesis and future works will also be presented.

7.7 Appendix

SOP of the linear cooling ramp experiment

1. Use Teflon tape to seal all non-Swagelok connections. Three turns are enough.

2. Keep all valves closed.
3. Open the top lid of the high-pressure vessel, place 20 g of sample (for example, dry water dispersion) into the high-pressure vessel. Tighten the top and bottom lid with a wrench but do not overtighten.
4. Open the main valve of the gas cylinder which is the source of CO₂ gas. Open valve 1 (shown in Figure 7-2), ball valve and the inlet valve so that CO₂ gas can flow through gaslines into the high-pressure vessel. The pressure inside the vessel can be read from the pressure gauge. Clockwise rotate the regulator attached to the gas cylinder to increase the pressure. Upon pressurization to 1 MPa (145 psi), close the ball valve. Check if there is a leak in the Parr reactor. The leak can be known from the decrease in the reading of the pressure gauge. If there is a leak, proceed to 5.1. If there is no leak, proceed to 5.2.
 - 5.1 Use Swagelok Snoop (liquid leak detector) to detect each connection, including the top and bottom lids. After the leaking point has been detected, Counter clockwise rotate the regulator and then open ball valve and valve 2 to release pressure in the gaslines/reactors to atmospheric pressure. Then tighten the leaking points.
 - 5.2 Reopen the ball valve and pressurize the reactor to the target pressure. After reaching the target pressure (can be read from the pressure gauge), close ball valve to isolate the Parr reactor from the gaslines. Then counter clockwise rotate the regulator and open valve 2 to release the pressure inside gaslines to atmospheric pressure. Also close the main valve of the gas cylinder.
6. Use a wrench to detach the Parr reactor from other gas lines. Move the Parr reactor and immerse it inside the bath. Set the linear cooling program at a constant rate of 0.001 K/s. Capture the image of pressure reading and bath temperature by two webcams every 5 mins, respectively.
7. After the linear cooling ramp, open the ball valve to release the pressure inside the pressure vessel.
8. Pour the sample by opening the bottom lid, then rinse the reactor with water and dry it at the fume hood.

8 Conclusions, Limitations, and Future Works

8.1 Conclusions

The main conclusions and findings of the presented work were summarized in this chapter. In previous chapters, all concluding remarks were already discussed. Therefore, the aim of this chapter is to provide a concise review of the results and discussions that have been extensively discussed in previous sections. The key findings are summarized below.

8.1.1 Specific Surface Free Energy of Clathrate Hydrate

In Chapter 3, we used an experimental method for the determination of the specific surface free energy (γ_{sv}) of THF model hydrate. A smooth THF hydrate surface was prepared by mixing milli-Q water and THF in a sealed glass petri dish. THF hydrate formed in the petri dish was prevented from dissociation by an ice bath surrounding it. Surface tension values of homologous testing liquids were measured using a Wilhelmy plate method and validated by the literature value. Contact angle of homologous testing liquids on an ice and THF hydrate surface was measured for several times and the average value was calculated. By extrapolating the “Zisman” plot, the critical surface tension (γ_c) value of ice and THF hydrate was determined. The γ_c value of ice was found to be very similar to the value reported by Adamson et al. for the same homologous series. Then we used the measured γ_c value of THF hydrate and the γ_{sv} values of ice reported in the literature to deduce the γ_{sv} value of THF hydrate. The deduced γ_{sv} value of THF hydrate was somewhat lower than that of ice and in the range from 60.4 mJ/m² to 124.2 mJ/m², with an average of 92.3 mJ/m², which is consistent with the γ_{sv} value Kashchiev et al. estimated for methane hydrate. This result showed the hydrophilic nature of a clathrate hydrate surface.

8.1.2 Critical Shear Stress of Clathrate and Semi-Clathrate Hydrates on Solid Substrates

In Chapter 4, we investigated the shear adhesive strength of Structure II (sII) – forming

tetrahydrofuran (THF) hydrate and TBAB semi-clathrate hydrate on substrates with different hydrophobicity. Five solid substrates with the contact angle of water in air ranging from 0° to $117 \pm 3^\circ$ were prepared and used in this study. The critical shear stress (tangential adhesive strength) of THF hydrate was compared to that of tetrabutylammonium bromide (TBAB) semi-clathrate hydrate on the same five substrates. We also investigated the impact of a common Kinetic Hydrate Inhibitor (KHI), Polyvinylpyrrolidone (PVP), on the critical shear stress of these hydrates. The results showed that the critical shear stress diminished with heating and became unmeasurably small just below the dissociation temperature of the hydrates. This lowering of the critical shear stress with heating is in contrast to the normal adhesive strength between a gas hydrate particle and a solid surface that has been known to increase with heating due to capillary attractive action. Addition of PVP increased the critical shear stress of both THF clathrate hydrate and TBAB semi-clathrate hydrate on all substrates. Interestingly, the critical shear stress of the hydrates was higher on the hydrophobic substrates than on the hydrophilic ones. Our results imply that the quasi-liquid layer may have acted as an effective lubricant layer that reduced the static friction. Our findings may be valuable to flow assurance related to hydrate deposition on pipeline walls during hydrodynamic transport.

8.1.3 Nucleation Curves of Carbon Dioxide Hydrate in the Absence of a Solid Wall

In Chapter 5, we made a setup that determines the nucleation curves of structure I (sI)-forming CO_2 hydrate in a quiescent quasi-free water droplet supported by a bulk of liquid perfluoromethyldecalin under isobaric conditions. The results were compared to the nucleation rates of CO_2 hydrate in a quiescent water surface that was in direct contact with stainless-steel walls. We assessed the convergence of the nucleation curves with the increasing numbers of nucleation data, compared our results to the nucleation rates of methane/propane mixed gas hydrate in quiescent quasi-free water droplets and the nucleation rates of gas hydrates of various guest types in the presence of solid walls reported in the literature. We found (1) 400 nucleation

events are sufficient to construct a reliable nucleation curve; (2) addition of stainless-steel walls promoted the nucleation kinetics of CO₂ hydrate, as it did to methane /propane mixed gas hydrate, (3) the kinetic nucleation parameter was significantly lower than the theoretically expected value whereas the thermodynamic nucleation parameter was comparable to both the theoretically expected value and the experimentally determined value reported in the literature, (4) CO₂ hydrate nucleated over a substantially shallower supercooling range and had higher nucleation rates than methane /propane mixed gas hydrate, both in the presence and in the absence of a solid wall, indicating the effect of guest type on gas hydrate nucleation kinetics.

8.1.4 Mechanisms of the Memory Effect of Clathrate Hydrates

In Chapter 6, we used the same setup as Chapter 5 to investigate the mechanism of the memory effect of gas hydrate nucleation. We prepared dissociated quiescent quasi-free water droplets supported by a bulk liquid of perfluoromethyldecalin contained in a Teflon sample cell and dissociated quiescent water surface in direct contact with a stainless-steel wall. We used linear cooling ramp experiments under isobaric conditions to determine the nucleation curves of CO₂ hydrate in these samples that have a hydrate formation thermal history. Systematically comparing the nucleation curves of both freshly prepared samples and samples with a history of CO₂ hydrate formation in both the stainless-steel sample cell and the quasi-free water droplets, as well as the nucleation curves of methane – propane mixed gas hydrates previously reported, a coherent picture emerged. After the examination on existing hypotheses, we proposed a dual mechanism of the memory effect: solid wall contribution (interfacial gaseous states) and guest supersaturation contribution. The “amount” of the memory effect contributed by these two components was quantified for the first time based on the comparison of nucleation curves. The impurity imprinting component, with the interfacial gaseous states as the entity of the “impurity”, and the guest supersaturation component, with or without nanobubbles in the bulk water, are comparable in size, albeit the former is the larger one.

8.1.5 Kinetic Promotion of Gas Hydrate Formations Using Dispersions

In Chapter 7, we investigated the nucleation and crystal growth kinetics of CO₂ hydrate in dry water in the presence of an anionic surfactant, sodium dodecyl sulfate (SDS), and seven water-insoluble nucleation promoters. Our results showed that doping a small amount of nucleation promoters did not ruin the stability of dry water or weaken the promoting effect of dry water on CO₂ hydrate nucleation kinetics while showing a promoting effect on CO₂ hydrate crystal growth kinetics which was independent of the dose of the promoters in the dry water. SDS had no promoting effect on the nucleation kinetics of CO₂ hydrate, regardless of whether the water was dispersed or non-dispersed, but significantly promoted crystal growth kinetics of the CO₂ hydrate formation in dry water. We concluded that dispersion and the doping of the additives (SDS/nucleation promoters) promoted CO₂ hydrate nucleation and crystal growth, respectively. This synergistic effect can be utilized to store more CO₂ in a hydrate form at a faster rate, which is significant for the application of gas hydrate in carbon capture and sequestration and relief of the greenhouse effect.

8.2 Industrial contributions

In this thesis, a methodology for the determination of the specific surface free energy of clathrate hydrate that does not need high pressure to form was innovatively established, which can be referenced by academia/industry.

The shear adhesive strength between clathrate/semi-clathrate hydrate and substrates was characterized. Based on the results, we found that shear adhesive strength increases with supercooling and the addition of PVP. Therefore, in a multi-phase flow, the industry is advised to mitigate the possibility of adhesion of hydrate plugs on the inner walls of pipelines by heating the susceptible sections locally, such as valves, because of the lower local temperature caused by the Joule–Thomson effect. Also, the kinetic hydrate inhibitors (KHIs) should be used with caution in oil & gas pipelines, especially at deep supercooling conditions, because we have shown the

detrimental effect of them on hydrate-substrate adhesion once KHIs fail to function.

The investigation on CO₂ hydrate nucleation kinetics illustrated the major influence of the guest type and a solid wall. The quantification of nucleation rates helped the academia understand the kinetics of gas hydrate nucleation. With the baseline of CO₂ hydrate nucleation kinetics established in this work, the industry is advised to compare the nucleation rates of CO₂ hydrate across systems of different scales and complexities (stirring, additives, solid walls) so that the nucleation rates of CO₂ hydrate can be maximized from the perspective of the application of CO₂ hydrate. On the other hand, although the guest employed here is CO₂, methane hydrate nucleation kinetics in a gas-dominant flow (a realistic model of the quasi-free water droplet system) can be qualitatively inferred according to the results shown in this work. That is, the methane hydrate nucleation curve is anticipated to shift to a higher supercooling range and have a lower nucleation rate compared to CO₂ hydrate. Our results for CO₂ hydrate indicate the highest temperature of methane hydrate nucleation in a methane-dominant flow system. If the industry can maintain the temperature of pipelines comparable to this critical temperature, flow assurance problems due to methane hydrate formation will not occur.

The elucidation of the mechanism of the memory effect contributes positively to the industry. Since the interfacial gaseous states are believed to be a factor causing the memory effect and different solid walls should have varied potency of forming such interfacial gaseous states, the industry might find appropriate solid walls so that the size of the memory effect can be either increased or decreased. For example, when the released methane from the dissociation of methane hydrate sediments is transported with dissociated water in pipelines, the memory effect should be minimized. When faster and easier hydrate formation is desired, the memory effect can be utilized. For example, the presence of a hydrophobic solid wall like Teflon has been reported to render the formation of interfacial gaseous states after hydrate dissociation more likely, thus maximizing the size of the memory effect.

The investigation of the effect of dispersion and additives on CO₂ hydrate formation kinetics enables faster and more CO₂ storage in a hydrate form, which is a breakthrough to the bottleneck that hinders the application of clathrate hydrate in gas storage. Our results have shown that gas uptake capacity of hydrate formation in dry water can be further improved by adding additives and this finding can easily be transformed to practice, leading to the improvement of gas storage efficiency and capacity of clathrate hydrates. The industry is highly recommended to research the synergism between dry water and other additives to achieve even better gas storage performance of clathrate hydrates. Meanwhile, our findings are also applicable to carbon capture and sequestration and the relief of the greenhouse effect, which is a main environmental concern nowadays.

8.3 Limitations

In the work of Chapter 3, we used reported value of the specific surface free energy of ice to deduce the specific interfacial free energy (γ_{slc}) value between ice and a liquid of surface tension value of γ_c which neither wets nor dewets ice. During this back calculation process, a limitation is that the specific surface free energy value of ice might not be accurate, which influences the accuracy of the value of γ_{slc} . Another limitation is that we assumed that the value of γ_{slc} of ice is equal to that of THF hydrate. This assumption cannot be validated by experiment because such a liquid that neither wets nor dewets ice or THF hydrate is highly possible hypothetical given the extrapolation of the Zisman plot. A third limitation is that although the contact angle measurement of testing liquids on either an ice or a THF hydrate surface was repeated for several time and the average value was calculated for a higher accuracy of Zisman plot, the roughness or the heterogeneity of sample surface which was supposed to affect contact angle measurement (e.g. by contact pinning) was not examined quantitatively. This factor causes large error bars of the data points and a poor linear fitting of data points, yielding less accurate γ_c . The last limitation is the inability of the extension of experimental procedure to other gas hydrate that requires high pressure

to form, such as CO₂ and methane hydrate.

In the work of Chapter 4, we calculated the shear adhesive strength by dividing the measured force by the cross-sectional area of sample holder. However, because of the surface roughness of solid substrate, actual hydrate-substrate contact area might be higher than the nominal cross-sectional area of sample holder, which renders true shear adhesive strength being overestimated. Unfortunately, this surface roughness effect was not quantified so we do not know how severe the deviation of the true shear adhesive strength from the measured value. Secondly, although our results showed that the shear adhesive strength becomes unmeasurably low at low supercooling which was speculated by the presence of QLL, our setup cannot validate its presence experimentally, let alone estimate the thickness of it. Thirdly, our measurement was conducted at atmospheric pressure, which limits the measurement of the shear adhesive strength for methane/natural gas hydrate. Fourthly, we prepared a superhydrophilic substrate (piranha solution cleaned glass) but did not prepare a superhydrophobic substrate with water contact angle on it higher than 150°, which limits our assessment of the shear adhesive strength over the entire range of substrate's water wettability. Fifthly, our experiments are limited to a lab scale. That is to say, many factors encountered in field operations are not considered. For example, we used milli-Q water rather than brine which is the main component of produced water. The effect of water properties like salinity, pH and a range of impurities are not involved in our research. The substrates used are not corroded and have no scales. The grade of stainless steel used in this work is 304 rather than K55, which is commonly used in the petroleum industry.

In the work of Chapter 5, we used a high-pressure chamber as the reactor of CO₂ hydrate nucleation. Its thick wall and large volume lead to slow heat transfer to the coolant surrounding it, thus large thermal lag. This deficiency limits the linear cooling ramp to a slow rate, which causes low efficiency of nucleation data collection. The large volume also renders fast pressure decrease as cooling, making the maintenance of an isobaric condition, difficult. Secondly, because quasi-

free water droplets nucleated at a deep supercooling (lower than 273 K), it is difficult to visually distinguish ice nucleation from CO₂ hydrate nucleation, from which the accuracy of CO₂ hydrate nucleation curves might be weakened. The third limitation lies in the linear cooling ramp itself, that is, thermal lag, detection lag and guest undersaturation, which has been elaborated in detail in section 5.4. The last limitation is the lack of characterization of the CO₂ hydrate. For example, the determination of hydration number of CO₂ hydrate.

In the work of Chapter 6, since we used the same setup, limitations in the work of Chapter 5 applies as well. In addition, we did not experimentally ascertain the existence of bulk nanobubbles and/or interfacial gaseous states after hydrate dissociation.

In the work of Chapter 7, the main limitation is the inability to determine the nucleation rate of CO₂ hydrate in dry water because of the tightly coated water droplets by nanosilica prevent us from detecting nucleation event visually. This impedes us from understanding the role of dispersion in nucleation in a straightforward manner. We used the volume expansion factor of 1.234 in the literature for CO₂ hydrate to calculate gas moles in the reactor after CO₂ hydrate formation. However, the density of gas hydrate is not a fixed value depending on hydration number which is not measured in this work. Therefore, using the literature value might limit the accuracy of the calculation of gas uptake capacity and gas-to-hydrate conversion.

8.4 Future works

Based on the findings of this study, future work can be conducted from following aspects:

- A new setup could be designed for the measurement of the specific surface free energy of other gas hydrate, for example, methane hydrate and CO₂ hydrate. This requires the injection of testing liquid on the surface of gas hydrate under high pressure condition.
- An experimental procedure for the preparation of a smooth and flat gas hydrate surface could be developed. For example, gas hydrate formation in the confinement.

- Study on the shear adhesive strength can be extended to a wider supercooling range, other kinds of additives and higher hydrophobicity of substrates. Meanwhile, the surface roughness of solid substrates should be uniformed by treatments to rule out the effect on calculated shear adhesive strength.
- Nucleation curves of CO₂ hydrate can be derived in quasi-free water droplets in the presence of different nucleation promoters, such as AgI, to investigate and rank their promoting performance on CO₂ hydrate nucleation kinetics after comparison with the baseline established in this work.
- Nucleation curves of CO₂ hydrate can be derived in quiescent water in contact with solid walls of various materials, shapes (like a sharp corner) and length of TPCL to investigate the dependence of hydrate nucleation kinetics on them.
- Nucleation curves of methane hydrate in the presence and absence of a stainless-steel wall might be established in the future.
- Advanced techniques like transmission electron microscopic can be employed for the identification of bulk nanobubbles in dissociated water.
- Nucleation potency of interfacial gaseous states on different solid walls after hydrate dissociation can be investigated.
- A more hydrophobic nanomaterial than H18 nanosilica might be fabricated to disperse bulk water into smaller droplets to optimize CO₂ gas uptake capacity of dry water CO₂ hydrate.
- Synergistic effect between nucleation promoter and dry water made from SDS solution on methane/natural gas hydrate formation and gas uptake capacity can be investigated.

Reference

- Adamova, T. P., A. S. Stoporev and A. Y. Manakov (2018). "Visual studies of methane hydrate formation on the water–oil boundaries." Crystal Growth & Design **18**(11): 6713-6722.
- Adamova, T. P., A. S. Stoporev, A. P. Semenov, B. I. Kidyarov and A. Y. Manakov (2018). "Methane hydrate nucleation on water—methane and water—Decane boundaries." Thermochimica Acta **668**: 178-184.
- Adamson, A. W., F. P. Shirley and K. T. Kunichika (1970). "Contact angles on molecular solids: I. ice." Journal of Colloid and Interface Science **34**(3): 461-468.
- Alhejaili, A., P. Babu and N. Daraboina (2020). "Effect of salts on TBAB semi clathrate hydrate formation: Application to produced water desalination." Energy & Fuels **34**(10): 12810-12821.
- Aman, Z. M., E. P. Brown, E. D. Sloan, A. K. Sum and C. A. Koh (2011). "Interfacial mechanisms governing cyclopentane clathrate hydrate adhesion/cohesion." Physical Chemistry Chemical Physics **13**(44): 19796-19806.
- Aman, Z. M., L. E. Dieker, G. Aspenes, A. K. Sum, E. D. Sloan and C. A. Koh (2010). "Influence of model oil with surfactants and amphiphilic polymers on cyclopentane hydrate adhesion forces." Energy & Fuels **24**(10): 5441-5445.
- Aman, Z. M. and C. A. Koh (2016). "Interfacial phenomena in gas hydrate systems." Chemical Society Reviews **45**(6): 1678-1690.
- Aman, Z. M., W. J. Leith, G. A. Grasso, E. D. Sloan, A. K. Sum and C. A. Koh (2013). "Adhesion Force between Cyclopentane Hydrate and Mineral Surfaces." Langmuir **29**(50): 15551-15557.
- Aman, Z. M., K. Olcott, K. Pfeiffer, E. D. Sloan, A. K. Sum and C. A. Koh (2013). "Surfactant adsorption and interfacial tension investigations on cyclopentane hydrate." Langmuir **29**(8): 2676-2682.
- Aman, Z. M., E. D. Sloan, A. K. Sum and C. A. Koh (2014). "Adhesion force interactions between cyclopentane hydrate and physically and chemically modified surfaces." Physical Chemistry Chemical Physics **16**(45): 25121-25128.
- Anderson, G. K. (2003). "Enthalpy of dissociation and hydration number of carbon dioxide hydrate

from the Clapeyron equation." The Journal of Chemical Thermodynamics **35**(7): 1171-1183.

Anderson, R., M. Llamedo, B. Tohidi and R. W. Burgass (2003). "Experimental measurement of methane and carbon dioxide clathrate hydrate equilibria in mesoporous silica." The Journal of Physical Chemistry B **107**(15): 3507-3514.

Aspenes, G., L. E. Dieker, Z. M. Aman, S. Høiland, A. K. Sum, C. A. Koh and E. D. Sloan (2010). "Adhesion force between cyclopentane hydrates and solid surface materials." Journal of Colloid and Interface Science **343**(2): 529-536.

Aspenes, G., L. E. Dieker, Z. M. Aman, S. Høiland, A. K. Sum, C. A. Koh and E. D. Sloan (2010). "Adhesion force between cyclopentane hydrates and solid surface materials." J Colloid Interface Sci **343**(2): 529-536.

Bagherzadeh, S. A., S. Alavi, J. Ripmeester and P. Englezos (2015). "Formation of methane nanobubbles during hydrate decomposition and their effect on hydrate growth." The Journal of chemical physics **142**(21): 214701.

Bai, D., G. Chen, X. Zhang and W. Wang (2012). "Nucleation of the CO₂ hydrate from three-phase contact lines." Langmuir **28**(20): 7730-7736.

Barwood, M. T., P. J. Metaxas, V. W. Lim, C. C. Sampson, M. L. Johns, Z. M. Aman and E. F. May (2022). "Extracting nucleation rates from ramped temperature measurements of gas hydrate formation." Chemical Engineering Journal **450**: 137895.

Bathe, M., S. Vagle, G. A. Saunders and E. F. Lambson (1984). "Ultrasonic Wave Velocities in the Structure-II Clathrate Hydrate THF17H₂O." Journal of Materials Science Letters **3**(10): 904-906.

Bhattacharjee, G. and P. Linga (2021). "Amino acids as kinetic promoters for gas hydrate applications: A mini review." Energy & Fuels **35**(9): 7553-7571.

Bishnoi, P., V. Natarajan and N. Kalogerakis (1994). "A Unified Description of the Kinetics of Hydrate Nucleation, Growth, and Decomposition a." Annals of the New York Academy of Sciences **715**(1): 311-322.

Bishnoi, P. R. and V. Natarajan (1996). "Formation and decomposition of gas hydrates." Fluid phase equilibria **117**(1-2): 168-177.

- Boinovich, L. B. and A. M. Emelyanenko (2014). "Experimental determination of the surface energy of polycrystalline ice." Doklady Physical Chemistry **459**(2): 198-202.
- Borgund, A. E., S. Høiland, T. Barth, P. Fotland and K. M. Askvik (2009). "Molecular analysis of petroleum derived compounds that adsorb onto gas hydrate surfaces." Applied Geochemistry **24**(5): 777-786.
- Boufares, A., E. Provost, D. Dalmazzone, V. Osswald, P. Clain, A. Delahaye and L. Fournaison (2018). "Kinetic study of CO₂ hydrates crystallization: Characterization using FTIR/ATR spectroscopy and contribution modeling of equilibrium/non-equilibrium phase-behavior." Chemical Engineering Science **192**: 371-379.
- Bowen, W. R., R. W. Lovitt and C. J. Wright (2000). "Application of atomic force microscopy to the study of micromechanical properties of biological materials." Biotechnology Letters **22**(11): 893-903.
- Brennen, C. E. (2014). Cavitation and bubble dynamics, Cambridge university press.
- Brown, E. P., S. Hu, J. Wells, X. Wang and C. A. Koh (2018). "Direct measurements of contact angles on cyclopentane hydrates." Energy & Fuels **32**(6): 6619-6626.
- Buchanan, P., A. K. Soper, H. Thompson, R. E. Westacott, J. L. Creek, G. Hobson and C. A. Koh (2005). "Search for memory effects in methane hydrate: structure of water before hydrate formation and after hydrate decomposition." The Journal of Chemical Physics **123**(16): 164507.
- Bylov, M. and P. Rasmussen (1997). "Experimental determination of refractive index of gas hydrates." Chemical Engineering Science **52**(19): 3295-3301.
- Cao, X., H. Wang, K. Yang, S. Wu, Q. Chen and J. Bian (2022). "Hydrate-based CO₂ sequestration technology: Feasibilities, mechanisms, influencing factors, and applications." Journal of Petroleum Science Engineering **219**: 111121.
- Carter, B. O., D. J. Adams and A. I. Cooper (2010). "Pausing a stir: heterogeneous catalysis in "dry water"." Green Chemistry **12**(5): 783-785.
- Carter, B. O., W. Wang, D. J. Adams and A. I. Cooper (2010). "Gas storage in "dry water" and "dry gel" clathrates." Langmuir **26**(5): 3186-3193.

Casco, M. E., F. Rey, J. L. Jordá, S. Rudić, F. Fauth, M. Martinez-Escandell, F. Rodríguez-Reinoso, E. V. Ramos-Fernández and J. Silvestre-Albero (2016). "Paving the way for methane hydrate formation on metal–organic frameworks (MOFs)." Chemical Science **7**(6): 3658-3666.

Cha, I., S. Lee, J. D. Lee, G.-w. Lee and Y. Seo (2010). "Separation of SF₆ from gas mixtures using gas hydrate formation." Environmental Science & Technology **44**(16): 6117-6122.

Chenwei, L., W. Zhiyuan, T. Jinlin, Y. Ci and L. Mingzhong (2020). "Fundamental investigation of the adhesion strength between cyclopentane hydrate deposition and solid surface materials." Chemical Engineering Science **217**: 115524.

Christiansen, R. L. and E. D. Sloan Jr (1994). "Mechanisms and kinetics of hydrate formation." Annals of the New York Academy of Sciences **715**(1): 283-305.

Cox, S. J., D. J. F. Taylor, T. G. A. Youngs, A. K. Soper, T. S. Totton, R. G. Chapman, M. Arjmandi, M. G. Hodges, N. T. Skipper and A. Michaelides (2018). "Formation of Methane Hydrate in the Presence of Natural and Synthetic Nanoparticles." Journal of the American Chemical Society **140**(9): 3277-3284.

Das, A., T. A. Farnham, S. Bengaluru Subramanyam and K. K. Varanasi (2017). "Designing ultra-low hydrate adhesion surfaces by interfacial spreading of water-immiscible barrier films." ACS applied materials & interfaces **9**(25): 21496-21502.

Dash, J., H. Fu and J. Wettlaufer (1995). "The premelting of ice and its environmental consequences." Reports on Progress in Physics **58**(1): 115.

Dash, J. G., H. Y. Fu and J. S. Wettlaufer (1995). "The Premelting of Ice and Its Environmental Consequences." Reports on Progress in Physics **58**(1): 115-167.

Dash, J. G., A. W. Rempel and J. S. Wettlaufer (2006). "The physics of premelted ice and its geophysical consequences." Reviews of Modern Physics **78**(3): 695-741.

Davies, S. R., K. C. Hester, J. W. Lachance, C. A. Koh and E. D. Sloan (2009). "Studies of hydrate nucleation with high pressure differential scanning calorimetry." Chemical Engineering Science **64**(2): 370-375.

de Reuck, A. V. S. (1957). "The Surface Free Energy of Ice." Nature **179**(4570): 1119-1120.

Dieker, L. E. (2009). Cyclopentane hydrate interparticle adhesion force measurements, Colorado School of Mines.

Dieker, L. E., Z. M. Aman, N. C. George, A. K. Sum, E. D. Sloan and C. A. Koh (2009). "Micromechanical Adhesion Force Measurements between Hydrate Particles in Hydrocarbon Oils and Their Modifications." Energy & Fuels **23**: 5966-5971.

Dong, S., M. Li, C. Liu, J. Zhang and G. Chen (2020). "Bio-inspired Superhydrophobic Coating with Low Hydrate Adhesion for Hydrate Mitigation." Journal of Bionic Engineering **17**(5): 1019-1028.

Döppenschmidt, A., M. Kappl and H.-J. Butt (1998). "Surface properties of ice studied by atomic force microscopy." The Journal of Physical Chemistry B **102**(40): 7813-7819.

Drachuk, A. O., V. P. Melnikov, N. S. Molokitina, A. N. Nesterov, L. S. Podenko, A. M. Reshetnikov and A. Y. Manakov (2015). "Dissociation behavior of "dry water" C₃H₈ hydrate below ice point: Effect of phase state of unreacted residual water on a mechanism of gas hydrates dissociation." Journal of Energy Chemistry **24**(3): 309-314.

Dufour, L. and R. J. P. Defay, New York-London (1963). "Thermodynamics of Clouds, Acad." 69.

Egemen, E., N. Nirmalakhandan and C. Trevizo (2000). "Predicting surface tension of liquid organic solvents." Environmental science & technology **34**(12): 2596-2600.

Ellison, A., H. Fox and W. Zisman (1953). "Wetting of fluorinated solids by hydrogen-bonding liquids." The Journal of Physical Chemistry **57**(7): 622-627.

Englezos, P. (1993). "Clathrate Hydrates." Industrial & Engineering Chemistry Research **32**(7): 1251-1274.

Englezos, P., N. Kalogerakis, P. Dholabhai and P. Bishnoi (1987). "Kinetics of formation of methane and ethane gas hydrates." Chemical Engineering Science **42**(11): 2647-2658.

Erstad, K., S. Høiland, P. Fotland and T. Barth (2009). "Influence of petroleum acids on gas hydrate wettability." Energy & Fuels **23**(4): 2213-2219.

Eslamimanesh, A., A. H. Mohammadi, D. Richon, P. Naidoo and D. Ramjugernath (2012). "Application of gas hydrate formation in separation processes: A review of experimental studies."

The Journal of Chemical Thermodynamics **46**: 62-71.

Esmailzadeh, F., N. Hamed, D. Karimipourfard and A. Rasoolzadeh (2020). "An insight into the role of the association equations of states in gas hydrate modeling: a review." Petroleum Science **17**: 1432-1450.

Fan, S., L. Yang, Y. Wang, X. Lang, Y. Wen and X. Lou (2014). "Rapid and high capacity methane storage in clathrate hydrates using surfactant dry solution." Chemical Engineering Science **106**: 53-59.

Fan, X., P. Ten, C. Clarke, A. Bramley and Z. Zhang (2003). "Direct measurement of the adhesive force between ice particles by micromanipulation." Powder technology **131**(2-3): 105-110.

Fandiño, O. and L. Ruffine (2014). "Methane hydrate nucleation and growth from the bulk phase: Further insights into their mechanisms." Fuel **117**: 442-449.

Farhang, F., A. V. Nguyen and K. B. Sewell (2014). "Fundamental Investigation of the Effects of Hydrophobic Fumed Silica on the Formation of Carbon Dioxide Gas Hydrates." Energy & Fuels **28**(11): 7025-7037.

Fossen, M., S. Hatscher and L. J. A. O. Ugueto (2023). "Combined Approach to Evaluate Hydrate Slurry Transport Properties through Wetting and Flow Experiments." ACS Omega **8**(3): 2992-3006.

Fox, H. and W. Zisman (1950). "The spreading of liquids on low energy surfaces. I. polytetrafluoroethylene." Journal of Colloid Science **5**(6): 514-531.

Frank, H. S. and M. W. Evans (1945). "Free volume and entropy in condensed systems III. Entropy in binary liquid mixtures; partial molal entropy in dilute solutions; structure and thermodynamics in aqueous electrolytes." The Journal of Chemical Physics **13**(11): 507-532.

Frank, H. S. and A. S. Quist (1961). "Pauling's model and the thermodynamic properties of water." The Journal of Chemical Physics **34**(2): 604-611.

Ganji, H., M. Manteghian, M. Omidkhah and H. R. Mofrad (2007). "Effect of different surfactants on methane hydrate formation rate, stability and storage capacity." Fuel **86**(3): 434-441.

Glew, D. (1962). "Aqueous solubility and the gas-hydrates. The methane-water system1." The Journal of Physical Chemistry **66**(4): 605-609.

Guo, Y., W. Xiao, W. Pu, J. Hu, J. Zhao and L. Zhang (2018). "CH₄ nanobubbles on the hydrophobic solid–water interface serving as the nucleation sites of methane hydrate." Langmuir **34**(34): 10181-10186.

Gupta, P., S. Mondal, R. L. Gardas and J. S. Sangwai (2023). "Investigation on the Effect of Ionic Liquids and Quaternary Ammonium Salts on the Kinetics of Methane Hydrate." Industrial & Engineering Chemistry Research. <https://doi.org/10.1021/acs.iecr.2c04595>

Hardy, S. (1977). "A grain boundary groove measurement of the surface tension between ice and water." Philosophical Magazine **35**(2): 471-484.

Hassanpouryouzband, A., E. Joonaki, M. V. Farahani, S. Takeya, C. Ruppel, J. Yang, N. J. English, J. M. Schicks, K. Edlmann and H. Mehrabian (2020). "Gas hydrates in sustainable chemistry." Chemical Society Reviews **49**(15): 5225-5309.

He, Y., E. S. J. Rudolph, P. L. Zitha and M. Golombok (2011). "Kinetics of CO₂ and methane hydrate formation: An experimental analysis in the bulk phase." Fuel **90**(1): 272-279.

He, Z., F. Mi and F. Ning (2021). "Molecular insights into CO₂ hydrate formation in the presence of hydrophilic and hydrophobic solid surfaces." Energy **234**: 121260.

Hillig, W. B. (1998). "Measurement of interfacial free energy for ice/water system." Journal of crystal growth **183**(3): 463-468.

Høiland, S., T. Barth, A. Blokhus and A. Skauge (2001). "The effect of crude oil acid fractions on wettability as studied by interfacial tension and contact angles." Journal of Petroleum Science and Engineering **30**(2): 91-103.

Høiland, S., K. Askvik, P. Fotland, E. Alagic, T. Barth and F. Fadnes (2005). "Wettability of Freon hydrates in crude oil/brine emulsions." Journal of Colloid and Interface Science **287**(1): 217-225.

Hu, G., Y. Ye, C. Liu, Q. Meng, J. Zhang and S. Diao (2011). "Direct measurement of formation and dissociation rate and storage capacity of dry water methane hydrates." Fuel Processing Technology **92**(8): 1617-1622.

Hu, S. and C. A. Koh (2017). "Interfacial properties and mechanisms dominating gas hydrate cohesion and adhesion in liquid and vapor hydrocarbon phases." Langmuir **33**(42): 11299-11309.

Hyodo, M., J. Yoneda, N. Yoshimoto and Y. Nakata (2013). "Mechanical and dissociation properties of methane hydrate-bearing sand in deep seabed." Soils and Foundations **53**(2): 299-314.

Israelachvili, J. N. (2011). Intermolecular and surface forces, Academic press.

Jacobson, L. C. and V. Molinero (2011). "Can amorphous nuclei grow crystalline clathrates? The size and crystallinity of critical clathrate nuclei." Journal of the American Chemical Society **133**(16): 6458-6463.

Jamialahmadi, M., M. Emadi and H. Müller-Steinhagen (2006). "Diffusion coefficients of methane in liquid hydrocarbons at high pressure and temperature." Journal of Petroleum Science and Engineering **53**(1-2): 47-60.

Jasper, J. J. (1972). "The surface tension of pure liquid compounds." Journal of Physical and Chemical Reference Data **1**(4): 841-1010.

Jeong, K., P. J. Metaxas, J. Chan, T. O. Kuteyi, Z. M. Aman, P. L. Stanwix, M. L. Johns and E. F. May (2019). "Hydrate nucleation and growth on water droplets acoustically-levitated in high-pressure natural gas." Physical Chemistry Chemical Physics **21**(39): 21685-21688.

Jeong, K., P. J. Metaxas, A. Helberg, M. L. Johns, Z. M. Aman and E. F. May (2022). "Gas hydrate nucleation in acoustically levitated water droplets." Chemical Engineering Journal **433**: 133494.

Jimenez-Angeles, F. and A. Firoozabadi (2014). "Induced Charge Density and Thin Liquid Film at Hydrate/Methane Gas Interfaces." Journal of Physical Chemistry C **118**(45): 26041-26048.

Kalogerakis, N., A. Jamaluddin, P. Dholabhai and P. Bishnoi (1993). Effect of surfactants on hydrate formation kinetics. SPE international symposium on oilfield chemistry, New Orleans, Louisiana, OnePetro.

Kang, K. C., P. Linga, K.-n. Park, S.-J. Choi and J. D. Lee (2014). "Seawater desalination by gas hydrate process and removal characteristics of dissolved ions (Na^+ , K^+ , Mg^{2+} , Ca^{2+} , B^{3+} , Cl^- , SO_4^{2-})." Desalination **353**: 84-90.

Kang, S.-P. and J.-W. Lee (2010). "Kinetic behaviors of CO_2 hydrates in porous media and effect of kinetic promoter on the formation kinetics." Chemical Engineering Science **65**(5): 1840-1845.

Kar, A., P. V. Acharya, A. Bhati, A. Mhadeshwar, P. Venkataraman, T. A. Barckholtz, H. Celio, F. Mangolini and V. Bahadur (2021). "Magnesium-promoted rapid nucleation of carbon dioxide hydrates." ACS Sustainable Chemistry Engineering **9**(33): 11137-11146.

Karaaslan, U. and M. Parlaktuna (2000). "Surfactants as hydrate promoters?" Energy & Fuels **14**(5): 1103-1107.

Kashchiev, D. (2000). Nucleation. UK, Elsevier.

Kashchiev, D. and A. Firoozabadi (2002). "Driving force for crystallization of gas hydrates." Journal of Crystal Growth **241**(1-2): 220-230.

Kashchiev, D. and A. Firoozabadi (2002). "Nucleation of gas hydrates." Journal of Crystal Growth **243**(3-4): 476-489.

Kashchiev, D. and A. Firoozabadi (2003). "Induction time in crystallization of gas hydrates." Journal of Crystal Growth **250**(3-4): 499-515.

Ke, W., T. M. Svartaas and D. Chen (2019). "A review of gas hydrate nucleation theories and growth models." Journal of Natural Gas Science and Engineering **61**: 169-196.

Kelland, M. A. (2006). "History of the development of low dosage hydrate inhibitors." Energy & Fuels **20**(3): 825-847.

Ketcham, W. and P. Hobbs (1969). "An experimental determination of the surface energies of ice." Philosophical Magazine **19**(162): 1161-1173.

Khan, M. N., C. J. Peters and C. A. Koh (2019). "Desalination using gas hydrates: The role of crystal nucleation, growth and separation." Desalination **468**: 114049.

Khandelwal, H., M. F. Qureshi, J. Zheng, P. Venkataraman, T. A. Barckholtz, A. B. Mhadeshwar and P. Linga (2020). "Effect of l-tryptophan in promoting the kinetics of carbon dioxide hydrate formation." Energy & Fuels **35**(1): 649-658.

Kim, H., J. Zheng, Z. Yin, S. Kumar, J. Tee, Y. Seo and P. Linga (2022). "An electrical resistivity-based method for measuring semi-clathrate hydrate formation kinetics: Application for cold storage and transport." Applied Energy **308**: 118397.

Kloubek, J. (1974). "Calculation of surface free energy components of ice according to its

wettability by water, chlorobenzene, and carbon disulfide." Journal of Colloid and Interface Science **46**(2): 185-190.

Koh, C. A., E. D. Sloan, A. K. Sum and D. T. Wu (2011). "Fundamentals and applications of gas hydrates." Annual Review of Chemical and Biomolecular Engineering **2**: 237-257.

Korosi, G. and E. S. Kovats (1981). "Density and surface tension of 83 organic liquids." Journal of Chemical and Engineering Data **26**(3): 323-332.

Kou, X., J.-C. Feng, X.-S. Li, Y. Wang and Z.-Y. Chen (2022). "Memory effect of gas hydrate: Influencing factors of hydrate reformation and dissociation behaviors." Applied Energy **306**: 118015.

Kumar, A., G. Bhattacharjee, B. Kulkarni and R. Kumar (2015). "Role of surfactants in promoting gas hydrate formation." Industrial & Engineering Chemistry Research **54**(49): 12217-12232.

Kumar, A., T. Sakpal, P. Linga and R. Kumar (2013). "Influence of contact medium and surfactants on carbon dioxide clathrate hydrate kinetics." Fuel **105**: 664-671.

Kvamme, B., A. Graue, E. Aspenes, T. Kuznetsova, L. Gránásy, G. Tóth, T. Pusztai and G. Tegze (2004). "Kinetics of solid hydrate formation by carbon dioxide: Phase field theory of hydrate nucleation and magnetic resonance imaging." Physical Chemistry Chemical Physics **6**(9): 2327-2334.

Kyung, D., H.-K. Lim, H. Kim and W. Lee (2015). "CO₂ hydrate nucleation kinetics enhanced by an organo-mineral complex formed at the montmorillonite–water interface." Environmental Science & Technology **49**(2): 1197-1205.

Lang, X., S. Fan and Y. Wang (2010). "Intensification of methane and hydrogen storage in clathrate hydrate and future prospect." Journal of Natural Gas Chemistry **19**(3): 203-209.

Lee, J., T. Yun, J. C. Santamarina and C. Ruppel (2007). "Observations related to tetrahydrofuran and methane hydrates for laboratory studies of hydrate-bearing sediments." Geochemistry, Geophysics, Geosystems **8**(6).

Lee, W., J.-Y. Shin, K.-S. Kim and S.-P. Kang (2016). "Kinetic promotion and inhibition of methane hydrate formation by morpholinium ionic liquids with chloride and tetrafluoroborate

anions." Energy & Fuels **30**(5): 3879-3885.

Li, H., P. Stanwix, Z. Aman, M. Johns, E. May and L. Wang (2016). "Raman spectroscopic studies of clathrate hydrate formation in the presence of hydrophobized particles." The Journal of Physical Chemistry A **120**(3): 417-424.

Li, H. and L. Wang (2015). "Hydrophobized particles can accelerate nucleation of clathrate hydrates." Fuel **140**: 440-445.

Li, R., Z. Sun and J. Song (2021). "Enhancement of hydrate formation with amino acids as promoters." Journal of Molecular Liquids **344**: 117880.

Li, S.-L., C.-Y. Sun, B. Liu, Z.-Y. Li, G.-J. Chen and A. K. Sum (2014). "New observations and insights into the morphology and growth kinetics of hydrate films." Scientific Reports **4**(1): 4129.

Li, X.-S., C.-G. Xu, Y. Zhang, X.-K. Ruan, G. Li and Y. Wang (2016). "Investigation into gas production from natural gas hydrate: A review." Applied Energy **172**: 286-322.

Li, Y., N. Wu, C. He, Z. Sun, Z. Zhang, X. Hao, Q. Chen, Q. Bu, C. Liu and J. Sun (2021). "Nucleation probability and memory effect of methane-propane mixed gas hydrate." Fuel **291**: 120103.

Liang, S., D. Rozmanov and P. G. Kusalik (2011). "Crystal growth simulations of methane hydrates in the presence of silica surfaces." Physical Chemistry Chemical Physics **13**(44): 19856-19864.

Lim, V. W., M. T. Barwood, P. J. Metaxas, M. L. Johns, Z. M. Aman and E. F. May (2022). "Nucleation rates of carbon dioxide hydrate." Chemical Engineering Journal **443**: 136359.

Lim, V. W., P. J. Metaxas, P. L. Stanwix, M. L. Johns, G. Haandrikman, D. Crosby, Z. M. Aman and E. F. May (2020). "Gas hydrate formation probability and growth rate as a function of kinetic hydrate inhibitor (KHI) concentration." Chemical Engineering Journal **388**: 124177.

Lin, W., G.-J. Chen, C.-Y. Sun, X.-Q. Guo, Z.-K. Wu, M.-Y. Liang, L.-T. Chen and L.-Y. Yang (2004). "Effect of surfactant on the formation and dissociation kinetic behavior of methane hydrate." Chemical Engineering Science **59**(21): 4449-4455.

Liu, C., Z. Wang, J. Tian, C. Yan and M. Li (2020). "Fundamental investigation of the adhesion

strength between cyclopentane hydrate deposition and solid surface materials." Chemical Engineering Science **217**.

Liu, C., X. Zeng, C. Yan, C. Zhou, M. Li and Z. Wang (2020). "Effects of Solid Precipitation and Surface Corrosion on the Adhesion Strengths of Sintered Hydrate Deposits on Pipe Walls." Langmuir **36**(50): 15343-15351.

Liu, H., S. Zhan, P. Guo, S. Fan and S. Zhang (2018). "Understanding the characteristic of methane hydrate equilibrium in materials and its potential application." Chemical Engineering Journal **349**: 775-781.

Liu, Y., B. Chen, Y. Chen, S. Zhang, W. Guo, Y. Cai, B. Tan and W. Wang (2015). "Methane storage in a hydrated form as promoted by leucines for possible application to natural gas transportation and storage." Energy Technology **3**(8): 815-819.

Lo, C., J. Zhang, P. Somasundaran, S. Lu, A. Couzis and J. Lee (2008). "Adsorption of surfactants on two different hydrates." Langmuir **24**(22): 12723-12726.

Maeda, N. (2015). "Is the surface of gas hydrates dry?" Energies **8**(6): 5361-5369.

Maeda, N. (2015). "Nucleation curves of model natural gas hydrates on a quasi-free water droplet." AIChE Journal **61**(8): 2611-2617.

Maeda, N. (2016). "Nucleation curves of methane–propane mixed gas hydrates in hydrocarbon oil." Chemical Engineering Science **155**: 1-9.

Maeda, N. (2016). "Nucleation curves of methane–propane mixed gas hydrates in the presence of a stainless steel wall." Fluid Phase Equilibria **413**: 142-147.

Maeda, N. (2018). "Interfacial nanobubbles and the memory effect of natural gas hydrates." The Journal of Physical Chemistry C **122**(21): 11399-11406.

Maeda, N. (2018). "Nucleation curves of methane hydrate from constant cooling ramp methods." Fuel **223**: 286-293.

Maeda, N. (2019). "Nucleation curve of carbon dioxide hydrate from a linear cooling ramp method." The Journal of Physical Chemistry A **123**(37): 7911-7919.

Maeda, N. (2020). Nucleation of Gas Hydrates. Cham, Switzerland, Springer International

Publishing.

Maeda, N. (2020). Nucleation of Gas Hydrates. Nucleation of Gas Hydrates, Springer: 111-148.

Maeda, N., Z. M. Aman, K. A. Kozielski, C. A. Koh, E. D. Sloan and A. K. Sum (2013). "Measurements of Cohesion Hysteresis between Cyclopentane Hydrates in Liquid Cyclopentane." Energy & Fuels **27**(9): 5168-5174.

Maeda, N., K. J. Rosenberg, J. N. Israelachvili and R. M. Pashley (2004). "Further studies on the effect of degassing on the dispersion and stability of surfactant-free emulsions." Langmuir **20**(8): 3129-3137.

Maeda, N. and X.-d. Shen (2019). "Scaling laws for nucleation rates of gas hydrate." Fuel **253**: 1597-1604.

Maeda, N., D. Wells, N. C. Becker, P. G. Hartley, P. W. Wilson, A. D. Haymet and K. A. Kozielski (2011). "Development of a high pressure automated lag time apparatus for experimental studies and statistical analyses of nucleation and growth of gas hydrates." Review of Scientific Instruments **82**(6): 065109.

Majid, A. A., J. Worley and C. A. Koh (2021). "Thermodynamic and kinetic promoters for gas hydrate technological applications." Energy & Fuels **35**(23): 19288-19301.

Makkonen, L. (1997). "Surface melting of ice." The Journal of Physical Chemistry B **101**(32): 6196-6200.

Makogon, I. U. r. F. (1981). Hydrates of natural gas, PennWell Books Tulsa, Oklahoma.

Makogon, Y. F. (1981). Hydrates of Natural Gas, translated from Russian by WJ Cieslewicz. Tulsa, Oklahoma.

Manakov, A. Y. and A. S. Stoporev (2021). "Physical chemistry and technological applications of gas hydrates: topical aspects." Russian Chemical Reviews **90**(5): 566-600.

Mason, B. J. (1952). "The spontaneous crystallization of supercooled water." Quarterly Journal of the Royal Meteorological Society **78**(335): 22-27.

Matsumoto, K., M. Murase, K. Ehara, J. Sakamoto and J. Ueda (2017). "Investigation on adhesion force of TBAB hydrate to cooling copper surface." International Journal of Refrigeration **78**: 121-

127.

Max, M. D. (2003). Natural gas hydrate in oceanic and permafrost environments. Netherlands, Springer Science & Business Media.

Max, M. D. and A. H. Johnson (2018). Exploration and production of oceanic natural gas hydrate: Critical factors for commercialization. Switzerland, Springer.

McDonald, J. E. (1953). "Homogeneous nucleation of supercooled water drops." Journal of Atmospheric Sciences **10**(6): 416-433.

Medina, A., A. Pineda and C. Trevino (2003). "Imbibition driven by a temperature gradient." Journal of the Physical Society of Japan **72**(5): 979-982.

Meng, Z., S.-L. Yang, Y. Cui, Z.-Y. Zhong, C.-G. Liang, L. Wang, K. Qian, Q.-Z. Ma and J.-R. Wang (2018). "Enhancement of the imbibition recovery by surfactants in tight oil reservoirs." Petroleum Science **15**: 783-793.

Metaxas, P. J., V. W. Lim, C. Booth, J. Zhen, P. L. Stanwix, M. L. Johns, Z. M. Aman, G. Haandrikman, D. Crosby and E. F. May (2019). "Gas hydrate formation probability distributions: Induction times, rates of nucleation and growth." Fuel **252**: 448-457.

Mirzaeifard, S., P. Servio and A. D. Rey (2019). "Multiscale modeling and simulation of water and methane hydrate crystal interface." Crystal Growth & Design **19**(9): 5142-5151.

Mohr, S., R. Pétuya, J. Wylde, J. Sarria, N. Purkayastha, Z. Ward, S. Bodnar and I. N. Tsimpanogiannis (2021). "Size dependence of the dissociation process of spherical hydrate particles via microsecond molecular dynamics simulations." Physical Chemistry Chemical Physics **23**(19): 11180-11185.

Morita, M., M. Matsumoto, S. Usui, T. Abe, N. Denkov, O. Velev and I. B. Ivanov (1992). "Interfacial properties and emulsion stability in fluorinated oil—non-fluorinated oil—surfactant (s) systems." Colloids and surfaces **67**: 81-93.

Muller-Bongartz, B., T. Wildeman and R. Sloan (1992). A Hypothesis For Hydrate Nucleation Phenomena. The Second International Offshore and Polar Engineering Conference, San Francisco, California, OnePetro.

Naeiji, P. and F. Varaminian (2017). "Effect of Sodium Dodecyl Sulphate on Gas Hydrate Formation Kinetics of Methane and Ethane Mixtures." Gas Processing Journal **5**(1): 65-74.

Naeiji, P., F. Varaminian and M. Rahmati (2017). "Comparison of the thermodynamic, structural and dynamical properties of methane/water and methane/water/hydrate systems using molecular dynamic simulations." Journal of Natural Gas Science and Engineering **44**: 122-130.

Natarajan, V., P. Bishnoi and N. Kalogerakis (1994). "Induction phenomena in gas hydrate nucleation." Chemical Engineering Science **49**(13): 2075-2087.

Naullage, P. M., A. A. Bertolazzo and V. Molinero (2019). "How do surfactants control the agglomeration of clathrate hydrates?" ACS Central Science **5**(3): 428-439.

Nerheim, A. R., T. M. Svartaas and E. K. Samuelsen (1992). Investigation of hydrate kinetics in the nucleation and early growth phase by laser light scattering. The Second International Offshore and Polar Engineering Conference, San Francisco, California, OnePetro.

Nesterov, A. N. and A. M. Reshetnikov (2019). "New combination of thermodynamic and kinetic promoters to enhance carbon dioxide hydrate formation under static conditions." Chemical Engineering Journal **378**: 122165.

Nguyen, N. N., R. Berger, M. Kappl and H.-J. Butt (2021). "Clathrate Adhesion Induced by Quasi-Liquid Layer." Journal of Physical Chemistry C **125**(38): 21293-21300.

Nguyen, N. N., R. d. Berger and H.-J. r. Butt (2019). "Surface premelting and interfacial interactions of semi-clathrate hydrate." The Journal of Physical Chemistry C **123**(39): 24080-24086.

Nguyen, N. N., R. d. Berger, M. Kappl and H.-J. r. Butt (2021). "Clathrate Adhesion Induced by Quasi-Liquid Layer." The Journal of Physical Chemistry C **125**(38): 21293-21300.

Nguyen, N. N. and A. V. Nguyen (2017). "Hydrophobic effect on gas hydrate formation in the presence of additives." Energy & Fuels **31**(10): 10311-10323.

Nguyen, N. N., A. V. Nguyen, K. M. Steel, L. X. Dang and M. Galib (2017). "Interfacial Gas Enrichment at Hydrophobic Surfaces and the Origin of Promotion of Gas Hydrate Formation by Hydrophobic Solid Particles." The Journal of Physical Chemistry C **121**(7): 3830-3840.

Nguyen, N. N., C. V. Nguyen, T. A. Nguyen and A. V. Nguyen (2022). "Surface Science in the Research and Development of Hydrate-Based Sustainable Technologies." ACS Sustainable Chemistry & Engineering **10**(13): 4041-4058.

Nicholas, J. W., L. E. Dieker, E. D. Sloan and C. A. Koh (2009). "Assessing the feasibility of hydrate deposition on pipeline walls—Adhesion force measurements of clathrate hydrate particles on carbon steel." Journal of Colloid and Interface Science **331**(2): 322-328.

Ohmura, R., S. Matsuda, T. Uchida, T. Ebinuma and H. Narita (2005). "Clathrate hydrate crystal growth in liquid water saturated with a guest substance: observations in a methane+ water system." Crystal Growth & Design **5**(3): 953-957.

Ohmura, R., M. Ogawa, K. Yasuoka and Y. H. Mori (2003). "Statistical study of clathrate-hydrate nucleation in a water/hydrochlorofluorocarbon system: Search for the nature of the “memory effect”." The Journal of Physical Chemistry B **107**(22): 5289-5293.

Okutani, K., Y. Kuwabara and Y. H. Mori (2008). "Surfactant effects on hydrate formation in an unstirred gas/liquid system: An experimental study using methane and sodium alkyl sulfates." Chemical Engineering Science **63**(1): 183-194.

Oyama, H., W. Shimada, T. Ebinuma, Y. Kamata, S. Takeya, T. Uchida, J. Nagao and H. Narita (2005). "Phase diagram, latent heat, and specific heat of TBAB semiclathrate hydrate crystals." Fluid Phase Equilibria **234**(1-2): 131-135.

Parent, J. and P. Bishnoi (1996). "Investigations into the nucleation behaviour of methane gas hydrates." Chemical Engineering Communications **144**(1): 51-64.

Park, J., K. Shin, J. Kim, H. Lee, Y. Seo, N. Maeda, W. Tian and C. D. Wood (2015). "Effect of Hydrate Shell Formation on the Stability of Dry Water." The Journal of Physical Chemistry C **119**(4): 1690-1699.

Phan, A., H. M. Stoner, M. Stamatakis, C. A. Koh and A. Striolo (2022). "Surface morphology effects on clathrate hydrate wettability." Journal of Colloid and Interface Science **611**: 421-431.

Podenko, L., A. Drachuk, N. Molokitina and A. Nesterov (2018). "Effect of silica nanoparticles on dry water gas hydrate formation and self-preservation efficiency." Russian Journal of Physical

Chemistry A **92**(2): 255-261.

Prasad, P. S. and B. Sai Kiran (2018). "Clathrate hydrates of greenhouse gases in the presence of natural amino acids: storage, transportation and separation applications." Scientific Reports **8**(1): 1-10.

Qiu, Y. and V. Molinero (2018). "Why is it so difficult to identify the onset of ice premelting?" The Journal of Physical Chemistry Letters **9**(17): 5179-5182.

Radhakrishnan, R. and B. L. Trout (2002). "A new approach for studying nucleation phenomena using molecular simulations: Application to CO₂ hydrate clathrates." The Journal of Chemical Physics **117**(4): 1786-1796.

Ripmeester, J. A. and S. Alavi (2016). "Some current challenges in clathrate hydrate science: Nucleation, decomposition and the memory effect." Current Opinion in Solid State and Materials Science **20**(6): 344-351.

Ripmeester, J. A., J. S. Tse, C. I. Ratcliffe and B. M. Powell (1987). "A New Clathrate Hydrate Structure." Nature **325**(6100): 135-136.

Rodger, P. M. (2000). "Methane hydrate: melting and memory." Annals of the New York Academy of Sciences **912**(1): 474-482.

Roozeboom, H. B. J. R. d. T. C. d. P. B. (1884). "Sur l'hydrate de chlore." **3**(2): 59-72.

Roozeboom, H. B. J. R. d. T. C. d. P. B. (1884). "Sur l'hydrate de l'acide sulfureux." **3**(2): 29-58.

S. B. Cha, H. O., T. R. Wildeman and E. D. Sloan (1988). "A third-surface effect on hydrate formation." The Journal of Physical Chemistry **92**(23): 6492-6494.

Sakamaki, R. Y., K.; Ohmura, R.; Grzelak, E.; Wu, D. T.; Sum, K. (2011). Calculation of interfacial tensions between hydrate and liquid phases using molecular simulation. 7th International Conference on Gas Hydrate (ICGH); Edinburgh: Scotland, UK.

Saleh, K., L. Forny, P. Guigon and I. Pezron (2011). "Dry water: From physico-chemical aspects to process-related parameters." Chemical Engineering Research and Design **89**(5): 537-544.

Schaefer, R., M. Glicksman and J. Ayers (1975). "High-confidence measurement of solid/liquid surface energy in a pure material." Philosophical Magazine **32**(4): 725-743.

- Sefidroodi, H., E. Abrahamsen and M. A. Kelland (2013). "Investigation into the strength and source of the memory effect for cyclopentane hydrate." Chemical Engineering Science **87**: 133-140.
- Seo, Y., S. Lee, I. Cha, J. D. Lee and H. Lee (2009). "Phase equilibria and thermodynamic modeling of ethane and propane hydrates in porous silica gels." The Journal of Physical Chemistry B **113**(16): 5487-5492.
- Shimada, W., T. Ebinuma, H. Oyama, Y. Kamata, S. Takeya, T. Uchida, J. Nagao and H. Narita (2003). "Separation of gas molecule using tetra-n-butyl ammonium bromide semi-clathrate hydrate crystals." Japanese Journal of Applied Physics **42**(2A): L129.
- Shimada, W., M. Shiro, H. Kondo, S. Takeya, H. Oyama, T. Ebinuma and H. Narita (2005). "Tetra-n-butylammonium bromide–water (1/38)." Acta Crystallographica Section C: Crystal Structure Communications **61**(2): o65-o66.
- Shipp, W. E. (1970). "Surface tension of binary mixtures of several organic liquids at 25. deg." Journal of Chemical and Engineering Data **15**(2): 308-311.
- Simons, S. and R. Fairbrother (2000). "Direct observations of liquid binder–particle interactions: the role of wetting behaviour in agglomerate growth." Powder Technology **110**(1-2): 44-58.
- Sloan, E. D. (2010). Natural gas hydrates in flow assurance. UK, Gulf Professional Publishing.
- Sloan, E. D. and C. A. Koh (2008). Clathrate Hydrates of Natural Gases. Boca Raton, CRC Press.
- Sloan, E. D., C. A. Koh, A. Sum, A. L. Ballard, J. L. Creek, M. Eaton, J. Lachance, N. McMullen, T. Palermo, G. Shoup and L. Talley (2011). Natural Gas Hydrates in Flow Assurance. Burlington, MA, USA, Gulf Professional Publishing.
- Sloan, E. D., S. Subramanian, P. Matthews, J. Lederhos and A. Khokhar (1998). "Quantifying hydrate formation and kinetic inhibition." Industrial & Engineering Chemistry Research **37**(8): 3124-3132.
- Sloan Jr, E. and F. Fleyfel (1991). "A molecular mechanism for gas hydrate nucleation from ice." AIChE Journal **37**(9): 1281-1292.
- Sloan Jr, E. D. (2003). "Fundamental principles and applications of natural gas hydrates." Nature

426(6964): 353-359.

Smith, J. D., A. J. Meuler, H. L. Bralower, R. Venkatesan, S. Subramanian, R. E. Cohen, G. H. McKinley and K. K. Varanasi (2012). "Hydrate-phobic surfaces: fundamental studies in clathrate hydrate adhesion reduction." Physical Chemistry Chemical Physics **14**(17): 6013-6020.

Song, J. H., A. Couzis and J. W. Lee (2010). "Investigation of macroscopic interfacial dynamics between clathrate hydrates and surfactant solutions." Langmuir **26**(23): 18119-18124.

Song, Y., Y. Zhu, W. Liu, J. Zhao, Y. Li, Y. Chen, Z. Shen, Y. Lu and C. Ji (2014). "Experimental research on the mechanical properties of methane hydrate-bearing sediments during hydrate dissociation." Marine and Petroleum Geology **51**: 70-78.

Sowa, B. and N. Maeda (2015). "Statistical study of the memory effect in model natural gas hydrate systems." The Journal of Physical Chemistry A **119**(44): 10784-10790.

Sowa, B., X. H. Zhang, D. E. Dunstan, K. Kozielski, P. G. Hartley and N. Maeda (2014). "Formation of Ice, Tetrahydrofuran Hydrate, and Methane/Propane Mixed Gas Hydrates in Strong Monovalent Salt Solutions." Energy & Fuels **28**: 6877-6888.

Sowa, B., X. H. Zhang, K. Kozielski, P. G. Hartley and N. Maeda (2011). "Influence of dissolved atmospheric gases on the spontaneous emulsification of alkane- ethanol- water systems." The Journal of Physical Chemistry C **115**(17): 8768-8774.

Span, R. and W. Wagner (1996). "A new equation of state for carbon dioxide covering the fluid region from the triple-point temperature to 1100 K at pressures up to 800 MPa." Journal of Physical and Chemical Reference Data **25**(6): 1509-1596.

Stoner, H. M., A. Phan, A. Striolo and C. A. Koh (2021). "Water wettability coupled with film growth on realistic cyclopentane hydrate surfaces." Langmuir **37**(42): 12447-12456.

Stoporev, A. S., A. Y. Manakov, L. K. Altunina, L. A. Strelets and V. I. Kosyakov (2015). "Nucleation rates of methane hydrate from water in oil emulsions." Canadian Journal of Chemistry **93**(8): 882-887.

Stoporev, A. S., A. P. Semenov, V. I. Medvedev, B. I. Kidyarov, A. Y. Manakov and V. A. Vinokurov (2018). "Nucleation of gas hydrates in multiphase systems with several types of interfaces."

Journal of Thermal Analysis and Calorimetry **134**(1): 783-795.

Stoporev, A. S., A. P. Semenov, V. I. Medvedev, A. A. Sizikov, P. A. Gushchin, V. A. Vinokurov and A. Y. Manakov (2018). "Visual observation of gas hydrates nucleation and growth at a water–organic liquid interface." Journal of Crystal Growth **485**: 54-68.

Stoporev, A. S., L. I. Svarovskaya, L. A. Strelets, L. K. Altunina and A. Y. Manakov (2018). "Effect of reactor wall material on the nucleation of methane hydrate in water-in-oil emulsions." Mendelevov Communications **28**(3): 343-344.

Suess, E., M. Torres, G. Bohrmann, R. Collier, D. Rickert, C. Goldfinger, P. Linke, A. Heuser, H. Sahling and K. J. G. M.-A. G. U. Heeschen (2001). "Sea floor methane hydrates at Hydrate Ridge, Cascadia margin." **124**: 87-98.

Sugimoto, T., T. Takahashi, H. Itoh, S.-i. Sato and A. Muramatsu (1997). "Direct measurement of interparticle forces by the optical trapping technique." Langmuir **13**(21): 5528-5530.

Tabaaza, G. A., I. U. Haq, D. B. Zain and B. Lal (2022). "Toxicological issues of conventional gas hydrate inhibitors." Process Safety Progress **41**: S135-S140.

Takahashi, M., T. Kawamura, Y. Yamamoto, H. Ohnari, S. Himuro and H. Shakutsui (2003). "Effect of shrinking microbubble on gas hydrate formation." The Journal of Physical Chemistry B **107**(10): 2171-2173.

Takeya, S., A. Hori, T. Hondoh and T. Uchida (2000). "Freezing-memory effect of water on nucleation of CO₂ hydrate crystals." The Journal of Physical Chemistry B **104**(17): 4164-4168.

Tariq, M., E. Connor, J. Thompson, M. Khraisheh, M. Atilhan and D. Rooney (2016). "Doubly dual nature of ammonium-based ionic liquids for methane hydrates probed by rocking-rig assembly." RSC advances **6**(28): 23827-23836.

Taylor, C. J., L. E. Dieker, K. T. Miller, C. A. Koh and E. D. Sloan Jr (2007). "Micromechanical adhesion force measurements between tetrahydrofuran hydrate particles." Journal of Colloid and Interface Science **306**(2): 255-261.

Thomas, F., D. Dalmazzone and J. F. Morris (2021). "Contact angle measurements on cyclopentane hydrates." Chemical Engineering Science **229**: 116022.

Tohidi, B., R. Anderson, H. Mozaffar and F. Tohidi (2015). "The Return of Kinetic Hydrate Inhibitors." Energy & Fuels **29**(12): 8254-8260.

Tohidi, B., R. Burgass, A. Danesh, K. Østergaard and A. Todd (2000). "Improving the accuracy of gas hydrate dissociation point measurements." Annals of the New York Academy of Sciences **912**(1): 924-931.

Trivedi, V. and S. V. Dalvi (2020). "Enhancing CO₂ hydrate formation: Effect of coconut fibers on nucleation kinetics of CO₂ hydrates." Journal of Crystal Growth **549**: 125865.

Tsimpanogiannis, I. N. (2021). "A novel hybrid method for the calculation of methane hydrate–water interfacial tension along the three-phase (hydrate–liquid water–vapor) equilibrium line." The Journal of Chemical Physics **155**(2): 024702.

Turnbull, D. (1950). "Formation of crystal nuclei in liquid metals." Journal of Applied Physics **21**(10): 1022-1028.

Turner, D. J. (2005). Clathrate hydrate formation in water-in-oil dispersions, Colorado School of Mines.

Turner, D. J., K. T. Miller and E. D. Sloan (2009). "Methane hydrate formation and an inward growing shell model in water-in-oil dispersions." Chemical Engineering Science **64**(18): 3996-4004.

Uchida, T., T. Ebinuma and T. Ishizaki (1999). "Dissociation condition measurements of methane hydrate in confined small pores of porous glass." The Journal of Physical Chemistry B **103**(18): 3659-3662.

Uchida, T., T. Ebinuma, S. Takeya, J. Nagao and H. Narita (2002). "Effects of pore sizes on dissociation temperatures and pressures of methane, carbon dioxide, and propane hydrates in porous media." The Journal of Physical Chemistry B **106**(4): 820-826.

Uchida, T., K. Yamazaki and K. Gohara (2016). "Gas nanobubbles as nucleation acceleration in the gas-hydrate memory effect." The Journal of Physical Chemistry C **120**(47): 26620-26629.

Uchida, T., K. Yamazaki and K. Gohara (2016). "Generation of micro-and nano-bubbles in water by dissociation of gas hydrates." Korean Journal of Chemical Engineering **33**(5): 1749-1755.

Vanderwaals, J. H. and J. C. Platteeuw (1959). "Clathrate Solutions." Advances in Chemical Physics **2**: 1-57.

Veluswamy, H. P., W. I. Chin and P. Linga (2014). "Clathrate hydrates for hydrogen storage: the impact of tetrahydrofuran, tetra-n-butylammonium bromide and cyclopentane as promoters on the macroscopic kinetics." International Journal of Hydrogen Energy **39**(28): 16234-16243.

Veluswamy, H. P., Q. W. Hong and P. Linga (2016). "Morphology study of methane hydrate formation and dissociation in the presence of amino acid." Crystal Growth & Design **16**(10): 5932-5945.

Veluswamy, H. P., R. Kumar and P. Linga (2014). "Hydrogen storage in clathrate hydrates: Current state of the art and future directions." Applied Energy **122**: 112-132.

Verrett, J., D. Posteraro and P. Servio (2012). "Surfactant effects on methane solubility and mole fraction during hydrate growth." Chemical Engineering Science **84**: 80-84.

Vlasic, T. M., P. D. Servio and A. D. Rey (2019). "THF hydrates as model systems for natural gas hydrates: comparing their mechanical and vibrational properties." Industrial & Engineering Chemistry Research **58**(36): 16588-16596.

Vysniauskas, A. and P. Bishnoi (1983). "A kinetic study of methane hydrate formation." Chemical Engineering Science **38**(7): 1061-1072.

Vysniauskas, A. and P. Bishnoi (1985). "Kinetics of ethane hydrate formation." Chemical Engineering Science **40**(2): 299-303.

Walsh, M. R., G. T. Beckham, C. A. Koh, E. D. Sloan, D. T. Wu and A. K. Sum (2011). "Methane hydrate nucleation rates from molecular dynamics simulations: Effects of aqueous methane concentration, interfacial curvature, and system size." The Journal of Physical Chemistry C **115**(43): 21241-21248.

Wang, J., R. Wang, R.-H. Yoon and Y. Seol (2014). "Use of Hydrophobic Particles as Kinetic Promoters for Gas Hydrate Formation." Journal of Chemical & Engineering Data **60**(2): 383-388.

Wang, P., Y. Teng, Y. Zhao and J. Zhu (2021). "Experimental Studies on Gas Hydrate-Based CO₂ Storage: State-of-the-Art and Future Research Directions." Energy Technology **9**(7): 2100004.

Wang, S., S. Fan, Y. Song, X. Lang, Y. Wang, G. Li and J. Chen (2019). "The effect of NaCl concentration and corrosion on cohesion/adhesion forces of structure-II hydrate particles." Scientia Sinica-Physica Mechanica & Astronomica **49**(3).

Wang, X. and M. Dennis (2015). "An experimental study on the formation behavior of single and binary hydrates of TBAB, TBAF and TBPB for cold storage air conditioning applications." Chemical Engineering Science **137**: 938-946.

Wei, Y. and M. Nobuo (2023). "Nucleation Curves of Carbon Dioxide Hydrate in the Absence of a Solid Wall." Energy & Fuels **37**(5): 3760-3774.

Weixing Wang, C. L. B., Dave J. Adams and Andrew I. Cooper (2008). "Methane Storage in Dry Water Gas Hydrates." JACS communications **130**(35): 11608–11609.

Wilson, P. and A. Haymet (2010). "Hydrate formation and re-formation in nucleating THF/water mixtures show no evidence to support a “memory” effect." Chemical Engineering Journal **161**(1-2): 146-150.

Wu, Q. and B. Zhang (2010). "Memory effect on the pressure-temperature condition and induction time of gas hydrate nucleation." Journal of Natural Gas Chemistry **19**(4): 446-451.

Xue, K., J. Zhao, Y. Song, W. Liu, W. Lam, Y. Zhu, Y. Liu, C. Cheng and D. Liu (2012). "Direct observation of THF hydrate formation in porous microstructure using magnetic resonance imaging." Energies **5**(4): 898-910.

Yang, Q., J. B. You, B. Tian, S. Sun, D. Daniel, Q. Liu and X. Zhang "Water-mediated adhesion of oil sands on solid surfaces at low temperature." DOI 10.33774/chemrxiv-2021-flzvq: in press.

Yang, S.-o., D. M. Kleehammer, Z. Huo, E. D. Sloan and K. T. Miller (2004). "Temperature dependence of particle–particle adherence forces in ice and clathrate hydrates." Journal of Colloid and Interface Science **277**(2): 335-341.

Yeung, A. K. and R. Pelton (1996). "Micromechanics: a new approach to studying the strength and breakup of flocs." Journal of Colloid and Interface Science **184**(2): 579-585.

Yin, Z., J. Zheng, H. Kim, Y. Seo and P. Linga (2021). "Hydrates for cold energy storage and transport: A review." Advances in Applied Energy **2**: 100022.

Yoshizawa, H., Y. L. Chen and J. Israelachvili (1993). "Fundamental Mechanisms of Interfacial Friction .1. Relation between Adhesion and Friction." Journal of Physical Chemistry **97**(16): 4128-4140.

Yun, T. S., J. C. Santamarina and C. Ruppel (2007). "Mechanical properties of sand, silt, and clay containing tetrahydrofuran hydrate." Journal of Geophysical Research-Solid Earth **112**(B4).

Zare, M., A. Haghtalab, A. N. Ahmadi, K. Nazari and A. Mehdizadeh (2015). "Effect of imidazolium based ionic liquids and ethylene glycol monoethyl ether solutions on the kinetic of methane hydrate formation." Journal of Molecular Liquids **204**: 236-242.

ZareNezhad, B., M. Mottahedin and F. Varaminian (2014). "Effects of process variables on the initial gas hydrate formation rate: the case of ethane hydrate formation in the absence or presence of SDS kinetic promoter." Journal of Molecular Liquids **198**: 57-62.

Zarifi, M., J. Javanmardi, H. Hashemi, A. Eslamimanesh and A. H. Mohammadi (2016). "Experimental study and thermodynamic modelling of methane and mixed C1+ C2+ C3 clathrate hydrates in the presence of mesoporous silica gel." Fluid Phase Equilibria **423**: 17-24.

Zatsepina, O. Y. and B. A. Buffett (1997). "Phase equilibrium of gas hydrate: Implications for the formation of hydrate in the deep sea floor." Geophysical Research Letters **24**(13): 1567-1570.

Zdziennicka, A., J. Krawczyk, K. Szymczyk and B. Jańczuk (2017). "Components and parameters of liquids and some polymers surface tension at different temperature." Colloids and Surfaces A: Physicochemical and Engineering Aspects **529**: 864-875.

Zebardast, S. and A. Haghtalab (2022). "Thermodynamic modeling and measurement of CO₂ clathrate equilibrium conditions with a hydrophobic surface—An application in dry water hydrate." Chemical Engineering Science **251**: 117486.

Zeng, H., I. L. Moudrakovski, J. A. Ripmeester and V. K. Walker (2006). "Effect of antifreeze protein on nucleation, growth and memory of gas hydrates." AIChE journal **52**(9): 3304-3309.

Zerpa, L. E., Z. M. Aman, S. Joshi, I. Rao, E. D. Sloan, C. Koh and A. Sum (2012). Predicting hydrate blockages in oil, gas and water-dominated systems. Offshore technology conference, Houston, Texas, OnePetro.

Zerpa, L. E., J.-L. Salager, C. A. Koh, E. D. Sloan and A. K. Sum (2011). "Surface chemistry and gas hydrates in flow assurance." Industrial & Engineering Chemistry Research **50**(1): 188-197.

Zhang, F., X. Wang, B. Wang, X. Lou and W. Lipiński (2022). "Experimental and numerical analysis of CO₂ and CH₄ hydrate formation kinetics in microparticles: A comparative study based on shrinking core model." Chemical Engineering Journal **446**: 137247.

Zhang, G., X. Shi and F. Wang (2022). "Methane hydrate production using a novel spiral-agitated reactor: promotion of hydrate formation kinetics." AIChE Journal **68**(1): e17423.

Zhang, J., M. Di Lorenzo and Z. Pan (2012). "Effect of surface energy on carbon dioxide hydrate formation." The Journal of Physical Chemistry B **116**(24): 7296-7301.

Zhang, J. and J. W. Lee (2009). "Enhanced kinetics of CO₂ hydrate formation under static conditions." Industrial & engineering chemistry research **48**(13): 5934-5942.

Zhang, J., S. Lee and J. W. Lee (2007). "Kinetics of methane hydrate formation from SDS solution." Industrial & Engineering Chemistry Research **46**(19): 6353-6359.

Zhang, Q., C. Li, Q. Wu and B. Zhang (2018). "Effect of dry water on methane separation and recovery from coal mine gas based on hydrate." RSC advances **8**(48): 27171-27180.

Zhang, X., H. Li and N. Maeda (2021). "Nucleation curves of ice in quasi-free water droplets." Chemical Engineering Science **242**: 116751.

Zhang, X. and N. Maeda (2022). "Nucleation curves of ice in the presence of nucleation promoters." Chemical Engineering Science **262**: 118017.

Zhang, X. H., N. Maeda and V. S. Craig (2006). "Physical properties of nanobubbles on hydrophobic surfaces in water and aqueous solutions." Langmuir **22**(11): 5025-5035.

Zhao, J., L. Yao, Y. Song, K. Xue, C. Cheng, Y. Liu and Y. Zhang (2011). "In situ observations by magnetic resonance imaging for formation and dissociation of tetrahydrofuran hydrate in porous media." Magnetic Resonance Imaging **29**(2): 281-288.

Zhong, Y. and R. Rogers (2000). "Surfactant effects on gas hydrate formation." Chemical Engineering Science **55**(19): 4175-4187.

Zisman, W. A. (1964). Relation of the equilibrium contact angle to liquid and solid constitution,

ACS Publications.